DUAL FUNCTIONALITY ARTIFICIAL NEURAL NETWORK TECHNIQUE FOR WELLS TURBINE BASED WAVE ENERGY CONVERSION SYSTEM

SALWA MOHAMED YOUSRY METWALLY ATIA

A thesis submitted in partial fulfilment of the requirement of Staffordshire University for the degree of Doctor of Philosophy

June 2018

Acknowledgment

In the name of Almighty Allah, all praises to him for giving me the strength , blessings in completing this thesis and providing me a wonderful colleagues, friends and family who gave me patient and continuous support all the time.

Special grateful to my principal supervisor Prof Sarath Tennakon for his patient and advices especially in the final stages.

My deepest gratitude to my co-supervisor Dr Ahmed Kadry Abdelsalam who helped me to complete this work. I learned from him professional way of thinking, his advices, patience, expertise, continuous support and immense thoughts were very productive for me to accomplish my work.

Special thanks to Prof Yasser Gaber El-desouky and Dr Hady Elhelw who gave me the chance to join their team. Without their support it would not be possible to conduct this research.

Many thanks go to Dr.Abdel-Hamid Soliman. For his helpful suggestions, support, and sharp actions during my Ph.D. study.

Special thanks to Prof Yasser Galal for his continuous support and forceful advices, he is my role model for a great leader

Many appreciations to the management of Staffordshire University for allowing me to use the university' facilities during my Ph.D. study

I also appreciate the support of the Arab Academy for Science and Technology and Maritime Transport during my Ph.D. study.

Hammam Soliman and Brwene salah, my best friends who always stand by my side, without your help and support, I could not finish this work you deserve all the best always, many thanks to you my dear friends.

Rana Maher , my friend, time goes and you are always in my heart my lovely friend, Allah put you in my way to help me and to be one of the most reasons for finishing this Ph.D., thanks you my lovely friend for your pure heart, love, support and help

My husband Ramey Beshir, I would like to thank you for your continuous support and help in all my downs and ups you always encouraged me and gave me self-confidence.

My family mother, father, sister and brothers, you are the best, always gave me endless support, prayers and help, many thanks to you deeply from my heart for your warm feelings and unconditional love and support.

Finally my small sweet hearts Layal and Sojoud, I would like to apologize for my continuous busyness and I would like to thank you for your patient and warm love.

Abstract

Wave energy is of particular interest amongst new market-penetrating renewable energy resources. Although energy extraction from wave motion is still in its infancy, recent studies predict rapid development. Several studies have investigated various wave energy harvesting configurations. The oscillating water column (OWC) is the most common type. The OWC is based on a Wells turbine system coupled to a doubly fed induction generator (DFIG) grid connected via a back-to-back converter, which is inherently advantageous, enabling this arrangement to dominate the wave energy conversion field.

Like the majority of renewable energy sources, wave energy power must be carefully tracked in order to maximize efficiency, due to its non-linear relation with the differential pressure and the turbine speed. Several maximum power point techniques (MPPT) have been presented in the literature that varies in implementation complexity, tracking convergence, and fast tracking methods.

Despite several advantages offered by the OWC-based wave energy conversion system (WECS), the commonly installed Wells turbine suffers a critical phenomenon: stalling. During this operating condition, the turbine power is dramatically decreased causing a severe system disturbance, especially when grid integration is required. Various stalling avoidance techniques have been presented in the literature, including air flow control implementation and rotor speed control, in addition to variable-speed strategies. The air flow control-based techniques offer limited performance compared to rotor speed control.

This thesis develops a dual functionality enhanced-performance technique that avoids stalling phenomenon and maximizes the extracted power. A grid connected WECS Wells turbine coupled to DFIG, is mathematically modelled within. A robust decoupled active-reactive power control strategy is subsequently presented for grid connection purposes. A novel artificial neural network-based stalling avoidance and maximum power point tracking (MPPT) technique is proposed. The presented technique facilitates a simplified training procedure, adequate stalling avoidance, minimal grid power oscillations, fast convergence and wide turbine speed range operation. Rigorous simulation results using Matlab/Simulink software package, comparing the developed and classical techniques, are utilized to verify the presented technique effectiveness and superiority under operating conditions.

Table of Contents

List of Tables

List of Figures

List of Symbols

a	Area of turbine duct	m^2
b	Blade Height	m
C_a	Power Coefficients	-
C_t	Torque Coefficients	-
dp	Differential Pressure	Pa
i_{dr}	Direct Axis Rotor Current	A
i_{ds}	Direct Axis Stator Current	A
I_{gabc}	3-phase Grid Current	A
i_m	Magnetizing Current	A
i_{ms}	Stator Magnetizing Current	A
i_{qr}	Quadrature Axis Rotor Current	A
i_{qs}	Quadrature Axis Stator Current	A
i'_r	Rotor Current Referred to Stator Side	A
i_r	Rotor Current	A
J	Moment of Inertia	$Kg.m^2$
K_{ir}	Integral Gain of PI controller	-
K_{pr}	Proportional Gain of PI controller	-
L	Blade chord length	m
L_0	Equivalent Inductance	H
L_{lr}	Rotor Leakage Inductance	H
L_{ls}	Stator Leakage Inductance	H
L_m	Magnetizing Inductance	H
L_r	Rotor Self Inductance	H
L_s	Stator Self Inductance	H
n	Number of blades	-
n_m	Mechanical Speed	r.p.m
n_s	Synchronous Speed	r.p.m

P	Pressure at the Turbine Duct	Pa
p	No. of Poles	-
P_{in}	Power to Turbine from the OWC Duct	W
P_{mech}	Mechanical Power	W
P_r	Rotor Active Power	W
P_s	Stator Active Power	W
Q	Flow Rate	-
Q_r	Rotor Reactive Power	Var
Q_s	Stator Reactive Power	Var
R	Mean radius of the turbine	M
R_r'	Rotor Resistance Referred to Stator Side	Ω
R_r	Rotor Resistance per Phase	Ω
R_s	Stator Phase Winding Resistance	Ω
rx	Additional external resistance in series with the DFIG rotor winding	Ω
S	DFIG Slip	-
T_e	Electromagnetic Torque	N.m
T_{mech}	Mechanical Torque	N.m
T_g	Torque Imposed by Generator	N.m
T_t	Turbine Torque	N.m
v_{dr}	Direct Axis Rotor Voltage	V
v_{ds}	Direct Axis Stator Voltage	V
v_{qr}	Quadrature Axis Rotor Voltage	V
v_{qs}	Quadrature S Axis Stator Voltage	V
V_x	Airflow speed at the turbine	m/s
$\emptyset$	Flow Coefficient	-
ρ	Air Density	Kg/m^3
η_t	Turbine Performance Efficiency	-

ω_r	Rotor Angular Velocity	rad/s
ω_t	Turbine Angular Velocity	rad/s
σ	Leakage Factor	-
ψ_{qr}	Quadrature Axis Rotor Flux	wb
ψ_{qs}	Quadrature Axis Stator Flux	wb
ψ_{dr}	Direct Axis Rotor Flux	wb
ψ_{ds}	Direct Axis Stator Flux	wb
ψ_m	Mutual Flux	wb
ψ_s	Stator Flux	wb
ω_e	Stator Supply Frequency	rad/s
ω_m	Rotor Mechanical Speed in rad/s	rad/s
ω_s	Synchronous speed	rad/s
ω_{slip}	Slip Angular Speed	rad/s

List of Abbreviations

ANN	Artificial Neural Network
AWS	Archimedes Wave Swing
DFIG	Doubly Fed Induction Generator
EU	European Union
FOPID	Fractional Order PID
GHG	Greenhouse Gas
GSC	Grid-Side Converter
IG	Induction Generator
IGBT	Insulated Gate Bipolar Transistor
IRENA	International Renewable Energy Agency
LE	Leading Edge
LIMPET	Land Installed Marine Powered Energy Transformer
LPMSG	Linear Permanent Magnet Synchronous Generator
MPPT	Maximum Power Point Tracking
nftool	Neural Fitting Tool
NREAP	National Renewable Energy Action Plans
OTEC	Ocean Thermal Energy Conversion
OWC	Oscillating Water Column
PB	Power Buoy
PID	Proportional, Integral, Derivative
PMG	Permanent Magnet Generators
PMSG	Permanent Magnet Synchronous Generator
PTO	Power Take-Off
PV	Photovoltaic
PWM	Pulse Width Modulation
QUB	Queen's University Of Belfast
RSC	Rotor-Side Converter
SCIG	Squirrel Cage Induction Generator
SFO	Stator Flux Oriented
TFEC	Total final energy consumption
VSI	Voltage-Source Inverter
VSR	Voltage Source Rectifier
WEC	Wave Energy Conversion
WECs	Wave Energy Converters

Chapter 1
Introduction

This chapter defines the presented Ph.D. project background, problem definition, project objectives, and thesis structure.

1.1 Background

Recent concerns about climate change, rising fuel prices and the security of the supply have encouraged policy makers to rapidly adopt renewable sources in the energy generation market [1]. The European Commission Climate Action package defines the "20-20-20" targets. These targets specify a reduction in EU greenhouse gas emissions of at least 20% below 1990 levels, that 20% of EU (European Union) energy is to be generated from renewable resources and that there must be a 20% reduction in primary energy use compared to projected levels [2].

According to 2050 Road-Map, the share of renewable energy in the power sector would increase from 25% in 2017 to 85% by 2050, mostly through growth in solar and wind power generation. This transformation would require new approaches to power system planning, system and market operations, and regulation and public policy. As low-carbon electricity becomes the main energy carrier, the share of electricity consumed in end-use sectors would need to double from approximately 20% in 2015 to 40% in 2050. Electric vehicles (EVs) and heat pumps would become more common in most parts of the world. In terms of final energy, renewable electricity would provide just under 60% of total renewable energy use, two and a half times its contribution to overall renewable energy consumption today [3].

At present, different types of renewable technologies are under consideration, in addition to the more traditional solar, wind and geothermal methods. Among these technologies, the exploitation of the energy present in the seas seems to be a favourable solution and represents an important field of research [4]. Energy can be extracted from the sea from several physical phenomena: salinity, temperature gradient, tides, waves, and ocean currents [1].

Many different approaches to wave energy conversion have been developed [5, 6]. The Marine Institute and Sustainable Energy in Ireland states that ‘‘Europe's accessible

wave power resource is calculated to be of the order of 320,000MW with the highest resource available near the west of Ireland" [5]. A number of coastal Member States have included ocean energy targets within published National Renewable Energy Action Plans (NREAPs). Generally, and within the NREAPs, ocean energy accounts both wave and tidal energy [5].

Publishing targets for ocean energy indicates not only the potential wave energy resource that exists in some Member States, but also signifies increasing support for ocean energy development. This is further evidenced by financial, legal and dedicated sectorial strategies approved by national governments, including Ireland. The ocean energy targets provide a development scale, which will potentially be faced within the European Union (EU) by 2020 [6].

Table 1.1 presents an estimation of total contribution (installed capacity and gross electricity generation) expected from ocean (wave and tidal technologies) to meet the binding Member State 2020 targets, in selected years from 2010 to 2020 [6]. According to the European Renewable Energy Council [6], ocean energy will represent 0.15% of electricity consumption in 2020. The Council states that installed capacity is expected to increase from 245MW in 2010 to 2543MW in 2020.

Table 1.1 Estimation of total contribution wave and tidal for 2010–2020 [6]

Member state	***Source (Tide, Wave, Ocean)***					
	2010 (MW)	***2013 (MW)***	***2014 (MW)***	***2015 (MW)***	***2017 (MW)***	***2020 (MW)***
Belgium	n/a	n/a	n/a	n/a	n/a	n/a
Denmark	0	0	0	0	0	0
France	240	271	287	302	333	380
Germany	0	0	0	0	0	0
Greece	0	0	0	0	0	0
Ireland	0	0	0	0	125	500
Italy	0	0	0	0	1	3
Portugal	5	10	35	60	100	250
Spain	0	0	0	0	30	100
Sweden	0	0	0	0	0	0
The Netherlands	0	0	0	0	0	0
United Kingdom	0	0	0	0	400	1300

Wave Energy Conversion technology (WEC) converts wave energy into mechanical energy and then uses a pickup power system to generate electricity [7]. WEC systems are classified based on location and principle of operation.

Oscillating Water Column (OWC) systems form a major class of wave energy converters that has been extensively studied, with the largest number of commercial prototypes deployed into the sea [8]. The main advantage of OWC systems, when compared with other WECs is its low cost and maintenance. The simplicity of the OWC system is that there is only one moving part of the energy conversion mechanism, which is the rotor of the turbine, located above water level, rotating at a relatively high velocity and directly driving a conventional electrical generator [7, 8].

Self-rectifying turbines are used by OWCs because; the rotational direction remains unchanged regardless of the direction of the airflow. The axial-flow Wells turbine, invented in the mid-1970s, is the most popular self-rectifying turbine. Many generators have been proposed to couple the OWC turbine [8], but the doubly fed induction generators (DFIGs) and permanent magnet synchronous generators are the most common for the wave energy converter.

The DFIG offers adequate performance, is sufficient for a wide speed range required as is typical of wave energy resources and is the most suitable for the OWC converter technology. A back-to-back AC-DC-AC converter is included in the DFIG rotor circuit [9]. The system's overall cost is lower in the DFIG case than in the full rated power converter associated with permanent magnet synchronous generator (PMSG)-based OWC systems, due to the reduced power rated converters. Vector control, commonly known as field-oriented control, in the DFIG case is used in order to ensure decoupling between the active and reactive power control.

1.2 Problem Definition

The most common OWC wave energy conversion system that features a DFIG coupled to Wells turbine is investigated. Turbine performance is hampered by stalling, leading to a significant distortion of the output torque and power. This results in degraded overall system performance, as seen as grid injected power reduction. This phenomenon is present under specific operating conditions, especially when the flow coefficient (ratio

between air velocity inside the OWC chamber to the turbine speed) reaches its critical value. This is a major technical problem to which a solution must be found.

In addition, conventional renewable energy sources exhibit non-linear behaviour with varying environmental conditions. A robust fast-convergence maximum power point technique must be used for the OWC-based WECS, because the delivered turbine power varies non-linearly with the chamber differential pressure and the turbine speed.

1.3 Aims and Objectives

The aim of this thesis is to develop a control technique in order to avoid the undesirable stalling, which occurs on Wells turbine based OWC systems. This results in maximum power tracking for the grid side under a wide range of operating conditions. In order to achieve this target, the following objectives are sought:

1. Survey wave energy conversion systems in order to fully understand the state-of-the-art technology
2. Investigate established OWC DFIG-based decoupled control techniques
3. Investigate Wells turbine modelling
4. Develop an improved performance technique suitable for Wells turbine stalling avoidance and maximum power point tracking
5. Validate the developed technique by comparing to classical techniques using simulation results under a wide range of operating conditions

1.4 Thesis Layout

The thesis is presented in the remaining five chapters as follows:

- **Chapter Two**: In this chapter an introduction on renewable energy, ocean wave energy and the associated types of wave energy converters are presented, as well as a brief guide on selecting the suitable generator for each wave energy converter.
- **Chapter Three:** The details of OWC, Wells turbine mathematical modelling and operation, DFIG operation, d-q dynamic analysis and decoupled active-reactive power control supported by simulation results are presented.
- **Chapter Four:** A review of stalling avoidance techniques and the Wells turbine stalling phenomenon are presented. The developed artificial neural network (ANN)

based stalling avoidance technique is also discussed with associated simulation results.

- **Chapter five:** An overview on maximum power point tracking together with intensive literature review on OWC based Wells turbine MPPT techniques are presented. The proposed dual function ANN technique for MPPT and stalling avoidance is also discussed and compared to a classical perturb and observe algorithm with simulation results under different operating conditions.
- **Chapter six:** Conclusions drawn from the research are discussed and suggestions for future work are presented.

Chapter 2
Wave Energy Conversion Systems Configurations and Generator Selection-an Overview

In this chapter, an overview of the common commercial prototypes wave energy conversion systems is presented, in addition to the associated generator selection guide.

2.1 Global Renewable Energy Production Profile

In many jurisdictions and countries around the world, wind energy is expected to make up the majority of renewable energy targets [1]. This is evident from the ambitious targets set by many countries for wind energy installations. Apart from hydropower, wind energy is considered one of the most commercially viable forms of renewable energy. Over the past ten years, global wind power capacity has grown at an average cumulative rate of over 30% with global installations producing more than 120 GW [10].

In addition, solar energy is becoming increasingly important in the drive to energy independence and climate balance. Its major advantages include being a clean energy source, requiring low maintenance costs, offering direct conversion to electricity in the photovoltaic case and being inexpensive [11].

As illustrated in Figure 2.1 (a), renewable power generating capacity witnessed its largest annual increase in 2016, with an estimated 161 GW of capacity added. Total global renewable power capacity increased 9% compared to 2015, to nearly 2017 GW at year's end. Photovoltaic (PV) for the first time accounted for more additional power capacity (net of decommissioned capacity) than any other generating technology. PV energy production represented 47% of newly installed renewable power capacity in 2016, while wind and hydropower accounted for the remainder, contributing 34% and 15.5%, respectively [12].

However according to 2050 Roadmap of global energy transformation, in 2017 the power sector added 167 GW of renewable energy capacity globally, a robust growth of 8.3% over the previous year and a continuation of previous growth rates since 2010 averaging 8% per year. Renewable power generation accounts for an estimated quarter of total global power generation, a new record. New records were also set for solar and wind

installation, with additions of 94 GW in solar photovoltaic (PV) and 47 GW wind power, including 4 GW of offshore wind power [3].

. By 2050, all countries can substantially increase the proportion of renewable energy in their total energy use. REmap, a global roadmap prepared by the International Renewable Energy Agency (IRENA), recommends that renewables can make up 60% or more of many countries' total final energy consumption (TFEC). For instance, China could increase the share of renewable energy in its energy use from 7% in 2015 to 67% in 2050. In the EU, the share could grow from about 17% to over 70%. India and the United States could see shares increase to two thirds or more. The updated renewable energy share in TFEC (%), Reference and REmap cases, 2015-2050 is presented in Figure 2.1(b) [3].

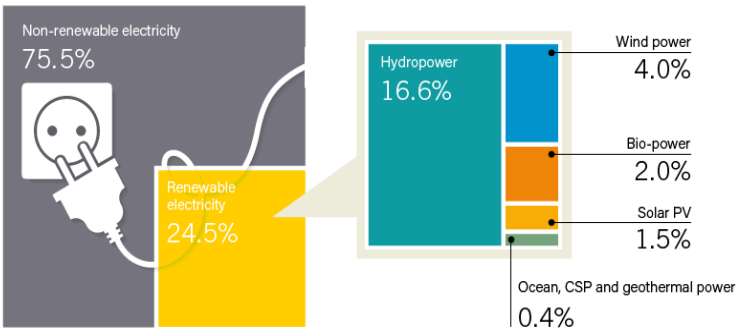

(a)

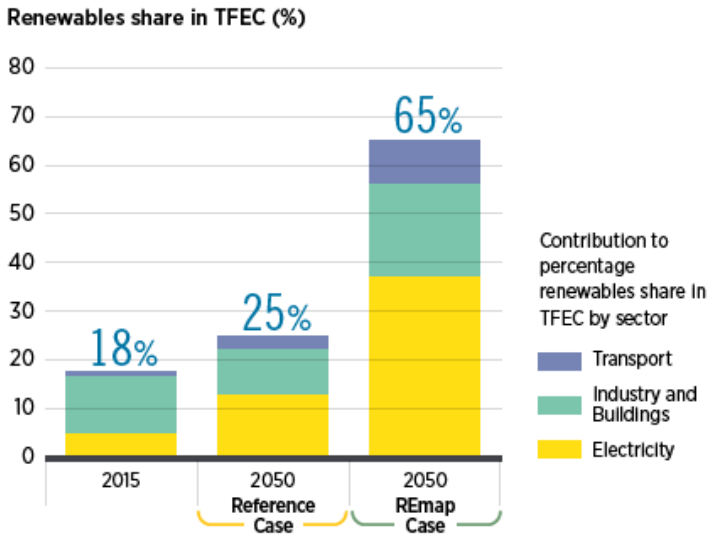

(b)

Figure 2.1 Estimated Renewable Energy Share of Global Electricity (a) Production End-2016 [12], (b) Production According to 2050 Roadmap [3]

Wave energy is still in its infancy and does not yet share the commercial success of wind energy, despite the large global resource for wave energy. While both resources are technically unconstrained, a common issue of variability is shared that can make large-scale integration into electrical grids challenging.

The world's oceans constitute one of the largest inventories of untapped renewable power [13]. With a dwindling supply of fossil fuels and increasing questions surrounding depleting resources, ocean wave energy can play a critical role in power generation. The successful deployment of large-scale grid-connected ocean power plants will contribute toward reduction in greenhouse gas emission and ensure local and regional energy security [10, 14, 15, 16].

2.2 Ocean Wave Energy

There are three different technologies to harness ocean wave energy:

- Ocean thermal energy conversion (OTEC): uses the difference in sea temperature between the surface and the deep ocean to drive a heat engine and generate electricity, two types of OTEC technologies exist [17]:
    a) ***Open Loop Cycle OTEC:*** Open loop cycle technologies use warm surface ocean water placed in a pressurized receptacle, which causes it boil. Steam from the boiling water turns a turbine that is connected to a generator. The steam, almost fresh water, is then condensed with the cold ocean water as shown in Figure 2.2(a)
    b) ***Closed loop cycle OTEC:*** is similar to open loop cycle OTEC, but uses a working fluid, like ammonia, that boils at a lower temperature than water. The working fluid creates steam and runs a turbo generator as shown in Figure 2.2(b). The steam is condensed with the cold water from lower depths, and the ammonia condenses to the working fluid.
- Ocean current conversion (also called ocean stream and tidal stream): ocean currents are driven by wind and solar heating of the waters near the equator, although some ocean currents result instead from variations in water density and salinity. These currents are relatively constant and flow in one direction only, in contrast to the tidal currents closer to shore where the varying

gravitational pulls of the sun and moon result in diurnal high tides. Some examples of ocean currents are the Gulf Stream, Florida Straits Current, and California Current. Ocean currents tend to be concentrated at the surface, although significant current continues at depths below ships drafts use devices that operate like undersea wind turbines, extracting energy from moving currents of water. Turbines can have either horizontal or vertical axis of rotation as shown in Figure 2.3 cables, or anchors are required to keep the turbines stationary relative to the currents with which they interact. Prototype horizontal axis turbines, similar to wind turbines, have been built and tested. Vertical axis turbines are either drag or lift designs [18].

- Wave energy conversion: extracts energy from ocean wave motion.

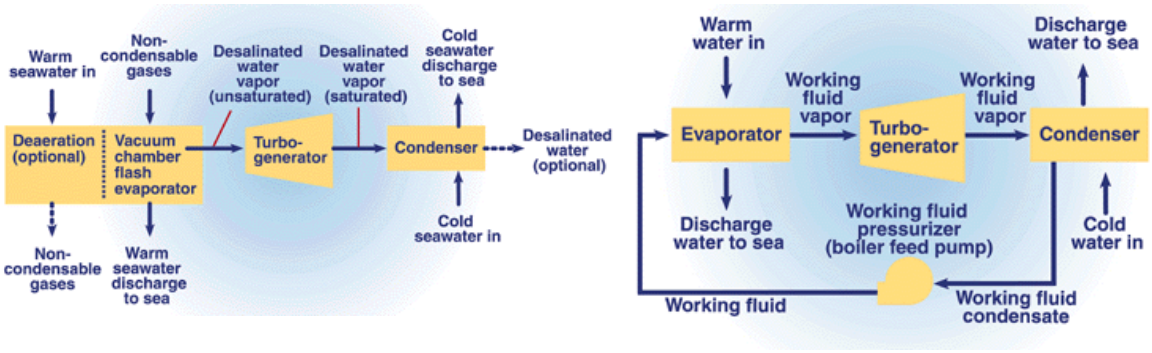

(a) (b)

Figure 2.2 OTEC technologies (a) Open Loop OTEC, (b) Closed Loop OTEC [17]

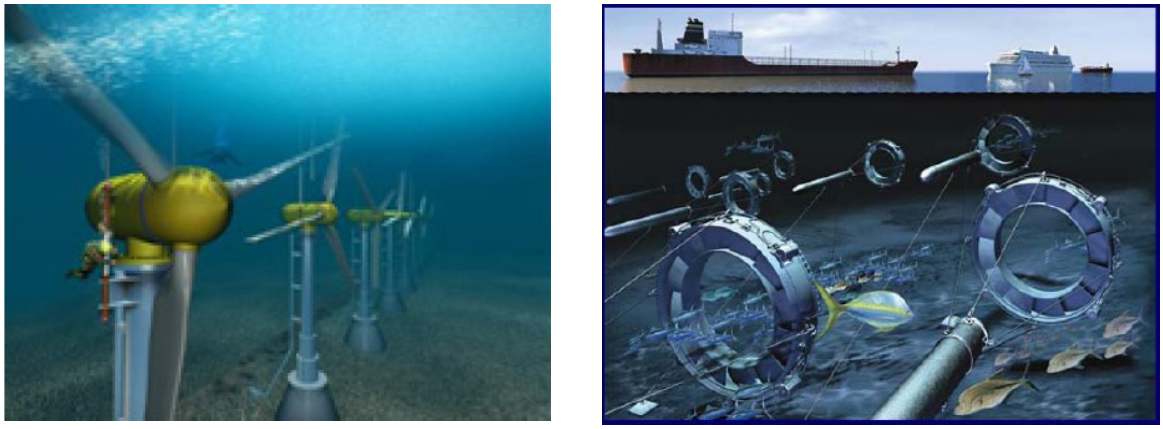

(a) (b)

Figure 2.3Visualization of Two Possible Turbine and Anchor Technologies (a)Vertical Technology, (b) Horizontal Technology [18]

The first prominent wave energy device was designed in France at the end of the eighteenth century. The modern history of wave energy conversion, however, dates back to the 1970s [1].

The majority of ocean energy projects continue to be demonstration projects, all poised to be leveraged into full commercial deployment. The UK remains a leader in both development and commercialization of technologies and projects Scotland, in particular, intends to supplement its energy resource base with effective variant renewables that facilitate installing new electricity generation projects [19].

Ocean waves arise due to the transfer of energy from the sun to wind then water. Solar energy creates wind, which then blows over the ocean, converting wind energy to wave energy. Once converted, this wave energy can travel thousands of miles with little energy loss. Most importantly, waves are a regular source of power with an intensity that can be accurately predicted several days before its arrival. Furthermore, wave energy is more predictable than wind or solar energy [2, 10]. The characteristics of wave energy are as follows:

- The larger the wave, the more power.
- Energy is determined by height, speed, length, and water wave density.
- Waves characterized by wind and sea floor dimensions.
- Wave power is strong at the surface and reduces with depth.

The technical advantages of wave power generation lie in its predictability. A major drawback to solar and wind energy is susceptibility to sudden and unpredictable spikes and drops in production. When renewable power generation is installed, grid operators often keep conventional power plants operating in standby mode to provide reserve capacity that is immediately ready (spinning reserve). This activity can lead to an overall increase in greenhouse gas (GHG) emissions. Because wave activity can be confidently predicted days in advance, there is time for other generating stations in an electricity grid to modify the production on a day-by-day basis, reducing the need for spinning reserves and the accompanying GHG emissions [1, 7, 13].

Figure 2.4 shows an Atlas of the global power density distribution of the oceans where the numbers indicate kW/m. The north and south temperate zones have the best sites for capturing wave power. The prevailing winds in these zones blow strongest in winter.

Increased wave activity is found between the latitudes of 30° and 60° on both hemispheres, induced by the prevailing western winds blowing in these regions [20].

The oceanic wave climate (i.e. far offshore) offers enormous levels of energy. As waves approach the shore, energy is dissipated, leading to lower wave power levels on the shoreline. Therefore, the energy availability is sensitive to location, particularly the distance from the shoreline [7, 20].

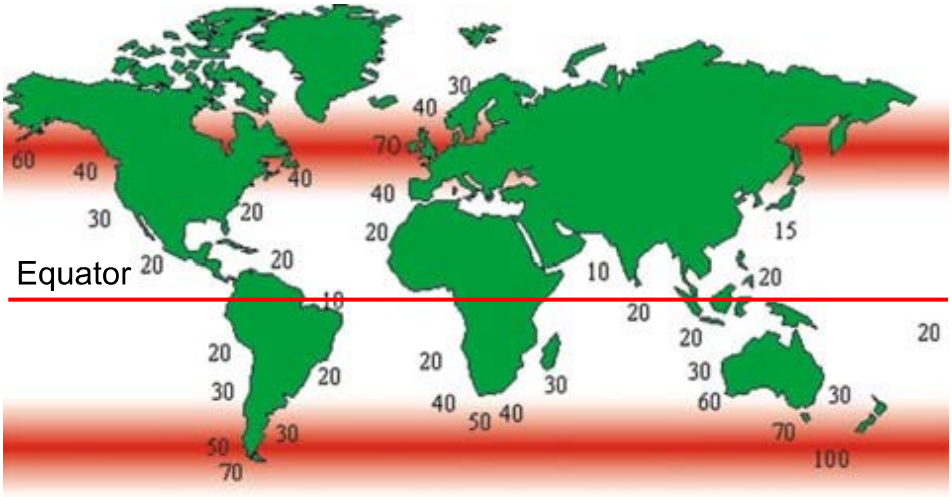

Figure 2.4 Atlas of Global Ocean Power Density Distribution [20]

The advantages of wave energy from an economic, environmental and technical view set it apart from other renewable energy sources. Wave Energy Converters' (WECs) capital costs are already reasonably low, and are likely to decrease further as the industry expands and specialized industries emerge for WEC subcomponents. Environmentally, WEC systems are relatively benign. The majority of environmental impacts occur during the construction and installation phases, but once in operation, WECs release no Green House Gases (GHGs) and are unlikely to affect migratory fish patterns or coastal eco-systems [1]. A WEC can even have positive environmental effects, as the mooring lines that keep it in place provide artificial reef habitat for sea life [2, 10]. WEC systems also have low a visibility profile, and only protrude a few meters from the ocean surface, installed several kilometers offshore. This makes wave energy more appealing to nearby residents who might otherwise object to wind turbines or solar arrays being unsightly [1, 21, 22].

2.3 Wave Energy Converters

WECs transform wave energy into mechanical energy, and then use a power take-off (PTO) system to generate electricity. The PTO system is classified into three primary forms [19, 23]:

- Rotary turbo-generators driven by oscillating air flow.
- Hydraulic motor-generators run by a pressurized fluid.
- Direct-drive linear generators directly operated by sea motions

WEC technologies can be classified into three categories: onshore, near-shore and offshore, as shown in Figure 2.5 [21, 22].

On shore WEC technologies can be placed on the sea floor in shallow water, integrated in breakwater-like structures or fixed to rocky cliff; all offering the benefits of simpler installation and maintenance. These technologies do not require deep-water moorings or longer electrical cables under water [7]. In addition, a much less powerful wave regime is encountered [22].

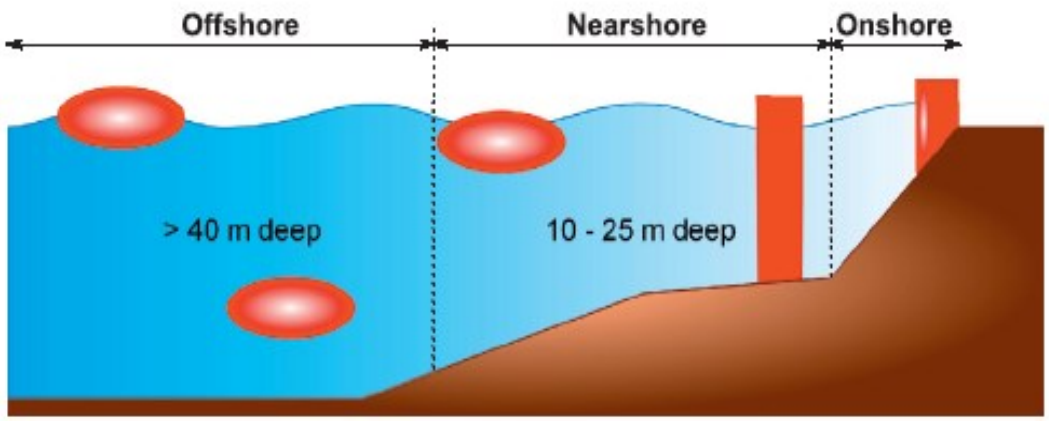

Figure 2.5 Classifications of Wave Energy Converters Based on Location from Shoreline [24]

The near-shore WEC technologies are deployed at moderate water depths, between 10 and 25 meters and up to 0.5 km from the shore. Advantages are identical to those of shoreline installations but operate at higher wave power levels [25]. The main problem exists with the extreme wave loads a large fixed structure must resist in addition to the unit cost [25].

The offshore WEC technologies exploit powerful wave regimes seen in deep water, at greater than 40m depth. Recent offshore technologies focused on modular units arranged

in arrays yielding high power output. High reliability is required in order to avoid excessive maintenance-related costs [7, 24]. Common WECs for each type are presented in Figure 2.6.

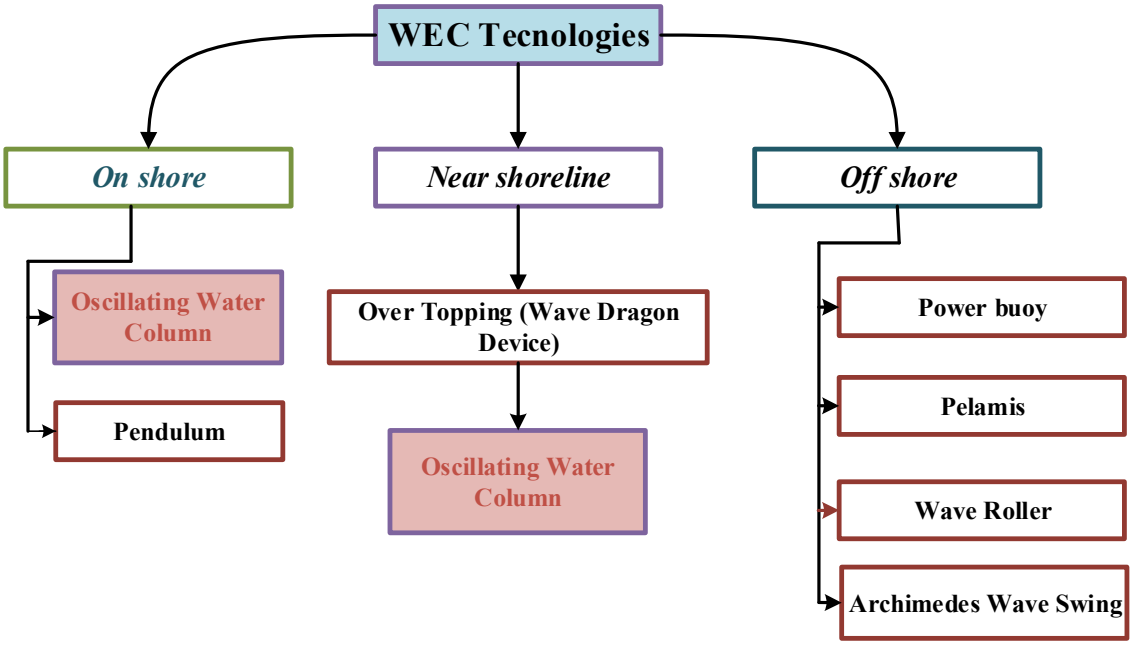

Figure 2.6 Common WEC Technologies [21, 22]

2.3.1 Oscillating Water Column (OWC) Wave Energy Converter

The OWC is the most developed shoreline or on-shore WEC technology [7]. It consists of a chamber built on shore with the layout shown in Figure 2.7. Ocean/sea waves push an air pocket up and down behind a breakwater. The air then passes through an air turbine. When the wave returns to the sea, an air depression circulates through the turbine in the opposite direction. The overall operating principle is clarified in Figure 2.8. This turbine, however, has been designed to continue rotating in the same direction irrespective of the direction of the airflow [7, 20]. The advantages and disadvantages of the OWC were summarized in Table 2.1 [8, 24].

The OWC technology has been successfully implemented in a number of locations, with varying degrees of efficiency. The most common examples are:

(i) Wavegen's LIMPET [26]
(ii) Energetech's Australia Wave Energy System [27].
(iii) Pico power plant [28]
(iv) Oceanlinx GreenWave [29]
(v) Yongsoo power plant [8]

Figure 2.7 OWC Wave Energy Converters [7]

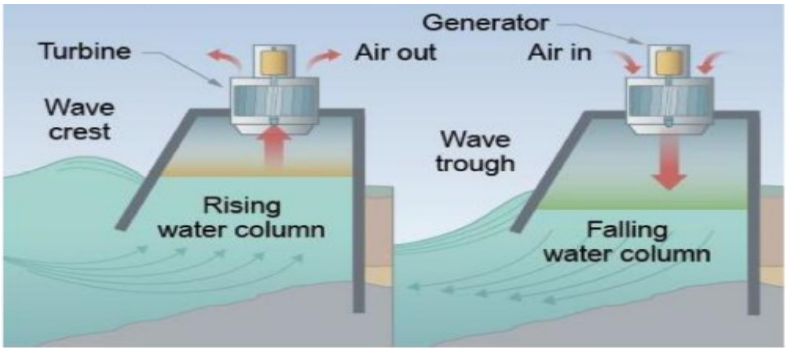

Figure 2.8 OWC Operation Principles [7]

Table 2.1 OWC advantage and disadvantage

Aspects	***Advantages***	***Disadvantages***
Life Time	Moving parts are housed outside of the water for a longer lifetime of the materials	
Maintenance	Low requirement	
Cost	Low	
Location and construction	Can be built near shore for easy access to the power grid as well for maintenance No greenhouse gases release	Construction requires coastal destruction Requires very specific location characteristics
Noise		Noise level increases with machine size and especially with high flow velocity and rotor blade speed

A 500 kW shoreline wave energy collector LIMPET (Land Installed Marine Powered Energy Transformer) [30], shown in Figure 2.9 was constructed on the Hebridean Island of Islay in the late summer of 2000. This plant was developed from the successful 75 kW prototype shoreline Oscillating Water Colum (OWC) wave energy converter, which was built by the Queen's University of Belfast (QUB) in 1991 and operated to provide design data and experience until its decommissioning in 1999. Although it was the focus of a long-term development program toward the establishment of fully commercial wave energy, LIMPET is grid connected and supplies power to the national grid under the terms of the Scottish Renewable Order. The project received support under the EU Joule program with QUB leading the scientific investigations, and Wavegen was responsible for the operation of the device. Wavegen Limited was a wave energy company based in Inverness, Scotland, founded in 1990 by Allan Thomson, and then sold to Voith Hydro in 2005. The company closed in 2013 [31].

Figure 2.9 OWC Wave LIMPET [32]

To overcome the problems of traditional turbines, LIMPET employs a Wells turbine that rotates in the same direction irrespective of the airflow direction [31, 26].

The collector is tilted such that the resonance of the internal water column coincides with the peak energy period of the waves, easing the passage of water into the water column. The collector was divided into three chambers, with large holes at the top of each dividing wall to allow the air above the three water columns to combine and feed the turbine-generation system .This design optimized performance for annual average wave intensities of 15 – 25 kW/m at a 10 m depth contour. The setup contains a pair of Wells

turbines, each connected to a 250 kW induction generator, so the overall capacity is 500KW, designed to supply power into the Islay grid [32].

Wavegen determined that LIMPET's low performance was related to issues with project management, and not due to the design or technology. LIMPET was successful despite its low performance, due to the following [32]:

- Provided valuable experience in construction and operation to be used to develop future projects.
- The ability of the structure to withstand hostile conditions on an exposed cliff edge was demonstrated.
- The community approved the design as low profile as less intrusive.
- Generated electricity used to power an electric bus.

Energetech's Australia Wave Energy System is an Oscillating Water Column located off the coast of Port Kembla, New South Wales, Australia as shown in Figure 2.10. Located 200 m from the Port Kembla Harbor Breakwater, it was designed to generate 500 kW of power [27].

The system uses a Denniss-Auld variable pitch turbine, with higher conversion efficiency than the Wells turbine. The turbine drives an induction generator [27, 33].

Figure 2.10 Energetech's Australia Wave Energy System [33]

The device employs a parabolic wall to focus the wave energy into the collector. The ends of the wave plane are reflected by the parabolic wall and converge on the focus

of the parabola. At the focus, the water rises and falls with amplitude of approximately three times that of the incoming waves .The center of the collector sits at the focus of the parabolic wall. The plant also includes a small desalination unit that can produce nearly 2000 liters of fresh drinkable water per day using only seawater and wave energy power [34]. The project became operational in December 2006, when a local power utility purchased the electricity generated and sold it to residents in the local community [27].

Two full-sized fixed-structure OWC plants (the so-called European pilot plants) were constructed; one on the island of Pico, Azores, Portugal, and the other on the island of Islay, Scotland, UK. Both were equipped with Wells turbines. The Pico plant, rated 400 kW, was completed in 1999 and is still operational. It was built standing on the sea bottom, adjacent to a vertical cliff as represented in Figure 2.11 [28].

Figure 2.11 Back View of the OWC Power Plant on the Island of Pico, Azores, Portugal [28].

A large bottom-standing OWC named The GreenWAVE, rated 1 MW, was recently constructed by the Australian company Oceanlinx, as shown in Figure 2.12. However, an accident to the airbags supporting the 3000-tonne structure occurred.

On the 2nd of March 2014, complications were experienced during transportation of the device, 24 hours into the launch. The device was set down in shallow waters off the Fleurieu Peninsula in South Australia. As a result of the transportation complications, the device was damaged beyond repair [29].

Figure 2.12 Oceanlinx GreenWAVE, Australia, in Port Adelaide [29].

A recently completed bottom-standing OWC, rated 500 kW, was installed at Yongsoo, 1 km off the coast of Jeju Island, South Korea, as shown in Figure 2.13. The plant is 37 m long and 31.2 m wide and was completed in 2015 [8].

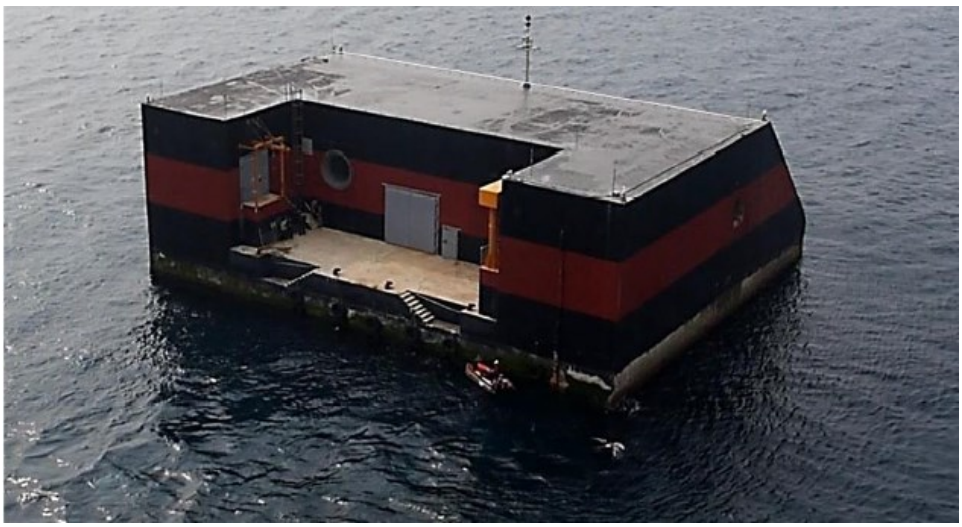

Figure 2.13 Back View of the Bottom-Standing Plant at Yongsoo, Jeju Island, South Korea [8]

2.3.2 Pendulum System

The Pendulum system is also installed on the shoreline and consists of a parallelepiped concrete box, which is open to the sea at one end, as illustrated in Figure 2.14.

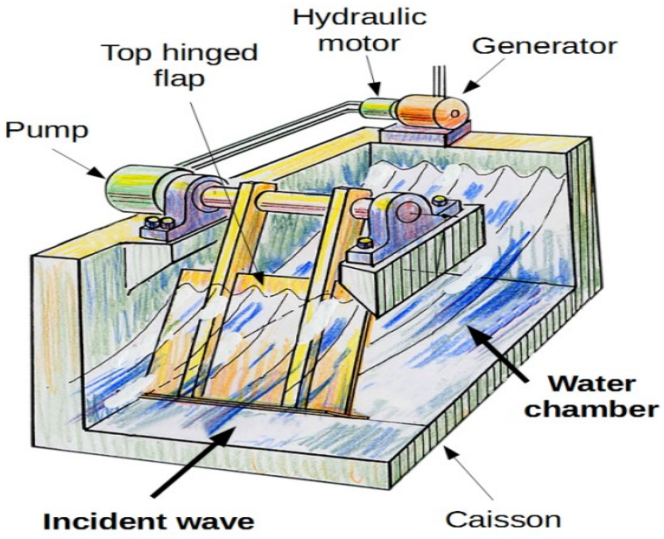

Figure 2.14 Pendulum System [35]

A pendulum flap is hinged over the opening, so that the action of the waves causes it to swing back and forth. This motion is then used to power a hydraulic pump and an electric generator [20]. The best known converter of this type is a Japanese device called the *pendulor,* which is comprised of a box, open to the sea on one side, where a flap is hinged horizontally from the top. When waves strike the flap it begins to oscillate like a pendulum and this motion can be converted into electricity using hydraulic rams. Small devices of this type have been built and tested, but a larger plant of 200 kW has been designed for a site in Sri Lanka [35]. An earlier device of this type, the Japanese Pendulum, had the flap hinged near the surface, hanging downwards, inserted into the caisson structure [36].

2.3.3 Overtopping Wave Energy Converter:

The overtopping wave energy converter works in much the same way as a hydroelectric dam. Waves roll into a collector, which funnels the water into a hydro turbine, as depicted in Figure 2.15. The turbines are coupled to generators, which produce electricity. The waves continue out to the ocean, after flowing through the turbines. A mesh grid is installed to extract trash and marine debris before the waves pour into the turbine. The overtopping WEC can be placed on the shoreline or near the shore, but are most commonly placed in a near shore location. As with the OWC, the overtopping WEC may be slack or fixedly moored to the ocean bottom. It should be noted that overtopping wave energy converters are not as common as OWCs [37].

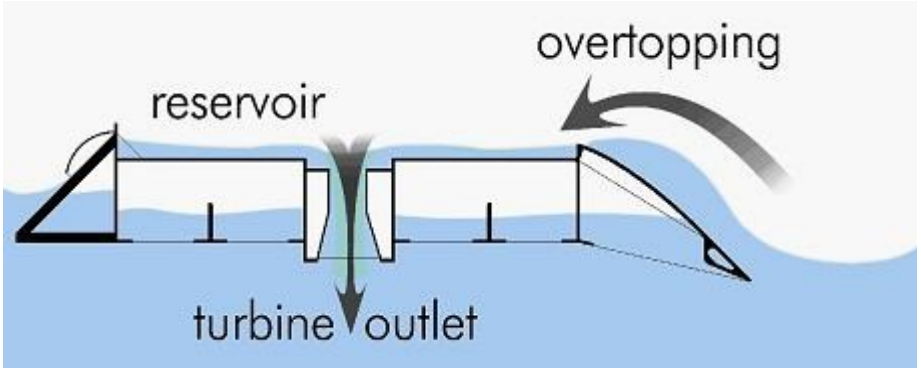

Figure 2.15 Overtopping Wave Energy Converter [37]

Wave Dragon System is a floating slack-moored energy converter of the overtopping type that can be configured into a single unit or into arrays. Groups of 200 Wave Dragon units result in a wave power park with a capacity comparable to a traditional fossil fuel-based power plant. The Wave Dragon system, as presented in Figure 2.16, was placed in Nissum Bredning, Denmark, and was connected to the grid in May 2003 as the world's first near shore wave energy converter with a rating of 1.5 MW [38]. Construction is very simple and the turbines are the only moving parts. This is essential for devices operating near-shore, where the extreme forces affect any moving parts. The Wave Dragon water turbines are a well proven technology with a 90 year track record, as opposed to the power take off systems of the competitors. The expected economic lifetime of a Wave Dragons power take off system is 25 years, which is much higher than that expected from the air turbines, high pressure hydraulics and linear generators, as proposed for the competing wave energy devices [39]. In comparison to traditional hydroelectric power stations, this new technology is quite competitive [40].

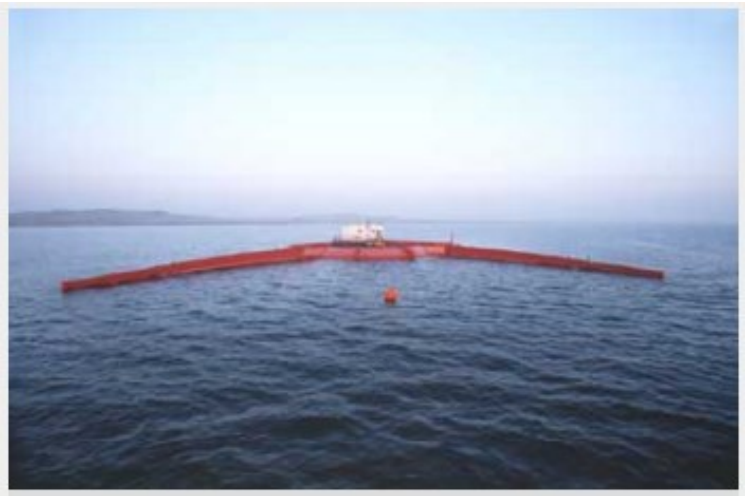

Figure 2.16 Wave Dragon Wave Energy Converter [39]

2.3.4 Power Buoy

The Power Buoy (PB) was developed by the Ocean Power Technologies Company for converting wave energy into electric power. This system utilizes the Power Buoy technology, which consists of modular ocean-going buoys, as shown in Figure 2.17. The rising and falling of the waves move the buoy-like structure creating mechanical energy which is converted into electricity and transmitted to shore via a secure, undersea transmission line. A 40 kW buoy has a diameter of 4 m and is 16 m tall, with 5 m of the unit rising above the ocean surface. Using a three-point mooring system, the buoys are designed to be installed 8 km offshore in water 40 to 60 m deep [7].

The PB system locks-up and stops power generation in the case of extreme waves, and then unlocks and begins power generation when the wave heights return to normal. The PB uses conventional mooring systems, as it is possible to arrange into arrays scalable to hundreds of megawatts [41].

Figure 2.17 Power Buoys Wave Energy Converter [7]

2.3.5 Pelamis Wave Energy Conversion

The Pelamis Wave Energy Converter, a Scottish creation, consists of six articulated cylinders of 3.5 m in diameter and 30 m in length (floaters) connected to four cylinders of 3.5 m in diameter and 5 m in length (power modules). This articulated structure with 140 m in a total length is placed semi-submerged offshore in deep waters, as shown in Figure 2.18. Due to the waves' natural occurrence, its structure can move up and down and side to side, as a 'sea snake' (or 'Pelamis' in Greek) [42, 43].

Figure 2.18 Sea Snake Structure Wave Energy Converter [43]

As the hinges bend, hydraulic fluid is pumped, creating pressurized oil to drive a hydraulic motor driving an electric generator, mounted inside the 5 m floating power module, as shown in Figure 2.19 [44].

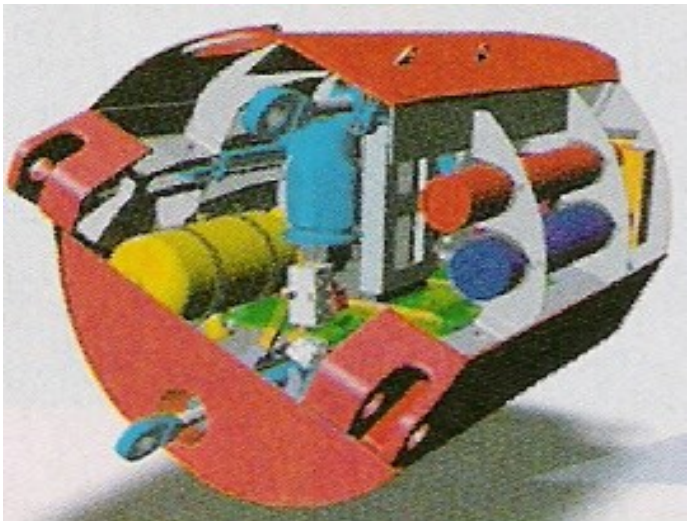

Figure 2.19 Inside View of the Pelamis Power Module Wave Energy Converter [44]

Each of the four modules has a 250 kW electric generator, making the total power 750 kW for each Pelamis unit. A 10 kV three-phase power transformer is situated in the front floater to the electric energy across underwater power cables to a substation on land [44, 45].

A wave farm utilizing Pelamis technology was recently installed in *Aguçadora Wave Park,* about three miles off Portugal's northern coast, near Póvoa do Varzim. The wave farm uses three Pelamis P-750 machines, developing a total power of 2.25 MW. Other plans for wave farms include a 3 MW array of four 750 kW Pelamis devices in the

Orkneys, off northern Scotland, and a 20 MW Wave Hub development off the north coast of Cornwall, England [15, 42, 43, 46].

The advantage of the Pelamis wave energy converters can be summarized as follows:

- Offshore, out of sight
- Higher energy potential than in shallow water (wave power at deep ocean sites can be as much as eight times that of coastal sites)
- Does not change wave patterns
- Does not disrupt wildlife
- Runs quieter than other technologies

The disadvantages of Pelamis wave energy converters:

- High cost associated with electricity transmission from the offshore system to land
- Navigation hazard

2.3.6 Wave Roller Energy Converter

The Wave Roller System is a plate lying on the bottom of the sea, whose fore-and-aft movement caused by the bottom waves is collected by a piston, as illustrated in Figure 2.20. The piston compresses oil to power a hydraulic motor, which drives an electric generator to produce electrical energy [47].

Cumulative electricity produced by Wave Roller units, shown in Figure 2.21, for the local power grid in Peniche, Portugal, exceeded predictions even in low sea states. The research team is currently examining results from rougher sea states as waves become more turbulent with the approach of winter [48].

Figure 2.20 Wave Roller plate Wave Energy Converter [48]

Performance data from the first month of operation by the Wave Roller Power plant in Portugal matched forecasts, based on previous simulations and testing. In spite of unseasonably calm seas with an average wave power of only 13.4 kW/m, the mechanical efficiency of the power take-off and the quantity of electricity produced were well in line with expectations [48].

Figure 2.21 Wave Roller Units [48]

After maintenance and minor modifications, the power plant was re-configured and redeployed with only one operational panel. Subsequently the plant was organized with two- and three-panel configurations to gather as much data as possible about the different deployment configurations.

A commercial scale Wave Roller is a single-panel unit. A 300 kW Wave Roller array was initially deployed deeper than its design depth in order to collect validation data for previous tank tests and to fine-tune the software that enables array optimization for future projects. The next deployment will set one of the units at the optimum depth of a commercial scale Wave Roller-unit [48].

2.3.7 The Archimedes Wave Swing (AWS)

The AWS converter was developed by a Dutch company, Teamwork Technology, in 1993 [29]. AWS is an offshore point-absorber originally equipped with a linear

generator as a power take-off system. It is submerged near the shore in 50m of water. An AWS is an air-filled cylindrical steel chamber whose lid (the floater) is a vertically moving body, while the bottom (the silo) is fixed. In Figure 2.22, the prototype of the AWS can be seen, which was submerged and tested in 2004 off the northern coast of Portugal [49].

The force is generated by the variations in wave pressure above the converter, exciting the system lifting and lowering the floater [49, 50]. When a wave crest is above the AWS, the volume of the chamber is reduced. The opposite occurs when a wave trough is above the converter. In this case, the pressure exerted by the water will be lower than the pressure inside the chamber, causing the lid of the chamber to rise [50].

A direct-drive, permanent magnet, linear synchronous generator is used for energy conversion. The air within the chamber behaves like a spring whose stiffness can be adjusted by pumping water into or out of the chamber. When the height of the waves exceeds the limit for the device, water brakes are activated in order to decrease the wave force acting on the system. These actions together with the generator provide damping [51].

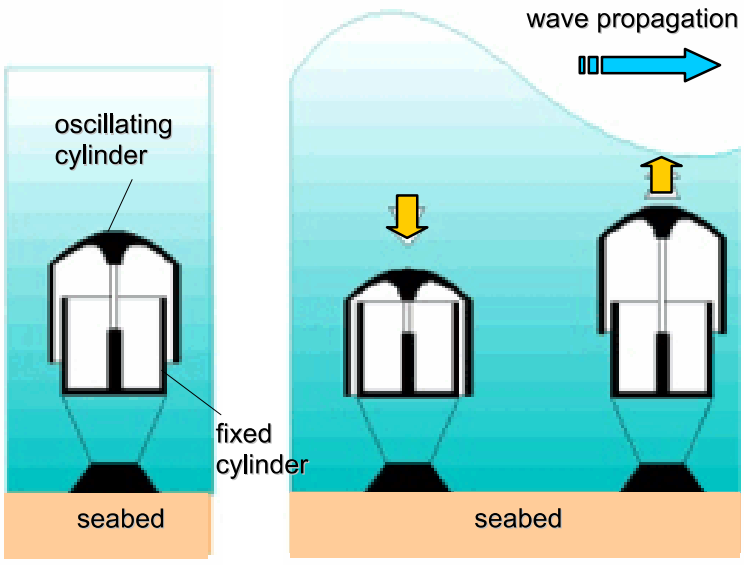

Figure 2.22 Archimedes Wave Swing [50]

The following characteristics are required for optimal use:

- 40 - 100m of water depth outside of main commercial shipping lanes
- Secure electricity power grid onshore

- Sea-bed suitable for laying power cables to shore [52]

Figure 2.23 presents a full scale offshore AWS, which was successfully tested in Portugal in October 2004. The tests verified the technology delivering AWS wave power to the Portuguese grid.

Figure 2.23 AWS Prototype in Portugal [52]

A pre-commercial pilot project off the coast of Portugal has three AWS devices and produces 8 MW of power. Another AWS machine was installed off Orkney in 2007 by AWS Ocean Energy with eventual plans to create a 100-machine wave park at a cost of £250 million [52].

The AWS has novel advantages due to its sub-sea location and the unique way in which it captures power [53]:

- Storm avoidance in retracted position and robust design provides high survivability
- High power density reduces footprint and makes AWS a competitive choice for utility developers
- Environmental impact is minimal and positive effects on marine life may be experienced

The disadvantages of an AWS include the following:

- Seawater is constantly acting on the seals of the linear generator, and high pressure – contributes to stresses within the seals

- Because of the high attraction forces between the stator and the translator, the bearings are stressed, which is undesirable because it leads to additional wear and maintenance.

2.4 PESTILE Analysis comparing various WECs

In this section, a comparison illustrated in Table 2.2 regarding several risk factors is implemented according to PESTILE analysis in order to indicate how these WECs are reliable according to the available commercial prototypes.

Table 2.2 PESTILE analysis of various WECs

<table>
<tr><th rowspan="2">Risk Factors</th><th rowspan="2">Description</th><th colspan="7">Most Common Wave Energy Conversion Systems</th></tr>
<tr><th>OWC</th><th>PENDULUM</th><th>OVERTOPPING</th><th>BUOY</th><th>PELAMIS</th><th>WAVE ROLLER</th><th>AWS</th></tr>
<tr><td>P</td><td>Need country to country agreement</td><td>L</td><td>L</td><td>L</td><td colspan="4">M
as they are offshore technologies so may installed between two countries</td></tr>
<tr><td>E</td><td>Cost</td><td colspan="2">L
As they are need low maintenance and no need for long undersea cables</td><td>M</td><td>H</td><td>H</td><td>H</td><td>H</td></tr>
<tr><td>S</td><td>Community approval for installation based on sightseen</td><td>M</td><td>H</td><td>H</td><td>L</td><td>L</td><td>L</td><td>L</td></tr>
<tr><td rowspan="2">T</td><td>Civil work</td><td>Onshore Or near</td><td>onshore</td><td>Near shore</td><td colspan="4">Offshore</td></tr>
<tr><td>maintenance</td><td>L</td><td>L</td><td>M</td><td colspan="4">H</td></tr>
<tr><td>L</td><td>Need government approval</td><td colspan="7">H</td></tr>
<tr><td rowspan="2">E</td><td>Affect sea life</td><td>L</td><td>L</td><td>M</td><td>H</td><td>H</td><td>H</td><td>H</td></tr>
<tr><td>Affect shoreline</td><td>H</td><td>H</td><td>M</td><td>L</td><td>L</td><td>L</td><td>L</td></tr>
</table>

PESTLE (Political Economical Social Technological Legal Environmental) ,
L: Low, M:Medium, H:High

2.5 Utilized Generators for Common WECs

OWC devices, which utilize the coupling between wave motion and an air chamber to drive an air turbine, are suited to using off-the-shelf electrical components, and are among the most favoured commercial devices. Part of the reason for this is the fact that standard rotary generators can be deployed in these devices.

Nominal turbine speeds in OWC WECs are typically in the range of 400-1500 rpm, with the lower speed range corresponding to impulse turbines and the higher to Wells turbines. The types of generator directly coupled to the turbine are listed as follow [23]:

1- Doubly fed induction generator (DFIG)
2- Squirrel cage induction generator (SCIG)
3- Linear permanent magnet synchronous generator (LPMSG)
4- Permanent magnet synchronous generator (PMSG)

In each case, the capability to implement a wide range of speed control through power electronic frequency converters is utilized and aided by airflow control. This results in maximized turbine efficiency [23].

The standard induction generator is used, because it is inexpensive, robust, easy to control and compatible in size with the application. Permanent magnet generators (PMG) offer better dynamic performance and are thus more suited to variable loads. From a cost perspective, the induction machines are less expensive. From a risk perspective, an induction machine is less likely to damage itself or its converter if forced to over-speed; hence, it is safer to operate in harsh conditions on a less stable grid [54].

In transportation and conveyor systems, linear electrical generators are used as an alternative drive system, replacing pneumatic/hydraulic systems or rotating electric machines driving a spindle. Almost all linear electrical generators are connected to the grid by means of a frequency converter [55].

The major drawback of linear electrical generators is the relatively low distribution of the technology. Another disadvantage is the fluctuating price of the magnets, which could result in a rapid increase of overall costs [24].

A summary of generator technologies used in prototypes and commercial projects are listed below in Table 2.3.

Table 2.3 Summary of generator technologies used in WECs

Reference No.	***WEC Type***	***Generator Type***	***Project Name***	***no of Units***	***Location***	***Rating per Unit***
[56, 57, 58, 59]	*AWS*	*LPMSG*	AWS	3	Portugal	250 kW
[60, 61, 62]	*OWC*	*DFIG*	Mutriku	-	Spain	300kW
[63, 64, 65, 66]	*OWC*	*IG*	LIMPET	2	Scotland	250 kW
[67, 68, 69]	*Overtopping*	*PMSG*	Wave Dragon	16	Denmark	250 kW
[24]	*BUOY*	*PMSG*	*OPTs Power Buoy*	-	Hawaii and New Jersy	150 kW
[35]	*Pendulum*	-	*Small devices in Sri Lanka*	-	Sri Lanka	200 kW
[24]	*Pelamis*	*IG*	*Sea Snake*	3	Portugal	750 kW

OWC and AWS are the most popular WECs used. This is further evidenced from the number of cited articles that show wide utilization of several prototypes of the same. Table 2.3 illustrates the most popular types of electric generator used in WEC technologies, associated with performance and converter type [23, 24, 54, 55].

From Tables 2.3 and 2.4, the preferred generator to operate with the OWC WEC is the IG/DFIG, while in case of AWS WEC, the LPMSG is preferred [70, 71].

Table 2.4 Comparison between various WECS generators

Generator Type	Associated Converter Configuration	Advantages	Disadvantages
PMSG (Rotary or Linear)	Full power stator connected	• Presence of stator and full power converter behind the grid provide significantly decoupled performance • Due to fully rated converter, there is greater flexibility in meeting the requirement of renewable energy grid codes	• Very sensitive to corrosion • High cost due to presence of permanent magnets and fully controlled converter • Sensitive to mechanical shock and vibration
DFIG	Back to back converter configuration	• Reduced converter cost, as it handles 30%-40% of the generator power • High efficiency	• Requires constant maintenance due to the presence of brushes • Sensitive to grid faults
IG	Soft starts system	• Low cost	• Fixed speed • Needs regular maintenance for the brushes • Requires output capacitor bank for reactive power supply

2.6 Conclusion

Based on the previous discussion it can be concluded that the OWC coupled to DFIG is advantageous due to reduced cost, simple construction, location, low maintenance requirements and the variety of applied commercial prototypes. The presented thesis therefore adopts the OWC coupled to DFIG-based WECs in the forthcoming analysis.

Chapter 3
Investigation of Doubly Fed Induction Generator Based on Oscillating Water Column Energy Conversion System

In this chapter, the oscillating water column wave energy converter is discussed in details. The Wells turbine mathematical modelling is presented; in addition to doubly fed induction generator d-q representation. Decoupled active-reactive control for the wave energy conversion system is investigated associated with rigorous simulation results

3.1 Oscillating Water Column Wave Energy Converter Basic Principles

The oscillating water column (OWC) energy conversion system, illustrated in Figure 3.1, operates much like a wind turbine via the principle of wave induced air pressurization. A closed containment housing (air chamber) is placed above the water and the passage of waves changes the water level within the housing. If the housing is completely sealed, the rising and falling water level will increase and decrease the air pressure within the housing. With this concept in mind, a turbine is placed on top of the housing through which air may flow. Air flows into the housing during a wave trough and flows out of the housing during a wave crest. Because of this bidirectional airflow, the turbine must be designed to rotate in only one direction irrespective of the direction of airflow. The Wells turbine is designed for this application and is used in most OWC devices [72, 73].

The OWC energy equations are similar to those used for wind turbines. In this way, the power available from the airflow in the OWC chamber is expressed as (3.1). The air flow kinetic energy term,$\frac{v_x^3.3.a.\rho}{2}$ is common to wind turbine analysis, but the air pressure term, $p.V_x.a$, is a representative term for this application only. From equation (3.1), it can be observed that the size of the duct and the air flow through the duct play a significant role in the OWC system design [73, 74].

$$P_{in} = \left(p + \frac{\rho V_x^2}{2}\right).V_x.a \tag{3.1}$$

P_{in} is the power available to turbine from the OWC duct, p is the pressure at the turbine duct, ρ is the air density, V_x is the airflow speed at the turbine and a is the area of turbine duct [74].

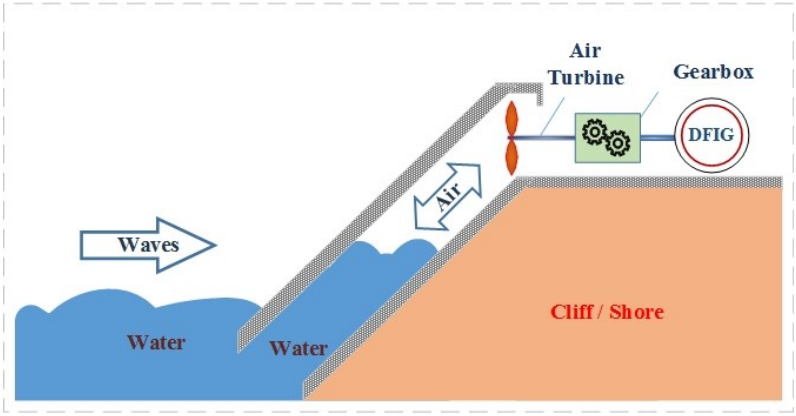

Figure 3.1 Oscillating Water Column Construction [73]

3.2 Waves Model

For the study of regular waves, it is necessary to consider the spectrum of the wave climate, which indicates the amount of wave energy at different wave frequencies. This representative spectrum is obtained by an offshore wave rider buoy in deep water, measuring a wide range of oceanographic parameters [74]. As presented in Figure 3.2, the regular wave can be written as follows:

$$P_{wavefront} = C_g * E_{denisty} = \frac{\rho_w * g * A^2 * \lambda}{16T} * \left[1 + \frac{\frac{4\pi h}{\lambda}}{\sin\left(\frac{4\pi h}{\lambda}\right)}\right] \tag{3.2}$$

where $P_{wavefront}$ is the incident wave power, C_g is the wave group velocity, $E_{denisty}$ is the wave energy density, ρ_w is the density of water, g is the acceleration of gravity, A is the wave amplitude, h is the water depth, T is the wave period and λ is the wavelength defined by [75]:

$$\lambda = \frac{g * T^2}{2\pi} \tanh\left(\frac{2\pi h}{\lambda}\right) \tag{3.3}$$

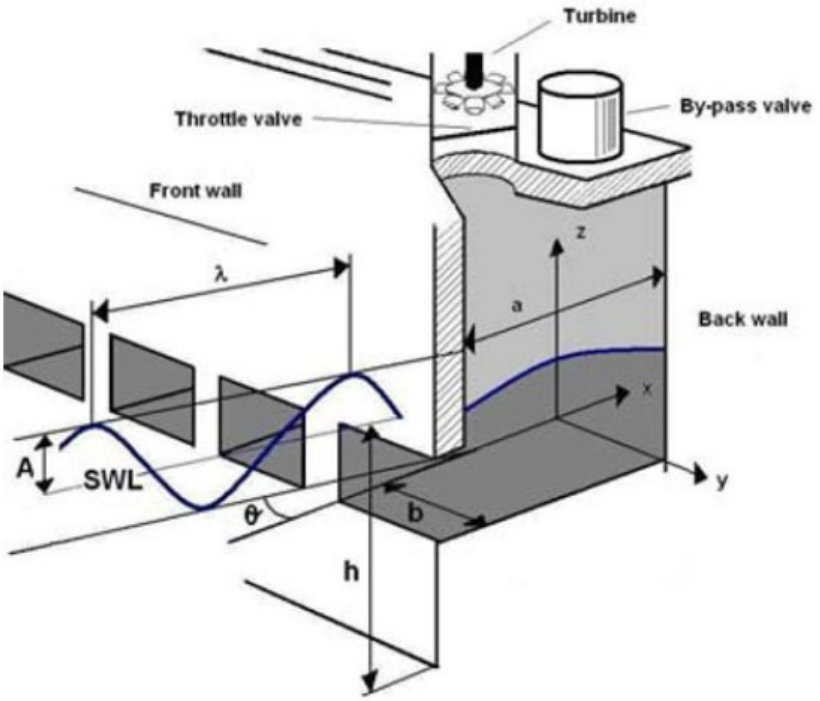

Figure 3.2 Capture Chamber for OWC Converter [75]

3.3 Oscillating Water Column Placement

OWC devices are placed on the shoreline or near the shore. The shoreline devices are placed where the waves break on the beach. The near shore devices are solidly moored to the ocean floor in the same manner as offshore wind turbines so as to respond to changes in mean water level as tides. The housing is placed just above the water surface [76].

Both near shore and shoreline placements have advantage and disadvantages. Of foremost importance is that the wave energy is greater offshore than on the shoreline [40]. Wave energy concentration near shore through natural phenomena such as refraction or reflection can compensate for some of this energy dissipation, but there are few areas where this occurs. The detriment to being offshore is that installation and maintenance costs increase. Both the near shore and shoreline OWCs are visible over the ocean surface; hence both experience public resistance to their installation. The shoreline device interferes with beachgoers more directly and met the most public resistance [37, 77]. With the need for public acceptance, the near shore OWC is the better device [37].

The changing mean ocean surface level tides may present problems for a fixedly moored OWC. Nonetheless, a fixedly moored device maintains its position better than a

slack moored device so as to provide more resistance to incoming waves and therefore produce more energy [77]. Another tradeoff between the fixedly and slack moored OWC is that while the fixedly moored OWC collects more energy, the slack moored OWC provides flexibility in rough seas that might damage a fixedly moored device. The installation costs of a slack moored device are less than a fixedly moored device because a rigid foundation does not need to be constructed [78].

3.4 Air Pressure and Flow Control

A bypass valve is one of the most important elements used in controlling an OWC. The bypass valve releases extra air pressure caused by waves whose amplitude exceed normal operating conditions. If this surplus pressure is not released, the turbine will stall. In addition to avoiding stall, the bypass valve acts to control the rotational speed of the turbine by limiting the flow of air through the turbine. This functionality is similar to blade pitch control for a wind turbine. Pitch control may accompany bypass valves as a method of controlling the turbine speed and excessive air pressure conditions within the chamber [76].

Bypass valves are presumed to permit linear airflow with infinite pressure relief ability [35]. In practice, bypass valves are not linear due to airflow turbulence. There is also an upper air flow limit that restricts the rate at which pressure may be released [79].

These assumptions are acceptable within limits, but are not valid for extreme conditions, which are likely to be encountered in an oceanic environment. The one way to overcome these limits is to install valves with larger capacity or to install multiple smaller valves [72].

For the sake of the analysis, the response time of the bypass valves is assumed to be infinitesimal. In reality, the time it takes the valve to respond cannot be neglected. Not only does the valve itself take time to smooth transients, the valve control system takes time to react to changing conditions [37]. The topic of decreasing the response time has not received much attention within the literature. The control method depends on the air chamber dimensions, the turbine and valves used, and wave climate [37, 79]. Hence, a generic solution is recommended.

Air pressure and flow control aim to improve the response time and prevent stalling phenomena. This objective may be achieved using bypass valves [37, 72, 76].

3.5 Air Turbines

Because of the reciprocating air flow of the OWC, conventional unidirectional air turbines cannot be used. In the past, this problem was solved by employing rectifying valve-systems to correct the flow direction. Currently, self-rectifying air turbines are used such as the Dennis-Auld turbine, the impulse turbine [80, 81] and Wells turbine [82, 83], which are presented in Figure 3.3 [24].

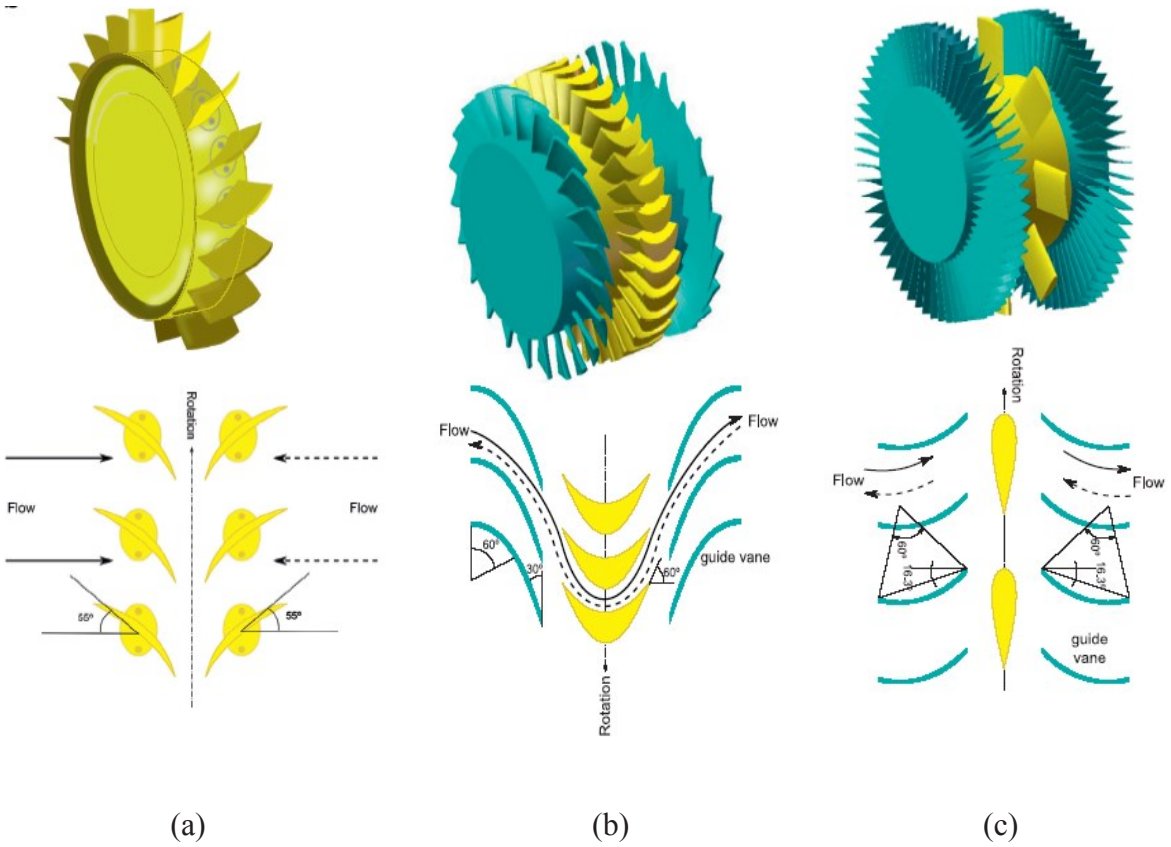

(a) (b) (c)

Figure 3.3 Air Turbines for WECs. (a) Dennis Auld Turbine, (b) Impulse Turbine and (c) Wells Turbine [81].

The Dennis-Auld air turbine was developed in Australia [84] and it was installed in the Oceanlinx OWC [29]. It is a self-rectifying turbine similar to a variable pitch Wells turbine. The blades are located on the periphery of the rotor hub in a neutral position, parallel to the axial direction of the flow, rather than tangential to the direction of rotation, as in the Wells and Impulse turbines. The Dennis-Auld turbine has a larger pitching range

than the Wells turbine, resulting in a greater solidity (total blade area divided by turbine weep area) which increases the efficiency of the device [82, 84].

The Impulse air turbine was invented in 1975 by I.A. Babinsten. It is a self-rectifying turbine with an axis of rotation linked to the direction of an air flow. As with the Wells turbine, it has self-pitch-controlled guide vanes [80]. An example of its deployment is the wave energy plant of Niigata-Nishi port [85]. The advantages and disadvantages of Impulse turbines compared to Wells turbines cannot be qualified, due to the wide range of turbine versions for both types [80, 82].

The Wells air-turbine was invented by Dr. Alan Wells at Queen's University in the mid-1970s. It is a self-rectifying axial-flow turbine, meaning its torque is not sensitive to the direction of the air flow. It is the most common turbine in the OWCs (LIMPET OWC [86], Mutriku OWC [74], Pico [87]), because of its relatively high speed rotation with low air flow velocity, and satisfactory peak efficiency (70%–80% for full sized turbine) for a relatively low cost. Disadvantages include low torque for small flow rates, noise, relatively low power-to-size ratio and the power output drop due to the aerodynamic losses at flow rates beyond the critical value. Many Wells turbine configurations are available, including those with guide vanes, those with self-pitch-controlled blades, those with a biplane turbine with guide vanes and contra-rotating Wells turbines [80, 81].

3.6 Wells Turbines

Over the past twenty years, most OWC research has focused on the Wells turbine to extract power from bidirectional air flow, which drives an electric induction generator mounted on the same shaft [80], as illustrated in Figure 3.4.

Relative to the blade, the direction of air flow is at a non-zero angle of attack, α. The net force acting on the blade in the direction of motion is then given by [37]:

$$F = L \sin \alpha - D \cos \alpha \tag{3.4}$$

Where L and D are the lift and drag forces acting on the blade, respectively. It is clear from the force diagram in Figure 3.5 that the direction of the net force is the same, irrespective of whether the air is flowing upward or downward inside the air column [37].

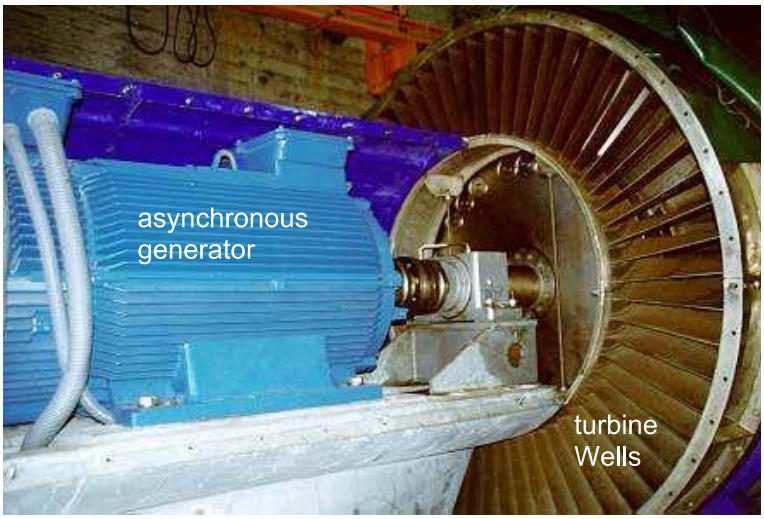

Figure 3.4 Wells Turbine Coupled to Induction Generator Assembly [37]

The shape of the blade is designed to maximize the net force on the blade. The operational efficiency of a Wells turbine is approximately 80%. At low air velocities the turbine absorbs power from the generator in order to maintain a constant rotational speed. For large air velocities the airflow around the blades is turbulent, and the net force in the direction of the blade becomes erratic, reducing the efficiency [88].

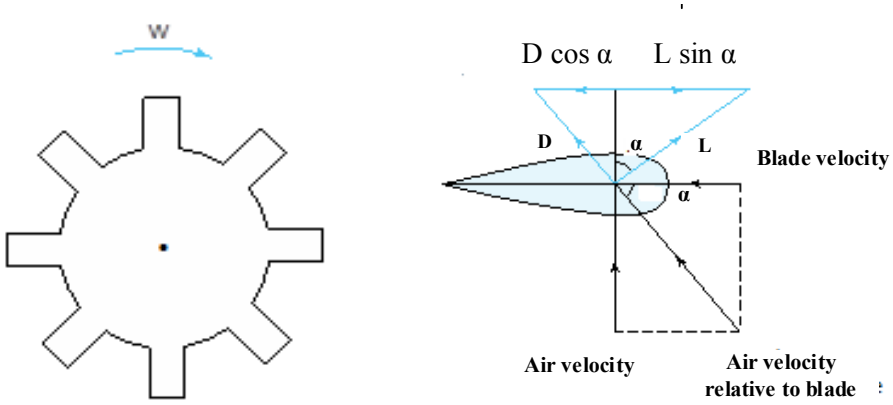

(a) (b)

Figure 3.5 Wells Turbine Blades (a) Plan View of Blades and (b) Velocity and Forces in Blade Reference Frame [37]

3.7 Wells Turbine Model

The Wells turbine is an axial-flow turbine that converts an oscillating flow into a unidirectional rotary motion to drive an electrical generator. The turbine always rotates in

the same direction for inbound and outbound air flow [89, 90]. The primary input for the design of a Wells turbine is the pneumatic power, based upon the pressure drop and the volume flow rate [52, 62]. The turbine modelling equations can be presented as follows [73, 75]:

$$dp = C_a * k * \left(\frac{1}{a}\right) * [v_x^2 + (r * \omega_t)^2] \quad (3.5)$$

$$T_t = C_t * k * r * [v_x^2 + (r * \omega_t)^2] \quad (3.6)$$

Where C_a *and* C_t are the power and torque coefficients, respectively, r is the mean radius of the turbine and ω_t is the turbine angular velocity. The subscripts r and s in the following equations indicates either rotor or stator, respectively. K is the turbine constant defined as [74]:

$$k = \frac{\rho b n l}{2} \quad (3.7)$$

Where n is the number of blades, l the blade chord length, b is the blade height and ρ is the air density. It may then be deduced that the turbine torque (T_t) [73, 74] is

$$T_t = \frac{dp * C_t * r * a}{C_a} \quad (3.8)$$

The flow coefficient, $\emptyset$, is defined as a non-dimensional quantity corresponding to the tangent of the angle of attack at the blade tip. The flow coefficient is defined as

$$\emptyset = \frac{v_x}{r * \omega_t} \quad (3.9)$$

The flow rate, Q and turbine performance efficiency,η_t can be calculated as:

$$Q = v_x * a \quad (3.10)$$

$$\eta_t = \frac{T_t * \omega_r}{dp * Q} = \frac{C_t}{C_{a*\emptyset}} \quad (3.11)$$

A detailed description of the OWC numerical model may be found in [91, 60].

The turbine power and torque can be calculated based on the relationship between the coefficients C_t and C_a and the flow coefficient $\emptyset$, which compose the characteristic curves of the Wells turbine, as illustrated in Figure 3.6. The curve shows that when $\emptyset$ approaches a critical value (typically 0.3), the torque coefficient drops drastically. This is commonly known as the stalling behaviour of the Wells turbine [92, 93]. The power coefficient C_a is not affected by the changes in C_t as it mainly depends on the input turbine power as shown in equation 3.11 while the turbine output power is only affected by C_t.

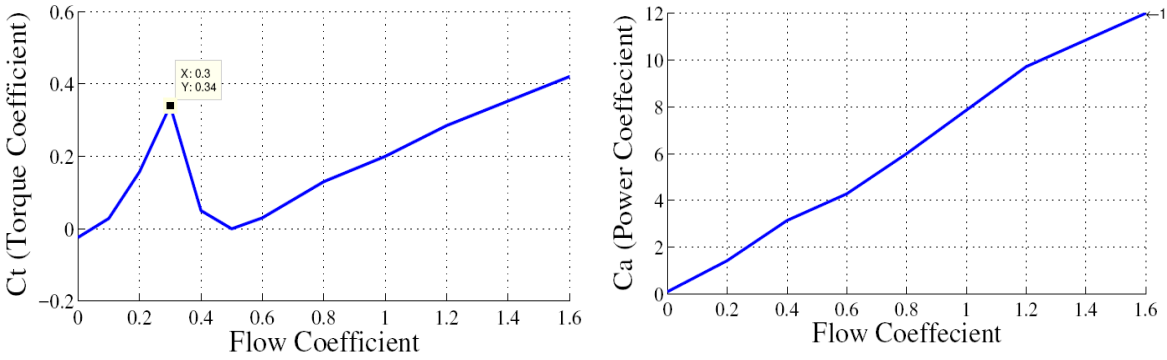

(a) (b)

Figure 3.6 Wells Turbine (a) Torque Coefficient and (b) Power Coefficient [55]

The torque and consequently the turbine efficiency in equations (3.8) and (3.11) drop drastically during the stalling behaviour, depending on the rotational speed. As a result, the performance of the Wells turbine is limited by the stalling phenomenon of the turbine blades. This is why air flow control is particularly relevant in a Wells turbine [92, 93]. The undesired stalling behaviour can be avoided or delayed if the turbine accelerates fast enough in response to the incoming airflow. The equation for the turbo generator can be written as follows [76]:

$$J\left(\frac{\partial \omega_t}{\partial t}\right) = T_t - T_g \tag{3.12}$$

Where J is the moment of inertia of the system and T_g is the torque imposed by generator.

For simulation model purposes, pressure drop is considered to be the turbine input, which considers the spectrum of the wave climate. This can be modelled as $|7000sin(0.1\pi t)|$ *Pa,* as shown in Figure 3.7 [92, 61].

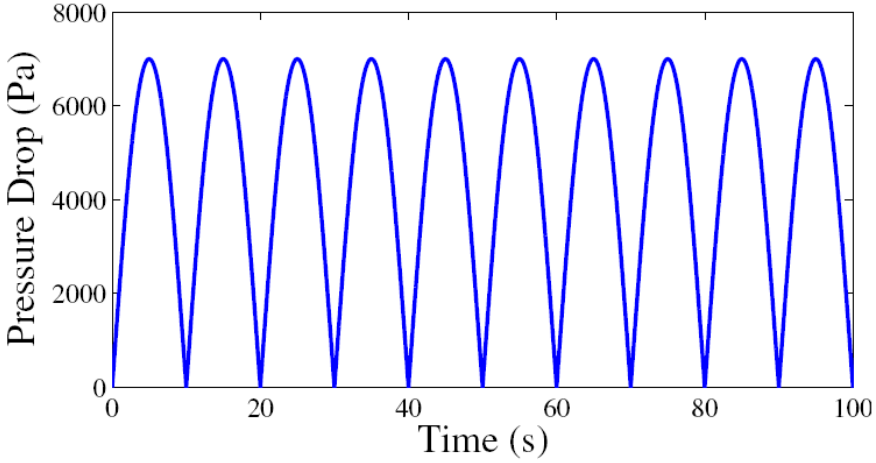

Figure 3.7 Pressure Drop Relative to the Spectrum Wave Climate [74, 76]

3.8 Doubly Fed Induction Generator

The main reasons for the popularity of the doubly fed induction generators (DFIG) are the ability to supply power at constant voltage and frequency even while the rotor speed varies and the fact that the machine converter handles the fraction of stator power [71, 94, 95]. The DFIG system therefore operates in both sub- and super-synchronous modes with a rotor speed range around the synchronous speed. The stator circuit is directly connected to the grid while the rotor winding is connected via slip rings to a three-phase AC-DC-AC converter as shown in Figure 3.8. For variable-speed systems where the speed range requirements are small, for example ±30% of synchronous speed, the DFIG offers adequate performance and is sufficient for the speed range required to exploit typical wave resources [96, 97].

Generally, DFIG systems utilize closed-loop current control for a back-to-back active front end voltage-source inverter (VSI). At this stage, the voltage source inverter can be viewed as a three-phase voltage source whose magnitude and phase can be altered instantaneously. Therefore, the VSI can be used to regulate the rotor current. In order to properly position, the physical position of the rotor is required from a mechanical position sensor, for example. The rotor current (flux) can be oriented optimally with respect to the stator flux to generate the desired torque [96].

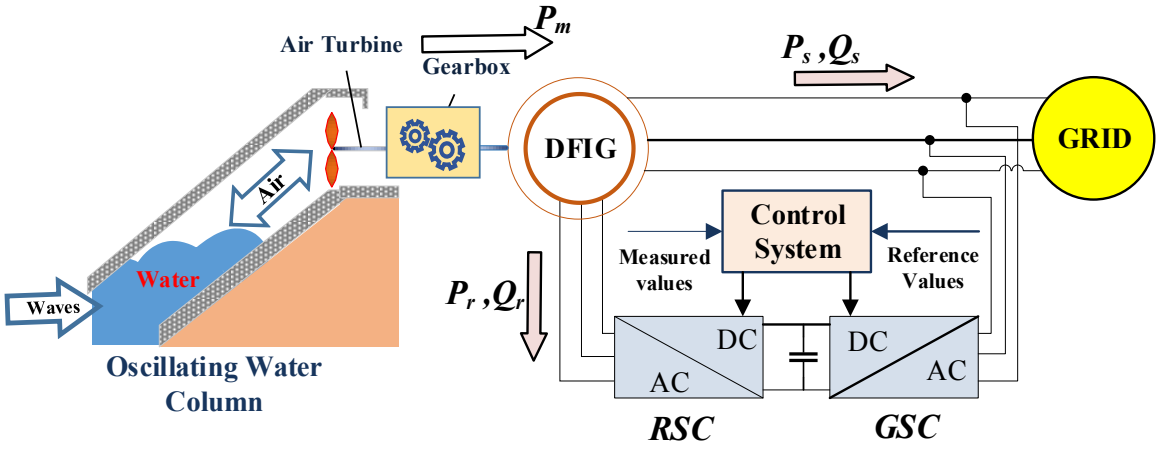

Figure 3.8 Grid connected Oscillating Water Column (OWC) Wave Energy System through AC – DC-AC Converter

The AC-DC-AC system consists of a rotor-side converter (RSC) and a grid-side converter (GSC), which are connected "back-to-back." As shown in Figure 3.8, between the two converters, a DC-link capacitor is placed, as energy storage, in order to reduce

variations in the DC-link voltage. With the rotor-side converter, it is possible to control the torque or the speed of the DFIG and the power factor at the stator terminals. The grid-side converter will keep the DC-link voltage constant, regardless of the magnitude or direction of the rotor power. The grid-side converter works at the grid frequency (leading or lagging in order to generate or absorb a controllable magnitude of reactive power). The rotor-side converter works at different frequencies, depending on the wave turbine speed [98, 99].

The two power electronic converters need only to handle 30% - 40% of the total power of the nominal generator [9, 97]. Therefore, the losses in the power electronic converter can be reduced, compared to a system where the converter must handle the entire load, as in the case of a full converter driving a permanent magnet synchronous generator [99]. The overall system cost is lower due to the partially rated power electronics [99, 100]. The DFIG system extracts maximum energy from low speeds technologies by optimizing the turbine speed, while minimizing mechanical stresses on the turbine. Another advantage of the DFIG technology is the ability for power electronic converters to generate or absorb reactive power, thus eliminating the need for capacitor banks, as in the case of a squirrel-cage induction generator [96, 101].

Figure 3.9 represents a per phase equivalent circuit for a doubly fed induction machine [96]. The stator side has two 'parasitic' components, R_s and L_s, which represent the stator phase winding resistance and the leakage inductance, respectively. The leakage inductance represents all the flux generated by the current in the stator windings that does not cross the air-gap of the machine, therefore does not contribute to the torque production. The magnetizing branch, L_m, represents the generation of useful flux in the machine – flux that crosses the air-gap either from stator to rotor or vice-versa [96, 98, 101, 102].

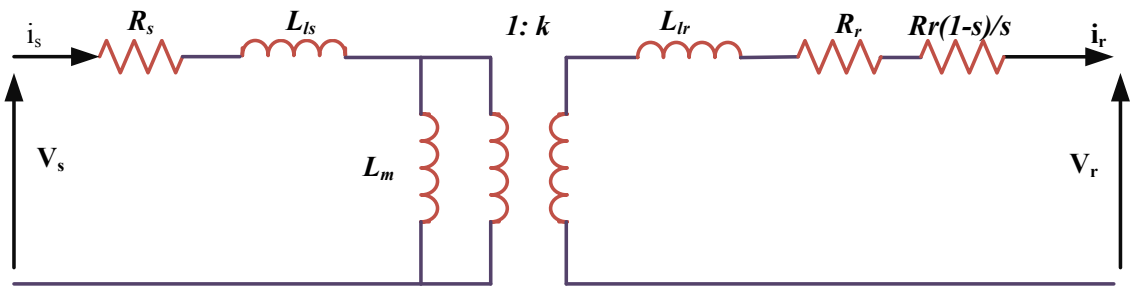

Figure 3.9 Per Phase Equivalent Circuit for a Doubly Fed Induction Machine [96]

The rotor circuit also has two parasitic elements. The rotor leakage reactance, L_r, and the rotor resistance R_r. In addition, the rotor circuit represents the generated

mechanical power by including an additional rotor resistance component, $R_r(1–s)/s$. Note that the rotor and stator circuits are linked via a transformer action which includes the ratio between the stator and rotor (1:k) windings, and the slip, s, of the machine. The slip is defined as [96, 98, 101]:

$$s = \frac{n_s - n_m}{n_s} \tag{3.13}$$

The mechanical torque generated by the machine is found by calculating the power absorbed (or generated) by the rotor resistance component $R_r = (1 - s)/s$ as follows [96, 98]:

$$P_{mech} = 3 * |i_r|^2 * \left(\frac{1-s}{s}\right) * R_r \tag{3.14}$$

In an ideal induction machine, the rotor and stator phase winding resistance and leakage inductance can be ignored. Consequently, the simpler per-phase equivalent circuit is represented as in Figure 3.10.

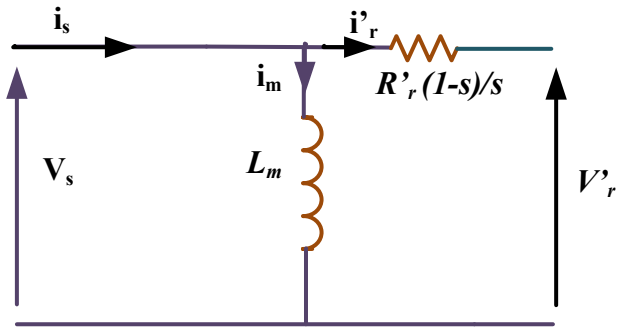

Figure 3.10 Simplified per Phase Equivalent Circuit [96]

By using this simplified circuit, mechanical torque production can be expressed as [96]:

$$T_{mech} = 3|i'_r|^2 * \left(\frac{1-s}{s}\right) * \frac{R'_r}{\omega_m} \tag{3.15}$$

$$\omega_m = \frac{(1-s)\omega_s}{p} \tag{3.16}$$

$$\psi_m = L_m i_m = \frac{|i'_r| * R'_r}{s * \omega_s} \tag{3.17}$$

$$T_{mech} = 3|i'_r|^2 * \left(\frac{1-s}{s}\right) * \frac{R'_r}{\omega_m} = 3 * p \frac{|i'_r| * R'_r}{s * \omega_s} |i'_r| = 3 * p * \psi_m * |i'_r| \tag{3.18}$$

The main conclusion is that the developed torque is controlled by a combination of the generated flux,ψ_m and the rotor current magnitude,i'_r if the two vectors are maintained in quadrature. In the DFIG system, torque is controlled by calculating the physical position and magnitude of the generated flux (by monitoring the applied stator voltage which is imposed by the grid voltage magnitude, frequency and phase) and regulating the rotor currents such that quadrature to the stator flux is maintained, with a magnitude that generates the desired torque [96, 98, 99].

3.9 Doubly Fed Induction Generator *d-q* Dynamic Model

In order to explore the definite behaviour of the DFIG, dynamic equations must be considered. From a machine control viewpoint, the *d-q* representation of an induction machine leads to control flexibility [98, 102]. The main advantage of the *d-q* dynamic model is that all sinusoidal variables in the stationary frame appear as DC quantities when referenced to the synchronous rotating reference frame [102]. The dynamic behaviour of the DFIG in the synchronous reference frame can be represented by the Park equations, provided all the rotor quantities are referenced to the stator side. Figure 3.11 shows the *d-q* dynamic model equivalent circuits [100, 103, 104].

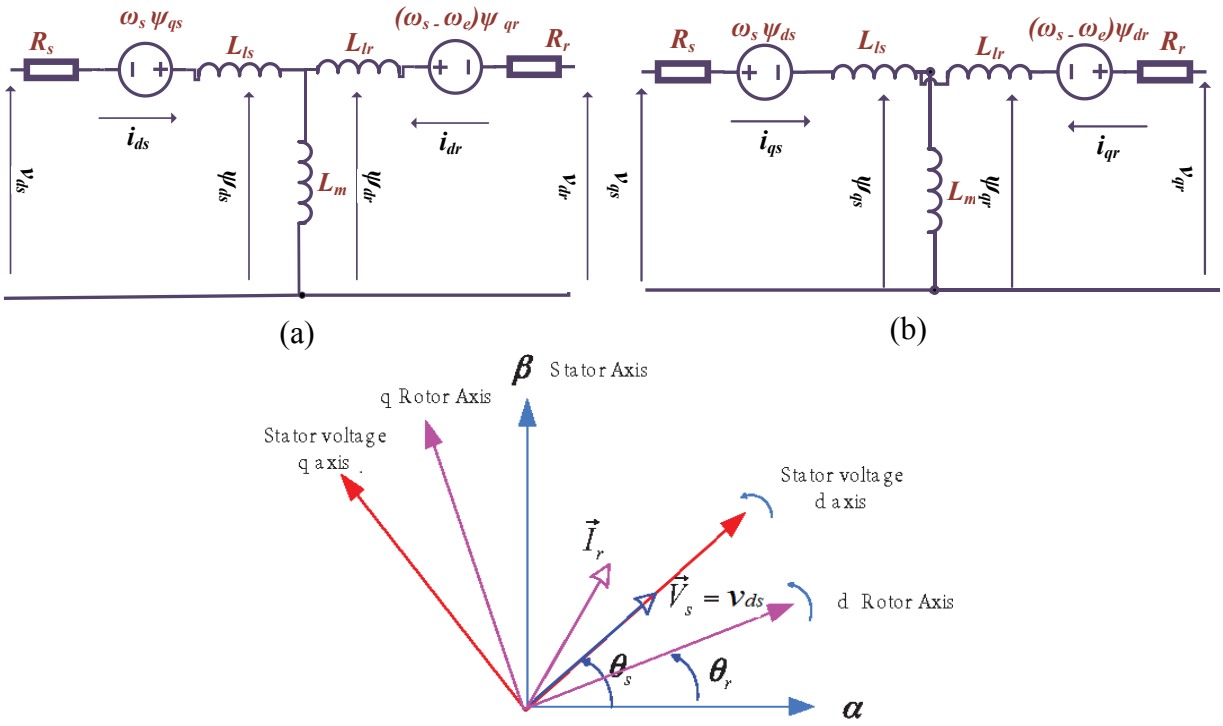

Figure 3.11 DFIG Modeling (a) Dynamic d –axis Equivalent Circuits for DFIG (b) Dynamic q-axis Equivalent Circuits for DFIG (c)Stator Flux Oriented Vector Diagram [61]

Hence, the classical electrical equations of the DFIG given by the stator and rotor *d-q* voltages in the Park frame are written as follows [103, 105]:

$$v_{qs} = R_s.i_{qs} + \frac{\partial}{\partial t}.\psi_{qs} + \omega_s.\psi_{ds} \quad (3.19)$$

$$v_{ds} = R_s.i_{ds} + \frac{\partial}{\partial t} * \psi_{ds} - \omega_s.\psi_{qs} \quad (3.20)$$

$$v_{qr} = R_r.i_{qr} + \frac{\partial}{\partial t}.\psi_{qr} + (\omega_s - \omega_e).\psi_{dr} \quad (3.21)$$

$$v_{dr} = R_r.i_{dr} + \frac{\partial}{\partial t}.\psi_{dr} - (\omega_s - \omega_e).\psi_{qr} \quad (3.22)$$

Hence, the DFIG electromagnetic torque is calculated [96]:

$$T_e = \frac{3}{2}.\left(\frac{p}{2}\right).(\psi_{ds}.i_{qs} - \psi_{qs}.i_{ds}) \quad (3.23)$$

For the quadrature axis flux component [103, 106]:

$$\psi_{qs} = L_s i_{qs} + L_m.i_{qr} \quad (3.24)$$

$$\psi_{qr} = L_r i_{qr} + L_m.i_{qs} \quad (3.25)$$

For the direct axis flux components [103, 106]:

$$\psi_{ds} = L_s i_{ds} + L_m i_{dr} \quad (3.26)$$

$$\psi_{dr} = L_r i_{dr} + L_m i_{ds} \quad (3.27)$$

Where the stator and rotor self-inductance are [96, 101]:

$$L_s = L_{ls} + L_m \quad (3.28)$$

$$L_r = L_{lr} + L_m \quad (3.29)$$

ω_s is the stator supply frequency, ω_e is the rotor electrical speed = $\omega_m * (\frac{p}{2})$ and T_e is the electromagnetic torque [103]. Neglecting the power losses associated with the stator and rotor resistances, the active and reactive stator powers are:

$$P_s = \frac{3}{2}\left(v_{ds}.i_{ds} + v_{qs}.i_{qs}\right) \quad (3.30)$$

$$Q_s = \frac{3}{2}\left(v_{qs}.i_{ds} - v_{ds}.i_{qs}\right) \quad (3.31)$$

While the active and reactive rotor powers are given by

$$P_r = \frac{3}{2}\left(v_{dr}.i_{dr} + v_{qr}.i_{qr}\right) \quad (3.32)$$

$$Q_r = \frac{3}{2}\left(v_{qr}.i_{dr} - v_{dr}.i_{qr}\right) \quad (3.33)$$

3.10 Doubly Fed Induction Generator Decoupled Vector Control

In order to achieve decoupled control of active and reactive power, the stator flux oriented (SFO) vector control scheme was adopted within [103].

Figure 3.12 and Figure 3.13 illustrate the DFIG decoupled vector control of the Rotor Side Converter (RSC) and Grid Side Converter (GSC), respectively. Figure 3.12 illustrates independent control of the stator active power (by means of speed control) and the reactive power (by means of rotor current regulation using RSC). Figure 3.13 illustrates the DC-link voltage and the grid reactive power control using the GSC.

3.10.1 Rotor Side Converter Control

The RSC control scheme consists of two cascaded control loops. The inner current control loops regulate independently the *d*-axis and *q*-axis rotor current components, i_{dr} and i_{qr}, respectively. Stator-flux oriented reference frame is the most commonly used method [107]. The outer control loops regulate both the stator active power (and the generator rotor speed) and the reactive power independently.

According to the stator-flux oriented reference frame, the *d*-axis is aligned with the stator flux linkage vector,ψ_s. The quadrature axis flux component must then be set to be zero to ensure independent active-reactive power control [101, 107]:

$$\psi_{ds} = L_s i_{ds} + L_m i_{dr} = \psi_s = L_m . i_{ms} \tag{3.34}$$

$$\psi_{qs} = 0 \tag{3.35}$$

Defining the leakage factor $\sigma = 1 - \left(\frac{L_m^2}{L_s . L_r}\right)$ and the equivalent inductance as$L_0 = \frac{L_m^2}{L_r}$, the rotor voltage and flux equations are (scaled to be numerically equal to the AC per-phase values) [96, 103, 106]:

$$i_{qs} = \frac{-L_m * i_{qr}}{L_s} \tag{3.36}$$

$$i_{ds} = \frac{L_m (i_{ms} - i_{dr})}{L_s} \tag{3.37}$$

$$P_s = \frac{-\frac{3}{2} . \omega_s . L_m^2 . i_{ms} . i_{qr}}{L_s} \tag{3.38}$$

$$Q_s = \frac{\frac{3}{2}.\omega_s.L_m^2.(i_{ms}-.i_{dr})}{L_s} \quad (3.39)$$

$$v_{dr} = R_r.i_{dr} + \sigma.L_r.\frac{\partial i_{dr}}{\partial t} - \omega_{slip}.\sigma.L_r.i_{qr} \quad (3.40)$$

$$v_{qr} = R_r.i_{qr} + \sigma.L_r.\frac{\partial i_{qr}}{\partial t} + \omega_{slip}.(L_0.i_{ms} + \sigma.L_r.i_{dr}) \quad (3.41)$$

$$\psi_{dr} = \frac{L_m^2}{L_s}.i_{ms} + \sigma.L_r.i_{dr} \quad (3.42)$$

$$\psi_{qr} = \sigma.L_r.i_{qr} \quad (3.43)$$

where, $i_{ms} = \frac{v_{qs}-R_s.i_{qs}}{\omega_s.L_m}$ and the slip angular speed is

$$\omega_{slip} = (\omega_s - \omega_e) \quad (3.44)$$

It can be concluded from Equations (3.38) and (3.39) that P_s and Q_s can be controlled independently by adapting the rotor current components, i_{qr} and i_{dr}, respectively. Consequently, the reference values of i_{dr} and i_{qr} can be determined from the outer power control loops, as illustrated in Figure 3.12

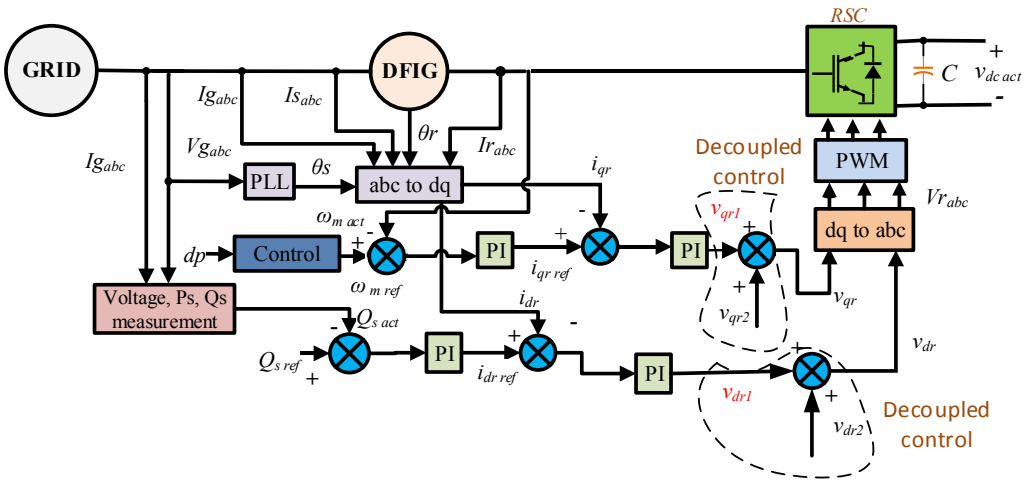

Figure 3.12 RSC Control

The actual values of the *d-q* rotor current components, i_{dr} and i_{qr}, can be calculated from the instantaneous three phase rotor currents Ir_{abc}, which can be transformed into *d-q* components by using the slip angle, θ_{slip} (i.e. the difference angle between grid and rotor frames in the SFO). The reference values of the *d*-axis rotor current, $i_{dr\,ref}$, and *q*-axis rotor current, $i_{qr\,ref}$, can be determined directly from the stator reactive power, Q_{sref}, and the controlled speed, ω_{ref}, in order to avoid stalling. The actual rotor

currents, i_{dr} and i_{qr}, are compared to the reference rotor currents, $i_{dr\,ref}$ and $i_{qr\,ref}$. The controller error output forms the signal v_{dr} and v_{qr} as follows [103, 107, 108]:

$$v_{dr1} = R_r.i_{dr} + \sigma.L_r.\left(\frac{\partial i_{dr}}{\partial t}\right) \tag{3.45}$$

$$v_{qr1} = R_r.i_{qr} + \sigma.L_r.\left(\frac{\partial i_{qr}}{\partial t}\right) \tag{3.46}$$

Rearranging (3.40), (3.41), (3.45), and (3.46) into matrix notation [108]:

$$\frac{\partial}{\partial t}\begin{bmatrix} i_{dr} \\ i_{qr} \end{bmatrix} = -\frac{R_r}{\sigma.L_r}\begin{bmatrix} 1 & 0 \\ 0 & 1 \end{bmatrix} i_{dr} + \frac{1}{\sigma L_r}\begin{bmatrix} v_{dr1} \\ v_{qr1} \end{bmatrix} \tag{3.47}$$

Equation (3.47) indicates that i_{dr} and i_{qr} respond to v_{dr1} and v_{qr1}, respectively, through a first-order transfer function without cross-coupling. It is therefore possible to design the following feedback loops and PI controllers [108]:

$$v_{dr1} = \left(K_{pr} + \frac{K_{ir}}{s}\right).(i_{dr\,ref} - i_{dr}) \tag{3.48}$$

$$v_{qr1} = \left(K_{pr} + \frac{K_{ir}}{s}\right).(i_{qr\,ref} - i_{qr}) \tag{3.49}$$

To ensure better tracking of the *dq*-axis rotor currents, compensation terms are added by substituting (3.48) and (3.49) in equations (3.40) and (3.41) to obtain the reference voltages v_{dr} and v_{qr} [108]:

$$v_{dr} = \left(K_{pr} + \frac{K_{ir}}{s}\right).\left(i_{dr\,ref} - i_{dr}\right) - \omega_{slip}.\sigma.L_r.i_{qr} \tag{3.50}$$

$$v_{qr} = \left(K_{pr} + \frac{K_{ir}}{s}\right).\left(i_{qr\,ref} - i_{qr}\right) + \omega_{slip}.(L_m.i_{ms} + \sigma.L_r.i_{qr}) \tag{3.51}$$

Where, K_{pr} and K_{ir} are the proportional and integral gains of the PI controller, respectively.

Finally, v_{dr} and v_{qr} are transformed to the PWM modulating signals, Vr_{abc}, by applying the inverse transformation of the stator-flux oriented with the synchronously rotating reference frame transformation, in order to be used by the PWM module to generate the IGBT gate control signals to drive the RSC switches.

3.10.2 Grid Side Converter Control

The PWM rectifier used in the GSC control is nothing more than an inverter working with reverse power flow controlling the DC voltage. The basic operating principle of a Voltage Source Rectifier (VSR) consists of keeping the load DC-link voltage at a desired reference value, using a feedback control loop regardless of the magnitude and direction of the rotor power. This reference value must be high enough to keep the diodes

of the converter blocked. Once this condition is satisfied, the DC-link voltage is measured and compared with the reference. Hence, it acts as a boost rectifier [109].

The GSC control scheme shown in Figure 3.13 also consists of two cascaded control loops. The inner current control loops regulates the *d*-axis and *q*-axis independently of the GSC AC-side current components, i_{dg} and i_{qg}, in the synchronously rotating reference frame. The outer control loops regulate the DC-link voltage and the reactive power exchanged between the GSC and the grid.

In order to derive the inner loop equations, the ac-side circuit equations of the GSC are used, which can be represented by [9]:

$$\frac{\partial}{\partial t}.I_{gabc} = -\frac{R_g}{L_g}.I_{gabc} + \frac{1}{L_g}\left(v_{gabc} - v_{sabc}\right) \tag{3.52}$$

According to the synchronously rotating reference frame transformation with the *d*-axis aligned to the grid voltage vector v_s ($v_s = v_{ds}$, $v_{qs} = 0$), the following *d-q* vector representation can be obtained for modelling the GSC ac-side [105, 108]:

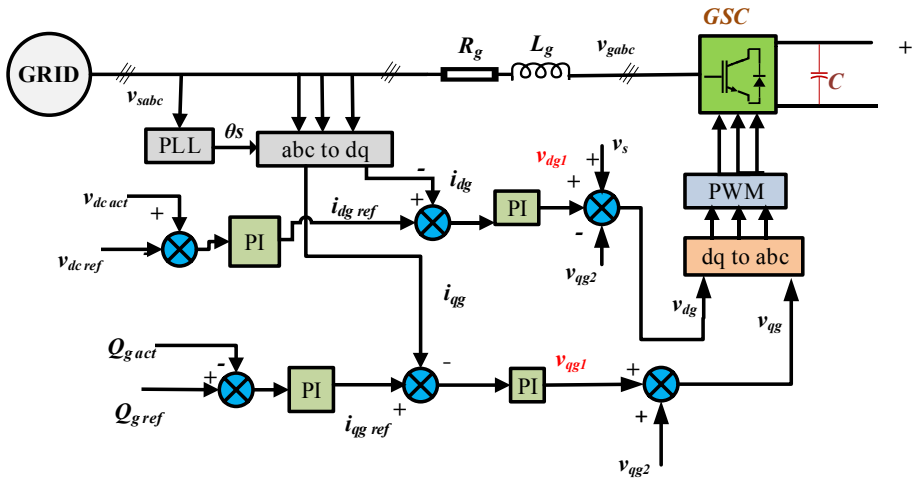

Figure 3.13 GSC Control

$$v_{dg} = R_g i_{dg} + L_g.\frac{\partial}{\partial t}\, i_{dg} - \omega_s.L_g.i_{qg} + v_{ds} \tag{3.53}$$

$$v_{qg} = R_g i_{qg} + L_g.\frac{\partial}{\partial t}\, i_{qg} + \omega_s.L_g.i_{qg} \tag{3.54}$$

By using the same process in (3.50) and (3.51), v_{dg} and v_{qg} can be obtained by the following feedback loops and PI controllers [9]:

$$v_{dg} = \left(k_{pg} + \frac{k_{ig}}{s}\right).\left(i_{dg\,ref} - i_{dg}\right) - \omega_s.L_g.i_{qg} + v_{ds} \tag{3.55}$$

$$v_{qg} = \left(k_{pg} + \frac{k_{ig}}{s}\right).\left(i_{qg\,ref} - i_{qg}\right) - \omega_s.L_g.i_{dg} \tag{3.56}$$

In order to adjust the DC-link voltage to 800 V and maintain the rectifier reactive power at zero, the reference values of *d*-axis grid current, $i_{dg\,ref}$, and *q*-axis grid current, $i_{qg\ ref}$, can be determined directly from the reference DC-link voltage, $v_{dc\,ref}$, and grid reactive power, $Q_{g\,ref}$.

The controlled v_{dg} and v_{qg} are transformed into v_{abc} in order to generate the required PWM signal to control the rectifier.

3.11 Investigated Decoupled Control Simulation Results

In the previous sections, a model for a DFIG based on an OWC was introduced, including the mathematical representation of the Wells turbine, DFIG and power converters. The control method used for the power converters, responsible for optimal power extraction from the waves, as well as grid interconnection, were presented for PWM-VSI topologies. Finally, a block diagram of a case study for a DFIG with GSC and RSC control topology was introduced, as shown in Figures 3.12 and 3.13. In order to investigate the performance of the controller for the DFIG-based Wells turbine, it was necessary to develop a comprehensive model of the whole system that would be robust enough to repeat the performance characteristics under different operational conditions. The model was created using SIMULINK, including elements from the MATLAB software package based on the block diagram presented in the Figures 3.12 and 3.13.

Figure 3.14 represents a simplified block diagram of the investigated DFIG based Wells turbine system. The system consisted of the three major components:

- A complete model of the DFIG with bi-directional converter
- The controllers for the DFIG based system
- A Wells turbine model

The investigated system parameters, including the Wells Turbine [56], DFIG and grid parameters are listed Table 3.1

The Wells turbine model was simulated by using MATLAB/Simulink libraries, equations listed in section 3.7 and the parameters listed in Table 3.1. The turbine model is presented in Figure 3.15.

The Wells Turbine, as presented in section 3.7, is an axial-flow turbine that converts an oscillating flow into a unidirectional rotary motion for driving an electrical generator. Hence, it always rotates in the same direction; both for inbound and outbound air flow [72]. The input of the Wells turbine is the oscillating differential pressure drop across the turbine rotor which is induced from the air flow off the OWC chamber. The main outputs of the turbine are the torque and the mechanical power.

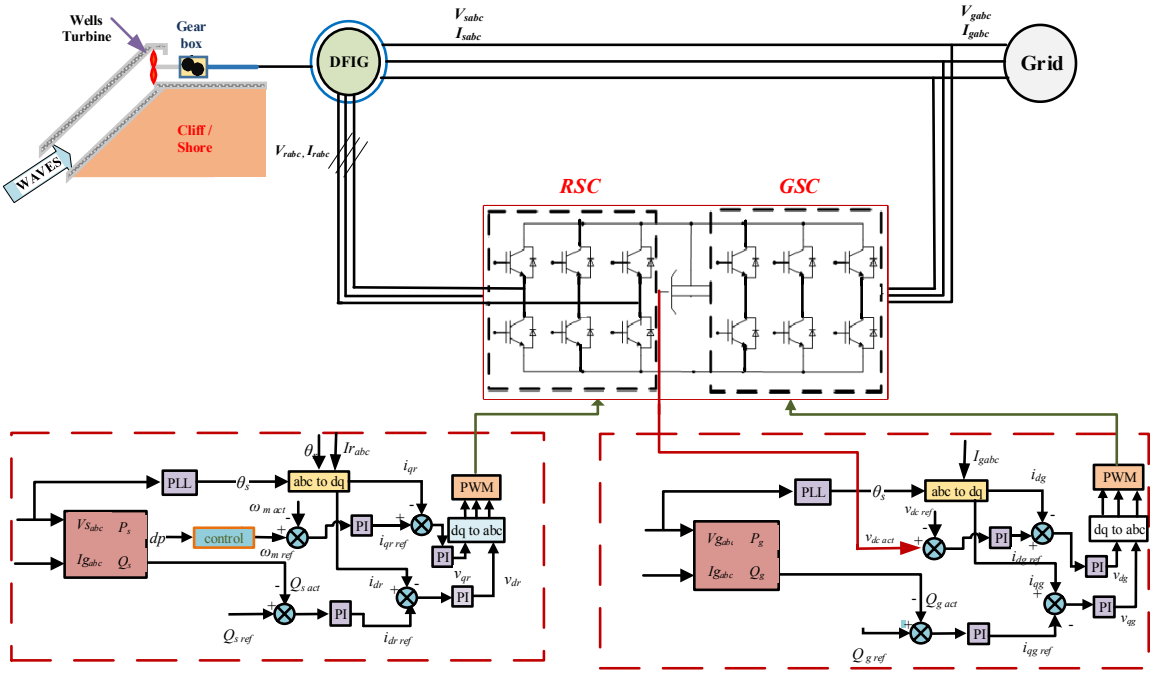

Figure 3.14 Simplified Block Diagram of DFIG System Based Wells Turbine

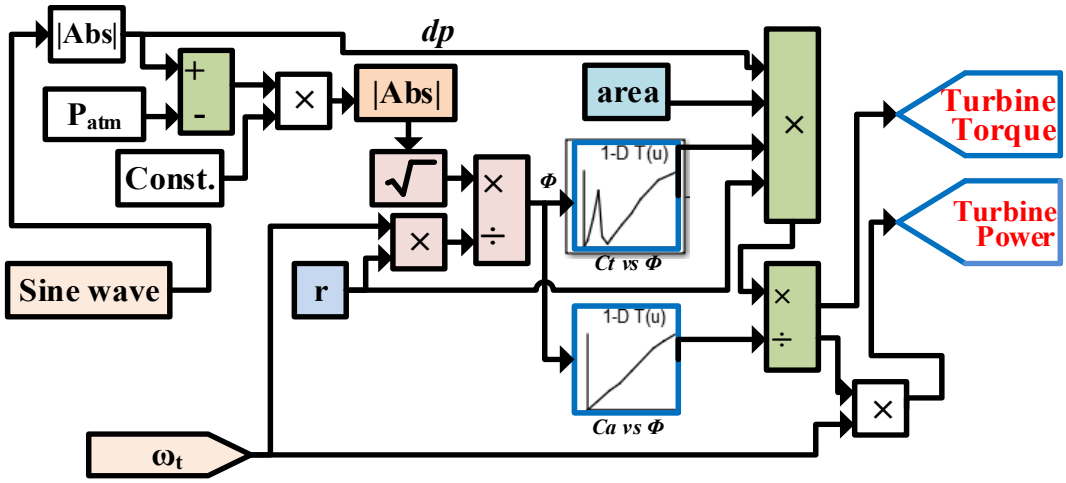

Figure 3.15 Wells Turbine Simulink Model.

The output torque of the turbine is used to drive the DFIG, according to the controlled speed of the RSC with the presence of a gearbox.

the two converter controllers, discussed in detail in Sections 3.10 (RSC and GSC), were implemented in the DFIG control scheme as shown in Figure 3.14 and the control results are below.

Table 3.1 Investigated system parameters

DFIG Parameters	
$R_s\ (\Omega)$	*0.0503*
$R_r\ (\Omega)$	*0.08233*
$L_m\ (H)$	*0.02711*
$L_{lr}\ (H)$	*0.000724*
$L_{ls}\ (H)$	*0.000724*
Poles	*2*
$P_{rated}\ (kW)$	*37*
Line voltage	*400*
Frequency(f) (Hz)	*50*
Wells Turbine Parameters	
N	*8*
k (Kg/m^2)	*0.7079*
r(m)	*0.7285*
a(m^2)	*1.1763*
l(m)	*0.38*
b(m)	*0.4*
Rectifier Parameters	
DC−link capacitor C (μF)	*1000*
DC link voltage (V)	*800*
Grid Parameters	
Grid voltage (V)	*400*
Grid frequency, f, (Hz)	*50*
Grid resistance (Ω)	*0.001*
Grid inductance (mH)	*5*

3.11.1 Grid Side Converter Controller Performance

The GSC attempted to achieve several tasks:

- Maintain constant DC-link voltage
- Exchange the energy between the grid and the DC-link
- Allow flexible control of the reactive power flow to the grid, however it is preferable to maintain a unity power factor

In the presented system, the reference voltage signal was set to 800 V, while the rectifier was forced to operate at a unity power factor. The performance of the GSC is illustrated as shown in Figure 3.16 (a) to (d).

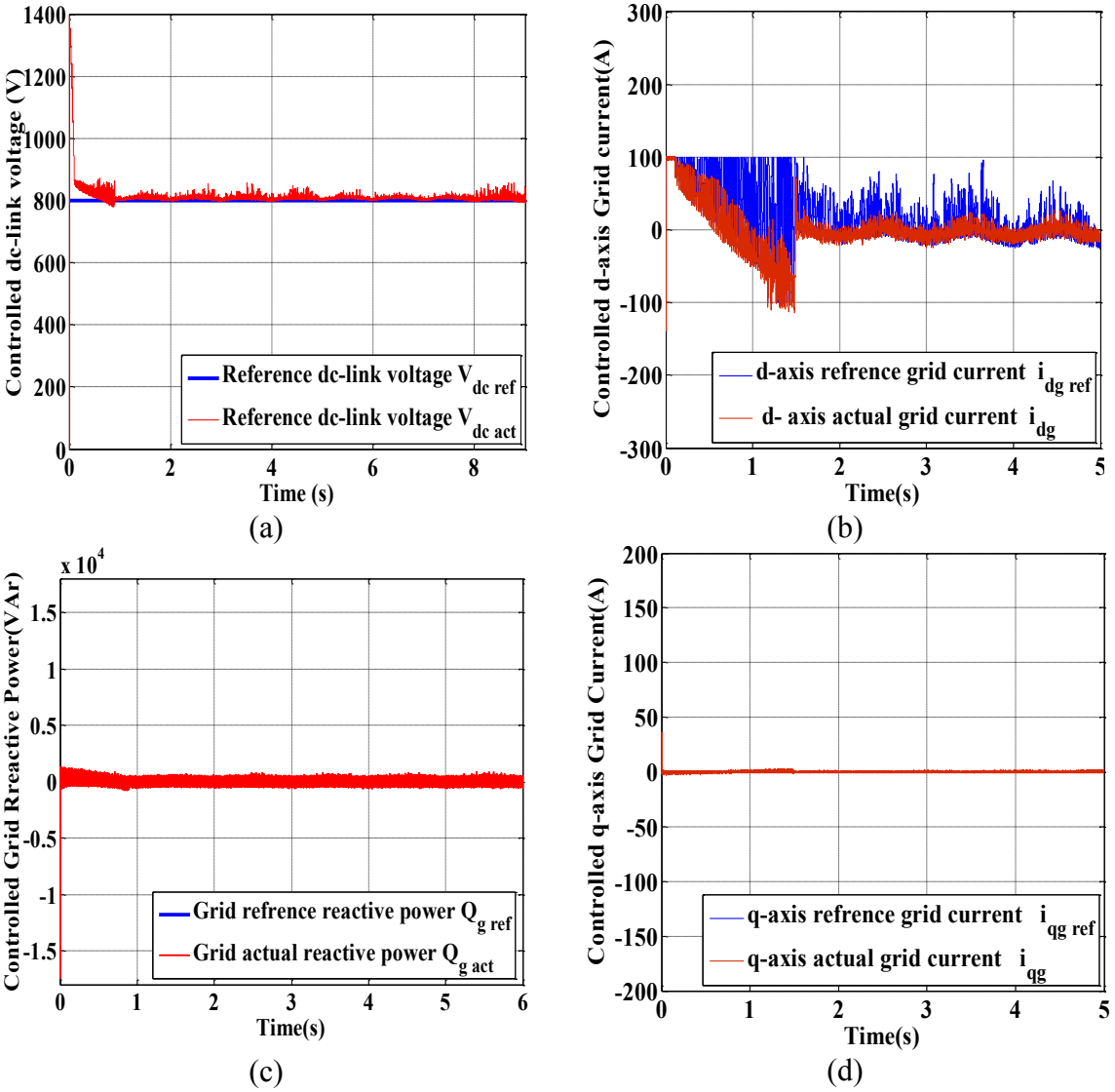

Figure 3.16 GSC Performance: (a) DC-link voltage, (b) Reference and Actual d-axis Grid Current, (c) Grid Reactive power, and (d) Reference and Actual q-axis Grid Current

In Figure 3.16 (a), the controller was able to maintain a constant DC link voltage at the required value 800 V. The error between the DC-link voltage command and the feedback voltage passes the PI regulator, and the result is that the active power current command, $i_{dg\,ref}$. The active power control ensures the DC-link voltage remains constant. Accordingly, the d-axis current tracks the reference value to satisfy the required DC-link voltage, as seen in Figure 3.16 (b).

For reactive power control, the system's input power factor goal is unity. Therefore, the reactive current should be controlled in order to achieve zero reactive power all the times. The controller was able to maintain the rectifier operation at unity power factor. It is clear in Figure 3.16 (c) and (d) that the grid reactive power is equal to zero and the q-axis current accurately tracks the reference value $i_{qg\ ref} = 0$

3.11.2 Rotor Side Converter Controller Performance

The RSC controller can be implemented using a speed-reactive power control $(\omega - Q)$ strategy. The Wells turbine operation in this strategy requires speed and reactive power control for optimum power extraction and reactive power support for the grid. These two requirements are independent and must be decoupled.

The command signals of the RSC speed controller include the desired turbine speed, which is directly related to the active power produced by the DFIG, and the required reactive power for the generator to maintain an appropriate power quality to the grid.

In order to clarify the decoupling technique effectiveness, two case studies were used to illustrate the decoupled control performance regarding the generator speed and grid reactive power.

***Case I:* Constant rotor speed and variable stator reactive power**

In this system, the decoupled control technique is examined at a constant rotor speed of 380 rad/s while the DFIG stator reactive power varies during the simulation interval.

The speed command signal is kept constant for optimum power extraction at a particular wave propagation, while the reactive power command signal varies from -10 KVAr (leading p.f) to 10 KVAr (lagging p.f) at times of 4 s and 7 s, respectively. This investigation shows the degree of independence between the speed, which is in direct proportion with the active power flow, and the reactive power flow in the DFIG. The results of this case are presented Figure 3.17.

As seen in Figure 3.17 (a), the system achieves the required reference reactive power for RSC as the *d*-axis current tracks its reference, as illustrated in Figure 3.17 (b). The rotor speed stays constant at 380 rad/s, as shown in Figure 3.17 (c) despite the changes of the reactive power as the *q*-axis current tracks its reference value, shown in Figure 3.17 (d).

The turbine torque and active power are illustrated in Figures 3.18 (a) and (b), respectively as a pulsating signal maintains a uniform pattern even during the reactive power variation. Under the proposed decoupled control for constant rotor speed, the power injected to the grid (stator active power) was also constant and was not affected by the variation of the reactive power command as shown in Figure 3.19 with an average of 15 kW. This test was performed to illustrate an important benchmark for the performance of the proposed converter scheme with a degree of independence between active and reactive power control capabilities in the DFIG stator field-oriented decoupled control technique.

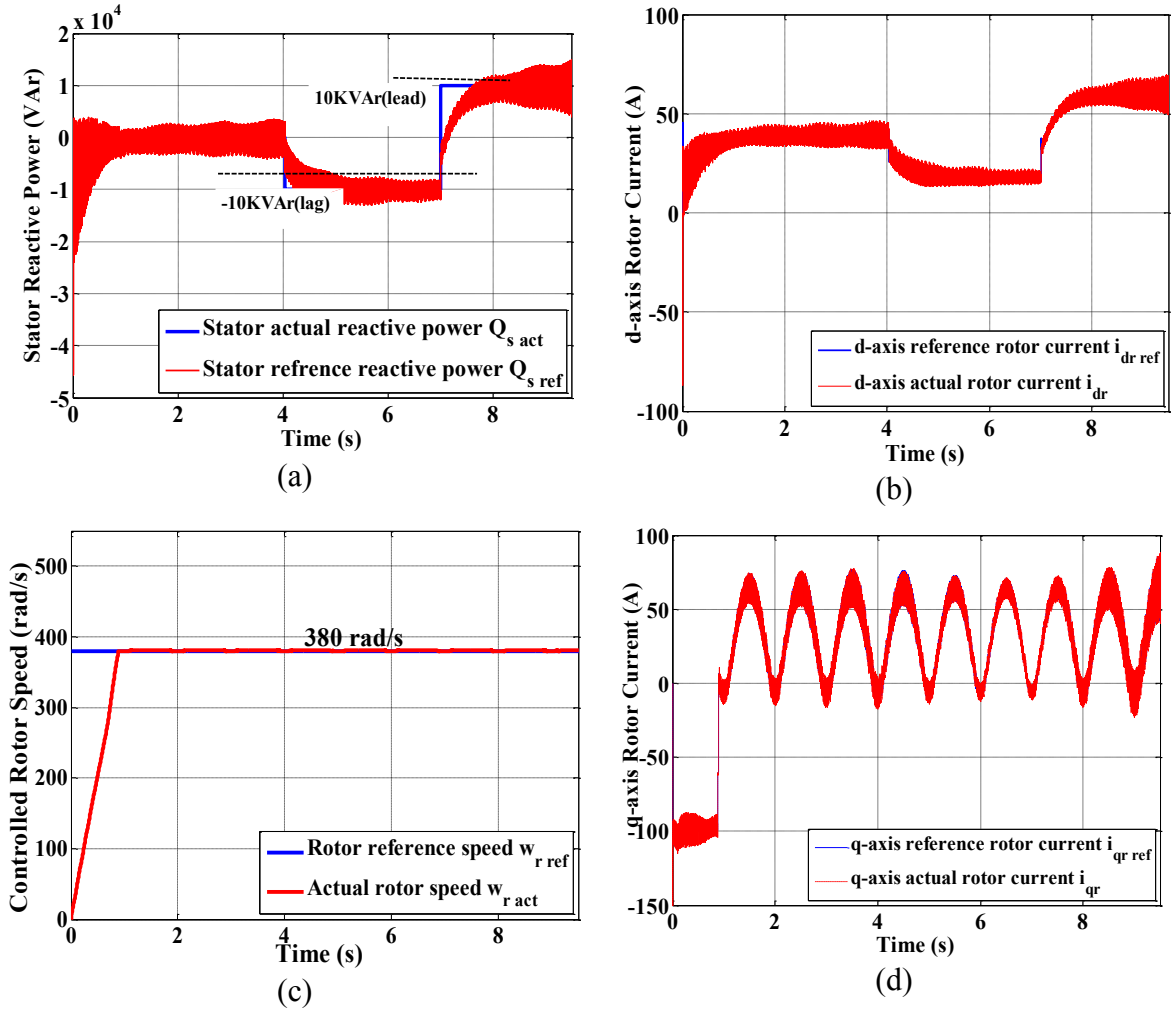

Figure 3.17 Case I Performance: (a) Stator Reactive Power (b) Controlled d-axis Rotor Current (c) Rotor Speed (d) Controlled q-axis Rotor Current

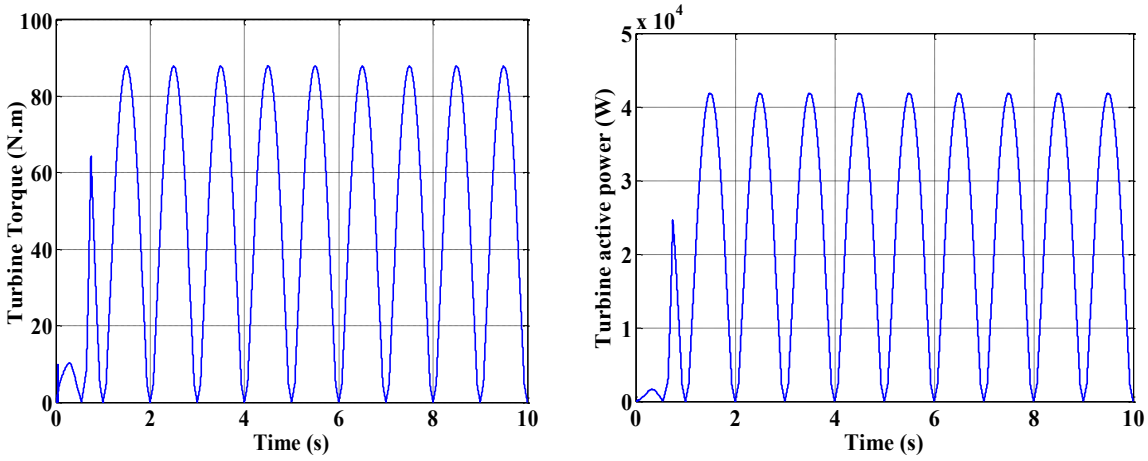

(a) (b)

Figure 3.18 Turbine performance During Case I (a) Turbine Torque, and (b) Turbine Active Power

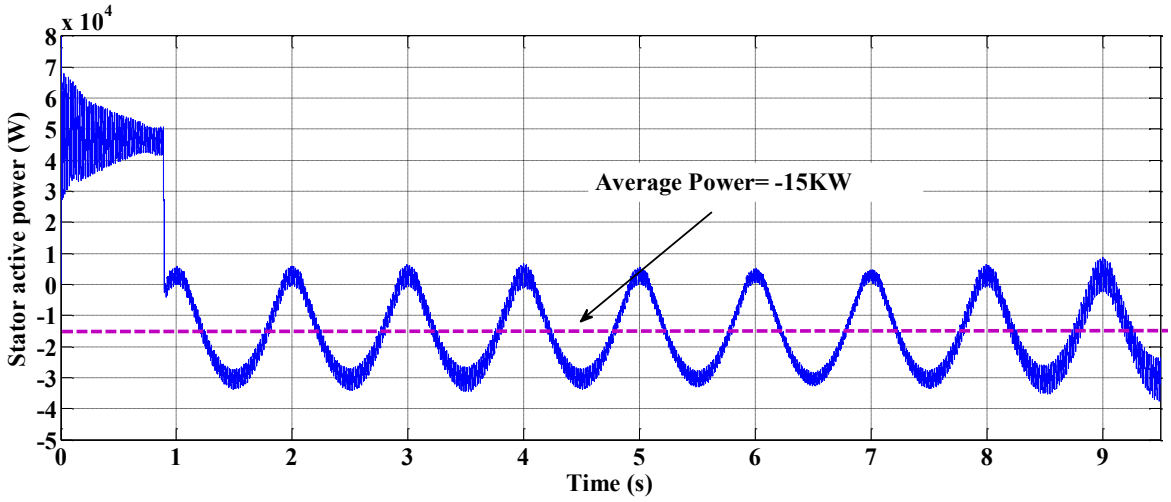

Figure 3.19 Case I DFIG Stator Active Power Performance

<u>Case II:</u> Variable Rotor Speed and Constant Stator Reactive Power

The proposed decoupled control was investigated with a variable rotor speed from 380 rad/sec to 420 rad/s. The reactive power command is imposed to be zero. As in Figure 3.12, both $\omega_{m\,ref}$ and $Q_{s\,ref}$ commands are compared to the corresponding measured values to obtain error signals which are fed to PI controllers whose outputs are the stator current commands $i_{qr\,ref}$ and $i_{dr\,ref}$, respectively. These current commands are compared to their corresponding measured values, producing error signals driving the PI current controller and generating the d-q voltage commands being fed to the PWM module. The system simulation results are shown in Figure 3.20.

Figure 3.20 (a) shows the speed of the DFIG accurately tracking the reference speed value as the speed command changes from 380 rad/s to 420 rad/s from t=3 s to t=6 s. The *q*-axis rotor current accurate reference performance is illustrated in Figure 3.20 (b).

As shown in Figure 3.20 (c), the reactive power reference command remains unchanged throughout the simulation and is kept constant at zero. The actual reactive power tracks the reference value during the overall simulation time interval, while the DFIG rotor speed changes. The *d*-axis rotor current reference aids in the fulfilment of the reference reactive power command, as shown in Figure 3.20 (d).

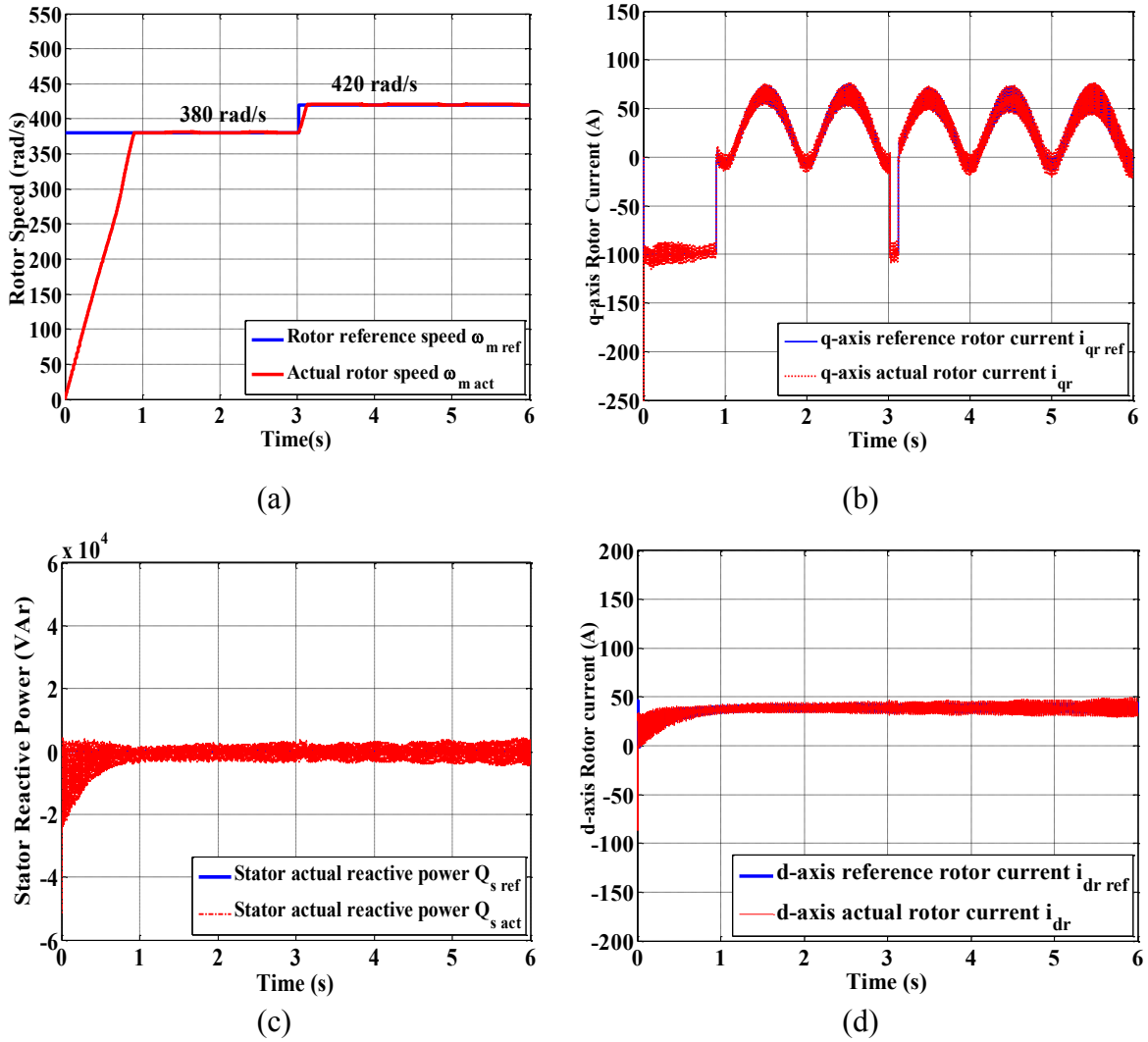

Figure 3.20 Case II Performance: (a) Variable DFIG Rotor Speed, (b) Controlled q-axis Rotor Current, (d) Stator Reactive Power, and (d) Controlled d-axis Rotor Current

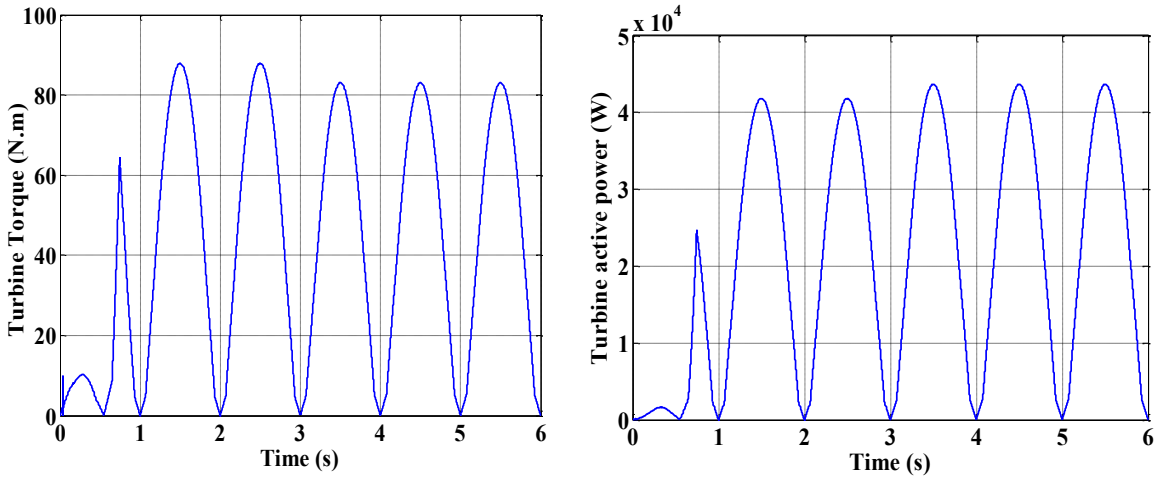

(a) (b)

Figure 3.21 Turbine Performance during Case II: (a) Turbine Torque, and (b) Turbine Active Power

The turbine torque and active power represented in Figure 3.21 change according to the variation in the rotational speed values, while the average stator active power varies with DFIG rotor speed. As illustrated in Figure 3.22, the DFIG stator average active power changes from -15 kW to -12 kW as the speed changes from 380 rad/s to 420 rad/s, respectively. The negative sign indicates power injection into the grid.

There was a sudden change in the average active stator power at t=3.2 s, which was due to the transient in the *q*-axis rotor reference current as a reflection to the step change in the DFIG rotor speed command.

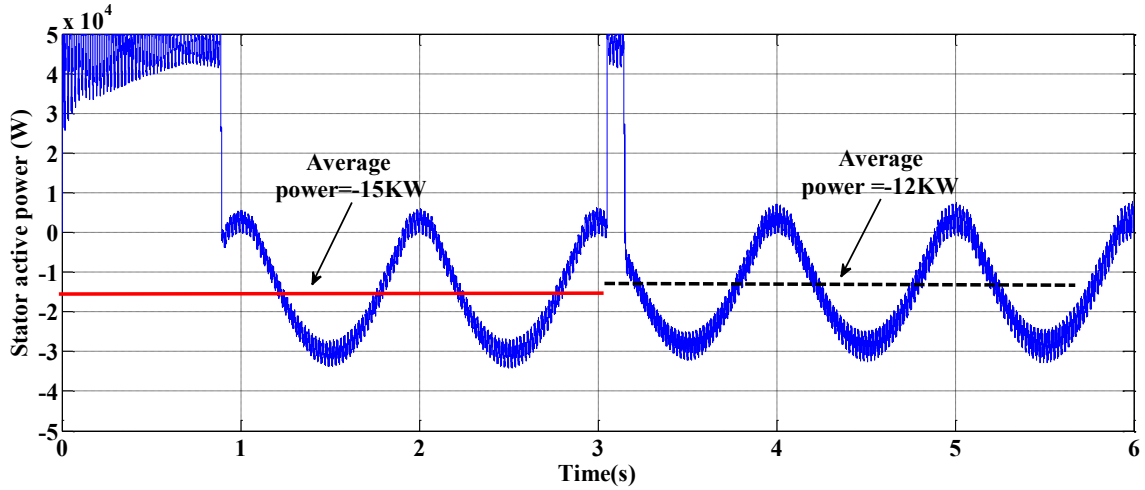

Figure 3.22 Case II DFIG Stator Active Power Performance

3.12 Conclusion

The investigated decoupled control illustrated in this chapter reveals the applicability of achieving enhanced performance over a wide range of operating conditions, by adequately controlling the back-to-back converter associated with the coupled DFIG. The investigated Wells turbine model revealed the occurrence of stalling, which dramatically affects the turbine output torque/power. The following chapter discusses in detail the stalling phenomenon, turbine performance at stall, in addition to stalling phenomenon avoidance techniques presented in the literature. Moreover, an enhanced performance stalling avoidance technique is proposed.

Chapter 4

Wells Turbine Proposed Stalling Avoidance Artificial Neural Network-Based Technique

Firstly, this chapter introduces a common problem in Wells turbine operation, namely the stalling phenomenon. An intensive literature review on the stalling prevention techniques is presented. The core of this chapter is the proposed artificial neural network based stalling avoidance technique. The proposed ANN is presented focusing on its structure and training process. The proposed ANN stalling prevention Technique performance is attested via rigorous simulation under various operating conditions to validate its effectiveness and applicability over wide range of operation.

4.1 Introduction to Stalling Phenomenon

During the last decade, dynamic stall phenomena have been studied on rotating aerofoils, predominantly in helicopter research [110, 111, 112, 113, 114]. Precise prediction of periodic aerodynamic loads on helicopter blades is essential to measuring blade life, and these loads are the main factor in limiting the performance of these structures [115, 116, 117].

Recently, dynamic stall has also been gaining great consideration within the field of wind turbine aerodynamics [118, 119]. Stalling phenomenon is unavoidable, even for pitch regulated turbines. Several factors influence this critical issue, including turbulent inflow, yaw positioning and wind shear [110].

The dynamics of the flow over an aerofoil must be introduced in order to understand stalling phenomena. An aerofoil will stall when the air completely separates from the top side (or suction side) of the blade. The left tip of the blade in Figure 4.1, where the flow impinges, is called the leading edge (LE) and the right tip, where the flow leaves, is called the trailing edge (TE). On the top (or suction side), the air is primarily accelerated from the leading edge (LE), causing a reducing pressure gradient. As the flow reaches the maximum thickness of the aerofoil, it begins to decelerate, causing pressure to increase and facilitating a positive pressure gradient. This pressure gradient causes an unsteady condition, which may cause flow separation. Separation in the figure below is characterized by the reversed flow over the aerofoil surface past the separation point. If the angle of attack of the aerofoil increases, this separation point moves forward towards the

LE, making the flow separation area bigger until it reaches a point where the entire aerofoil separates, starting from the LE. This condition is called stall [120, 121].

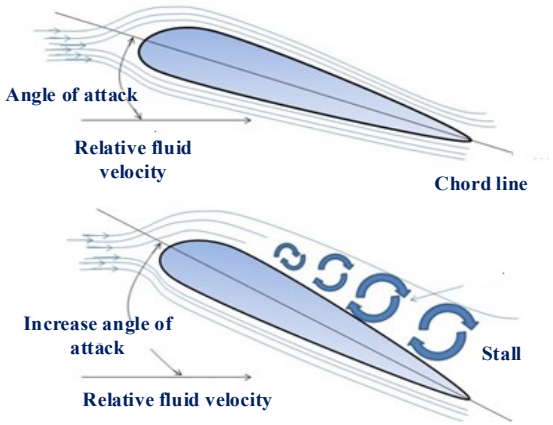

Figure 4.1 Stalling Phenomenon Representation [120]

4.2 Stalling Phenomenon Behaviour in Wells Turbine

The performance of a Wells turbine is limited by the presence of the stalling on the turbine blades. In order to clarify the nature of the stalling behaviour, previous concepts regarding the operation of the system must be introduced. The computation of the torque and power developed by the turbine are based on the behaviour of the power and torque coefficients with respect to the flow coefficient [60, 122]. The characteristic curves of torque and power coefficients (C_t, C_a) of the turbine under investigation have been previously illustrated in Figure 3.6 (a) and (b), respectively.

When the airflow velocity increases as $v_x = f(\emptyset, r, \omega_t)$, the flow coefficient also increases as presented in equation (3.9) provoking stall in the turbine. This behaviour is also observable in Figure 4.2 when the flow coefficient reaches 0.3, which is the stalling critical value. This value may change depending on the characteristic curve of each turbine.

It is necessary to consider the spectrum of the wave climate in the wave modelling, which indicates the amount of wave energy at different wave frequencies. Considering this data for the standard input pressure drop, the system was experimentally modelled as $|7000sin\,(0.1\pi t)|\ Pa$, as shown previously in Figure 3.7 in chapter 3 [61, 123, 124].

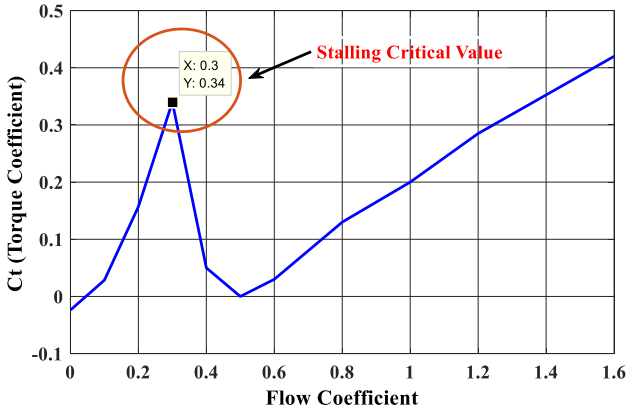

Figure 4.2 Variation of Torque Coefficient with Respect to Flow Coefficient

4.3 MATLAB/ Simulink Model with Initiation of Stall

The primary input for the design of a Wells turbine is the air power, based upon the pressure amplitude and the volume flow rate at the turbine inlet. The performance indicators that determine the onset of stalling behaviour are the pressure drop, power, torque and efficiency, which all vary with the flow rate. The equations used to model the turbine are given above as equations (3.2) to (3.7), while the simulation turbine parameters and simulation model are presented in Table 3.1 and Figure 3.15.

A Wells Turbine simplified MATLAB/Simulink model is presented in Figure 4.3. The experimental differential pressure at the input of the turbine is used to calculate the flow coefficient and detect the presence of the undesired stalling phenomena.

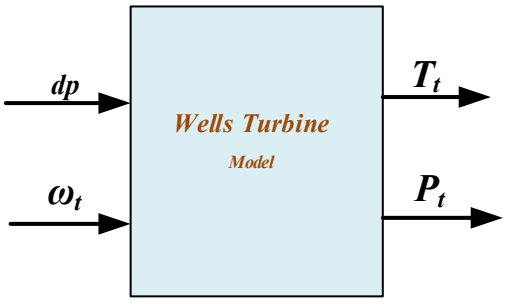

Figure 4.3 Wells Turbine Simplified Simulink Model

At a maximum value of 7000 Pa, the corresponding flow coefficient variation is illustrated in Figure 4.4. The turbine torque can be calculated from the flow, torque and power coefficient. The turbine power can then be evaluated corresponding to the turbine speed.

As presented in Figure 4.4 (b), the flow coefficient exceeds the critical limit of 0.3, leading to stall on the turbine blades, which affects the performance of turbine output torque and power as shown in Figure 4.5.

The impact of stall on the turbine torque and power is highly noticeable as turbine torque/power drops instantly at a turbine speed of $\omega_t = 314$ rad/s.

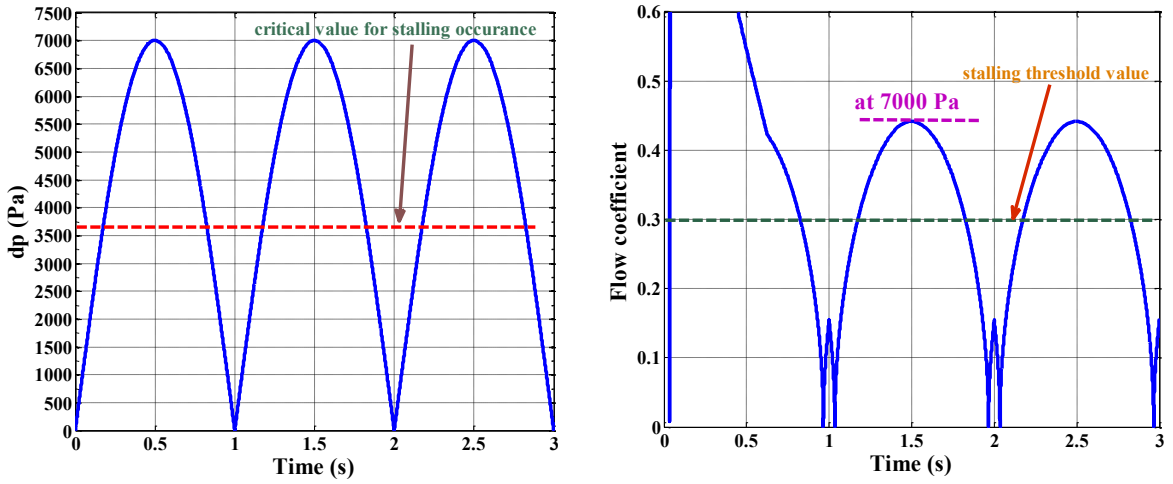

(a) (b)

Figure 4.4 (a) Turbine Differential Pressure and (b) Corresponding Flow Coefficient

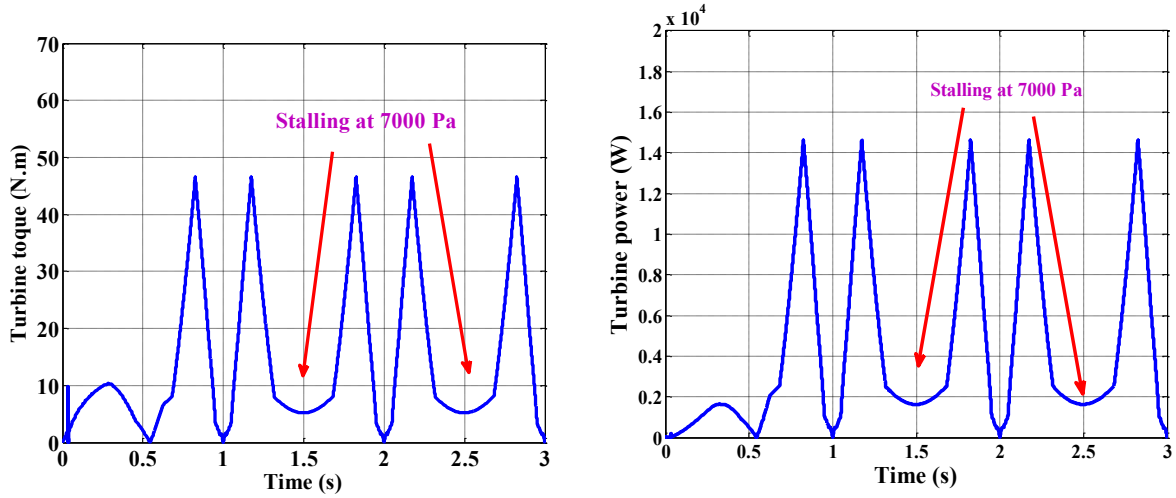

(a) (b)

Figure 4.5 Turbine performance during Stalling: (a) Torque, and (b) Power

The degraded performance of the turbine torque and power affects the stator active power injected to the grid. This is exemplified in Figure 4.6.

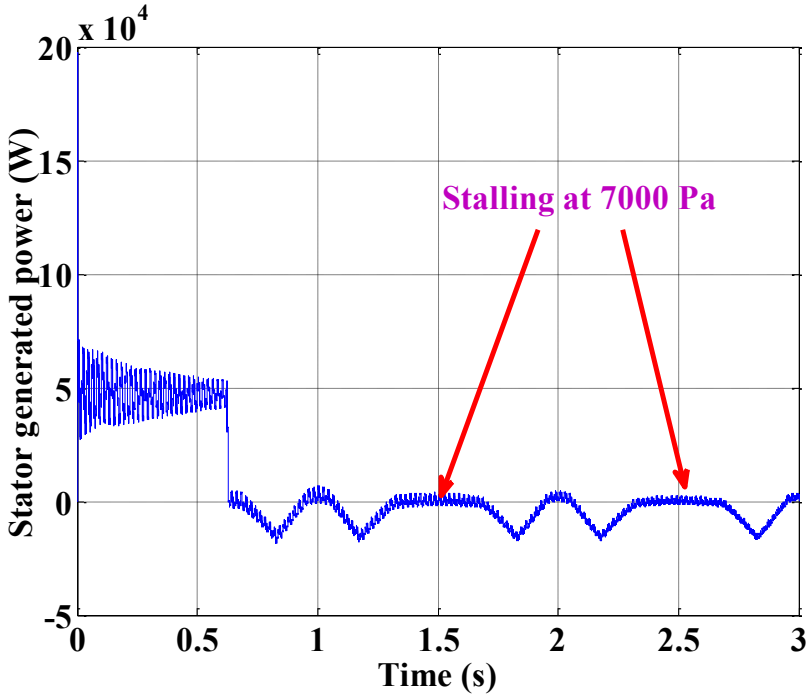

Figure 4.6 Stator Active Power during Stalling

4.4 Survey on Stalling Avoidance Techniques

In order to avoid the stall and optimize the produced power output, two control strategies have been previously presented in the literature: airflow control and rotational speed control algorithms [76, 86, 125].

4.4.1 Rotational Speed Control

Undesired stalling behaviour can be avoided if the turbine accelerates fast enough in response to the incoming airflow. This is achieved by increasing the accepted slip of the generator, allowing the system to reach higher speeds [44, 76, 65, 66].

Rotational speed control offers a method to react to unforeseen changes in the turbine speed, by ensuring that the average power of the generator is adequately adjusted according to the incident wave power level [76].

According to [126] rotational speed control is accomplished by adding external resistances (rx) in series with the DFIG rotor winding, as represented in Figure 4.7. The rx variation is performed with respect to different pressure drops in order to follow the torque/slip characteristics of higher velocities.

In this technique, intensive simulations must be carried out to acquire the optimal rx value that avoids stalling under various input differential pressure levels as presented in Table 4.1

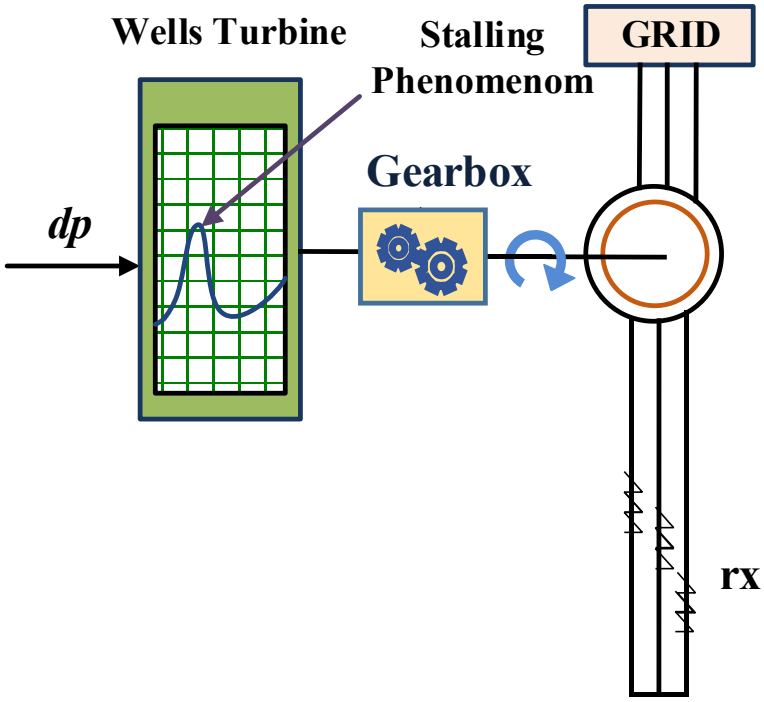

Figure 4.7 Stalling Avoidance Using Rotor Resistance Variation [126]

Although the variation of rx preserves the system, the value of the flow coefficient was not changed in order to not exceed the stall threshold value. These cases are highlighted in Table 4.1.

In Table 4.2, the literature presents only selected dp values with corresponding rx values that ensure the critical value avoidance in order to show that the system is effective. However, it is clear that the system fails in the remainder of the cases despite the increased system loses due to the added rx. The system response tightened due to the step-limited variation in rx.

Table 4.1 Flow coefficient versus pressure drop and rx [126]

dp(Pa)	***ϕ***	***rx(Ω)***
1000 sin(0.5t)	0-0.0541	0
3000 sin(0.5t)	0-0.1612	0
5000 sin(0.5t)	0-0.2708	0
5500 sin(0.5t)	0-0.2985	0
5550 sin(0.5t)	0-0.3080	0.
5800 sin(0.5t)	0-0.2992	0.1
5900 sin(0.5t)	0-0.3090	0.1
6000 sin(0.5t)	0-0.2988	0.2
6100 sin(0.5t)	0-0.3032	0.2
6200 sin(0.5t)	0-0.2975	0.3
6300 sin(0.5t)	0-0.3015	0.3
6500 sin(0.5t)	0-0.2990	0.4
6600 sin(0.5t)	0-0.3024	0.4
6800 sin(0.5t)	0-0.2993	0.5
6900 sin(0.5t)	0-0.3028	0.5
7100 sin(0.5t)	0-0.2981	0.6
7200 sin(0.5t)	0-0.3006	0.6
7500 sin(0.5t)	0-0.2981	0.7
7600 sin(0.5t)	0-0.3007	0.7
8000 sin(0.5t)	0-0.2989	0.8
8100 sin(0.5t)	0-0.3010	0.8
8500 sin(0.5t)	0-0.2981	0.9
8700 sin(0.5t)	0-0.3015	0.9

Table 4.2 Efficiency versus Pressure Drop and rx [126]

dp(Pa)	*Turbine power (Kw)* $Pt_{average}$	$Pin_{average}(Kw)$	*η (%)*	*rx(Ω)*
5500sin(0.5t)	25.053	51.798	48.37	0
6500sin(0.5t)	24.020	72.934	32.93	0
6500sin(0.5t)	32.194	66.626	48.32	0.4
6500sin(0.5t)	31.753	65.500	48.48	0.5
7500sin(0.5t)	17.834	98.006	18.20	0
7500sin(0.5t)	39.670	82.437	48.12	0.7
7500sin(0.5t)	38.609	79.818	48.37	0.9
8500sin(0.5t)	14.198	126.410	11.23	0
8500sin(0.5t)	18.367	121.300	15.14	0.3
8500sin(0.5t)	47.673	99.528	47.90	0.9

A proposed modification is represented in Figure 4.8, where an artificial neural network will adequately select the rx values to ensure stalling avoidance, with respect to the differential pressure drop.

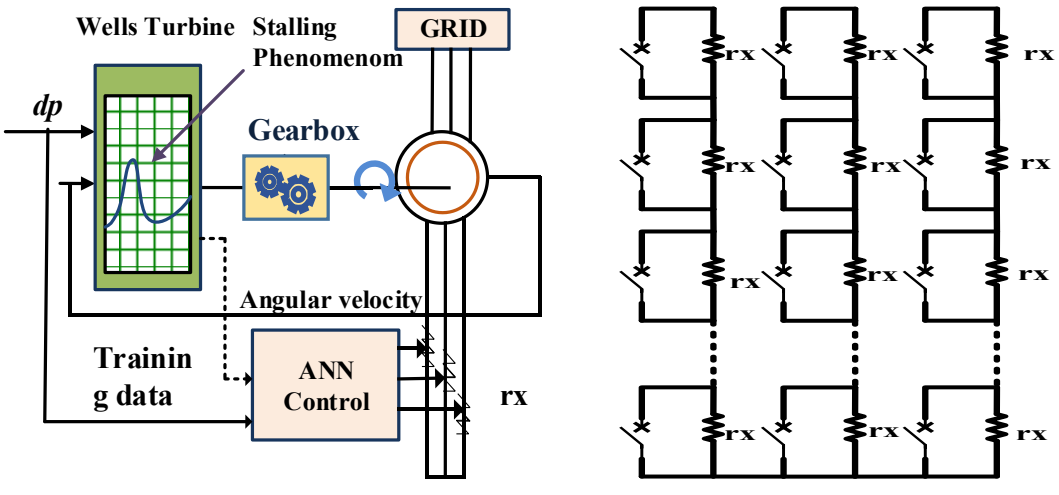

(a) (b)

Figure 4.8 System Model (a) With the Presence of ANN Control [66], and (b) Practical rx Variation using Shunt Bypass Switches

As shown in Figure 4.8 (a), an ANN algorithm with one hidden layer consisting of eight neurons was chosen by trial and error, to present adequate performance in dealing with this controlling problem. The input training data to the ANN algorithm is the differential pressure drop range and the flow coefficient, while the output training data is the estimated rx values corresponding to each pressure drop in order to avoid the stall.

The measure of success for this technique to be implemented was by using different differential pressure drop ranges corresponding with rx values in an uncontrolled (rx=0) and a controlled case (estimated rx by ANN), as presented in Table 4.3. The output generated power is compared with and without the presence of rx.

As shown in Table 4.3, the generated average power was maximized with the presence of rx due to the prevention of the stalling behaviour.

Although Table 4.3 [66] illustrates an enhanced system performance that appears as maximized grid power and stalling avoidance, the practical system response will be dramatically degraded from the simulation results. Whether being determined manually [126] or using an ANN in [66], the rx variation must be performed automatically, in discrete fixed-step changes as shown in Figure 4.8 (b). Hence, the claimed enhanced performance cannot exist.

Table 4.3 Generator power versus pressure drop and rx resistance [66]

dp_{max}	*Uncontrolled case (rx=0)* $Pg_{average}$	*Controlled case*		*% Retrieved output power*
		$Pg_{average}$	*rx(Ω) selected by ANN*	
4000	6.255	6.255	0.000012	0
6000	17.646	17.645	0.000066	0
8000	24.353	26.337	0.3547	8.15
8300	23.735	26.733	0.4575	12.63
9000	19.553	27.902	0.6853	42.69

Another technique has been presented in [60, 127] where an optimum value for slip is determined, with respect to the pressure drop range in order to prevent stall.

Based on this technique strategy, numerous simulations must be performed to carry out the flow coefficient variation in response to the variation of the differential pressure range and the DFIG slip [60, 127]. A summary of these values is presented in Table 4.4.

In essence, it is possible to derive an optimum range for the slip, as a function of the pressure drop to avoid stall in the turbine. The control block in Figure 4.9 (a) shows that the value of the DFIG slip is varied optimally based on Table 4.4 for each specific range of the input applied pressure drop.

In this study, the optimum slip selection criteria and the implementation were not verified. This may consist of a look-up table or a manual change in speed until the system shows stalling avoidance correspondent to each dp range. In addition, the range limits are mathematically driven which may mislead the user when operating beyond the specified ranges.

A modification was presented [127] as shown in Figure 4.9 (b), where an ANN was proposed to replace the vague optimum slip selection block. An ANN with one hidden layer consisting of eight neurons was chosen for this technique. ANN effectively matches the desired relationship between slip and the differential pressure. The accuracy of the network highly depends on the complexity of the chosen design and the quality of the information used to train the network.

Table 4.4 DFIG slip values with respect to differential pressure range [60, 127]

$dp = \lvert P_0 \sin(0.1\pi t)\rvert$ Pa / P_0	*Flow coefficient (∅)*	$Slip_{average}$
0-5500	0-0.2987	-0.0056
5500-5790	0-0.2999	-0.0234
5790-5975	0-0.2995	-0.0413
5975-6175	0-0.2999	-0-0600
6175-6375	0-0.2995	-0.0790
6375-6600	0-0.2995	-0.0986
6600-6850	0-0.2999	-0.1194
6850-7100	0-0.2998	-0.1406
7100-7375	0-0.2998	-0.1628
7375-7670	0-0.2999	-0.1860

Table 4.5 presents the DFIG average power in response to the differential pressure and controlled slip, in order to validate the control technique for both the controlled and uncontrolled cases [127].

The control system was found to suitably adjust the slip of the induction generator according to the pressure drop, in order to prevent stall and maximize the average generated output power.

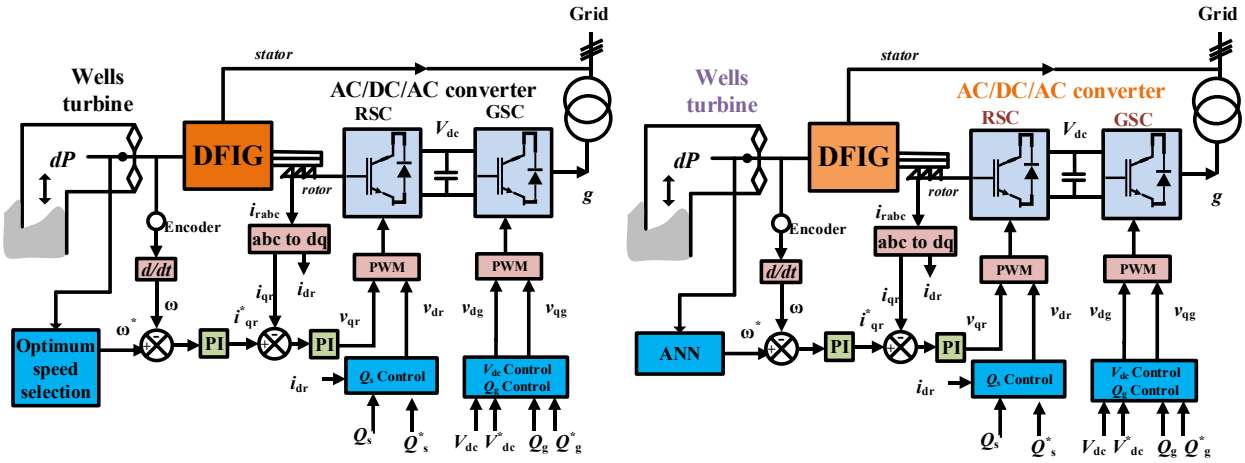

Figure 4.9 Stalling Phenomenon avoidance using Rotational Speed Control (a) Classical control [60], (b) Modified ANN Control [127]

Table 4.5 Controlled and uncontrolled cases of generated power [127]

$dp = \lvert P_0 \sin(0.1\pi t)\rvert$ Pa P_0	*Uncontrolled Case* $P_g(Kw)$	*Controlled Case* $P_g(Kw)$	*% Retrieved output power*
4000	11.920	11.920	0
5000	20.060	20.060	0
6000	25.202	25.570	1.4
7000	20.053	27.569	37.4
8000	15.012	29.480	96.3

.

The first instance of evolving the utilization of ANN in stalling phenomenon avoidance was described in [127]. However, the ANN training process showed no evidence of the training technique. In addition, the regression representations were not clarified, hence the input-to-output matching cannot be guaranteed. The utilization of optimal slip for a definite differential pressure change created limited accuracy, due to the inherit linearization. In addition, the construction of Table 4.4 required extensive recursive system simulations to attain the optimal slip suitable for each definite unsymmetrical pressure levels' variation

4.4.2 Air Flow Control

The purpose of the throttle-valve shown in Figure 4.10 is to regulate the pressure difference across the turbine in order to control the acceleration of the turbo-generator group, by throttling the valve in the duct. The valve is governed by an actuator, which is designed to allow modulation, in order to reduce or increase the flow rate through the turbine according to wave activity variations. The actuator drives the throttle valve into the demanded position against a counterbalance weight. Once in position, it is held steady by an electromagnetic brake. In the event of a control failure or if an emergency closure is required, the brake supply is interrupted and the valve closes under the influence of the weight [128, 129].

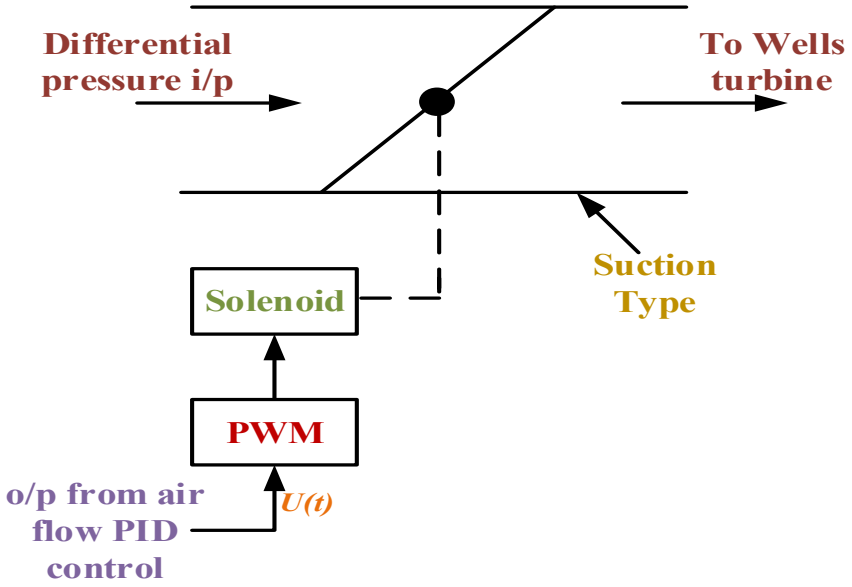

Figure 4.10 Throttle Air Valve Control Operation

In [130] a PID controller was proposed to regulate the DFIG power by modulating the throttle valve in order to avoid stall. The controlled model scheme is presented in Figure 4.11. This scheme was achieved by controlling the differential pressure drop with respect to the generated power required by the grid in order to avoid stall.

A Ziegler-Nichols based procedure was used for tuning the PID controller. The only drawback of the PID controller was its transitory state, because time evolved at longer time scale. The relatively long time for actuation significantly deteriorated the system's transient behaviour.

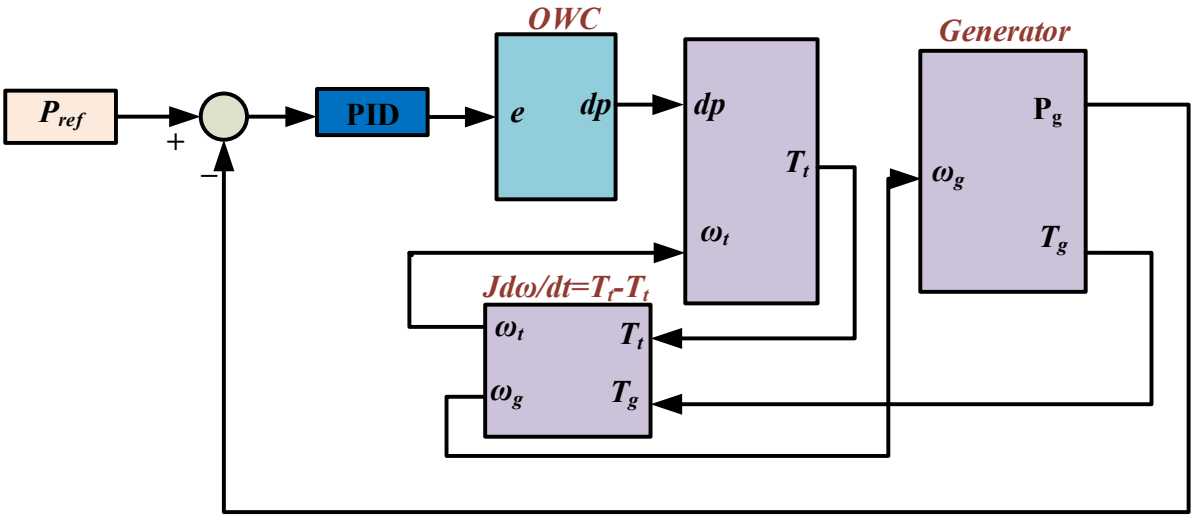

Figure 4.11 PID-based Airflow Control [130]

Finally, Table 4.6 shows the DFIG average power delivered at different pressure drop inputs for two different cases: the uncontrolled case and the air valve control case.

As illustrated, the generated power with the PID controller was maximized due to the prevention of stalling phenomena. Yet the DFIG power gain is limited when compared to the rotational speed variation techniques. Moreover, no results were shown for a wide range of input differential pressure variation.

In [76], a throttle valve control obtained by means of an anti-windup PID-based controller was used to manage the output of the generator. A Ziegler–Nichols-based experimental procedure was used to tune the controller [130].

Table 4.6 Generator average power versus pressure drop of controlled and uncontrolled cases [130]

dp_{max} (Pa)	*Uncontrolled Case Average Grid Power*	*Controlled Case Average Grid Power*	*% Retrieved output power*
4000	6.253	6.253	0
6360	20.060	20.060	0
8000	24.342	24.832	2
9000	20.053	22.562	12.5

Figure 4.12 presents the block diagram of the control scheme in this controller, the reference average grid power, Pg_{ref} and the feedback generating the error signal, $e(t)$,

which serves as input to the controller in order to maximize the power output by avoiding stall. The control signal, $u(t)$, then drives the throttle valve into the necessary position.

However, since the control actuator is a throttle valve subject to saturation, the integral windup effect must be considered, due to the control valve having physical limits. Once saturated, increasing the magnitude of the control signal further has no effect. In this case, there exists a difference between the desired and the measured output power values, and the resulting error will cause a continuous increment in the integral term that can create long time delays and possible instability.

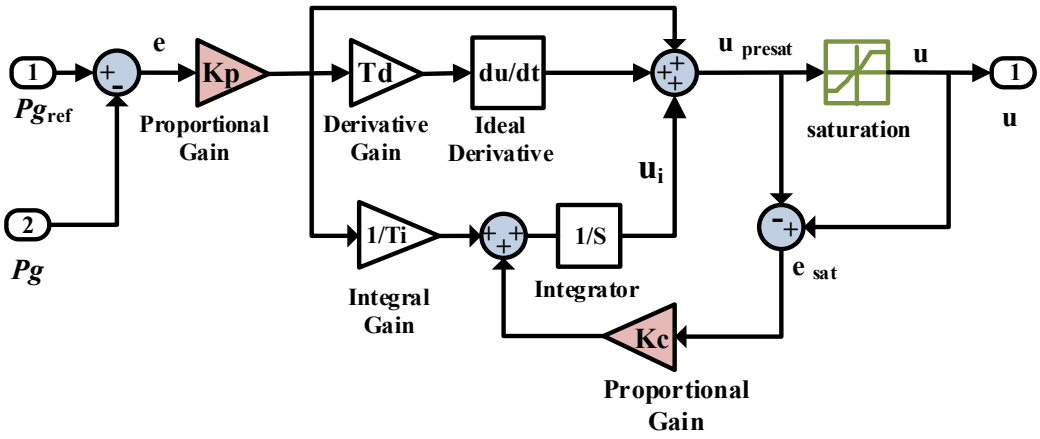

Figure 4.12 Anti-windup PID-based Airflow Control [76]

In [128], fractional order PID FOPID was proposed to control the unnecessary air flow across the turbine duct so that the error between the average output power and reference power would be reduced. Consequently, the stalling behaviour of a Wells turbine is avoided without subjecting the actuator to its physical limits.

Figure 4.13 represents the control scheme for the OWC wave power plant using the throttle valve FOPID controller to prevent the stalling phenomenon, where $\bar{P}_{ref}$ is the desired output average power and $\bar{P}_{gen}$ is the measured generated power.

The output of the FOPID controller represents the effective area of the valve to be conserved, which was further subtracted from the total area of turbine duct. Hence, the effective area of turbine duct varies in line with the changes in valve area. The desired output power is obtained by controlling the air flow rate. The transfer ratio between the valve input (control signal) and valve output has been taken to be unity for simplicity.

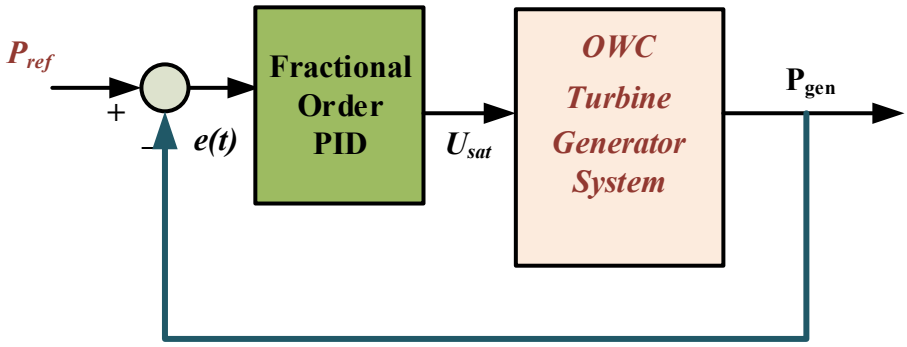

Figure 4.13 FOPID Controller for Air Flow Control [128]

The throttle valve, which works as the final control actuator, has a saturation effect. Thus, the FOPID output must be constrained such that saturation is avoided. When the valve is saturated, the output feedback has no effect on the valve response. The error between the actual and desired values still arises, because the integral values of the FOPID continue to increase. This may cause unnecessary increases in the control effort. When high flow rate passes through the turbine duct, the throttle valve position will not change in order to reduce the effective area of the valve, because of the high integral values within the FOPID controller. Thus, the anti-windup FOPID control was considered as an extension of the anti-windup PID control scheme earlier employed in [76]. The core structure of the anti-windup FOPID controller is presented in Figure 4.14.

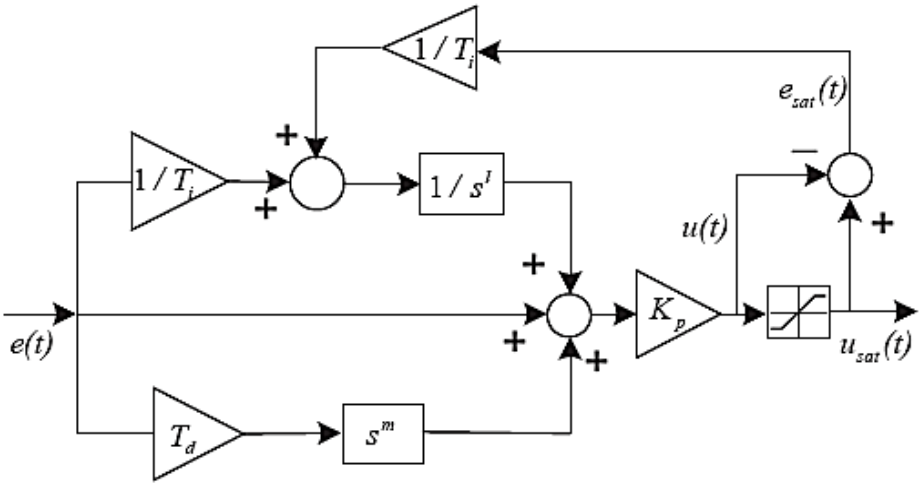

Figure 4.14 Detailed Model for Anti-windup FOPID controller [128]

Air flow control techniques face several problems, including the slow feedback with respect the tuning and the fact that the tuning procedure itself is not accurate enough, which tends to limit the generator power.

In the previously presented work, two control strategies of an OWC-Wells turbine-generator module were obtained in order to prevent stalling. The first strategy relies on the fact that the control system appropriately adapts the speed of the turbine either by controlling the slip of the DFIG or by adding extra resistance in series to the rotor winding to control the speed. The data required for slip and the series resistance are obtained mainly through trial and error. For the second strategy, a PID-type controller was implemented in order to address the desired power reference tracking problem. It was shown that the controllers avoid stalling behaviour and that the average power of the generator fed into the grid was improved in the controlled cases.

The obtained results reveal that the rotational speed control behaves better than the air flow control with respect to the maximum power extraction for stalling phenomenon prevention.

4.5 Proposed Artificial Neural Network-based Technique for Stalling Phenomenon Avoidance

A proposed ANN-based algorithm is presented to directly control the speed of the DFIG in order to accelerate the turbine to the maximum limits that guarantee stalling phenomenon avoidance and maximum power. This is achieved by using the flow coefficient equation (3.9), for the Wells turbine, which depends on the turbine speed and air flow speed, $\emptyset = f(v_x, \omega_t, r)$.

4.5.1 Introduction to Artificial Neural Networks

Artificial neural networks (ANN) were developed as generalizations of mathematical models of biological nervous systems [131]. A first wave of interest in neural networks (also known as *connectionist models* or *parallel distributed processing*) emerged after the introduction of simplified neurons by McCulloch and Pitts (1943) [131].

The basic structural design consists of three types of neuron layers: input, hidden, and output layers. In feed-forward networks, the signal flow is from input to output units. Data processing can extend over multiple units, but no feedback connections are present [132].

The number of hidden neurons affects how the network is able to separate data. A large number of hidden neurons ensure correct learning, and the network is able to correctly predict the data it has been trained on. However, its performance on new data,

mainly its ability to generalize, is compromised. Less hidden neurons lead to a network that is unable to learn the relationships amongst the data and the error will not fall below an acceptable level. Thus, selection of the number of hidden neurons is a vital decision [132, 133].

One of the advantages of neural networks is the ability to generalise; especially the ability to effectively interpret data which was not previously encountered, and still providing a sensible result. This property sets the neural network apart from those which use a look-up table, where it is necessary to store all of the information likely to be required [133, 134]. In addition, neural networks fast at computing, easy to implement and create independence from physical models [66].

4.5.2 Artificial Neural Network Structure and Training Data

The proposed ANN is a basic structure with three interconnected layers. The first layer consists of input neurons (input layer) that send data to the second layer (hidden layer), which in turn triggers the output neurons in the third layer (output layer), as presented in Figure 4.15. The proposed ANN used to vary the reference turbine speed with the differential input pressure to ensure stalling phenomenon avoidance is presented in Figure 4.16.

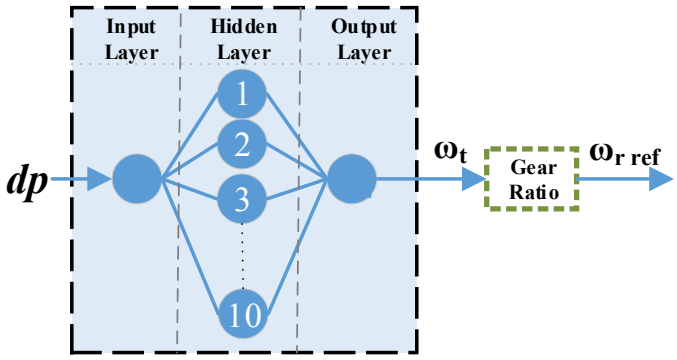

Figure 4.15 Proposed ANN Structure

The proposed ANN was designed to estimate the turbine speeds corresponding to various differential pressure drop values, in order to prevent the stalling behaviour for a wide range of operation. To ensure performance based on the utilized Wells turbine design modelling, the ANN training procedure is clarified in Figure 4.17.

In order to obtain optimum turbine speeds ensuring performance in preventing stall and maximizing the generated output power, the onset of stall was measured. Stalling behaviour occurred between pressure values of 3600 Pa and 7000 Pa, with the flow

coefficient adjusted to 0.2999, which is the critical threshold value for stalling, as presented in Figure 4.16 used by MATLAB/Simulink. The output speed curve of this simulated model is used as the ANN output training data.

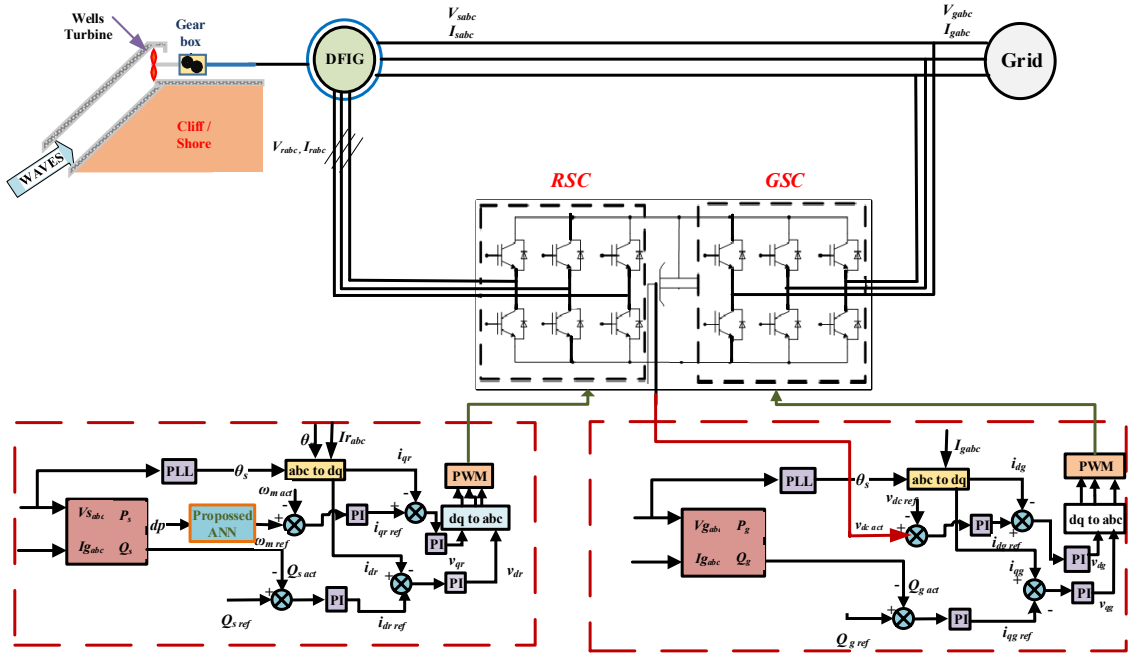

Figure 4.16 Schematic Diagram of the Proposed ANN based OWC WEC System Controller

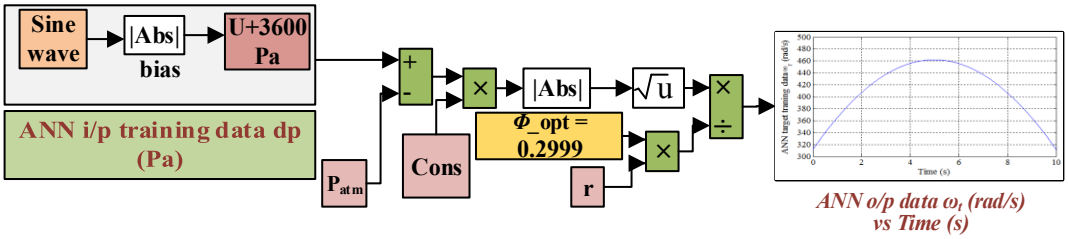

Figure 4.17 Proposed ANN Training Procedure Diagram

Two curves are shown in Figure 4.18. The peak input differential pressure curve is the input of the Simulink model and turbine speed curve ensures stalling avoidance. The output data is stored as a 2D-matrix to feed to the ANN for the training phase (input and output training data). The curves are stored as instantaneous values with a sampling time similar to the one used in SIMULINK model.

The sampling time considered 1µs; therefore, there are $10e^6$ instantaneous points for each curve. This massive data set is not crucial, as it is based on the turbine parameters and not the recursive system simulations as in [127]. This leads to increased accuracy, low time consumption and easy implementation. The differential input pressure curve is fed to the ANN input layer, while the turbine speed reference curve is fed to the ANN output

layer as shown in Figure 4.15. After all the training datasets are loaded to respective layers, 10 hidden neurons are selected.

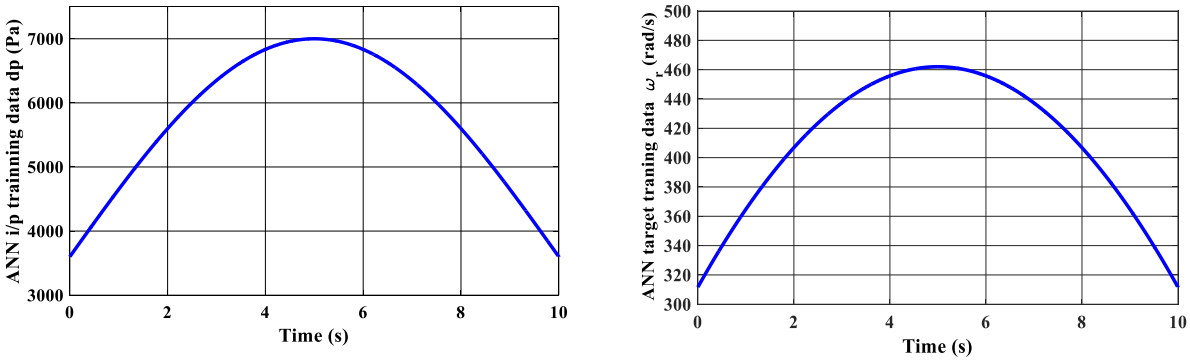

(a) (b)

Figure 4.18 Input-Output Data Representation used for ANN Training (a) Differential Input Pressure Curve (ANN input), and (b) Turbine References Speed Curve (ANN target)

The Neural Fitting Tool (nftool) in MATLAB was utilized. This tool is usually used for estimation and prediction problems in which the neural networks map between a set of numeric inputs and a corresponding set of numeric targets. The algorithm used in this training is Levenberg-Marquardt. Moreover, the selected training algorithm avoids over-fitting issues by stopping the training automatically when the generated results stop improving. During the training, the Regression factor R must be observed, which measures the correlation between the desired outputs and trained targets. The value of 1 signifies a close relationship, while 0 signifies a random relationship. The regression response of the trained ANN is shown in Figure 4.19. Note that all dataset inputs are exactly aligned to the regression line and the value of R is approximately one.

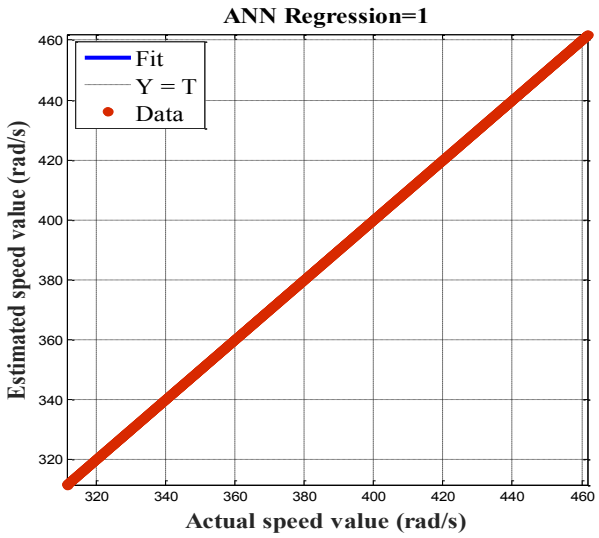

Figure 4.19 Regression Response of the Proposed Trained ANN

4.5.3 Simulation Results

The investigated system parameters were listed previously in Table 3.1. Two simulated operations are presented within: the simulation of the uncontrolled operation with the stalling occurrence under constant turbine speed and the operation under the proposed ANN control technique with the stalling phenomena avoidance and power increment. During each investigated operation, various input differential pressure averages of 7000 Pa, 6000 Pa, and 4000 Pa were implemented to ensure the validity of the proposed control algorithm as shown in Figure 4.20. The investigated differential pressure values were selected carefully to ensure stalling occurrence when no avoidance technique was adapted.

The simulation is illustrated in Figures 4.21 to 4.25. As presented in Figure 4.21, the turbine speed in the uncontrolled case is strictly constant, despite the input differential pressure variation, while under the ANN based proposed algorithm, the controlled turbine speed changed according to the input differential pressure value, in order to avoid the critical threshold limit of 0.3 and facing the stalling behaviour.

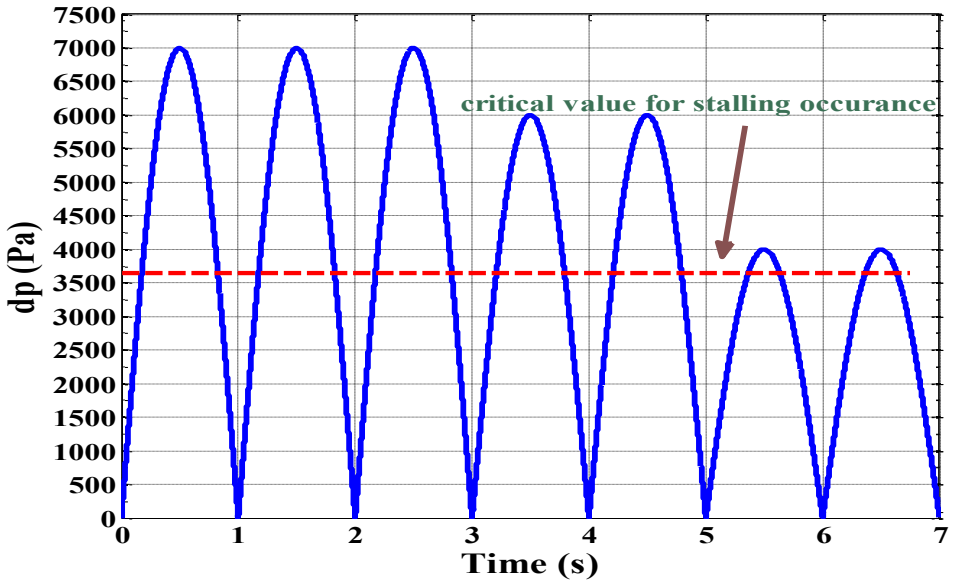

Figure 4.20 Investigated Differential Pressure Variation for the Proposed Stalling Avoidance ANN-based Technique

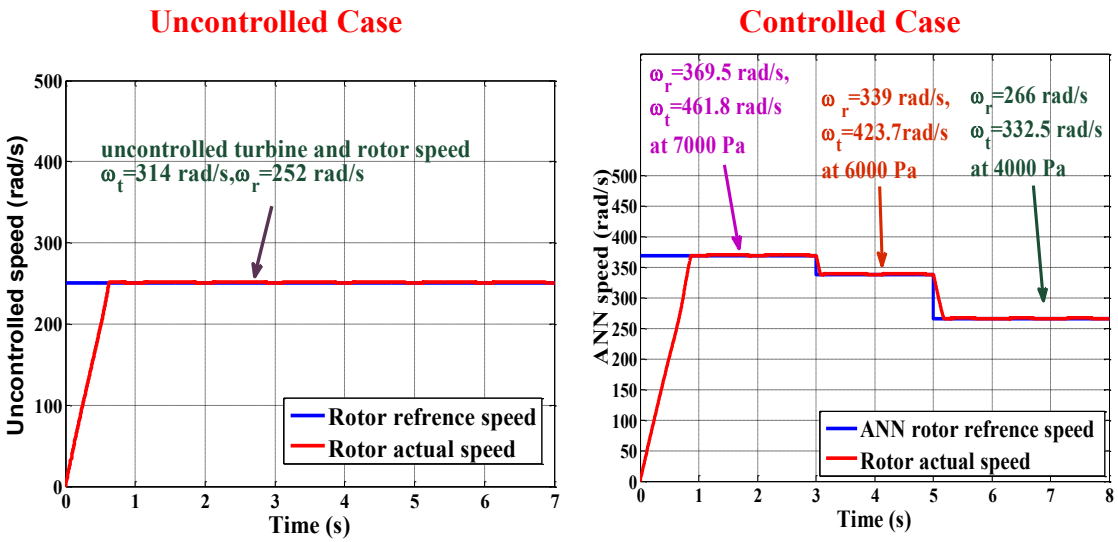

(a) (b)

Figure 4.21 Turbine Speed (a) Uncontrolled Case, and (b) Proposed ANN-based Case

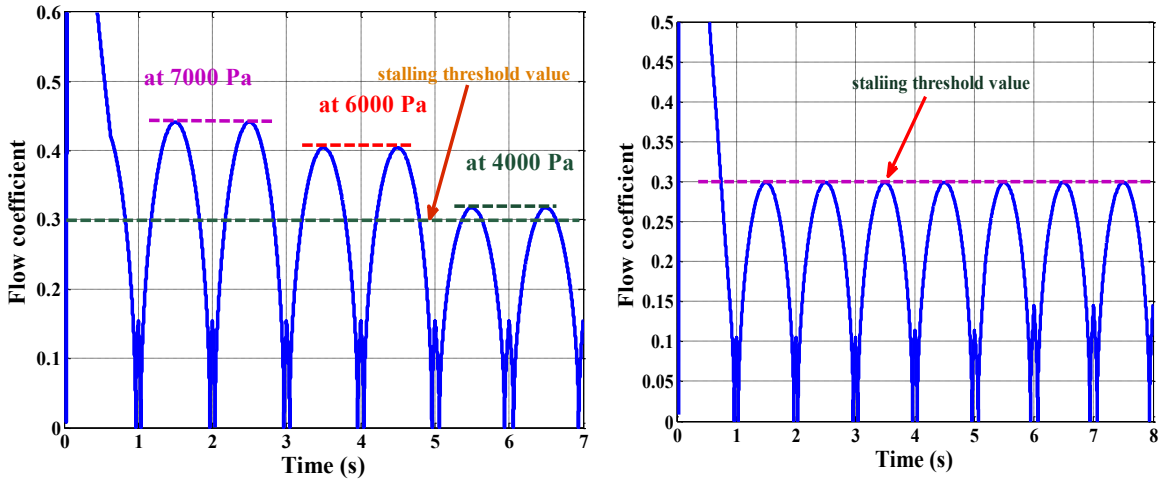

(a) (b)

Figure 4.22 Flow Coefficient Variation (a) Uncontrolled Case, and (b) Proposed ANN-based Controlled Case

The stalling phenomena occurrence under the uncontrolled case is shown in Figure 4.22 (a). As the flow coefficient exceeds the 0.3 critical threshold limit for all the investigated differential pressure levels, while under the proposed ANN control algorithm, stalling phenomenon prevention was achieved. This was accomplished by limiting the flow coefficient value below 0.3, even under varying input differential pressure levels as shown in Figure 4.22 (b).

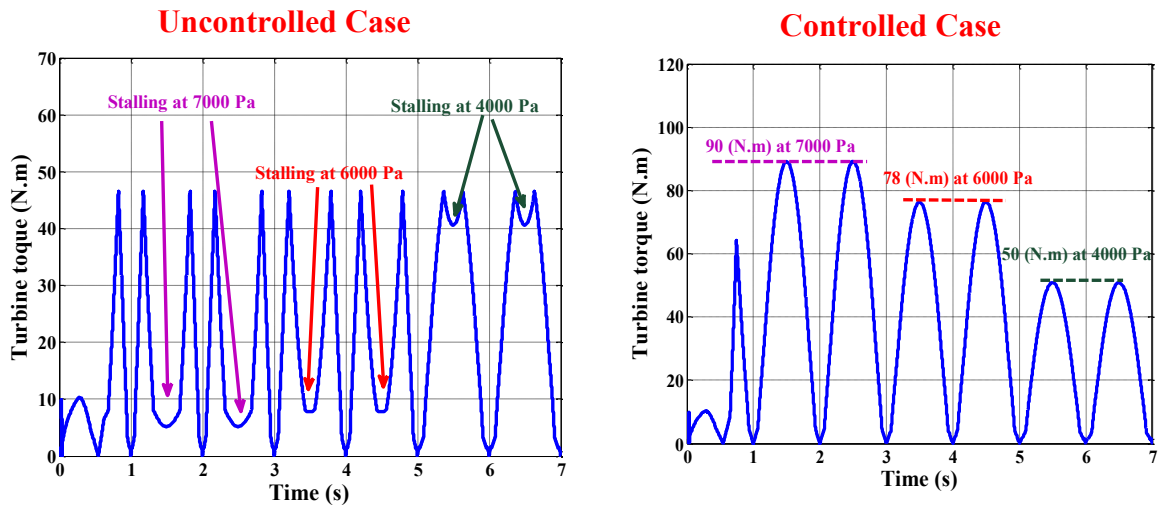

(a) (b)

Figure 4.23 Turbine Torque Performance (a) Uncontrolled Case, and (b) Proposed ANN-based Controlled Case

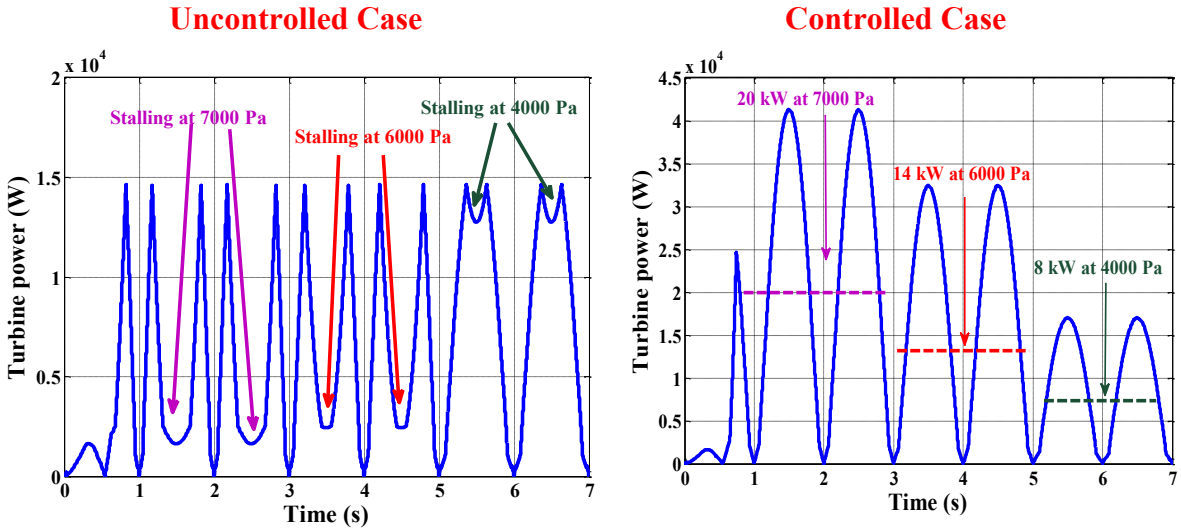

(a) (b)

Figure 4.24 Turbine Power (a) Uncontrolled Case, and (b) Proposed ANN-based Controlled Case

The turbine torque and power for the uncontrolled operation are presented in Figure 4.23 (a) and 4.24 (a) respectively. The turbine torque and power dropped instantly during stalling behaviour leading to a decrease in the average values of the torque and power for the controlled case under the proposed ANN algorithm, as shown in Figure 4.23 (b) and Figure 4.24 (b), respectively. The avoidance of stalling behaviour and maximizing average output turbine power was clarified under the proposed ANN-based technique

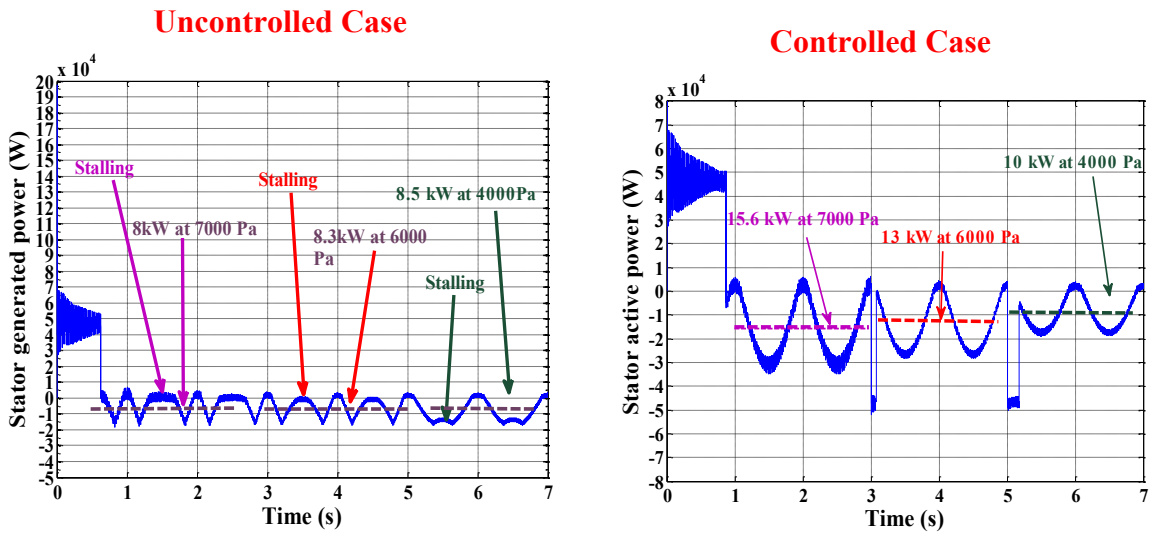

(a) (b)

Figure 4.25 Generated Active Power Performance (a) Uncontrolled Case, and (b) Proposed ANN-based Controlled Case

The proposed technique was effective in stalling prevention, and succeeded in preserving adequate stator active power, as shown in Figure 4.25 (b), compared to the poor performance of the uncontrolled case presented in Figure 4.25 (a).

Table 4.7 Generator average power versus pressure drop variation

dp_{max} (Pa)	*Uncontrolled case* $Pg_{average}$(kW)	*Controlled case* $Pg_{average}$(kW)	*% Retrieved output power*
4000	8.5	10	17.6
6000	8.3	13	56.6
7000	8	15.6	95

As shown in Table 4.7, the generated power under the proposed ANN controller is maximized, due to the prevention of the losses created by stalling phenomena. The generated average power at 7000 Pa is increased by 95%, compared to the ANN technique presented previously in [127] which increased by 37.4%.

It has been demonstrated that the proposed ANN design adequately appropriately adapts the rotor speed according to the pressure drop. Consequently, the rotor side converter is used as a control actuator to regulate the doubly fed induction generator for obtaining the maximum wave power generation without developing stall.

4.6 Conclusion

In this chapter, an enhanced ANN-based stalling prevention technique was developed. The proposed technique shows effective capabilities in stalling avoidance over a wide range of operating conditions. The enhanced performance was verified in the presented simulation results and compared to conventional alternatives. Despite the increased grid power associated with stalling avoidance, the issue of tracking the maximum power was not yet investigated, especially for a wide range of operation, where stalling is highly probable. The following chapter investigates the issue of MPPT techniques for OWC based WECS.

Chapter 5
Wells Turbine OWC WEC Proposed Maximum Power Point Tracking Enhanced Performance Technique

This chapter starts with literature review on common Maximum Power Point Tracking (MPPT) techniques for Wells turbine. Summarizing the pros and cons of the investigated techniques, a proposed ANN MPPT/stalling prevention Technique is presented. The proposed technique achieves dual functions: MPPT and stalling avoidance. In order to illustrate the superiority of the proposed technique, intensive simulations have been carried comparing the proposed technique to classical perturb and observe algorithm. The obtained results clearly verify the claimed dual functionality of the proposed technique under various operating conditions

5.1 Introduction

Maximum power point tracking (MPPT) is a technique commonly used with wind energy conversion systems, photovoltaic (PV) solar systems and recently in wave energy conversion systems to maximize power extraction under a wide range of operating conditions.

The amount of power extracted from a wind energy conversion system is governed by the accuracy with which the peak power points are tracked by the MPPT controller, regardless of the type of generator used [135]

The maximum power extracted from a wind turbine at a specific rotor speed is called the optimum rotor speed, ω_{opt}. This is the speed that corresponds to the optimum tip speed ratio, λ_{opt}. In order to target the maximum power, the turbine should always operate at λ_{opt}. This can be achieved by controlling the turbine rotational speed. The turbine mechanical power as a function of rotor speed at various wind velocities is shown in Figure 5.1 [135, 136].

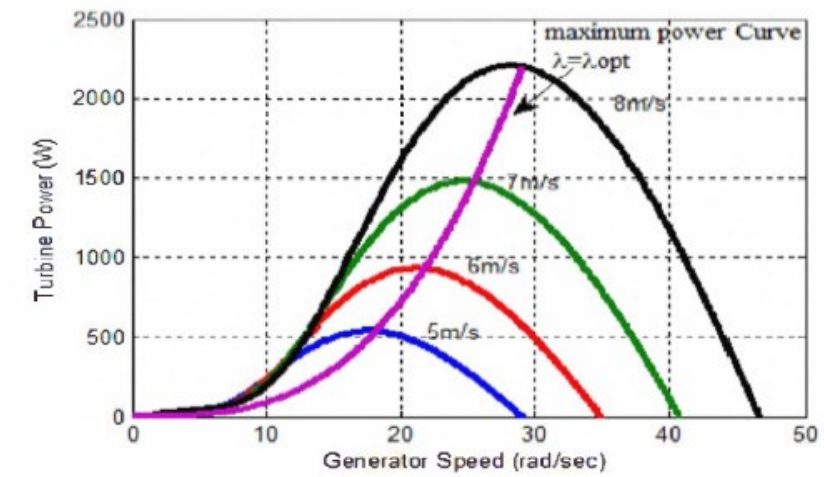

Figure 5.1 Wind Turbine Power vs Speed Characteristic Curve [135].

Similar considerations are inherent for PV systems under varying temperature and irradiance. The panel power versus voltage change is shown in Figure 5.2 for a *Kyocera KC200GT* photovoltaic panel as an example.

The PV panel environmental condition dependency mandates continuous tracking of the optimum panel voltage that must be reached to ensure operation at maximum extracted power. As shown in Figure 5.2, the optimum PV panel voltages need continuous tracking under varying irradiance and temperature levels [137, 138].

Common DC/DC converters can be utilized to vary the PV panel voltage to achieve the optimum operating condition [137].

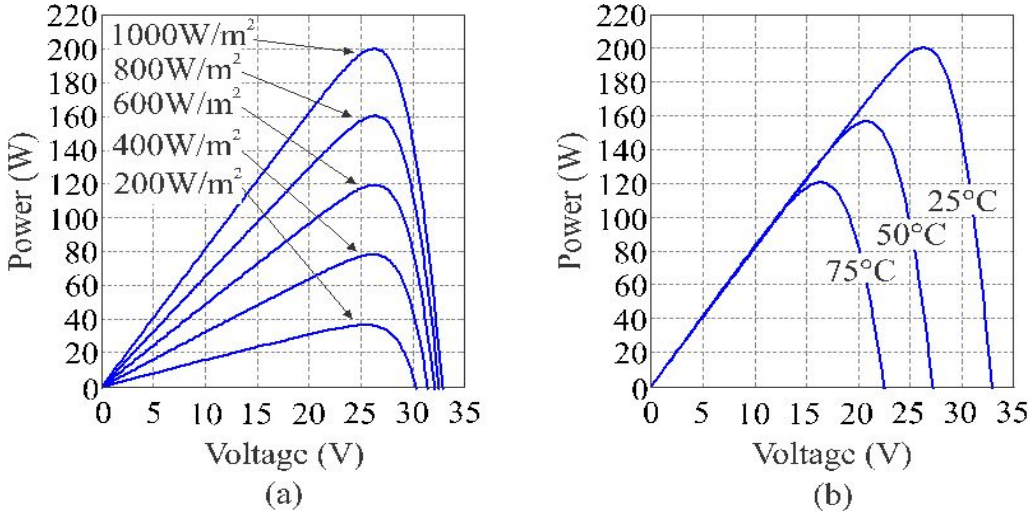

Figure 5.2 Power vs Voltage Variation for Kyocera KC200GT PV Module: (a) Under Constant Temperature and (b) Under Constant Solar Radiation [138]

In wave energy conversion systems, particularly for OWC coupled to Wells turbine systems, the performance was illustrated in chapter 4 and must be influenced by the flow

coefficient which depends on the input differential pressure to the OWC chamber and the turbine speed. Consequently, the flow coefficient must not exceed a critical threshold value to avoid stalling phenomenon, when the turbine torque and mechanical power decreases. Hence adequate control must exist for two main objectives: firstly in avoiding the undesired stalling phenomenon and in selecting the optimal reference turbine speed according to the variation of the input differential pressure.

The average generated power and the rotor speed variation for different input differential pressure conditions is shown in Figure 5.3. The average generated power is maximized at the identified rotor speeds. Consequently, these rotor speed values can be considered to be the reference speed values to run the turbine.

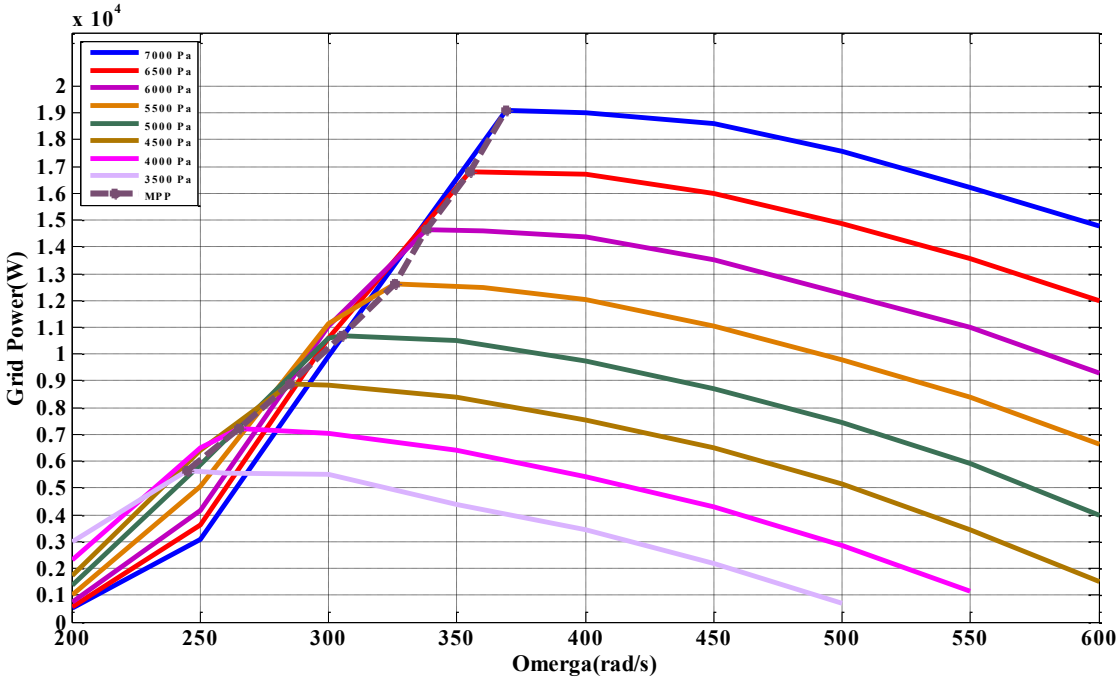

Figure 5.3 Generated Power versus Turbine Speed Characteristic curve for a Wells Turbine Coupled to OWC

5.2 Background

The maximum power point tracking strategy which was used successfully with other renewable energy systems is one of the most useful schemes for feeding the grid with the maximum power needed. This strategy has been applied using different control algorithms.

According to [139], data from Mutriku's power plant based on an OWC coupled to a Wells turbine has been used to drive a control algorithm to improve efficiency. Turbine

rotational speed must be determined based on the non-uniformity of the turbine torque coefficient.

The mechanical power depends on the turbine torque and rotational speed, and is maximized at specified rotational speed values as shown in Figure 5.4 [139].

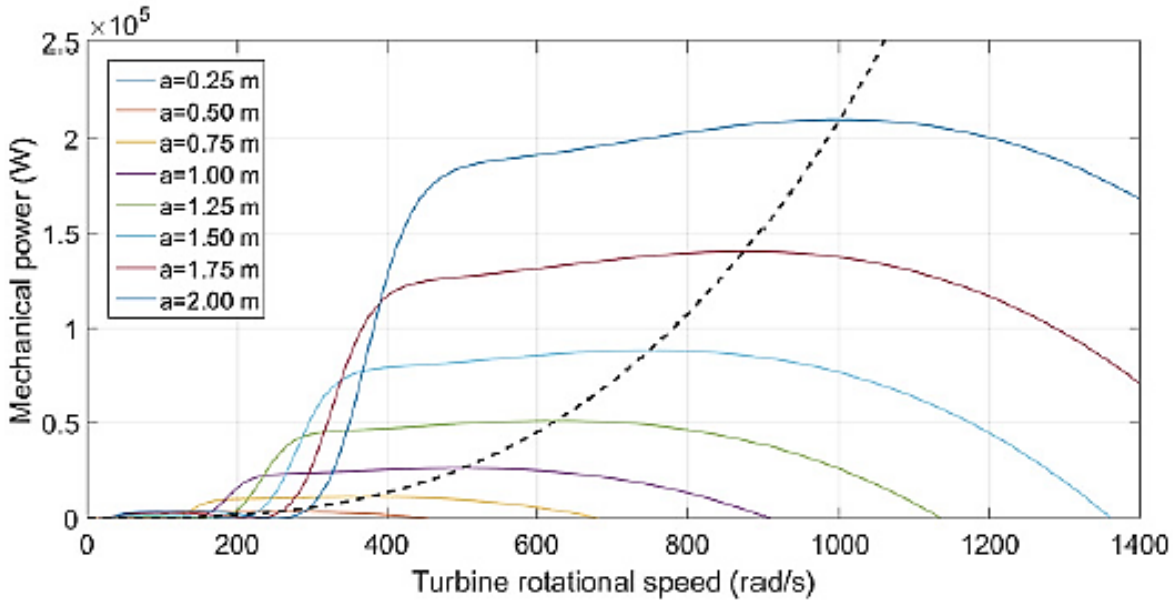

Figure 5.4 Mechanical Power versus Turbine Speed at Different Wave Incident Amplitudes [139]

The dashed line in Figure 5.4 represents the MPPT curve in order to maximize the turbine mechanical power. It can be approximately represented as [139]:

$$P_{max} = K.\omega_t^3 \quad (5.1)$$

where K= 2.098*10^{-4} N.m.s. The value of K has been obtained experimentally from the parameters of the Mutriku wave power plant, but will surely vary in other systems [139].

Figure 5.5 presents the rotational speed control scheme used to maximize the power generated to the grid.

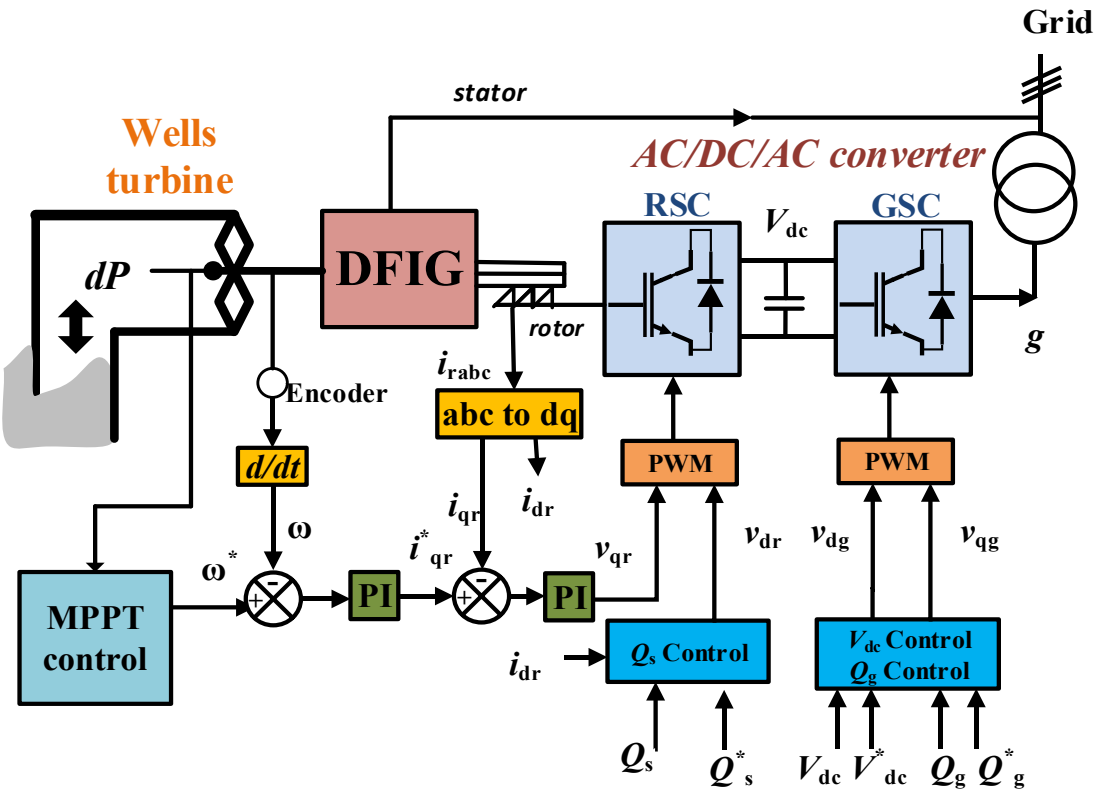

Figure 5.5 Rotational Speed Control Scheme [139]

The published technique utilized a traditional look-up table as a control scheme in order to estimate the optimum speed to produce maximum power injected to the grid by using the formula represented in equation (5.1). Consequently, the difference between the optimum and measured reference speed is applied to a traditional PI controller in order generate a PWM signal applied to the RSC.

The system effectiveness was tested by comparing the generated output power for three different cases: (i) uncontrolled case, (ii) air flow controlled case and (iii) MPPT associated with air flow control. It is important to note that in the MPPT control case, the air flow control is still running in order to ensure avoidance of stalling phenomena.

As presented in Figure 5.6 (a), the generated power, approximately 3.5 kW, is distorted in the uncontrolled case due to the presence of stalling phenomena. Figure 5.6 (b) shows that the presence of the air valve control ensures stalling phenomena avoidance and maximizes the power to be 4.5 kW, while in Figure 5.6 (c) the generated power is optimally maximized to reach a value of 5 kW in addition to stalling avoidance.

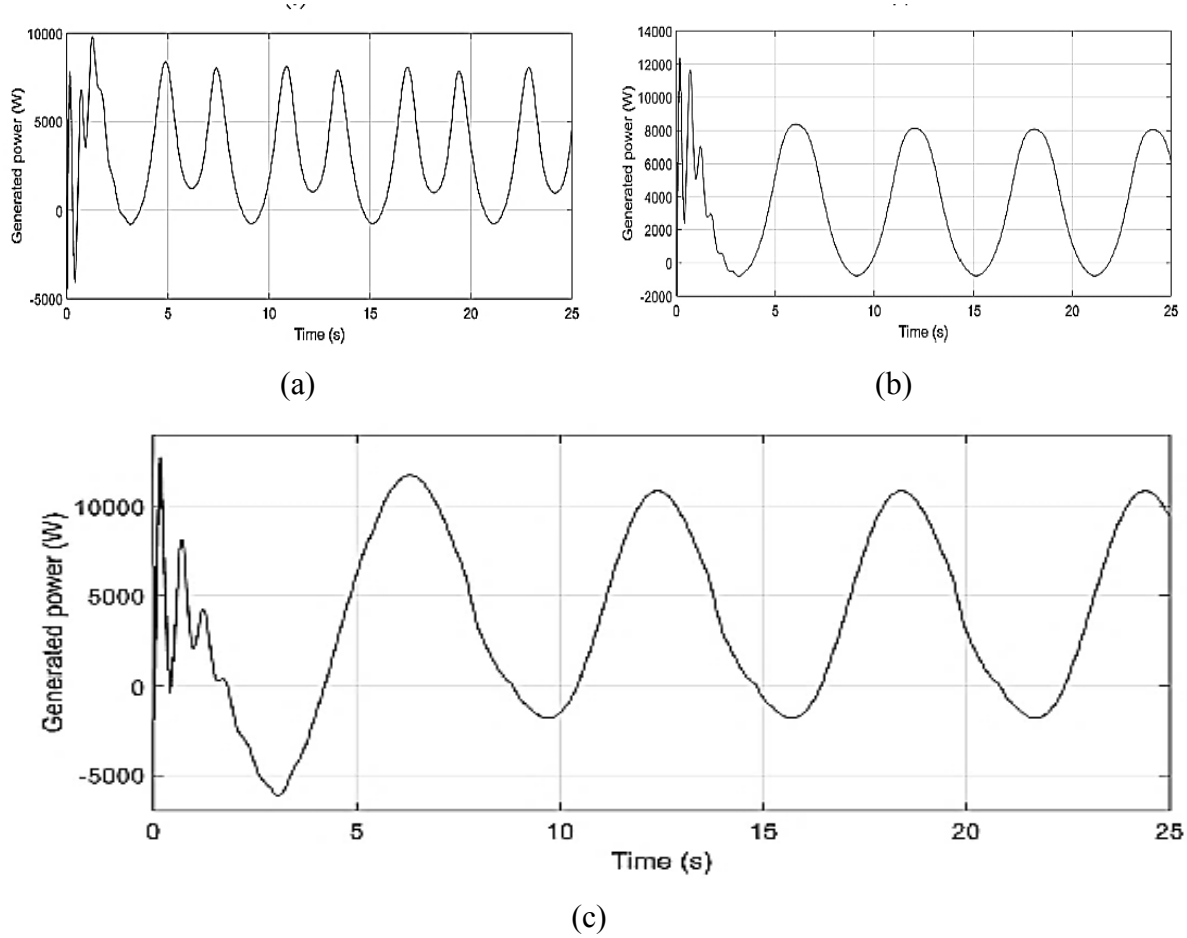

Figure 5.6 System Behaviour of Uncontrolled and Controlled Cases (a) Generated Power without Control Scheme, (b) Generated Power with Air Flow Control (c) Generated Power with MPPT and Airflow Control [139]

The presented technique offers limited improvement due to the dependency on an approximated relation between the maximum generated power and the optimal turbine speed. The look-up table contributes to this drawback due to the discrete implementation and interpolation. Moreover, extensive complexity is observed as the presented technique operates two simultaneous algorithms; one to perform MPPT and the other to ensure stalling avoidance, in addition to the prolonged setting time.

In [140], the MPPT strategy is accomplished by using a fuzzy logic control approach of a back step (BS) controller instead of a traditional PI controller. This is compared to the linear reference tracking (LRT) data in order to regulate the DFIG to operate at the optimum speed and consequently maximizes the power generated to the grid. In addition, the suitability of the technique is validated by comparing fuzzy logic control operation using BS to PI controllers.

Figure 5.7 represents the relation between the average mechanical power and the generator speed, under different differential pressure input values. The dotted line represents the interpolated maximum power curve. The selection of optimal reference turbine speed for a wide range of pressure drops is necessary to avoid the turbine stalling. Thus, an MPPT tracking scheme was developed to obtain the optimal reference speed that guarantees the maximum output power operation.

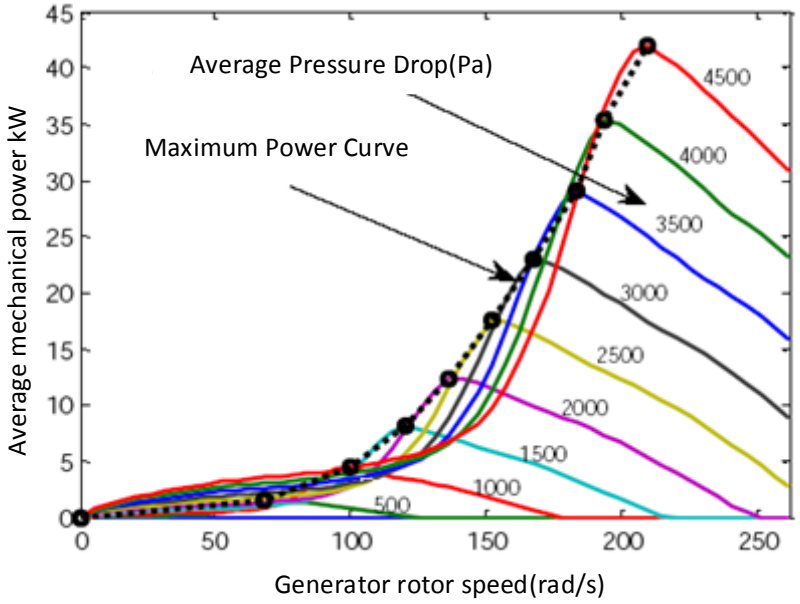

Figure 5.7 Power vs Speed Curve for OWC Wave Power Plant at Different Input Differential Pressures [140]

The presented control structure of a complete OWC wave power plant is represented in Figure 5.8. The fuzzy logic control estimates the generator reference speed and then the output is applied to a BS controller to generate the back-to-back converter PWM that ensures maximum power injected to grid.

A detailed control scheme is presented in Figure 5.9 (a), as the differential pressure drop and rotor speed are used as input variables to the Fuzzy Maximum Power Point Tracking (FMPPT) block, whose output is the optimal reference speed. The rotor speed is compared with the optimal reference speed and the error is used as the input to the BS controller. The essential feature of the BS control is the design of a control law U so that the actual rotor speed precisely tracks the reference speed for various ranges of input pressure drop.

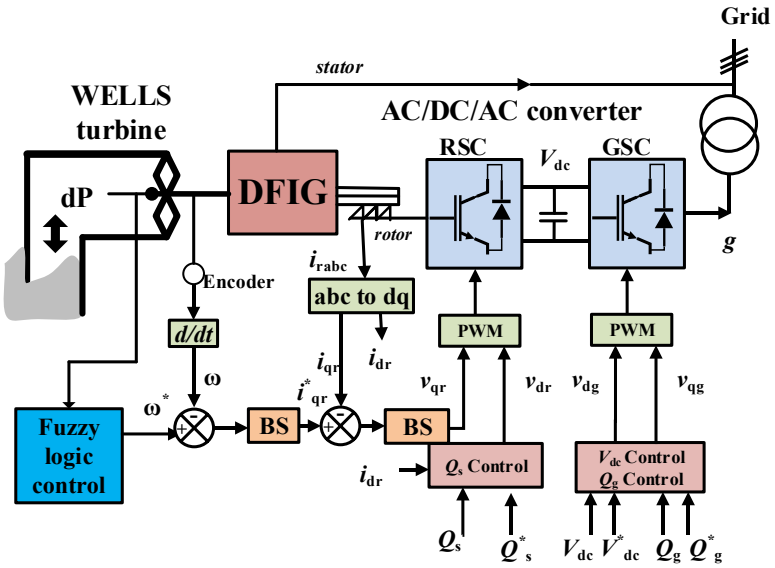

Figure 5.8 OWC System with Fuzzy Logic Control Algorithm [140]

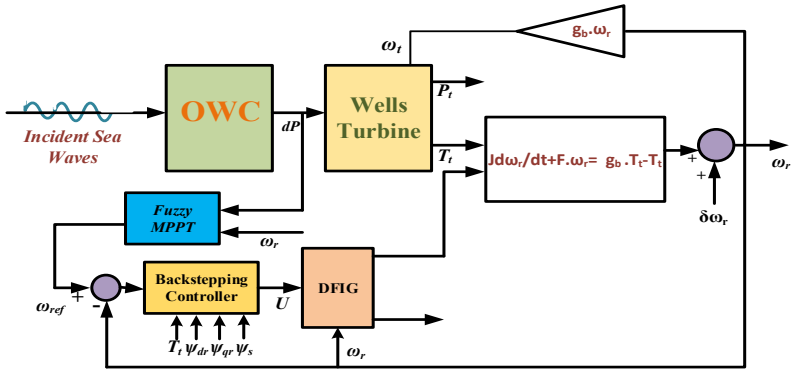

(a)

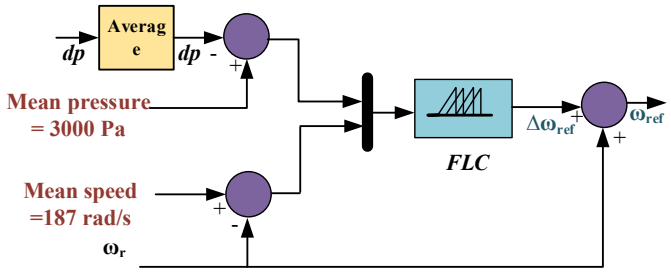

(b)

Figure 5.9 OWC Fuzzy Control used as MPPT (a) Fuzzy MPPT tracking based on back stepping control, (b) FMPPT tracking [140]

The BS controller output is $U = [V_{dr}\ V_{qr}]^T$ *which is converted from dq to abc to generate gate pulses for the rotor side converter (RSC) [140].*

The proposed fuzzy logic control features two input variables: (i) input pressure deviation (ΔdP) and (ii) rotor speed deviation ($\Delta\omega_r$). The output variable is the reference speed deviation ($\Delta\omega_{ref}$) that is added to the actual rotor speed in order to generate the optimal speed reference (ω_{ref}), as shown in Figure 5.9 (b). The mean value for speed and pressure are 187 rad/s and 3000 Pa, respectively [140]. Therefore, the expressions for input pressure deviation (ΔdP) and rotor speed deviation ($\Delta\omega_r$) can be written as:

$$\Delta\overline{dP} = \left(3000 - \overline{dP}\right)Pa \tag{5.2}$$

$$\Delta\omega_r = (187 - \omega_r)\ rad/s \tag{5.3}$$

The final feedback back stepping control law U, ensuring the stability of all the states involved *U,* can be expressed as:

$$U = \begin{bmatrix} K_2 e_2 + \dot{\psi}_{dref} - \frac{R_r L_m}{K}.\psi_s + \frac{R_r L_s}{K}\psi_{dr} + (\omega_r - \omega_e)\psi_{qr} \\ K_3 e_3 + \dot{\psi}_{qref-}(\omega_r - \omega_e)\psi_{dr} + \frac{R_r L_s}{K}\psi_{qr} \end{bmatrix} \tag{5.4}$$

Table 5.1 indicates how the fuzzy logic maximum power point tracking (FMPPT) method outweighs LRT estimation as the turbine efficiency increases, where the flow coefficient is within the permissible limit that prevents stalling occurrence.

Table 5.1 Performance assessment under LRT versus FMPPT control techniques [140]

Average pressure drop (Pa)	***Flow coefficient estimation***		***Average turbine efficiency (%)***		***Average mechanical power (kW)***	
	LRT	**FMPPT**	**LRT**	**FMPPT**	**LRT**	**FMPPT**
1500	0-0.1840	0-0.1840	24.94	24.94	5.56	5.56
2500	0-0.2150	0-0.2400	27.20	28.91	9.88	10.90
2500	0-0.2370	0-0.2923	28.70	31.20	15.10	17.80
3000	0-0.2530	0-0.2781	29.60	30.72	20.86	22.16
3500	0-0.2640	0-0.2890	30.14	31.10	27.07	28.49
4000	0-0.2724	0-0.2960	30.49	31.31	33.71	35.21
4500	0-0.2780	0-0.2999	30.70	31.42	40.71	42.26

In addition, the rotational speed tracking using FMPPT-BS control is superior to both the FMPPT-PI control and without control cases as indicated in Figure 5.10. The difference between the FMPPT-BS and FMPPT-PI controlled and the uncontrolled system can be seen in terms of the generated power, because the electrical output power in the FMPPT-BS control case is higher than both uncontrolled and FMPPT-PI control cases, as indicated in Figure 5.11.

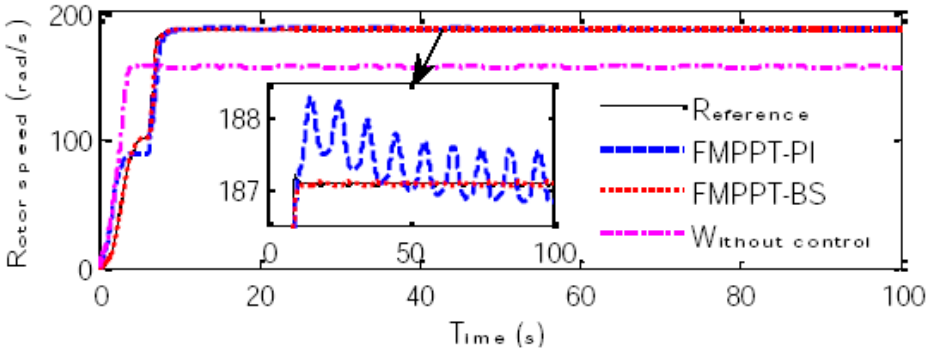

Figure 5.10 Comparison between PI and BS Control Techniques When Applied as FMPPT Controllers: Rotational Speed Tracking [140]

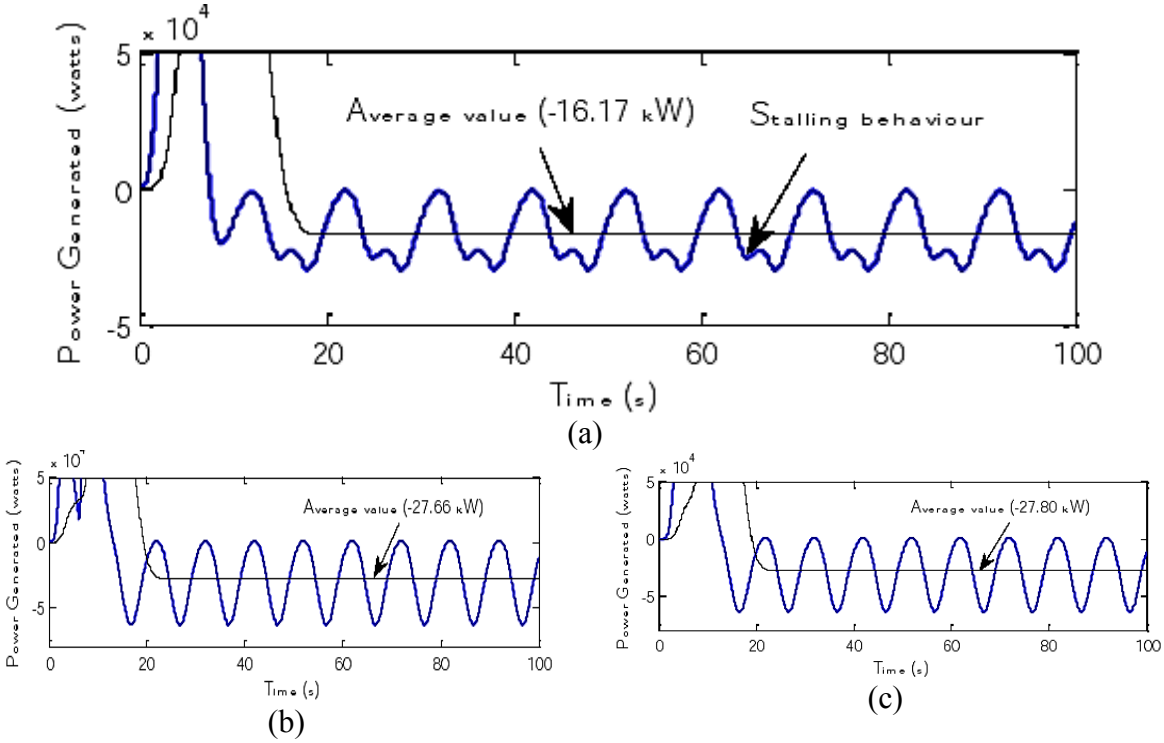

Figure 5.11 Generated Active Power (a) Uncontrolled Case, (b) FMPPT-PI control, (c) FMPPT-BS control [140]

The main weakness of these techniques is that the system is designer-dependent on fuzzification. Defuzzification and the membership formula relies on designer experience in the previous systems.

In [141], the rotational speed control loop was presented in order to optimize the output power of OWC-based Wells turbine power plants (Mutriku power plant). Using outward-looking sensors, a Maximum Power Point Tracking (MPPT) technique was employed to maximize the system efficiency. The control decisions were based on the pressure drop measured by pressure sensors located along the turbine. To validate, the performance of the controller was compared to uncontrolled case.

A similar speed control-based MPPT strategy was presented in [139]. However, in that case, the optimum rotational speed was empirically obtained from simulations and curve-fitting tools. The current research within this paper offers mathematical background to present how optimum rotational speed is obtained.

The mechanical power expression in terms of the rotational speed is

$$P_t = C_t K_a r \omega_t (v_t^2 + (r.\omega_t)^2) \tag{5.5}$$

To get the optimum mechanical speed for maximum mechanical power, equation (5.5) is differentiated with respect to the rotation speed and corresponds to zero as presented:

$$\omega_{opt} = -\frac{(v_t^2 + 3.(r.\omega_t)^2) C_{t_{opt}}}{(v_t^2 + (r.\omega_t)^2) \frac{\partial C_{t_{opt}}}{\partial \omega_t}} \tag{5.6}$$

In order to obtain the expression for ω_{opt}, as a function of the optimum flow coefficient, the following expression was formulated:

$$\omega_{opt} = -\frac{(\emptyset_{opt}^2 + 3) C_{t_{opt}}}{(\emptyset_{opt}^2 + 1) \frac{\partial C_{t_{opt}}}{\partial \omega_t}} \tag{5.7}$$

The flow coefficient should never exceed 0.3 in order to prevent stalling phenomena under normal operating conditions. The torque coefficient can be simplified within the operating range:

$$C_t = -5\emptyset^3 + 6\emptyset^2 - 0.15\emptyset - 0.02 \tag{5.8}$$

However, the value of the optimum flow coefficient can be found which, in this specific case is = 0.1294. It depends on C_t, which represents a design feature of Wells turbines. This value cannot be employed for use with other turbines. Hence, equations of mechanical power equation in (5.5) can be modified to:

$$P_t = C_t K_a r^3 \omega^3 (\emptyset^2 + 1) \tag{5.9}$$

Since the torque coefficient and the flow coefficients can be considered constant variables for extracting maximum power, equation (5.9) can be simplified to:

$$P_t = K_t \omega^3 \tag{5.10}$$

Hence, the goal of the flow controller is to keep the operating point around the optimum flow coefficient. The measurement of the current flow coefficient is also needed as a feedback element. This value is estimated from the measurements taken from the pressure drop sensor.

The modified flow coefficient with respect to the air flow velocity v_t (m/s) is:

$$\emptyset = \left(\frac{\pi.dp}{C_a K_a \omega^2} - 1\right)^{\frac{1}{2}} \tag{5.11}$$

Hence, the optimum value of the flow coefficient is known at the maximum power point. The block diagram of the flow controller is shown in Figure 5.12.

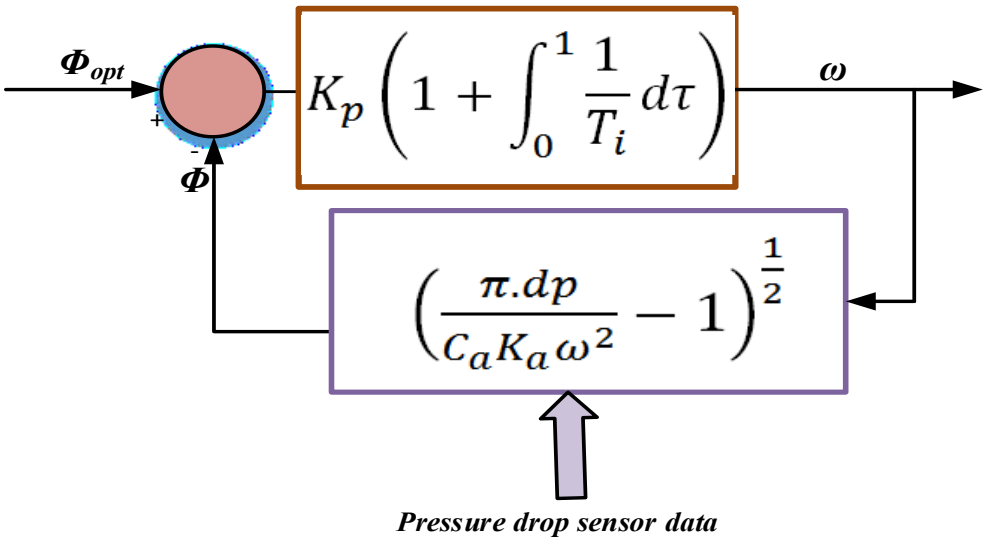

Figure 5.12 Flow Controller Structure [141]

Therefore the closed-loop control system can be represented as:

$$\emptyset_{opt}(s) = \frac{K_p\left(1+\frac{1}{T_i s}\right).\omega(s)}{1+K_p\left(1+\frac{1}{T_i s}\right)\left(\frac{\pi.dp(s)}{C_a.K_a.\omega^2(s)}-1\right)^{\frac{1}{2}}} \tag{5.12}$$

The direct chain flow controller is composed of a proportional-integral control law, which is conventionally used in many applications. In this case, it provides an acceptable performance with minimum tracking error. However, more advanced control systems might replace the above-mentioned controller in the future.

Figure 5.13 shows the block diagram of the plant model, which estimates the air flow through the turbine, taking into account different wave parameters at the surroundings of the breakwater of Mutriku

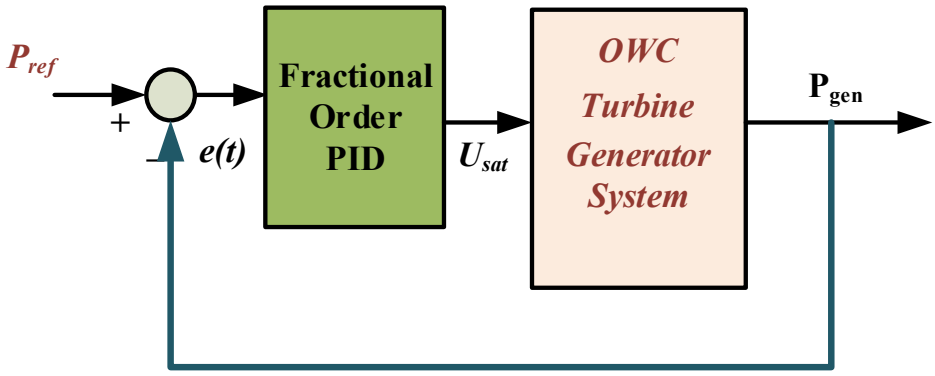

Figure 5.13 Plant Model Block Diagram [141]

The reference speed, ω_{ref}, is established based on the MPPT strategy. In this sense, the relation between ω_{ref} and the pressure drop, *dp*, must be optimized, so as to guarantee a maximum transmission of the mechanical torque to the turbo-generator shaft.

Three case studies were employed in order to compare the performance of this new control strategy. The first case study considers an uncontrolled plant. The second case study uses a traditional PI control scheme to implement the speed control strategy as in [139]. The third case study uses the flow controller and pressure sensors described above to implement an MPPT control by setting an optimum rotational speed, and consequently, maximizing the supplied power. Both controllers showed similar performance. Nevertheless, it can be seen that in case of the flow control, the rotational speed decreases faster when the wave recedes, so that it improves the system efficiency.

Figure 5.14 shows the comparison of the flow coefficient for the uncontrolled plant, the PI-based speed controller and the flow controller. In the case of uncontrolled plant, it can be seen that several wave flow coefficient values occur beyond the stalling threshold. In both controllers, the flow coefficient remains below the threshold value the majority of the time. Therefore, the controller not only guarantees the stalling behaviour avoidance, but also improves the power level supplied to the grid.

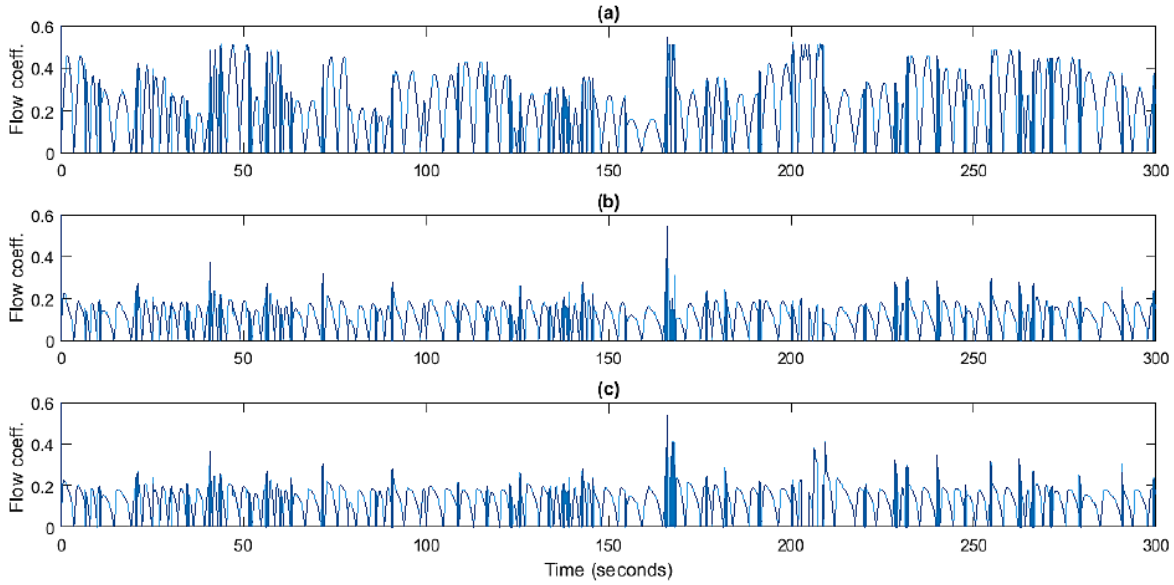

Figure 5.14 Flow Coefficient Variation (a) Uncontrolled Case (b) PI Controlled Case (c) Flow Control Case [141]

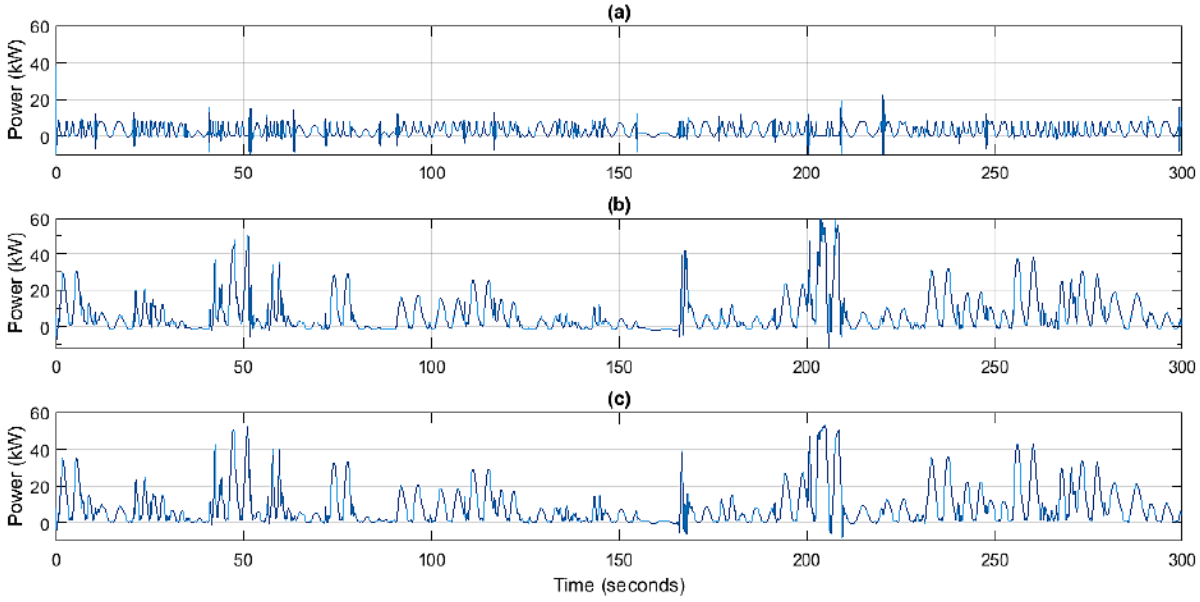

Figure 5.15 Generated Power (a) Uncontrolled case (b) PI controller (c) Flow Control [141]

Concerning the pressure drop in the turbine, the controlled case produces larger pressure drops, since it simply operates at higher rotational speeds.

Figure 5.15 shows the generated power comparison between the two controlled cases and the uncontrolled one. The supplied power increases significantly within the suggested controller, in comparison with the uncontrolled plant. This is particularly evident during high waves, where 50 kW peaks are obtained in the controlled case, while the uncontrolled case is only able to produce 15 kW that corresponds to 30% of available power.

As concluded, the maximum power extracted by both controllers is nearly identical. Dialoguing 5 min of operation, the average power produced by both the PI-based speed controller and the flow controller were compared in order to confirm the improvement of the sensor controlled case. Figure 5.15 (b) and (c) show that the PI controller produces 7.96 kW of average power, while flow control is able to produce 8.82 kW under the same sea conditions. Therefore, by means of the flow control strategy the output power has been increased by 1 kW in a 5 min period. This means that the conversion efficiency has been improved by 9.8%.

The main weakness of this methodology is that only proof the P_t equation for maximum power was achieved by curve fitting which used a previous look-up table technique in [139]. Differentiating the power equation with respect to rotational speed and equating it to zero was attempted. Moreover, the optimum flow equation presented was erroneously in derived.

Another drawback to this technique is that the declared sensors are compared to the PI controller technique during an intentionally selected 5 min period of operation that deceivingly expresses the superiority of the proposed technique. Hence, the wide operation range was neglected, where the PI based technique outweighs the proposed method.

5.3 Proposed ANN Maximum Power Point Tracking Algorithm

In this section, a traditional perturb and observe (P&O) technique was applied to a complete wave-to-wire system in order to verify the effectiveness of the proposed ANN MPPT control algorithm. Firstly, a classical perturb and observe MPPT technique is illustrated followed by the proposed ANN method. Rigorous simulation results are presented within showing the superiority of the proposed technique for various input differential pressure levels.

5.3.1 Perturb and Observe Algorithm and Simulation Results

P&O is a straightforward discrete-time hill climb searching (HCS) control, as it can be employed by perturbing the control variable and observing the resulting increase or decrease in power [135, 142].

This control technique is one of the simplest MPPT techniques that do not require any past knowledge of the system or any additional sensors apart from the measurement of

the power to be maximized. Thus, it is convenient for renewable energy conversion systems that monitor only a power maximum. Nevertheless, it is only applicable in slow-time varying systems. In rapidly changing wave conditions, there is a critical problem with the Hill climb searching (HCS) technique, which considerably weakens the performance the larger the perturbation step size [142, 143].

Choosing an appropriate step size is not straightforward. Though a larger step-size offers faster response, noticeable oscillations form around the peak point. A smaller step-size, however, improves the tracking efficiency but reduces the convergence speed, as shown in Figure 5.16 [135].

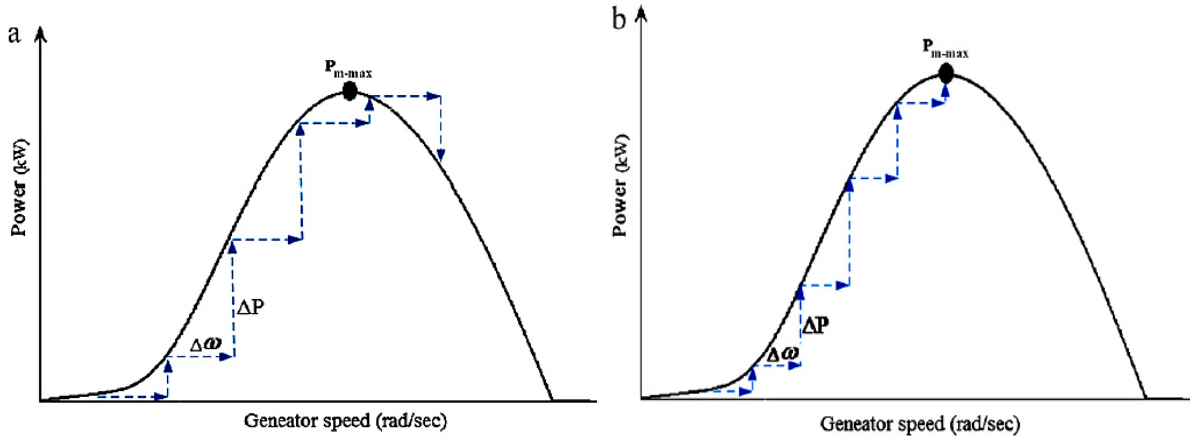

(a) (b)

Figure 5.16 HCS algorithm (a) Large step size Perturbation and (b) Small step size Perturbation [135]

The OWC based energy system using the P&O control algorithm for MPPT is represented in Figure 5.17.

In this algorithm a slight perturbation is introduced to the system, causing grid power altering. If the power increases due to the perturbation, the perturbation is continued in the same direction. Once a stable condition is reached, the OWC power oscillates around the peak power point. In order to maintain a small power variation, the perturbation size remains very small. The technique is advanced such that it sets a reference speed corresponding to the peak grid power; the initial value of the rotor speed was set at 200 rad/s and the step size was set as 20 rad/s, as an example in the simulated system. A PI controller forces the operating point to the reference power level. Remarkable power loss was noticed due to this perturbation in addition to maximum power tracking errors, under fast changing atmospheric conditions

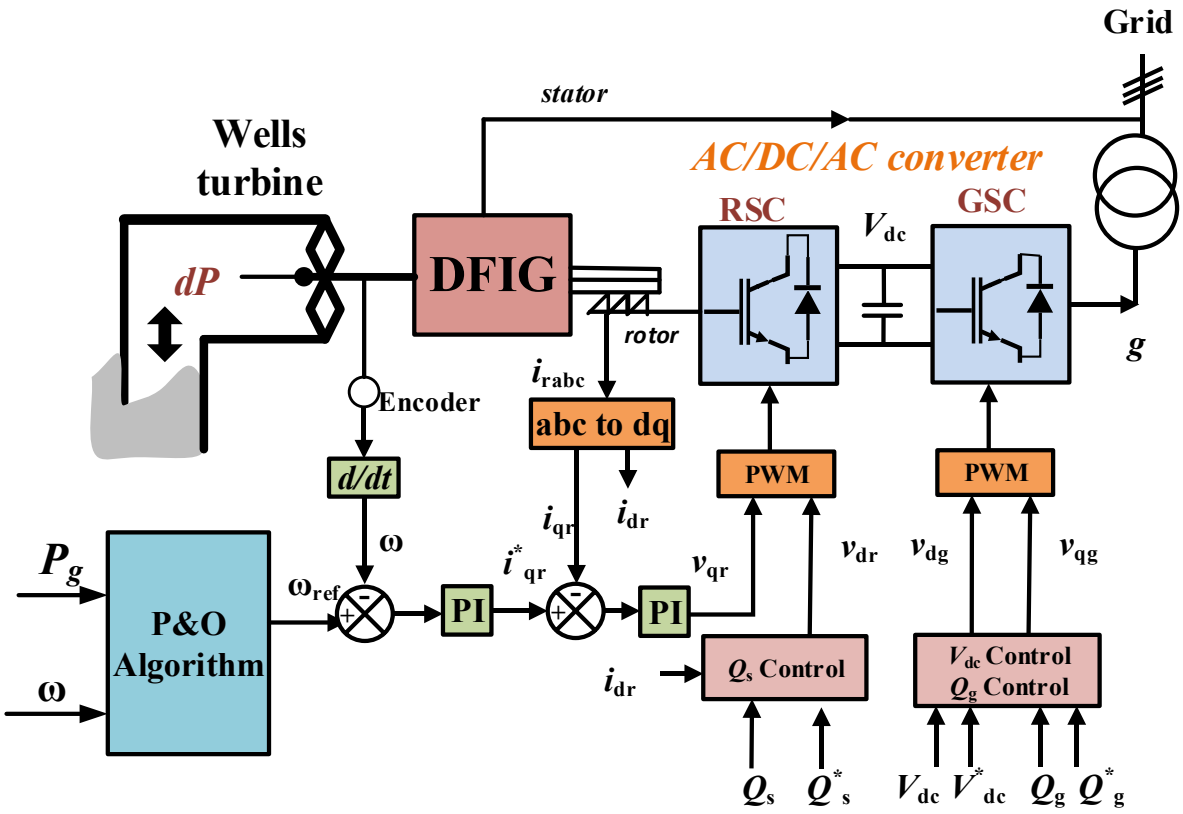

Figure 5.17 OWC System with P&O MPPT Algorithm

The flow chart of the P&O control algorithm achieved using a MATLAB m-file is represented in Figure 5.18.

The simulation results illustrating the system performance under classical P&O MPPT algorithm at maximum differential pressure of 7000 Pa are represented in figures from 5.19 to 5.21

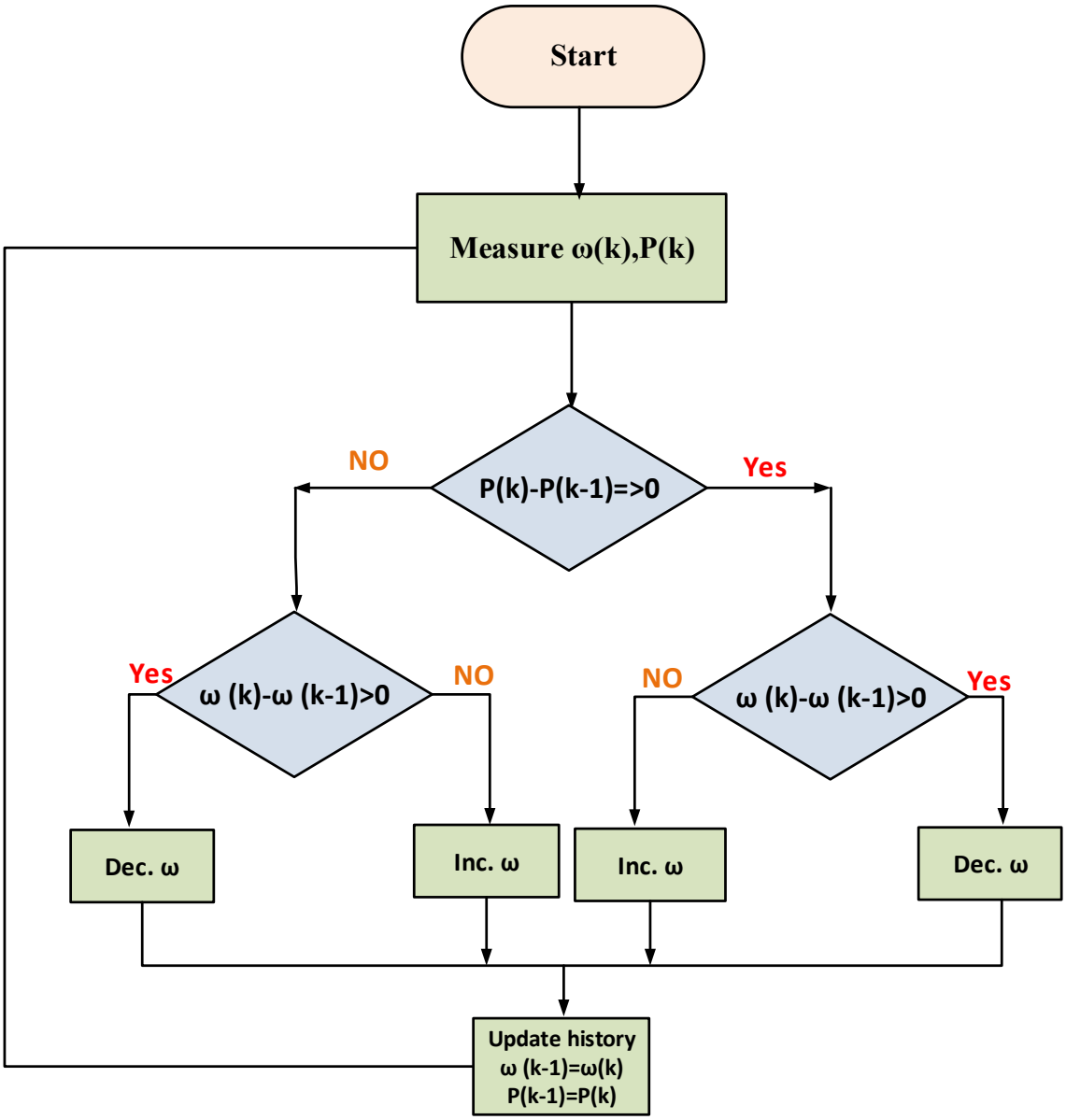

Figure 5.18 Classical P&O MPPT Algorithm Flow Chart

Figure 5.19 presents the flow coefficient of the uncontrolled operation and the operation with the P&O algorithm. As seen in Figure 5.19(a), the flow coefficient in the uncontrolled case exceeds the critical value of the stalling phenomena, while Figure 5.19(b) shows the P&O algorithm preserved the flow coefficient value to 0.3 to prevent stalling.

Figure 5.20 considers the speed in each operation. Figure 5.20 (a) shows that the rotor speed is 300 rad/s for the uncontrolled case while by using the P&O algorithm. The speed alternates around 380 rad/s to avoid the flow coefficient value violation, in addition to seeking the maximum power.

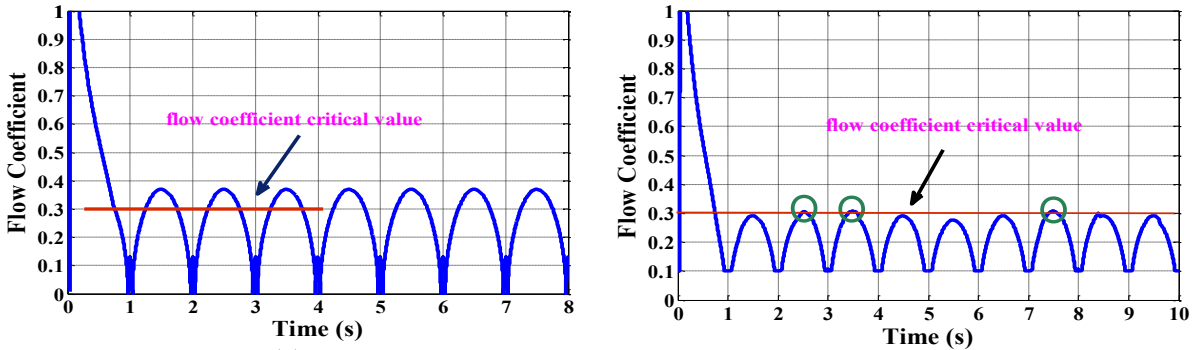

Figure 5.19 Flow Coefficient (a) Uncontrolled Case (b) P&O Algorithm Controlled case

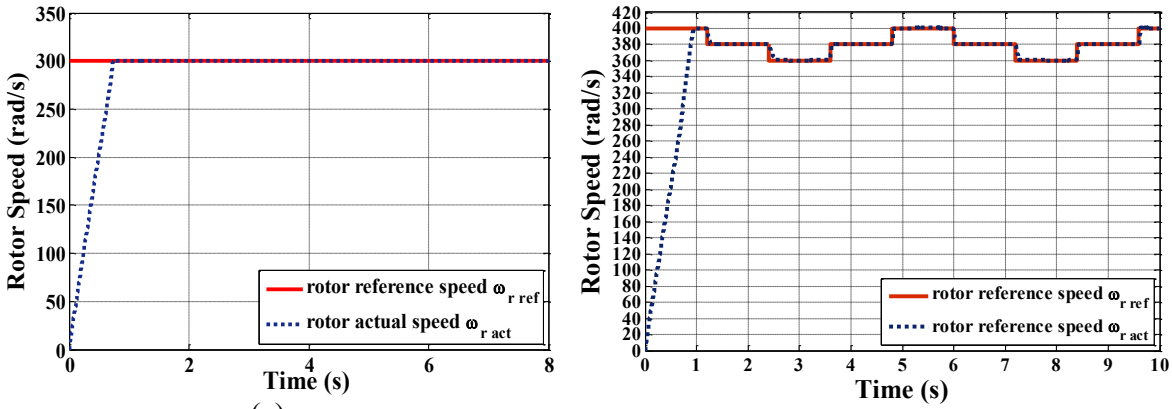

Figure 5.20 Rotor Speed (a) Uncontrolled Case (b) P&O Algorithm Controlled case

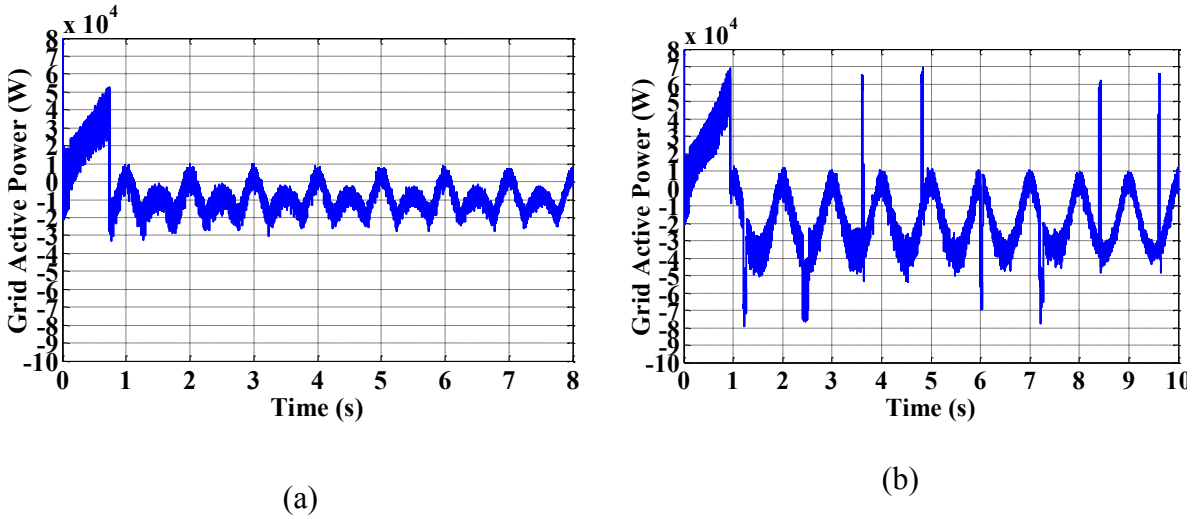

Figure 5.21 Grid Active Power (a) Uncontrolled Case (b) P&O Algorithm Controlled case

Figure 5.21 investigates the performance of the system grid active power. As presented in Figure 5.21 (a), the grid active power is distorted due the presence of stalling and its average grid active power is 9.5 kW, while in case of P&O the average grid active power is increased to 19 kW.

5.3.2 Proposed ANN Algorithm and Simulation Results

A general introduction to Artificial Neural Networks was presented in chapter 4. Hence this section will mainly focus on the ANN algorithm training and simulation results in order to maintain MPPT to the grid. A comparison between the uncontrolled case and the controlled cases using the classical P&O method and the proposed ANN algorithm are presented to ensure the correctness and stiffness of the proposed ANN Algorithm.

The proposed ANN is designed to estimate turbine speeds that correspond to various differential pressure drop values in order generate maximum power, while ensuring stalling prevention for a wide range of operation. The OWC based energy system using the ANN control algorithm for MPPT is represented in Figure 5.22.

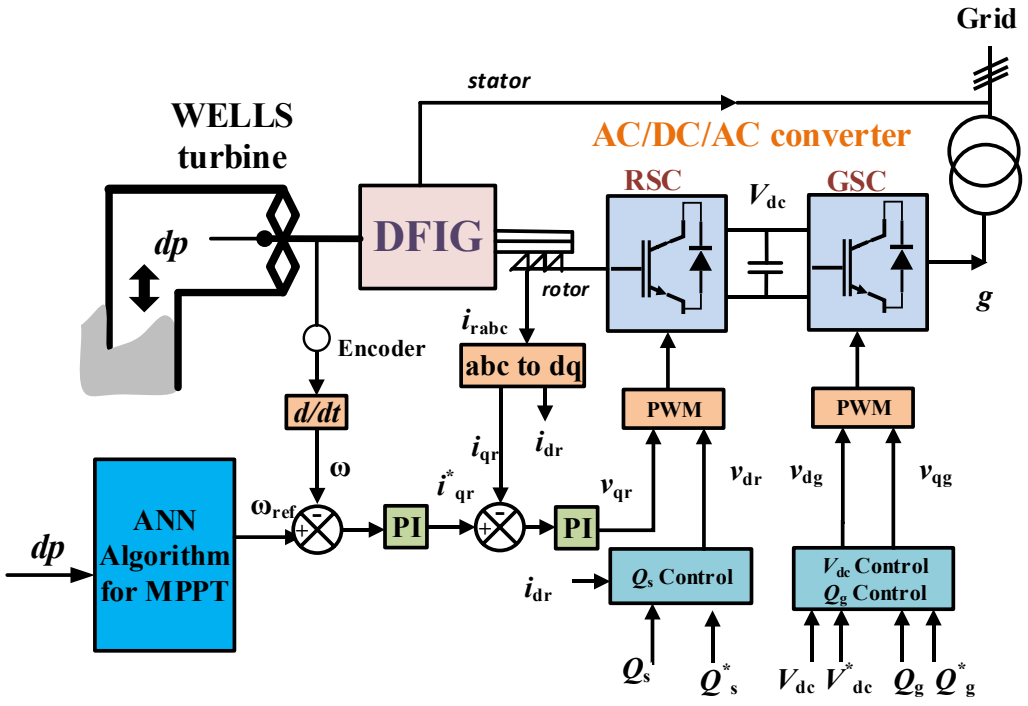

Figure 5.22 Complete OWC System with the proposed ANN MPPT Algorithm

In order to obtain an optimum turbine speed curve ensuring appropriate performance for tracking MPP, while preventing stalling phenomenon, the flow coefficient was adjusted to 0.2999, which is the critical threshold value as presented by

MATLAB/Simulink in Figure 5.23. The output speed curve of this simulated model is used as the proposed ANN output training data.

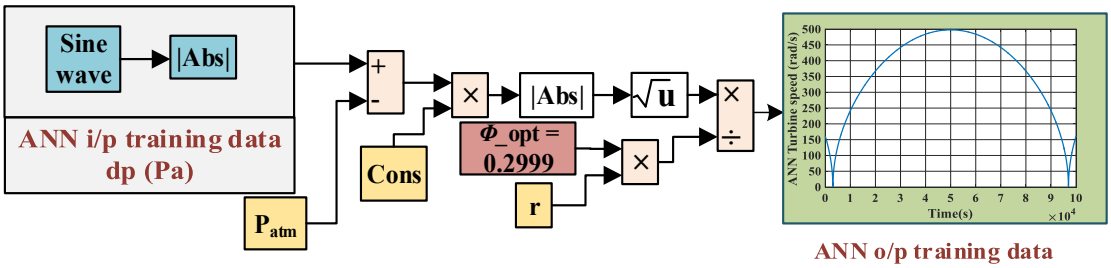

Figure 5.23 Proposed ANN Training Procedure Diagram

In Figure 5.24, the input differential pressure curve is shown, which is the input of the Simulink model, along with the turbine speed curve that ensures MPP and stalling avoidance. The output data is stored as a 2D-matrix to be fed into ANN as a training phase (input and output training data).

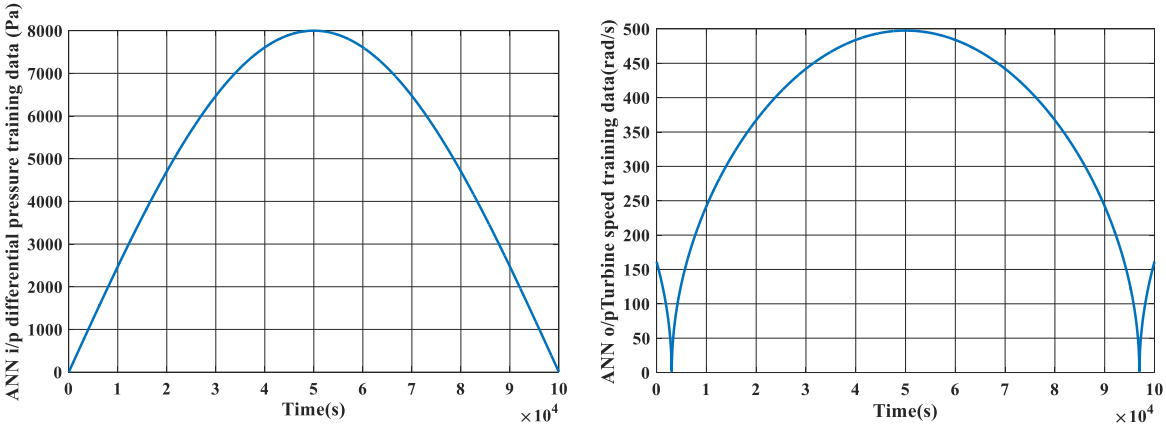

(a) (b)

Figure 5.24 Input-Output Data Representation used for the proposed ANN Training (a) Differential Input Pressure Curve (ANN input), and (b) Turbine References Speed Curve (ANN target)

The sampling time was 1µs. The differential input pressure curve was fed to the proposed ANN input layer, while the turbine speed reference curve was fed to the ANN output layer. Consequently, all the training datasets were loaded to respective layers. The hidden layer incorporates ten selected hidden neurons.

The Neural Fitting Tool (nftool) in MATLAB was utilized. This tool is usually used for estimation and prediction problems. The algorithm used in this training is Levenberg-Marquardt. Moreover, this training algorithm avoids over-fitting issues by stopping the training automatically when the generated results stop improving. The

correlation between the desired outputs and trained targets are measured by the Regression factor R. A value of one signifies a close relationship, while zero reflects a random relationship. The regression response of the trained ANN is shown in Figure 5.25. Nearly all the dataset inputs are aligned to the fitting line and the value of R is close to unity.

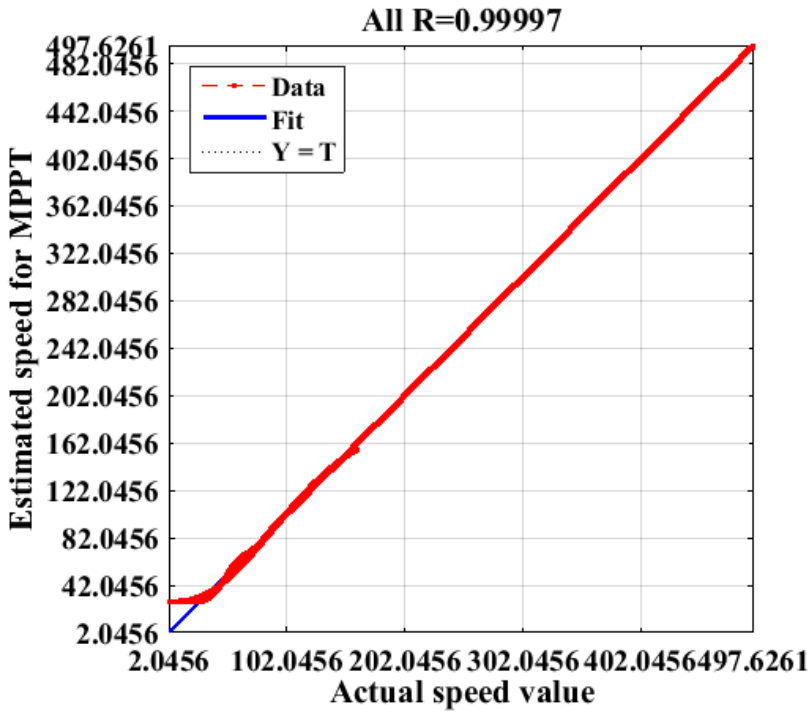

Figure 5.25 Regression Response of the Proposed Trained ANN Algorithm

Three simulated operations are presented: the uncontrolled operation with stalling under constant turbine speed, the classical P&O algorithm for MPPT and operation under the proposed ANN control technique with stalling phenomena avoidance. Three cases of various input differential pressure levels: 6000 Pa, 5000 Pa, and random variation wave are considered to ensure the validity of the proposed control algorithm.

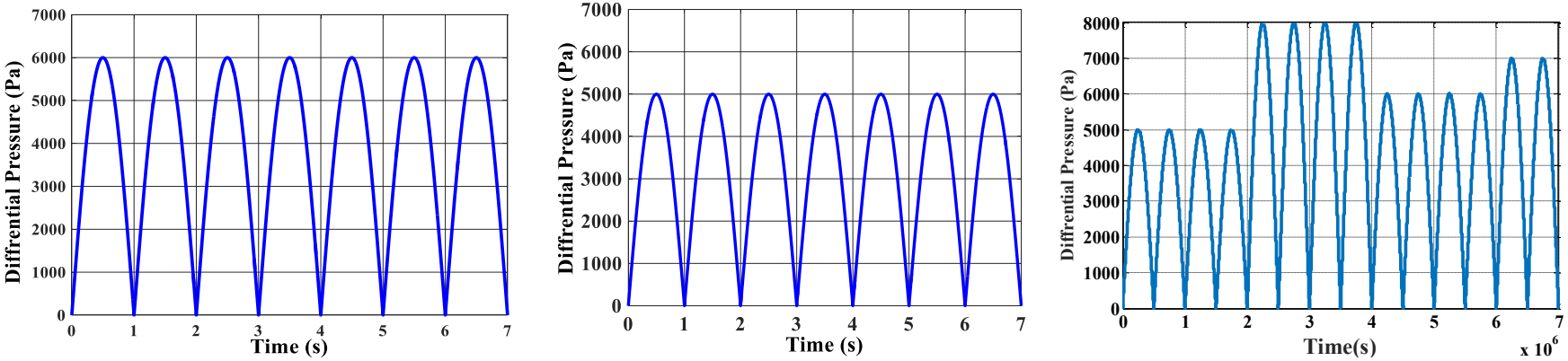

(a) (b) (c)

Figure 5.26 Differential Pressure (a) Case I at 6000 Pa Maximum Value (b) Case II at 5000 Pa Maximum Value (c) Case III Irregular Wave

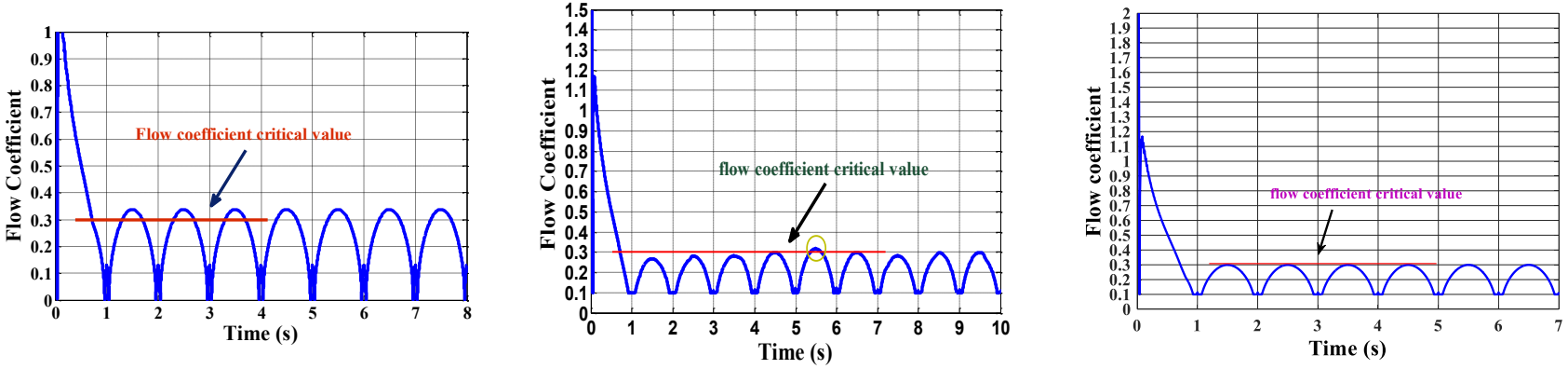

(a) (b) (c)

Figure 5.27 Flow Coefficient of Case I (a) Uncontrolled Operation (b) P&O Algorithm Controlled Operation (c) Proposed ANN Algorithm

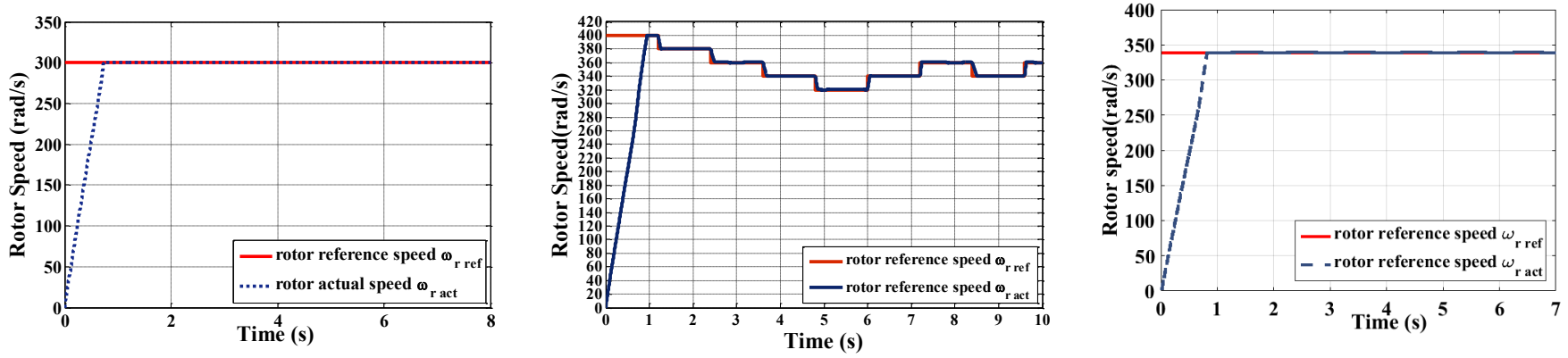

(a) (b) (c)

Figure 5.28 Rotor Speed of Case I (a) Uncontrolled Operation (b) P&O Algorithm Controlled Operation(c) Proposed ANN Algorithm

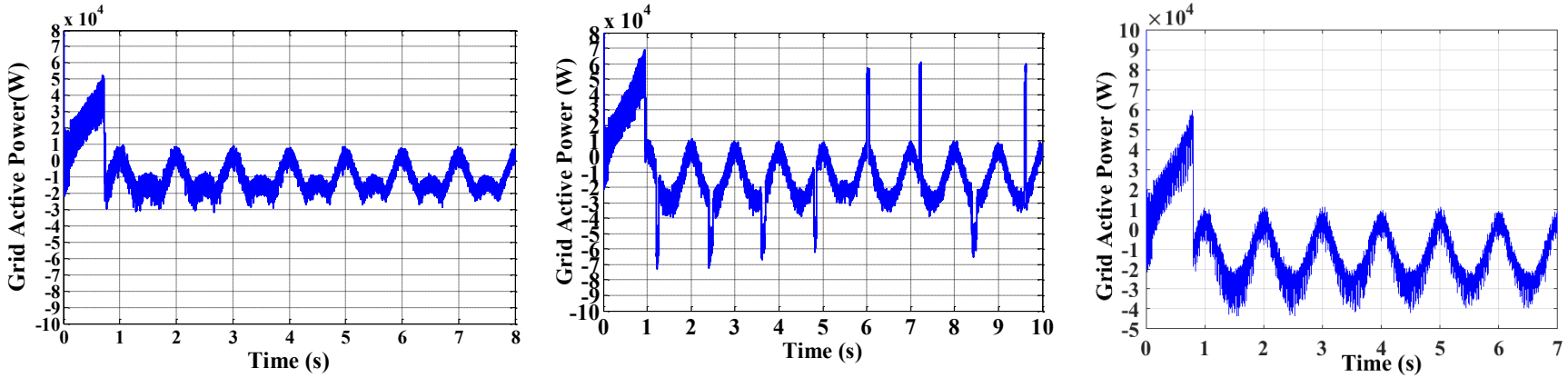

(a) (b) (c)

Figure 5.29 Grid Active Power of Case I (a) Uncontrolled Operation (b) P&O Algorithm Controlled operation {c) Proposed ANN Algorithm

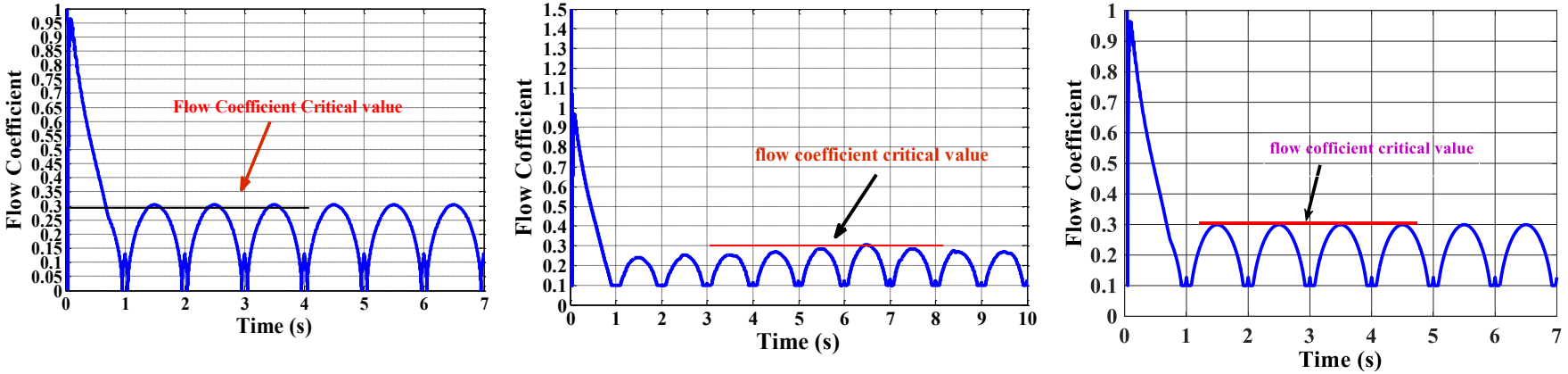

(a) (b) (c)

Figure 5.30 Flow Coefficient of Case II (a) Uncontrolled Operation (b) P&O Algorithm Controlled Operation(c) Proposed ANN Algorithm

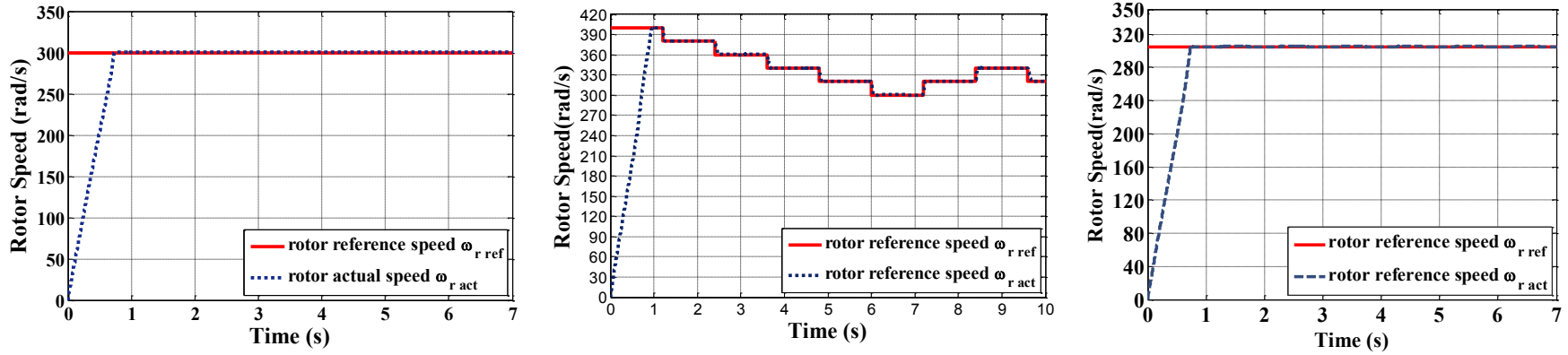

(a) (b) (c)

Figure 5.31 Rotor Speed of Case II (a) Uncontrolled Operation (b) P&O Algorithm Controlled Operation (c) Proposed ANN Algorithm

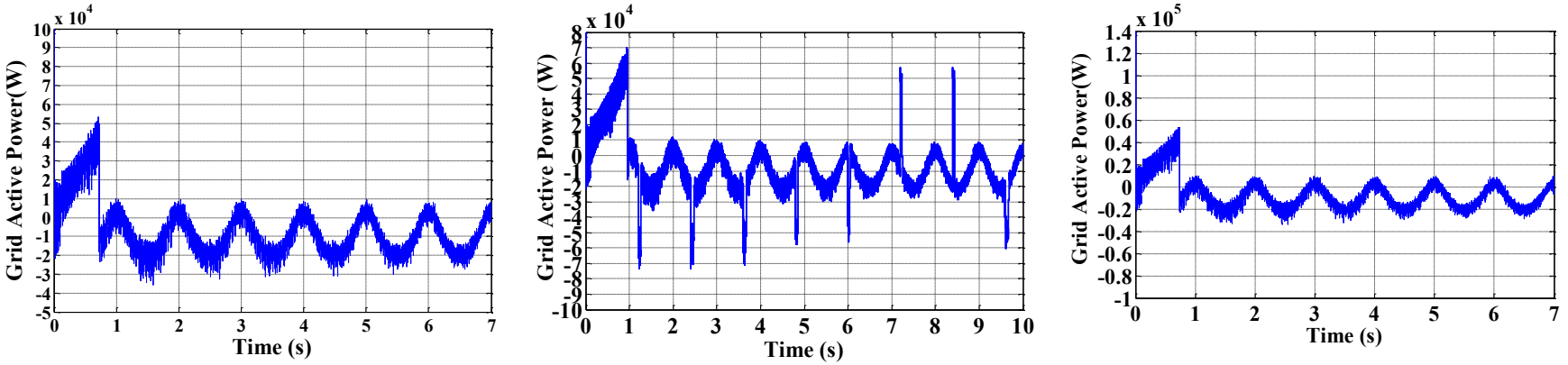

(a) (b) (c)

Figure 5.32 Grid Active Power of Case II (a) Uncontrolled Operation (b) P&O Algorithm Controlled Operation (c) Proposed ANN Algorithm

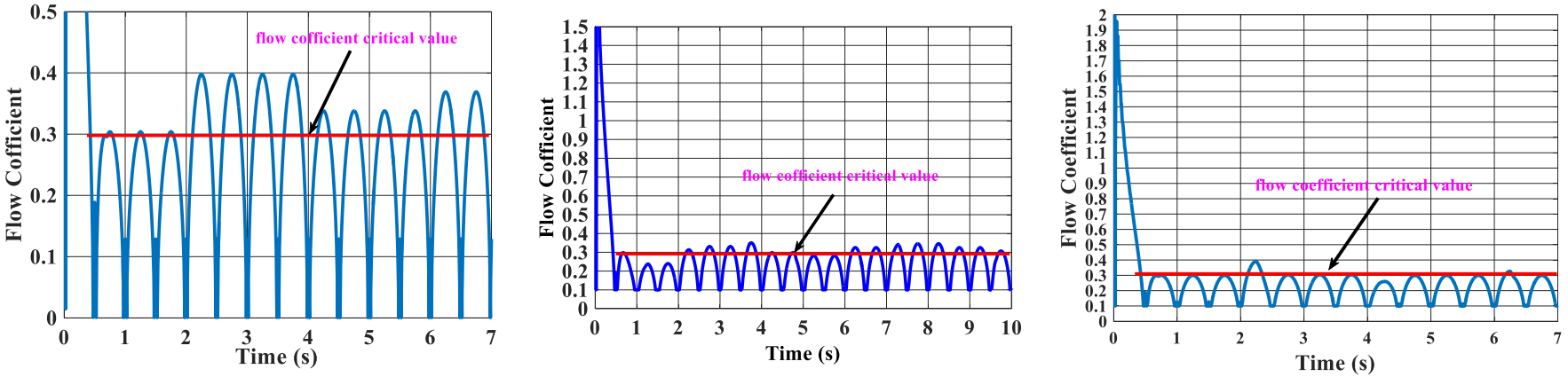

(a) (b) (c)

Figure 5.33 Flow Coefficient of Case III (a) Uncontrolled Operation (b) P&O Algorithm Controlled Operation (c) Proposed ANN Algorithm

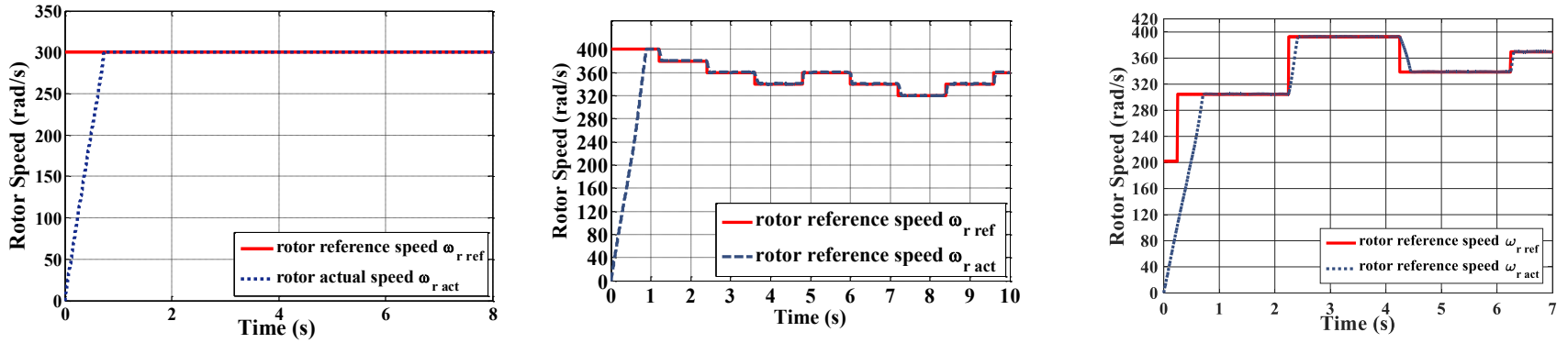

(a) (b) (c)

Figure 5.34 Rotor Speed of Case III (a) Uncontrolled Operation (b) P&O Algorithm Controlled Operation (c) Proposed ANN Algorithm

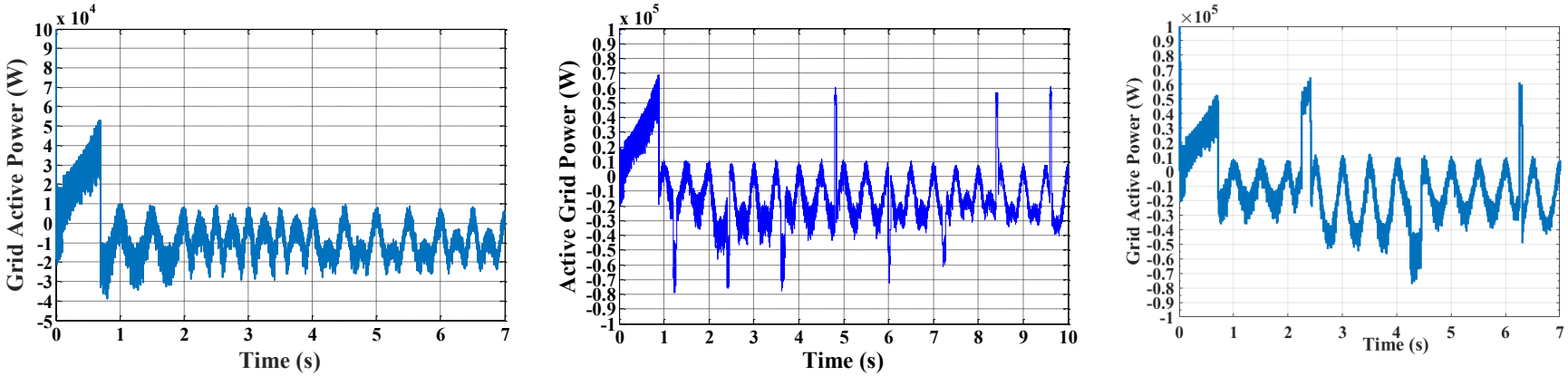

(a) (b) (c)

Figure 5.35 Grid Active Power of Case III (a) Uncontrolled Operation (b) P&O Algorithm Controlled Operation (c) Proposed ANN Algorithm

Figure 5.26 presents the differential pressure of the three cases. The first case operates at a maximum differential pressure of 6000 Pa, shown in Figure 5.26 (a), the second case operates at maximum pressure of 5000 Pa as shown in Figure 5.26 (b) and the last case represents an irregular wave.

The simulation results, illustrating system performance, were compared between uncontrolled operation, the classical P&O MPPT algorithm and the proposed ANN MPPT algorithm for case I when the maximum differential pressure was 6000 Pa. This is shown in Figures 5.27 to 5.29.

Figure 5.27 (a) shows the flow coefficient exceeded the critical value and the turbine is affected by the stalling phenomena. In Figure 5.27 (b), the P&O algorithm nearly avoids the occurrence of stalling phenomenon, but from 5s to 6s flow coefficient exceeds the critical value. In Figure 5.27 (c), the flow coefficient value is fixed to 0.3 without noticeable changes which indicates satisfactory performance of the proposed ANN algorithm.

Figure 5.28 (a) shows the generator speed of the uncontrolled operation, which is constant at a value of 300 rad/s in all cases. Figure 5.28 (b) shows the classical P&O attempt to capture the speed value that corresponds to maximum power while also keeping the flow coefficient fixed to 0.3. Although the speed oscillates around 340 rad/s under the P&O algorithm, the speed under the proposed ANN algorithm is effectively fixed to 340 rad/s as seen in Figure 5.28 (c).

Figure 5.29 illustrates the maximum grid active power in the three investigated operation cases. Figure 5.29 (a) represents the grid active power in the uncontrolled operation with an average value of 11 kW; while in the classical P&O the power oscillates around 14 kW as in Figure 5.29 (b). The average grid active power presents enhanced performance under the proposed ANN algorithm operation with a value equal to 14.6 kW as indicated in Figure 5.29 (c).

The simulation results for the second case when the maximum differential pressure is 5000 Pa are represented in Figures 5.30 to 5.32. As shown in Figure 5.30 (a), the flow coefficient exceeds the critical value slightly as the maximum differential pressure decreased and consequently the turbine is affected by the stalling phenomena. In Figure 5.30 (b), the P&O algorithm almost avoids the occurrence of stalling as it operates at a value smaller than the critical limit. Figure 5.30 (c), the flow coefficient value is strictly limited to 0.3, which indicates the enhanced performance of the proposed ANN algorithm.

Figure 5.31 (a) displays the generator speed under the uncontrolled operation, which is constant at 300 rad/s, while in Figure 5.31 (b) the classical P&O finds the speed value that ensures maximum power, keeping the flow coefficient bellow 0.3 after six seconds. The generator speed in this case oscillates around 320 rad/s, showing degraded power performance. The proposed ANN algorithm successfully converges on the rotor speed optimum value of 320 rad/s as indicated in Figure 5.31 (c) with minimal oscillations as compared to the P&O algorithm.

Figure 5.32 shows the maximum grid active power in the three system operations. Figure 5.32 (a) represents the grid active power in the uncontrolled operation with an average value equal to 10 kW; while in the classical P&O the average power oscillates around 10.5 kW, as in Figure 5.32 (b). Finally, the average grid active power was noticeably enhanced under the proposed ANN algorithm with a value of 10.8 kW, as indicated in Figure 5.32 (c).

The simulation results illustrating the system performance are shown in Figures 5.33 to 5.35. Figure 5.33 (a) shows that the flow coefficient exceeded the critical value of 0.3 for the whole wave signal as the maximum differential pressure changed every 2s from 5000 Pa to 8000 Pa to 6000 Pa to 7000 Pa. The P&O algorithm offered lower performance and could not accommodate rapid variation of the differential pressure due to stalling phenomenon throughout most of the time interval in Figure 5.33 (b). Figure 5.33 (c) showed the flow coefficient value fixed to 0.3, which indicates satisfactory performance of the proposed ANN algorithm excluding the transient period of the first 2s where the flow coefficient slightly exceeded the 0.3 boundary but quickly converged thereafter.

Figure 5.34 (a) shows the generator speed for the uncontrolled operation which is constant in all cases to 300 rad/s. Figure 5.34 (b), showing the classical P&O, varies the generator speed to achieve the maximum power while keeping the flow coefficient below 0.3. The generator speed under the proposed ANN algorithm is precisely changed following the rapid pressure variation, representing a rapidly accurate performance as shown in Figure 5.34 (c).

Figure 5.35 (a) represents the grid active power in the uncontrolled operation with different average active power values equal to 10 kW, 7.9 kW, 11 kW and 9.5kW. For the classical P&O, the power oscillated around 10.2 kW, 20 kW, 13.8kW and 18 kW as shown in Figure 5.35 (b). Finally, the average grid active power was more effective under the proposed ANN algorithm operation with values equal to 10.8 kW, 23.5kW, 14.6kW and

15.5 kW, respectively as indicated in Figure 5.35 (c). Hence, the proposed ANN based algorithm is more effective over the P&O method over the entire range of operation.

5.4 Conclusion

In this chapter, an enhanced dual function ANN-based MPPT/stalling prevention technique was developed. The proposed technique shows effective capabilities in dealing with both functions under a wide range of operating conditions. The enhanced performance was verified in the presented simulation results and compared to conventional perturb and observe classical technique.

Chapter 6
Conclusions and Recommendations for Future Work

6.1 Conclusions

In the presented thesis, OWC based wave energy conversion systems were investigated. Wells turbine modeling and performance of the same were studied. DFIG was utilized as the system main generator with a back-to-back converter implemented for grid connection purposes under decoupled *p-q* control. The investigation revealed the fact that Wells turbine suffers a common phenomenon known as stalling, where the generated power drops dramatically under certain operating conditions dependent on the turbine speed and the differential pressure inside the OWC chamber. Consequently, stalling prevention is important.

Various stalling prevention techniques were investigated. Air flow based techniques showed slow transient response and were dependent on the wave climate, chamber dimensions and differential pressure level. Regarding rotor speed control, Classical rotor resistance based stalling avoidance techniques showed limited enhancement due to fixed step variations, while optimal slip methods showed degraded performance due to the linearization of the slip ranges.

Consequently, a fast response, enhanced performance, and generic stalling avoidance technique was required. An ANN based Wells turbine stalling prevention technique was proposed in this thesis. The presented technique offers simplified implementation, direct training methodology, and a wider range of operation, in addition to rapid convergence with minimal grid power oscillations. Rigorous simulation results using Matlab/Simulink software package, under a wide range of operating conditions, were presented to validate the proposed ANN technique's superiority in comparison with classical methods.

Despite of the power gained by stalling avoidance, the turbine power stills needs an adequate maximum power tracking technique. A detailed review on various MPPT control techniques used in OWC based Wells turbines was presented. For high performance WECS, two control techniques must be implemented: stalling avoidance and a dedicated MPPT algorithm.

The proposed ANN-based stalling avoidance technique was modified to accommodate the MPPT feature using the same algorithm structure. Hence, simplified implementation was achieved with a preserved decoupled dual-functionality. A classical perturb and observe technique was investigated and simulated under several operating conditions. The proposed modified ANN-based technique shows enhanced performance, regarding MPPT over a wide range of operation, while preventing the turbine from stalling. Therefore, the proposed effectiveness of the dual-functionality technique has been proven.

6.2 Summary of Contributions

The summary of contributions is listed below:

- This thesis proposes a dual-function algorithm that ensures stalling avoidance and achieves maximum power point tracking (MPPT) using ANN. The proposed algorithm has been tested and was compared with classical dedicated stalling prevention techniques, as well as conventional MPPT algorithms.
- The training process of the ANN algorithm relies on input-output real data relations; hence no recursive simulations are needed. The developed technique shows adequate regression for enhanced system performance. The improvement was illustrated through high grid power for a wide range of input differential pressure variations**.**
- This combined-function technique contributes to OWC based energy conversion systems' rapid integration into the energy market by facilitating the required enhanced operations for the grid.
- Two IEEE conference papers accepted for publication and presented.

6.3 Recommendations for Future Work

1. Despite the rigorous simulation results presented in the thesis that reveal enhanced system performance under the proposed dual-function ANN based technique, experimentation can further contribute to that conclusion. A practical setup can open up opportunities to other research aspects regarding feedback sensor effect on overall performance, parameter sensitivity and turbine-generator inertia effects on the transient response at light loads.
2. Regarding recent restricted international grid codes, renewable energy systems connected to a grid must offer a high tolerance to various operating conditions. Among them, the critical low-voltage ride-through (LVRT) operation is required for weak network operation. Hence, the LVRT capabilities of the OWC WECS under the proposed ANN technique can be examined within these cases, revealing promising research to address.
3. Inspired from recent wind energy systems, the noticeable high power-to-weight ratio PMSG can be examined as a strong competitor to the classical DFIG. Yet, the proposed technique should be tailored to accommodate the PMSG nonlinearities and the modified decoupled active-reactive power control.

List of Publications

This section listed two IEEE international conference papers that disseminate the technical results elaborated from the presented thesis:

1. S. M. Yousry, A. K. Abdelsalam, Y. G. Dessouky, H. M. E. Helw and S. B. Tennakoon, "Stalling phenomenon prevention using artificial neural network based strategy for oscillation water column coupled to Wells turbine," *2017 19th European Conference on Power Electronics and Applications (EPE'17 ECCE Europe)*, Warsaw, 2017, pp. P.1-P.10.
2. S. M. Yousry, A. K. Abdelsalam, Y. G. Dessouky, H. M. El Helw and S. Tennakoon, "Decoupled control strategy for oscillating water column wave energy system based on doubly-fed induction generator," *2017 IEEE 3rd International Future Energy Electronics Conference and ECCE Asia (IFEEC 2017 - ECCE Asia)*, Kaohsiung, 2017, pp. 765-771.
3. S. M. Yousry, A. K. Abdelsalam, Y. G. Dessouky, H. M. El Helw and S. Tennakoon, "Dual function ANN based technique for Wells turbine based WECS," *IET, Generation, Transmission and Distribution, UNDER REVIEW*.

References

[1] P. Breeze, Power Generation Technologies, Elsevier Science, 2014.

[2] J. P. Deane, G. Dalton and B. P. \. Gallach{\'o}ir, "Modelling the economic impacts of 500MW of wave power in Ireland," *Energy Policy,* vol. 45, pp. 614-627, 2012.

[3] " Global Energy Transformation: A roadmap to 2050," International Renewable Energy Agency, Abu Dhabi, 2018.

[4] Wind, W. P. T. O. U. S. D. Energy Wind and W. Power, "U.S. Department of Energy Wind and Water Power Technologies Office Funding in The United States: Marine and Hydrokinetic Energy Projects Fiscal Years 2008 – 2012," 2013.

[5] A. M. O'Hagan, C. Huertas, J. O'Callaghan and D. Greaves, "Wave energy in Europe: Views on experiences and progress to date," *International Journal of Marine Energy,* vol. 14, pp. 180-197, 2016.

[6] E. U. ROADMAP, "European Renewable Energy Council (EREC), Mapping Renewable Energy Pathways towards 2020," EU Roadmap, EREC, Brussels, Citeseer, 2011.

[7] K. H. Mohamed, N. C. Sahoo and T. B. Ibrahim, "A survey of technologies used in wave energy conversion systems," in *Energy, Automation, and Signal (ICEAS), IEEE international Conference*, 2011.

[8] A. Alcao and J. Henriques, "Oscillating water column wave energy converters and air turbines: A review.," *Renewable Energy,* vol. 30, p. 1–34, 2015.

[9] K. Kerrouche, A. Mezouar and K. Belgacem, "Decoupled control of doubly fed induction generator by vector control for wind energy conversion system," *Energy procedia,* vol. 42, p. 239–248, 2013.

[10] T. Ahmed, K. Nishida and M. Nakaoka, "The commercial advancement of 16 MW offshore wave power generation technologies in the southwest of the UK," in *Power Electronics and ECCE Asia (ICPE \& ECCE), 2011 IEEE 8th International Conference on*, 2011.

[11] A. A. M. Sayigh, Solar energy engineering, Elsevier, 2012.

[12] R. Ren21, "Renewables 2017 Global Status Report," 2017.

[13] J. Callaghan and R. Boud, "Future Marine Energy. Results of the Marine Energy Challenge: Cost competitiveness and growth of wave and tidal stream energy," *Carbon Trust,* 2006.

[14] A. Estanqueiro, "Grid Integration on Ocean Energy Systems Integration of Ocean Power System sin the Grid: The Experience from Other REs," in *IEA-OES Meeting, Copenhagen, Denmark*, 2004.

[15] R. Henderson, "Design, simulation, and testing of a novel hydraulic power take-off system for the Pelamis wave energy converter," *Renewable Energy,* vol. 31, no. 2, p. 271–283, 2006.

[16] P. Frigaard, J. Tedd, J. P. Kofoed and E. Friis-Madsen, "3 Years Experience with Energy Production on the Nissum Bredning Wave Dragon Prototype," in *The Fourth CA-OE Workshop: Performance Monitoring of Ocean Energy Systems*, 2006.

[17] "Ocean Energy Technology. Overview," Federal Energy Management Program, July 2009.

[18] "OCEAN CURRENT ENERGY POTENTIAL ON THE U.S. OUTER CONTINENTAL SHELF," Available for Downloading at http://ocsenergy.anl.gov, May 2006.

[19] D. Dunnett and J. S. Wallace, "Electricity generation from wave power in Canada," *Renewable Energy,* vol. 34, pp. 179-195, 2009.

[20] L. Rodrigues, "Wave power conversion systems for electrical energy production," 2008.

[21] *Ocean Energy Conversion in Europe: Recent advancements and prospects,* 2006.

[22] B. Drew, A. R. Plummer and M. N. Sahinkaya, "A review of wave energy converter technology," *Proceedings of the Institution of Mechanical Engineers,* vol. 223, p. 887, 2009.

[23] D. L. O'Sullivan and A. W. Lewis, "Generator selection and comparative

performance in offshore oscillating water column ocean wave energy converters," *IEEE transactions on energy conversion,* vol. 26, no. 2, pp. 603-614, 2011.

[24] I. López, J. Andreu, S. Ceballos, I. M. Alegría and I. Kortabarria, "Review of wave energy technologies and the necessary power-equipment," *Renewable and Sustainable Energy Reviews,* vol. 27, pp. 413-434, 2013.

[25] H. Polinder and M. Scuotto, "Wave energy converters and their impact on power systems," in *2005 International Conference on Future Power Systems*, 2005.

[26] T. J. T. Whittaker, W. Beattie, M. Folley, C. Boake, A. Wright, M. Osterried and T. Heath, "The limpet wave power project–the first years of operation.," *Renewable Energy,* 2004.

[27] R. Bedard and G. Hagerman, "E2I EPRI Assessment - Offshore Wave Energy Conversion Devices," *Electricity Innovation Institute,* p. 11, 2004.

[28] A. F. d. O. Falcão, "The shoreline OWC wave power plant at the Azores," in *Fourth European Wave Energy Conference*, Aalborg, 2000.

[29] A. R. E. A. ARENA, *Arena.gov.au,* 2017.

[30] wikipedia, "https://en.wikipedia.org/wiki/Wavegen," 10 2017. [Online]. Available: https://en.wikipedia.org/wiki/Wavegen.

[31] T. V. Heath, "The Development and Installation of the Limpet Wave Energy Converter, science direct," in *World Renewable Energy Congress VI*, 2000.

[32] T. H. E. E. U. R. O. P. E. A. N. COMMISSION, *ISLAY LIMPET WAVE POWER PLANT , The Queen's University of Belfast Contract JOR3-CT98-0312, PUBLISHABLE,* vol. 1, 1998.

[33] New-Atlas, *https://newatlas.com/go/3932/,* Accessed 2017.

[34] A. F. O. Falcão, "Modelling of wave energy conversion," *Instituto Superior T{\'e}cnico, Universidade Te'cnica de Lisboa,* 2014.

[35] C. J. K. Gunawardane and T. Watabe, "Study on the performance of the "pendulor" wave energy converter in an array configuration," *Energies,* vol. 9, p. 282–308, 2016.

[36] S. Osanai, H. Kondo, Y. Mizuno and T. Watabe, "Feasibility Tests of New Pendular-Type Wave Energy Conversion Apparatus," *Coastal Engineering,* p. 4591–4600, 1996.

[37] J. Vining, "Ocean wave energy conversion," 2005.

[38] J. P. Kofoed, P. Frigaard, E. Friis-Madsen and H. C. Sørensen, "Prototype testing of the wave energy converter wave dragon," *Renewable energy,* vol. 31, p. 181–189, 2006.

[39] N. S. D. Phase, "Wave Dragon 1.5 MW," 2015.

[40] P. Bauer and B.Czech, "Wave Energy Converter Concepts : Design Challenges and Classification," in *IEEE Industrial Electronics Magazine*, vol. 6, 2012, p. 4–16.

[41] O. Power-Technologies, "www.oceanpowertechnologies.com," 11 2017. [Online]. Available: http://www.oceanpowertechnologies.com/.

[42] A. L. Rodrigues and A. S. Gar{\c{c}}{\~a}o, "Pelamis converter for wave energy extraction," in *5th Portuguese-Mozambique Conference of Engineering*, 2008.

[43] R. W. Yemm, R. M. Henderson and C. A. E. Taylor, "The OPD Pelamis WEC: Current status and onward programme," in *Proc. 4th European Wave Energy Conference, Alborg Denmark*, 2000.

[44] A. Cl{\'e}ment, P. McCullen, A. Falcão, A. Fiorentino, F. Gardner, K. Hammarlund, G. Lemonis, T. Lewis, K. Nielsen, S. Petroncini and others, "Wave energy in Europe: current status and perspectives," *Renewable and sustainable energy reviews,* vol. 6, pp. 405-431, 2002.

[45] Wikipedia, *https://en.wikipedia.org/wiki/Wave_power.*

[46] A. V. Rosa, Fundamentals of Renewable Energy Processes, 2 ed., Elsevier Science, 2009.

[47] W. a. C. D. a. B.-M. C. a. R. P. Chehaze, "Wave Roller Device for Power Generation," *Procedia Engineering,* vol. 145, pp. 144--150, 144--150.

[48] Aw-energycom, "Promising results from first grid-connected WaveRoller units – Initial outcomes surpass expectations"," 2017. [Online]. Available:

energy.com/promising-results-from-first-grid-connected-waveroller-units-initial-outcomes-surpass-expectations..

[49] M. G. S. Prado, F. Gardner, M. E. C. Damen and H. Polinder, "Modelling and test results of the Archimedes wave swing," *Power and Energy,* vol. 220, p. 855–868, 2006.

[50] J. S. D. Costa, P. Pinto and A. S. F. Gardner, "Modeling of an Ocean Waves Power Device AWS," *Control Applications,* vol. 1, p. 618–623, 2003.

[51] B. Czech, P. Bauer, H. Polinder, Y. Zhou and P. Korondi, "Comparing the electrical transmission systems for Archimedes Wave Swing parks," in *Proceedings of the 8th European Wave and Tidal Energy Conference (EWTEC2009), Uppsala, Sweden*, 2009.

[52] P. Meisen and A. Loiseau, "Ocean energy technologies for renewable energy generation," Global Energy Network Institute (GENI, 2009.

[53] L. Hamilton, "AWS MK II-Deployment, monitoring and evaluation of a prototype advanced wave energy device," *AWS Ocean Energy Ltd,* 2006.

[54] J. L. O. Amilibia and A. I. Aio, "Selection of the Electrical Generator for a Wave Energy Converter," *International Conference on Renewable Energies and Power Quality (ICREPQ'10),* pp. 125-134, 2010.

[55] J. Bard and P. Kracht, "Linear Generator Systems for Wave Energy Converters.," 2013.

[56] D. Val{\'e}rio, P. Beir{\~a}o and J. S. Costa, "Optimization of wave energy extraction with the Archimedes Wave Swing," *Ocean Engineering,* vol. 34, pp. 2330-2344, 12 2007.

[57] F. Wu, X. P. Zhang, P. Ju and M. J. H. Sterling, "Modeling and Control of AWS-Based Wave Energy Conversion System Integrated Into Power Grid," *IEEE Transactions on Power Systems,* vol. 23, pp. 1196-1204, 8 2008.

[58] F. Wu, X. P. Zhang and P. Ju, "Control strategy for AWS based wave energy conversion system," in *IEEE PES General Meeting*, 2010.

[59] F. Wu, X. P. Zhang, P. Ju and M. J. H. Sterling, "Optimal Control for AWS-Based Wave Energy Conversion System," *IEEE Transactions on Power Systems,* vol. 24, pp. 1747-1755, 11 2009.

[60] M. Amundarain, M. Alberdi, A. J. Garrido, I. Garrido and J. Maseda, "Wave energy plants: Control strategies for avoiding the stalling behaviour in the Wells turbine," *Renewable Energy,* vol. 35, pp. 2639-2648, 2010.

[61] M. Amundarain, M. Alberdi, A. J. Garrido and I. Garrido, "Modeling and simulation of wave energy generation plants: Output power control," *IEEE Transactions on Industrial Electronics,* vol. 58, pp. 105-117, 2011.

[62] A. L. Rodrigues, "Devices for sea wave power extraction to electrical energy conversion," *International Journal of Engineering and Industrial Management,* vol. 3, pp. 193-210, 2015.

[63] M. Amundarain, M. Alberdi, A. Garrido and I. Garrido, "Control of the stalling behaviour in Wave Power Generation Plants," in *Compatibility and Power Electronics, 2009. CPE'09.*, 2009.

[64] S. S. Rao and B. K. Murthy, "Control of induction generator in a Wells turbine based wave energy system," in *Power Electronics and Drives Systems, 2005. PEDS 2005. International Conference on*, 2005.

[65] M. A. Ormaza, M. A. Goitia, I. G. Hernandez and A. J. G. Hernandez, "Wells turbine control in wave power generation plants," in *2009 IEEE International Electric Machines and Drives Conference*, 2009.

[66] M. A. Ormaza, M. A. Goitia, A. J. G. Hernández and I. G. Hernández, "Neural control of the Wells turbine-generator module," in *Proceedings of the 48h IEEE Conference on Decision and Control (CDC) held jointly with 2009 28th Chinese Control Conference*, 2009.

[67] M. P. Kazmierkowski and M. Jasinski, "Power electronics for renewable sea wave energy," in *Optimization of Electrical and Electronic Equipment (OPTIM), 2010 12th International Conference on*, vol. 4, ieee, 2010, pp. 4-9.

[68] M. Jasinki, M. Malinowski, M. P. Kazmierkowski, H. C. Sorensen, E. Friis-Madsen

and D. Swierczynski, "Control of AC/DC/AC converter for multi MW wave dragon offshore energy conversion system," in *Industrial Electronics, 2007. ISIE 2007. IEEE International Symposium on*, 2007.

[69] Z. Zhou, W. Knapp, J. MacEnri, H. C. Sorensen, E. F. Madsen, I. Masters and P. Igic, "Permanent magnet generator control and electrical system configuration for wave dragon MW wave energy take-off system," in *Industrial Electronics, 2008. ISIE 2008. IEEE International Symposium on*, 2008.

[70] D. N. Veritas, "Guidelines on design and operation of wave energy converters," *Carbon Trust,* 2005.

[71] N. Telu and R. Telu, "Design, simulation and Control of Doubly Fed Induction Generator.," *International Journal of engineering research and Applications,* vol. 2, p. 634–639, 2012.

[72] R. Boud, Status and Research and Development Priorities, Wave and Marine Current Energy, United Kingdom, 2003.

[73] I. Garrido, A. J. Garrido, M. Alberdi, M. Amundarain and M. Sen, "Sensorless Control for an Oscillating Water Column Plant," *currents,* vol. 20, p. 21.

[74] M. Alberdi, M. Amundarain, A. J. Garrido and I. Garrido, "Ride through of OWC-based wave power generation plant with air flow control under symmetrical voltage dips," in *Control \& Automation (MED), 2010 18th Mediterranean Conference on*, 2010.

[75] A. El Marjani, F. C. Ruiz, M. A. Rodriguez and M. T. P. Santos, "Numerical modelling in wave energy conversion systems.," *Energy,* vol. 33, p. 1246–1253, 2008.

[76] M. Alberdi, M. Amundarain, A. J. Garrido, I. Garrido, O. Casquero and M. De la Sen, "Complementary control of oscillating water column-based wave energy conversion plants to improve the instantaneous power output," *IEEE Transactions on Energy Conversion,* vol. 26, pp. 1021-1032, 2011.

[77] M. E. McCormick, Ocean wave energy conversion, Courier Corporation, 2013.

[78] G. M. L. L. Barstow and J. P. Mathisen, "World Waves wave energy resource

assessments from the deep ocean to the coast," *Journal of Energy and Power Engineering,* vol. 5, 2011.

[79] A. J. N. A. Sarmento, A. B. Melo and M. T. Pontes, "The influence of the wave climate on the design and annual production of electricity by OWC wave power plants," *Journal of Offshore Mechanics and Arctic Engineering,* vol. 125, pp. 139-144, 2003.

[80] M. Takao and T. Setoguchi, "Air turbines for wave energy conversion," *International Journal of Rotating Machinery,* 2012.

[81] T. Setoguchi and M. Takao, "Current status of self rectifying air turbines for wave energy conversion," *Energy Conversion and Management,* vol. 47, p. 2382–2396, 2006.

[82] A. Gareev, "Analysis of variable pitch air turbines for oscillating water column (owc) wave energy converters," 2011.

[83] T. Finnigan and D. Auld, "Model testing of a variable-pitch aerodynamic turbine," in *The Thirteenth International Offshore and Polar Engineering Conference. International Society of Offshore and Polar Engineers*, 2003.

[84] F. O. Antonio, "Wave energy utilization: A review of the technologies," *Renewable and sustainable energy,* vol. 14, p. 899–918, 2010.

[85] M. Takao, E. Sato, T. Takeuchi, S. Nagata, K. Toyota and T. Setoguchi, "Sea Trial of an Impulse Turbine for Wave Energy Conversion.," in *Proceedings of International Symposium on Eco Topia Science*, 2007.

[86] C. B. Boake, T. J. T. Whittaker, M. Folley and H. Ellen, "Overview and initial operational experience of the LIMPET wave energy plant," in *The Twelfth International Offshore and Polar Engineering Conference. International Society of Offshore and Polar Engineers*, 2002.

[87] M. S. Lagoun, A. Benalia and M. E. H. Benbouzid, "Ocean wave converters: State of the art and current status," in *Energy Conference and Exhibition (EnergyCon)*, ieee, 2010, p. 636–641.

[88] A. Thakker and R. Abdulhadi, "Effect of blade profile on the performance of Wells

turbine under unidirectional sinusoidal and real sea flow conditions," *International Journal of Rotating Machinery,* vol. 2008, 2008.

[89] M. Alberdi, M. Amundarain, A. J. Garrido, I. Garrido and F. J. Sainz, "Control of oscillating water column-based wave power generation plants for grid connection," in *Control \& Automation (MED), 20th Mediterranean Conference on*, 2012.

[90] S. Muthukumar, R. Desai, V. Jayashankar, S. Santhakumar and T. Setoguchi, "Design of a stand-alone wave energy plant.," in *The Fifteenth International Offshore and Polar Engineering Conference. International Society of Offshore and Polar Engineers*, 2005.

[91] A. F. O. Falcão and J. C. C. Henriques, "Oscillating-water-column wave energy converters and air turbines: A review," *Renewable Energy,* vol. 85, p. 1391–1424, 2016.

[92] F. M'zoughi, S. Bouallegue and M. Ayadi, "Modeling and SIL simulation of an oscillating water column for ocean energy conversion," in *Renewable Energy Congress (IREC), 2015 6th International*, 2015.

[93] I. Garrido, A. J. Garrido, M. Alberdi, M. Amundarain and O. Barambones, "Performance of an ocean energy conversion system with DFIG sensorless control," *Mathematical Problems in Engineering,* vol. 2013, 2013.

[94] J. C. Bekker, "Efficient modelling of a wind turbine system for parameter estimation applications.," Stellenbosch University, 2012.

[95] L.-V. (. L. Staff, L.-V. (. Ltd and L.-V. , Principles of Doubly-Fed Induction Generators (DFIG), Lab-Volt, 2011.

[96] J. Fletcher and J. Yang, "Introduction to the doubly-fed induction generator for wind power applications," in *Paths to Sustainable Energy*, InTech, 2010.

[97] H. Abniki, M. Abolhasani and M. E. Kargahi, "Vector Control Analysis of Doubly-Fed Induction Generator in Wind Farms.," *Energy and Power,* vol. 3, p. 18–25, 2013.

[98] A. Petersson, "Analysis, Modelling and Control of Doubly-Fed Induction Generators for Wind Turbines," 2005.

[99] U. B. Bose, Modern power electronics and AC drives.Upper Saddle River, Prentice Hall, 2002.

[100] M. I. Abdelkader, A. K. Abdelsalam and A. A. H. Eldin, "Vector controlled brushless doubly fed twin stator cascaded induction generator for variable speed wind generation connected to weak grids," in *Power Electronics and Applications (EPE'15 ECCE-Europe), 2015 17th European Conference on. IEEE*, NIVERSITY OF TECHNOLOGY Goteborg, Sweden, 2015, p. 1–12.

[101] G. Abad, J. Lopez, M. Rodriguez, L. Marroyo and G. Iwanski, DOUBLY FED INDUCTION MACHINE MODELING AND CONTROL FOR WIND ENERGY GENERATION, vol. 85, Hoboken, New: John Wiley & Sons, 2011.

[102] S. H. W. E. HLAING, "Basic Concepts of Doubly Fed Induction Generator Driven by Wind Energy Conversion System," *International Journal of Scientific Engineering and Technology Research,* vol. 03, no. 15, pp. 3242-3246, 2014.

[103] M. T. I. Md and J. E. Quaicoe, "Vector control of a DFIG based wind turbine.," *Istanbul University-Journal of Electrical \& Electronics Engineering,* vol. 9, p. 1057–1066, 2010.

[104] A. K. Abdelsalam, M. I. Masoud, M. S. Hamad and B. W. Williams, "Modified indirect vector control technique for current-source induction motor drive,," *IEEE Transactions on Industry Applications,* vol. 48, p. 2433–2442, 2012.

[105] A. K. Abdelsalam, M. I. Masoud, S. J. Finney and B. W. Williams, "Vector control PWM-VSI induction motor drive with a long motor feeder: performance analysis of line filter networks," *IET electric power applications,* vol. 5, pp. 443-456, 2011.

[106] S. M. Yousry, A. K. Abdelsalam, Y. G. Dessouky, H. M. El Helw and S. Tennakoon, "Decoupled control strategy for oscillating water column wave energy system based on doubly-fed induction generator," in *Future Energy Electronics Conference and ECCE Asia (IFEEC 2017-ECCE Asia), 2017 IEEE 3rd International*, 2017.

[107] D. W. Novotny and T. A. Lipo, Vector Control and Dynamics of AC Drives, Clarendon Press, 1996.

[108] W. Qiao, "Dynamic modeling and control of doubly fed induction generators driven

by wind turbines.," in *Power Systems Conference and Exposition,PSCE'09. IEEE/PES*, 2009.

[109] S. Pati and S. Samantray, "Decoupled control of active and reactive power in a DFIG based wind energy conversion system with conventional PI controllers," in *Circuit, Power and Computing Technologies (ICCPCT), IEEE 2014 International Conference on*, 2014.

[110] E. Jumper, S. Schreck and Dimmick, *R "Lift-Curve Characteristics for an Airfoil Pitching at Constant Rate." AIAA 24th Aerospace Sciences Meeting,* Reno, Nevada, 1986, p. 86–0117.

[111] M. R. Visbal, "On the formation and control of the dynamic stall vortex on a pitching airfoil," *29th Aerospace Sciences Meeting, Aerospace Sciences Meetings,* 1991.

[112] J. M. Currier and K.-Y. Fung, "Analysis of the onset of dynamic stall," *AIAA journal,* vol. 30, pp. 2469-2477, 1992.

[113] L. W. Carr, "Progress in analysis and prediction of dynamic stall," *Journal of Aircraft,* vol. 25, p. 6–17, 1988.

[114] M. Hand, D. Simms, L. Fingersh, D. Jager, J. Cotrell, S. Schreck and S. Larwood, "Unsteady Aerodynamics Experiment Phase VI: Wind Tunnel Test Configurations and Available Data Campaigns," Golden, 2001.

[115] F. Rasmussen, J. T. Petersen and H. A. Madsen, "Dynamic Stall and Aerodynamic Damping.," *Journal of Solar Energy Engineering,* vol. 121, p. 150–155, 8 1999.

[116] S. Guntur, N. N. Sørensen, S. Schreck and L. Bergami, "Modeling dynamic stall on wind turbine blades under rotationally augmented flow fields.," *Wind Energy,* vol. 19, p. 383–397, 3 2016.

[117] C. Bak, J. Johansen and P. B. Andersen, "Three-dimensional corrections of airfoil characteristics based on pressure distributions," in *Proceedings of the European Wind Energy Conference*, Athens, 2006.

[118] B. M. ". Heath, The Aeronautical Journal of the Royal Aeronautical Society, June, 1970, p. 319–325.

[119] C. P. Butterfield, D. Simms, G. Scott and A. C. Hansen, "Dynamic stall on wind turbine blades," 1991.

[120] accessed 10/2017. [Online]. Available: https://www.quora.com/Mechanical-Engineering-Whats-the-difference-between-compressor-surge-and-stall-1.

[121] J. Kerwin, "Lecture notes hydrofoil and propellers," 2000.

[122] T. Setoguchi, K. Kaneko, H. Taniyama, H. Maeda and M. Inoue, "Impulse turbine with self-pitch-controlled guide vanes for wave power conversion: guide vanes connected by links.," *International Journal of Offshore and Polar Engineering,* vol. 6, p. 76–80, 1996.

[123] W. K. Tease, J. Lees and A. Hall, "Advances in oscillating water column air turbine development," in *Proc. of the Seventh European Wave and Tidal Energy Conference*, Porto, 2007.

[124] J. M. P. Conde and L. M. C. Gato, "Numerical study of the air-flow in an oscillating water column wave energy converter.," *Renewable energy,* vol. 33, p. 2637–2644, 2008.

[125] V. Jayashankar, K. Udayakumar, B. Karthikeyan, K. Manivannan, N. Venkatraman and S. Rangaprasad, "Maximizing power output from a wave energy plant," in *Power engineering society winter meeting*, 2000.

[126] M. Alberdi, M. Amundarain, F. J. Maseda and O. Barambones, "Stalling behaviour improvement by appropriately choosing the rotor resistance value in Wave Power Generation Plants," in *IEEE international conference on clean electrical power*, 2009.

[127] A. J. Garrido, M. Alberdi, I. Garrido, M. Amundarain and P. R. Moreno, "Control of oscillating water column (OWC) wave energy plants.," *Jornadas de Automática,* 2014.

[128] S. K. Mishra, S. Purwar and N. Kishor, "Air flow control of OWC wave power plants using FOPID controller.," in *Control Applications (CCA), 2015 IEEE Conferenceon*, Australia, 2015.

[129] F. Neumann, A. Brito-Melo, E. Didier and A. Sarmento, "Pico OWC recovery project: recent activities and performance data," in *Proc of the 7th European Wave and Tidal Energy Conference*, Porto, 2007.

[130] M. Amundarain, M. Alberdi, A. J. Garrido and I. Garrido, "Control strategies for OWC wave power plants," in *American Control Conference (ACC), 2010*, 2010.

[131] A. Abraham, "Artificial neural networks.," in *Handbook of measure system design*, Wiley Online Library, 2005.

[132] B. Yegnanarayana, Artificial neural networks, PHI Learning Pvt. Ltd., 2009.

[133] L. C. Jain, Electronic technology directions to the year 2000: proceedings; may 23-25, 1995, Adelaide, Australia, IEEE Computer Soc. Press, 1995.

[134] R. A. Y. Song, "Artificial neural networks in power systems. I. General introduction to neural computing.," *Power Engineering Journal,* vol. 11, p. 129–134, 6 1997.

[135] M. Abdullah, A. Yatim, C. Tan and R. Saidur, "A review of maximum power point tracking algorithms for wind energy systems," *Renewable and Sustainable Energy Reviews,* vol. 16, no. 5, pp. 3220--3227, 2012.

[136] M. A. Abdullah, A. Yatim and C. W. Tan, "A study of maximum power point tracking algorithms for wind energy system," *Clean Energy and Technology (CET), 2011 IEEE First Conference on,* pp. 321-326, 2011.

[137] N. Altin and E. Ozturk, "Maximum power point tracking quadratic boost converter for photovoltaic systems," *2016 8th International Conference on Electronics, Computers and Artificial Intelligence (ECAI),* pp. 1-4, 2016.

[138] S. V. Hudisteanu, T. D. Mateescu, C. G. Popovici and C.-N. Chereches, "The influence of the building integrated photovoltaic panels position on the conversion efficiency," *Buletinul Institutului Politehnic din lasi. Sectia Constructii, Arhitectura,* vol. 62, no. 2, p. 93, 2016.

[139] J. Lekube, A. J. Garrido and I. Garrido, "Rotational Speed Optimization in Oscillating Water Column Wave Power Plants Based on Maximum Power Point Tracking," *IEEE Transactions on Automation Science and Engineering,* vol. 14, no.

2, pp. 681-691, 2017.

[140] S. K. Mishra, S. Purwar and N. Kishor, "An Optimal and Non-Linear Speed Control of Oscillating Water Column Wave Energy Plant with Wells Turbine and DFIG," *INTERNATIONAL JOURNAL OF RENEWABLE ENERGY RESEARCH,* vol. 6, no. 3, pp. 995-1006, 2016.

[141] J. Lekube, A. J. Garrido, I. Garrido, E. Otaola and J. Maseda, "Flow Control in Wells Turbines for Harnessing Maximum Wave Power," *Sensors 2018,* vol. 18, no. 2, p. 535, 2018.

[142] R. D. Shukla and R. Tripathi, "Maximum power extraction schemes and power control in wind energy conversion system," *International Journal of Scientific and Engineering Research,* vol. 3, no. 6, pp. 1-7, 2012.

[143] A. M. Atallah, A. Y. Abdelaziz and R. S. Jumaah, "Implementation of perturb and observe MPPT of PV system with direct control method using buck and buck-boost converters," *Emerging Trends in Electrical, Electronics \& Instrumentation Engineering: An international Journal (EEIEJ),* vol. 1, no. 1, pp. 31-44, 2014.

[144] W. Qiao and R. G. Harley, "Grid connection requirements and solutions for DFIG wind turbines," in *Energy 2030 Conference, 2008. ENERGY 2008. IEEE*, 2008.

[145] J. H. R. Enslin, "The role of power electronics and storage to increase penetration levels of renewable power," in *Power and Energy Society General Meeting-Conversion and Delivery of Electrical Energy in the 21st Century, 2008 IEEE*, 2008.

[146] A. L. Rodrigues, "Devices for sea wave power extraction to electrical energy conversion," *International Journal of Engineering and Industrial Management,* pp. 193-210, 2015.

Appendix A- Matlab/Simulink file Screen-Shots

A.1 GSC CONTROL

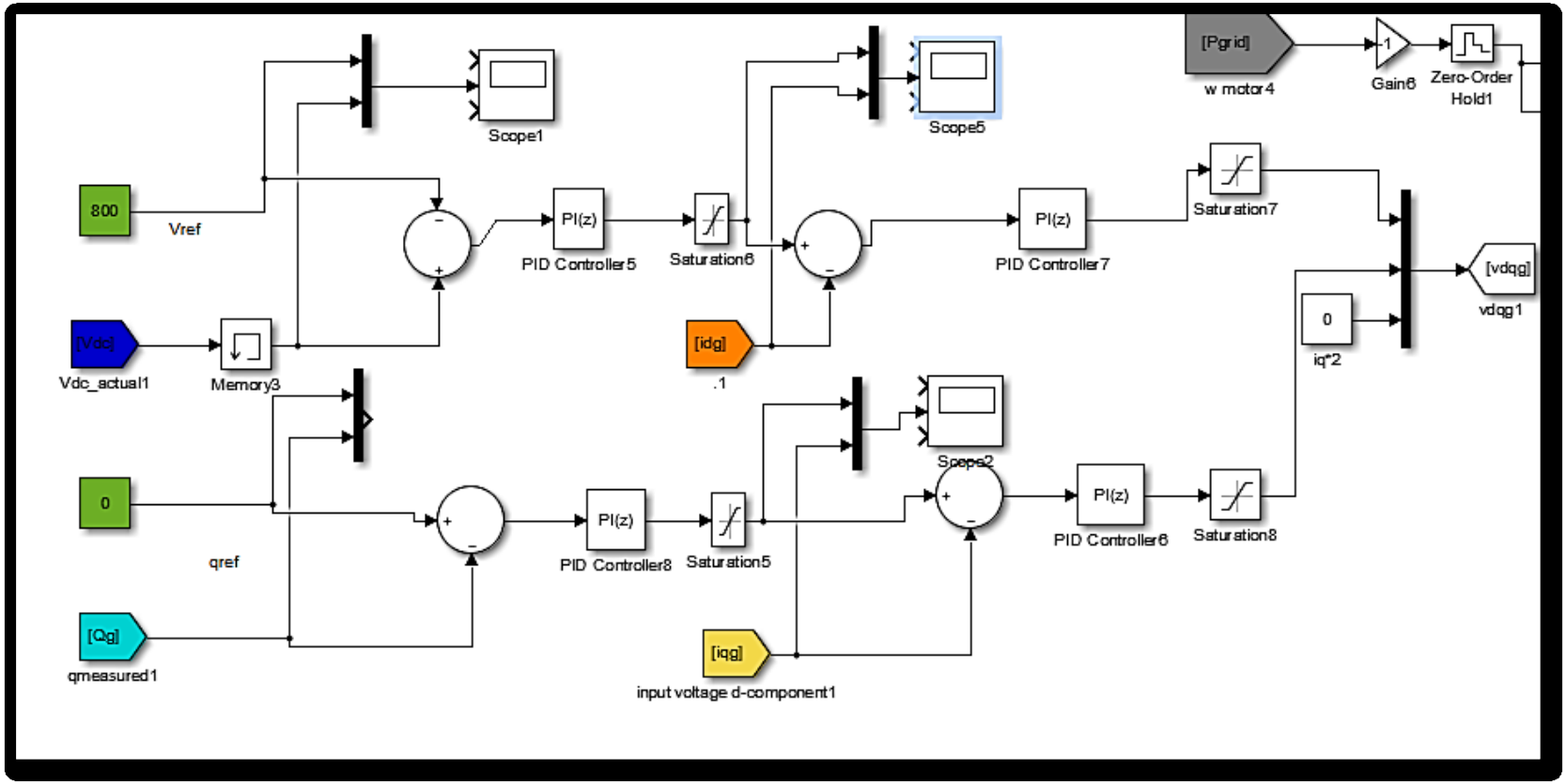

A.2 RSC CONTROL

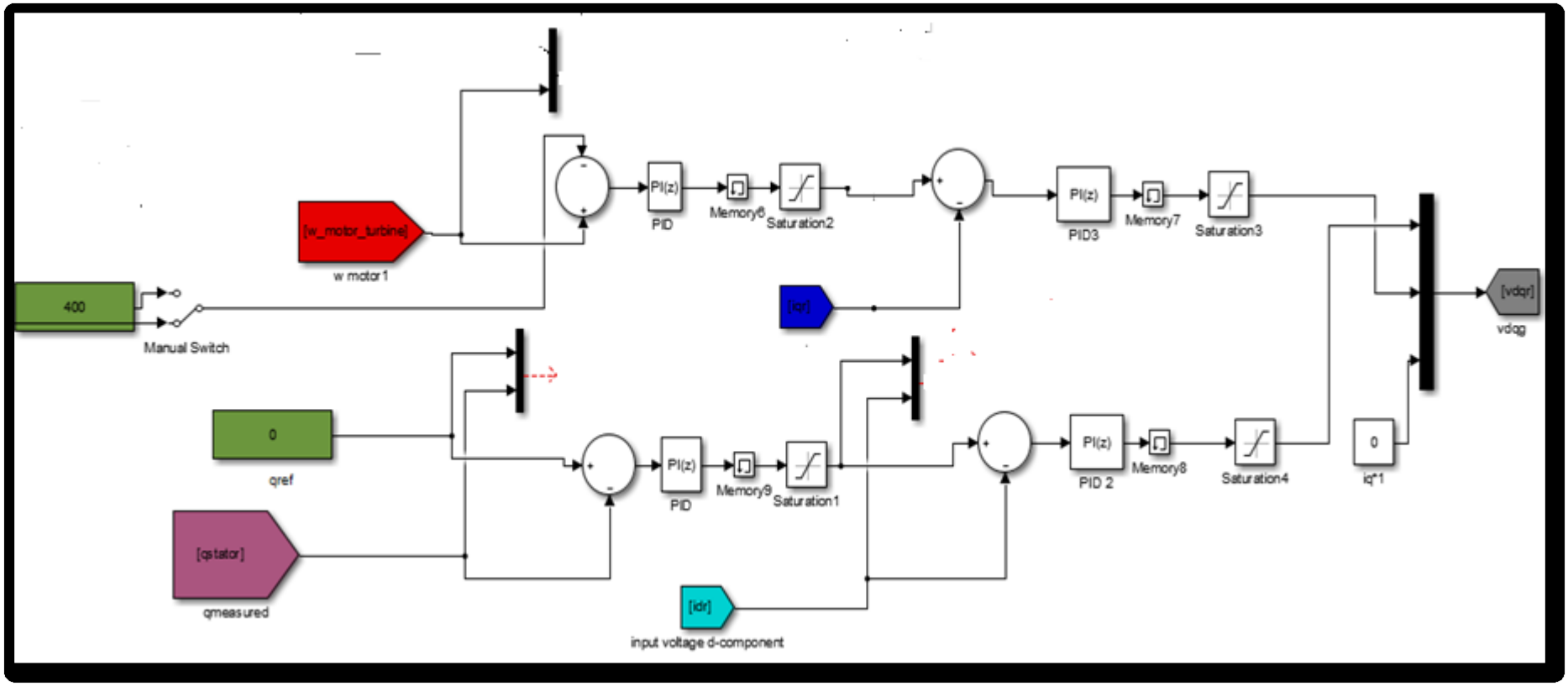

A.3 Perturb and Observe Control

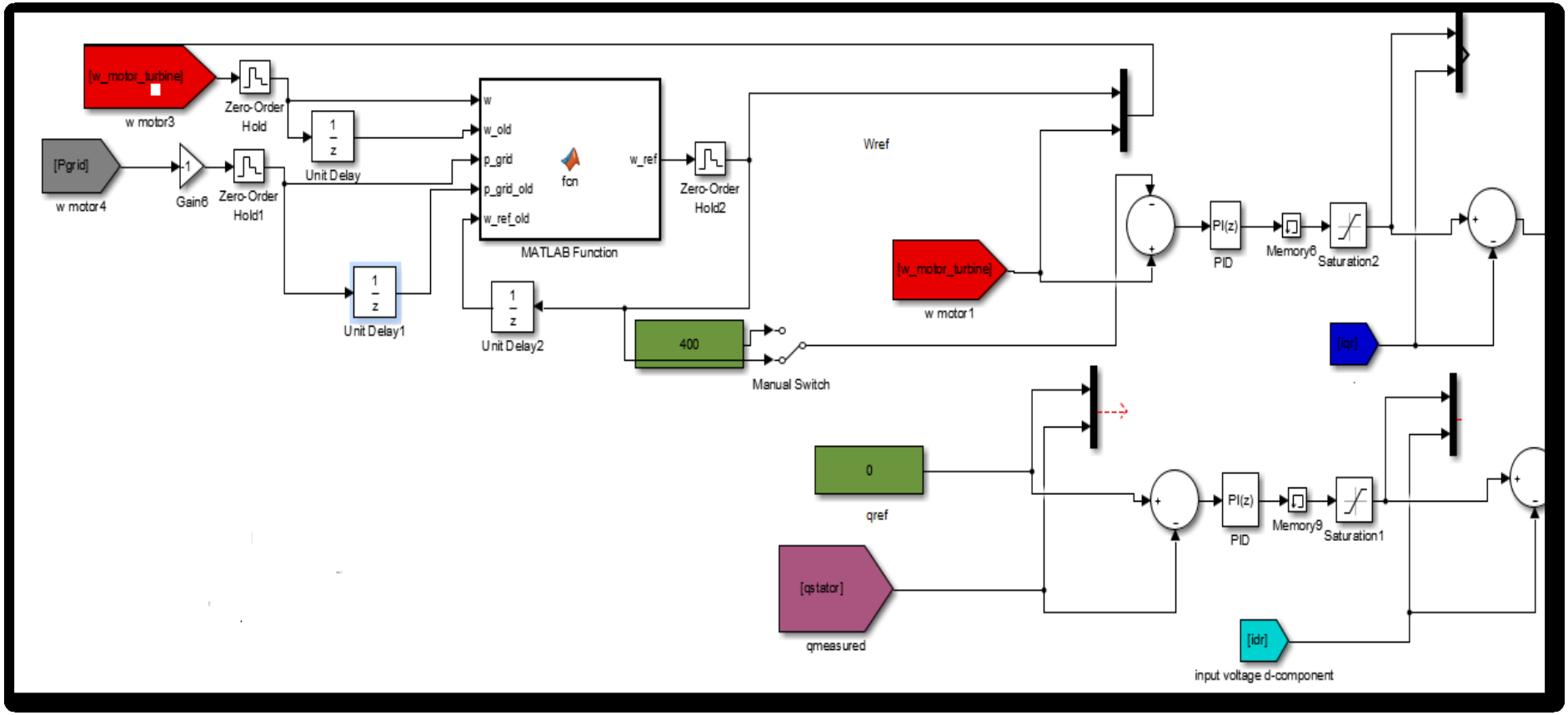

A.4 ANN Control for Stalling Prevention

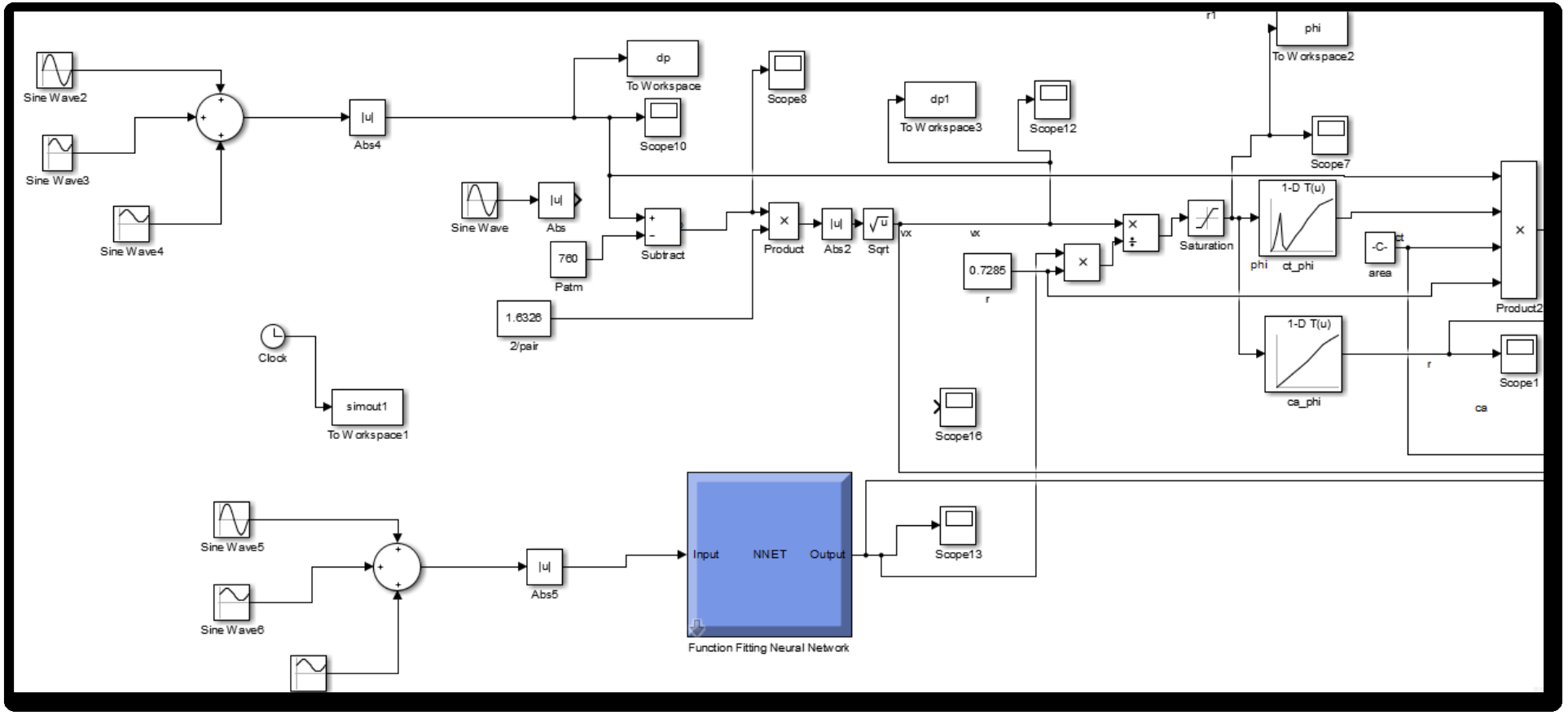

A.5 ANN for Dual Function

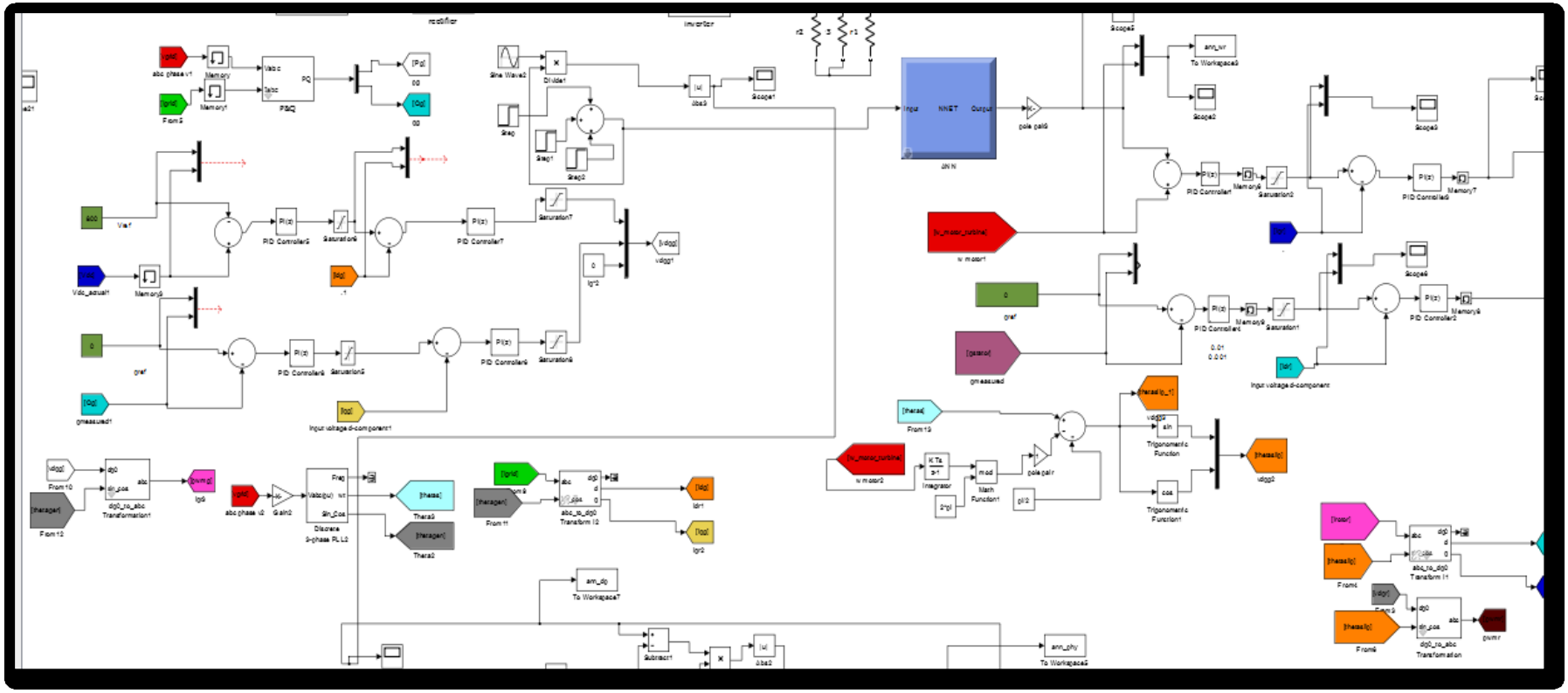

Appendix B- Publications

Stalling Phenomenon Prevention using Artificial Neural Network Based Strategy for Oscillation Water Column Coupled to Wells Turbine

Salwa M. Yousry[1,2],Ahmed K. Abdelsalam[1],Yasser G. Dessouky[1],Hadi M. El Helw[1] and Sarath B. Tennakoon[2]
[1]Electrical and Control Engineering Department, Arab Academy for Science and Technology Egypt
[2] Electrical and Electronic Department of Engineering, Staffordshire University UK
Email: Salwa.yousry@aast.edu, ahmed.kadry@aast.edu, ygd@aast.edu, h_elhelw@hotmail.com , S.B.Tennakoon@staffs.ac.uk

Keywords

≪Oscillating Water Column(*OWC*) ≫, ≪Wells Turbine≫, ≪Doubly Fed Induction Generator (*DFIG*)≫, ≪Decoupled control≫, ≪Stalling Phenomenon≫.

Abstract

In this paper, an Artificial Neural Network *ANN* based algorithm is proposed for energy conversion system adapting Oscillating Water Column *(OWC)* coupled to a Wells turbine. The presented algorithm integrates with the associated P-Q controlled grid connected Doubly Fed Induction Generator *(DFIG)* by calculating the optimized turbine speed that grantees stalling phenomenon avoidance.The proposed technique effectiveness has been attested by simulating various operation conditions featuring different input differential pressure levels. The presented technique offers simplified tuned algorithm in addition to fast transient response with minimal oscillation during steady state operation.

Introduction

Early twenty first century,with growing concerns over carbon emission and uncertainties in fossel fuel supplies, there is an increasing interest in clean and renewable energy sources [1, 2]. Renewable energy source has seen an enormous potential specially for ocean wave energy [3, 4]. Moreover, applicability and ted prutilization of wave energy conversion *(WEC)* technologies lead them to a significant penetration in the worldwide business electricity market [5].

WEC has economical, environmental, and technical advantages that differentiate it apart from other renewable energy sources. The capital cost of WEC technology is relatively low, and this will be likely decreased further as the industry expands[6]. The research in this paper is focused on a widely used type of WEC technology which is the Oscillating Water Column (*OWC*). OWC is the most common shoreline WEC sources used to transform the wave movement into a pneumatic energy [7, 8, 9]. This energy in turn is converted into mechanical energy by the use of Wells turbine [10, 11].

The OWC system coupled to Wells Turbine DFIG can be considered as a promising WEC techniques [12]. On the other hand, this type of turbines is predominantly sensitive to the airflow rate depending on the turbines rotational speed. The performance of Wells turbine is limited by the onset of stalling phenomenon on the turbine blades [13].

Thus, adequately matching DFIG speed to the available wave energy level increases turbine performance [5]. The advantage connecting DFIG to the power network is their ability to supply power at constant voltage and frequency, while the rotor speed varies and rotor converter handles fraction of stator power [14, 15].

Artificial Neural Network *(ANN)* has been widely applied in many science and engineering fields in recent years. The main advantages of the ANN are economy, fast computing, easy realization, and independence from physical model compared with the traditional methods such as experiment and numerical simulation [16].
Hence, the objective of the proposed study is to control DFIG speed by using ANN algorithm in order to avoid the undesired turbine blades stalling phenomena and convey a controlled desired level of the generated power.

OWC-Wells Turbine Model

The OWC effectively converts energy by transforming hydrodynamic wave action into reciprocating airflow. As shown in Fig.1, it consists of a capture chamber, partially submerged, which is open to the sea bellow the water line, as waves roll in from the ocean, the water column rises and falls, as a result the air pressure at the top of the column act accordingly [17]. Due the bidirectional nature of the airflow, a special turbine design called Wells turbine must be utilized in order to allow self-rectification. The OWC energy equations are similar to those used for wind turbines. In this way, the power available from the airflow in the OWC chamber may be expressed as (1).

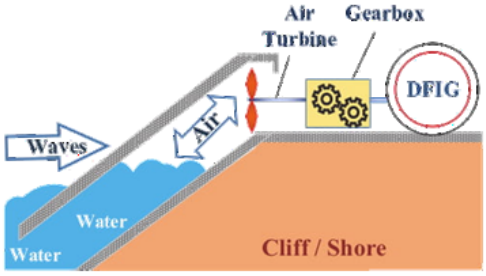

Fig. 1: System Under Investigation

$$p_{in} = \left(p + \frac{\rho \times V_x^2}{2}\right) \times V_x \times a \tag{1}$$

Where P_{in} is the power available to turbine in OWC duct, p is the pressure at the turbine duct, ρ is the air density, V_x is the airflow speed at the turbine and a is the area of turbine duct [18].

Wells Turbine Governing Equations

The Wells turbine is a particular axial-flow turbine that converts an oscillating flow into a unidirectional rotary motion for driving an electrical generator. However it presents the same uni-directional rotation both for positive and negative incident air pressure. The primary input for the design of a Wells turbine is the air power based upon the pressure amplitude and the volume flow rate at turbine inlet. The performance indicators are the pressure drop, power and efficiency, and their variation with the flow rate [19]. The equations used to model the turbine are given in [18, 20] and are described as follows:

$$dP = C_a.k.\left(\frac{1}{a}\right).\left[V_x^2 + (r.\omega_r)^2\right] \tag{2}$$

$$T_t = C_t.k.r\left[V_x^2 + (r.\omega_r)^2\right] \tag{3}$$

$$k = \rho.b.l.n/2 \tag{4}$$

where C_a, C_t are the power and torque coefficients shown in Fig.2(a) and Fig.2(b) repectively, r is the mean radius of the turbine, ω_r is the rotor angular velocity, and k is the turbine constant defined as [21]: with n the number of blades, b the blade height and l the blade chord length, so that the turbine torque

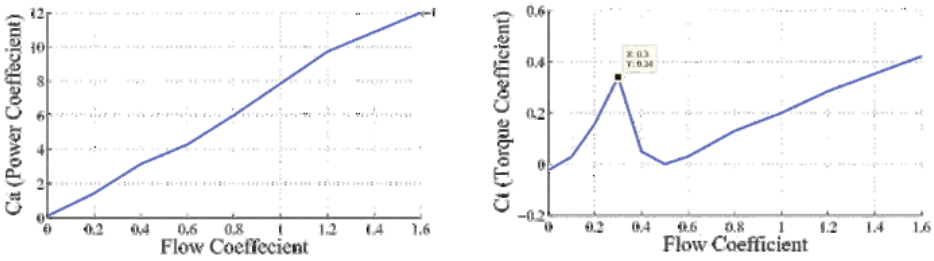

(a) Power Coefficient (C_a) Variation (b) Torque Coefficient (C_t) Variation

Fig. 2: Power and Torque Coefficients Variation versus Flow Coefficient.

can be expressed as [22, 8, 23]:

$$T_t = \frac{C_t.dP.a.r}{C_a} \tag{5}$$

The flow coefficient, ϕ, is usually defined as the non-dimensional quantity corresponding to the tangent of the angle of attack at the blade tip. The flow coefficient, the flow rate and turbine performance can be calculated as

$$\phi = V_x.(r.\omega_r)^{-1} \tag{6}$$

$$Q = V_x.a \tag{7}$$

$$\eta_t = \frac{T_t.\omega_r}{dP.Q} \tag{8}$$

The flow of turbine is directly proportional to the air flow velocity as given in (6). Thus, the increase in air flow velocity increases the flow coefficient which in turn increases the torque coefficient C_t until the value of flow coefficient reaches 0.3 [4, 24]. For flow coefficient higher than 0.3, the C_t value starts decreasing which leads to the known stalling phenomenon of Wells turbine [4, 17]. As a result, the performance of the Wells turbine is limited by the stalling phenomenon acting on the turbine blades. The undesired stalling behavior can be avoided or delayed if the turbine accelerates fast enough in response to the incoming airflow [12, 18, 25].

MATLAB / Simulink Model

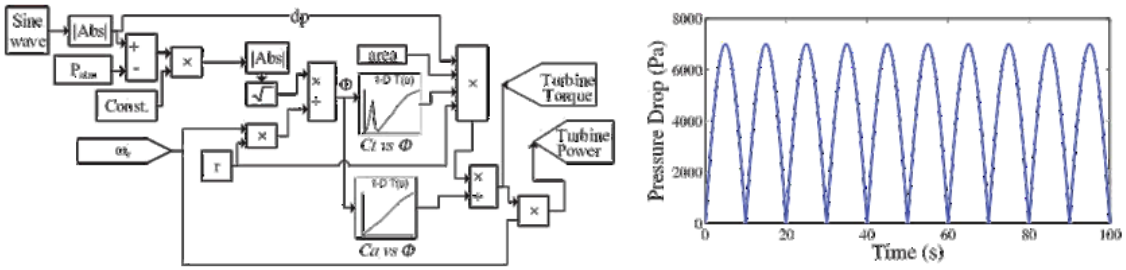

(a) Wells Turbine Model (b) OWC Diffrential Pressure Drop *dp*

Fig. 3: Wells Turbine MATLAB/SIMULINK Model

To drive the turbine model as shown in Fig.3(a), a pressure drop applied as input that takes into account the spectrum of the wave climate. So, it can be experimentally modelled as $|7000sin(0.1t)|Pa$ as shown in Fig.3(b) [4, 17].

Investigated Grid Connected Energy Conversion System

The investigated system incooperates a DFIG directly connected to the network through the stator, while the rotor is connected to the grid through a rotor side converter *RSC* and grid side converter *GSC* which is only required to handle a fraction (25% –30%) of the nominal power to achieve total control of the generator [26, 27].

DFIG modelling

The main advantage of the *d-q* dynamic model of the machine is that all the sinusoidal variables in the stationary frame appear as quantities referred to the synchronous rotating frame [12, 28, 15]. Hence, the equations for the generator are given by:
The stator and rotor *d-q* equations are [28, 29, 30]:

$$v_{qs} = R_s.i_{qs} + \frac{\partial}{\partial t}.\psi_{qs} + \omega_s.\psi_{ds} \tag{9}$$

$$v_{ds} = R_s.i_{ds} + \frac{\partial}{\partial t}.\psi_{ds} - \omega_s.\psi_{qs} \tag{10}$$

$$v_{qr} = R_r.i_{qr} + \frac{\partial}{\partial t}.\psi_{qr} + (\omega_s - \omega_e).\psi_{dr} \tag{11}$$

$$v_{dr} = R_r.i_{dr} + \frac{\partial}{\partial t}.\psi_{dr} - (\omega_s - \omega_e).\psi_{qr} \tag{12}$$

The flux linkage expressions in terms of the currents can be written as follows [12, 28]:

$$\psi_{qs} = L_s.i_{qs} + L_m.i_{qr} \tag{13}$$

$$\psi_{qr} = L_r.i_{qr} + L_m.i_{qs} \tag{14}$$

$$\psi_{ds} = L_s.i_{ds} + L_m.i_{dr} \tag{15}$$

$$\psi_{dr} = L_r.i_{dr} + L_m.i_{ds} \tag{16}$$

$$L_s = L_{ls} + L_m \tag{17}$$

$$L_r = L_{lr} + L_m \tag{18}$$

where ω_s is the stator supply frequency , ω_e is the rotor electrical speed $= \omega.(P/2)$ and T_e is the electromagnetic torque [28, 12]. Under stator- flux orientation *SFO*, in *d-q axis* component form, stator flux and electromagnetic torque equations are:

$$\psi_{ds} = L_s i_{ds} + L_m i_{dr} = \psi_s = L_m i_{ms} \tag{19}$$

$$\psi_{qs} = 0 \tag{20}$$

$$T_e = -\frac{3}{2}.p.L_0.i_{ms}.i_{qr} \tag{21}$$

Rotor Side Converter (RSC)

RSC circuit consist of two cascaded PI controlled loops. The inner current control loop independently adjust *d-axis* and *q-axis* rotor currents i_{dr} and i_{qr} respectively according to the reference values obtained by the outer loop and actual values measured by the main circuit. While the outer loop regulates reactive power. ANN algorithm is proposed to control the rotor speed in order to avoid the stalling phenomena, Fig.4(a) shows a simplified block diagram for the RSC controller.

Grid Side Converter (GSC)

The GSC circuit also consist of two cascaded PI controlled loops. Its inner current regulates independently the *d-axis* and *q-axis* stator currents i_{ds} and i_{qs} respectively according to the reference values

obtained by the outer loop. The outer control loop adjusts the desired DC-link voltage and regulate the reactive power exchanged between the GSC and the grid independently, Fig.4(b) shows a simplified block diagram for the GSC controller.

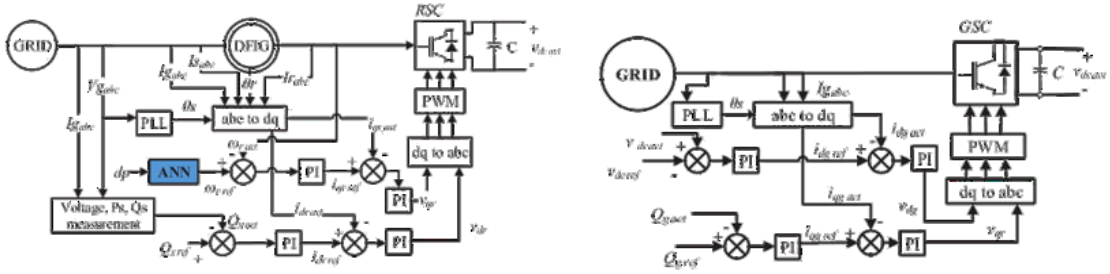

(a) RSC Control Block Diagram (b) GSC Control Block Diagram

Fig. 4: Proposed Decoupled DFIG Control

Proposed ANN Based Stalling Prevention Algorithm

Wells turbine performance always limited by the presence of the stalling phenomena on the turbine blades [27]. A proposed ANN based algorithm is presented in order to control the speed of the DFIG to accelerate the turbine to the limit that grantees the stalling phenomena avoidance.

ANN Structure

The proposed ANN configures a basic structure where three incorporates layers interconnected. The first layer consists of input neurons (input) that send data to the second layer (hidden layer), which in turn triggers the output neurons in the third layer (output). In this section the structure of the proposed ANN is given by Fig.5. The proposed ANN varies the reference turbine speed according with the differential input pressure in order to avoid the stalling phenomenon.

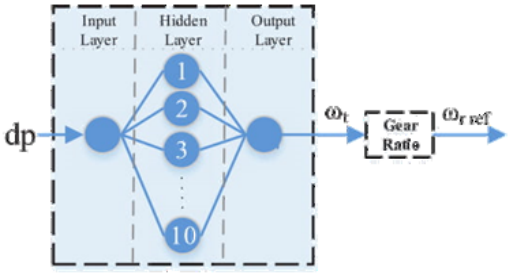

Fig. 5: Proposed ANN Structure

Training Algorithm

In this section, the process of collecting training data is discussed. As stated earlier, ANN is designed to estimate the speed corresponds to a certain pressure value in order to avoid stalling behaviour. To apply this, the block diagram shown in Fig.6 is designed. Since the stalling behaviour occurred during pressure values between 3700 Pa and 7000 Pa, the flow coefficient is adjusted to 0.2999 in order to obtain the optimum turbine speed curve. Eventually, two curves are shown in Fig.7 (pressure curve and speed curve) are stored as a 2D-matrix to fed to ANN for training phase. The curves are stored as instantaneous values with sampling time similar to the one considered in SIMULINK model. The sampling time considered is 1μs, therefore, there are $10e^6$ instantaneous point for each curve. The differential input pressure curve is fed to the ANN input layer, while the turbine speed reference curve used to ensure the avoidance of the stalling phenomenon is fed to the ANN output layer as shown in Fig.5. After all the training datasets loaded to respective layers, 10 hidden neurons is selected. The Neural Fitting Tool *nftool* in MATLAB

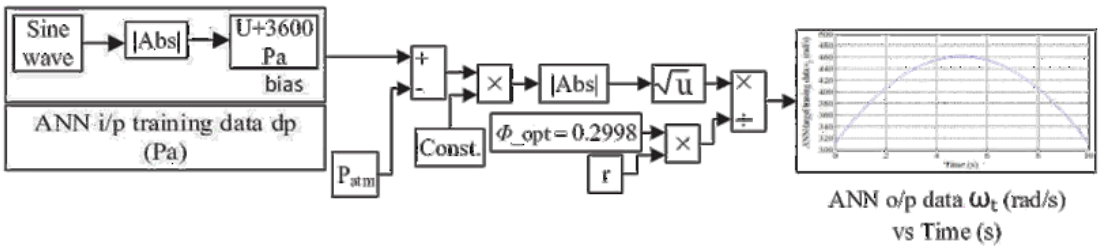

Fig. 6: Proposed ANN Training Data

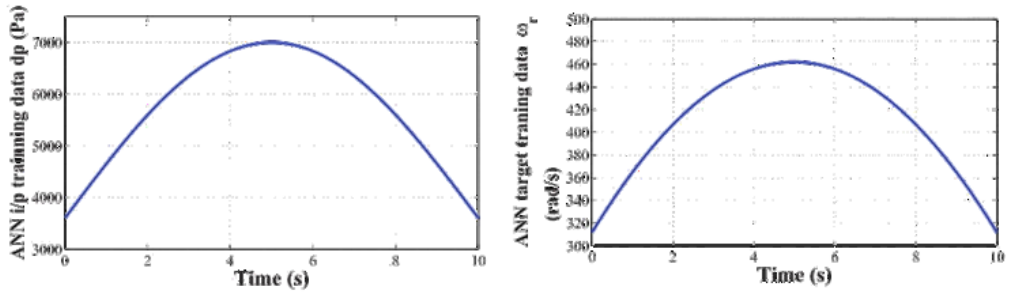

(a) Differential Input Pressure Curve (ANN input) (b) Turbine References Speed Curve (ANN target)

Fig. 7: ANN Input and Target Training Data

software package is utilized. This tool is usually used for estimation and prediction problems in which the neural network maps between a set of numeric inputs and corresponding set of numeric targets. The iteration algorithm used in this training is Levenberg-Marquardt. Moreover, the used training algorithm avoids the over fitting issues by stopping the training automatically when the generated results stop improving. During the training, the Regression factor R is important to be observed, which measures the correlation between the desired outputs and trained targets. The value of 1 means a close relationship, while 0 means a random relationship. The regression response of the trained ANN is shown in Fig.8. It can be noted that all the dataset inputs are exactly aligned to the fitting line and the values of R is close to 1.

Simulation Results

The investigated system parameters are listed in TableI

In the simulation section, two operating cases are investigated. The first case is uncontrolled operation while the second case is the operation under the proposed control technique. During each investigated case, various input differential pressure levels of 7000 Pa, 6000 Pa, and 4000 Pa respectively are implemented.

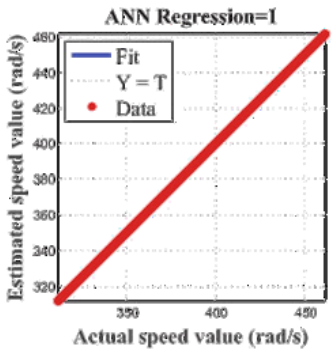

Fig. 8: Regression Response of the Trained ANN

Table I: DFIG, Grid and Wells Turbine Parameters

DFIG	Grid	Wells Turbine
P_{rated}=37kW	v_{line}= 400V	n= 8
v_{line}= 400V,f=50 Hz	f= 50Hz	b= 0.4m
p=number of poles=2		k= 0.7079Kg/m
R_r=0.08233Ω		a= 1.1763m^2
L_{lr} = 0.000724H		r= 0.7285m
R_s=0.0503Ω		
L_{ls}=0.000724H		
L_m=0.02711H		

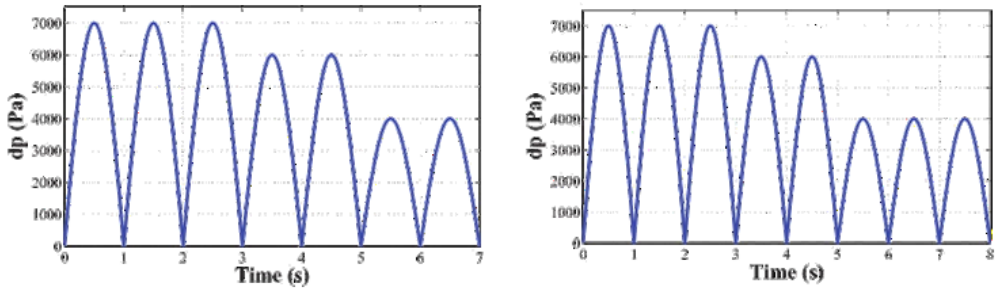

(a) Uncontrolled Input Differential Pressure (b) Controlled Input Differential Pressure

Fig. 9: Input Differential Pressure.

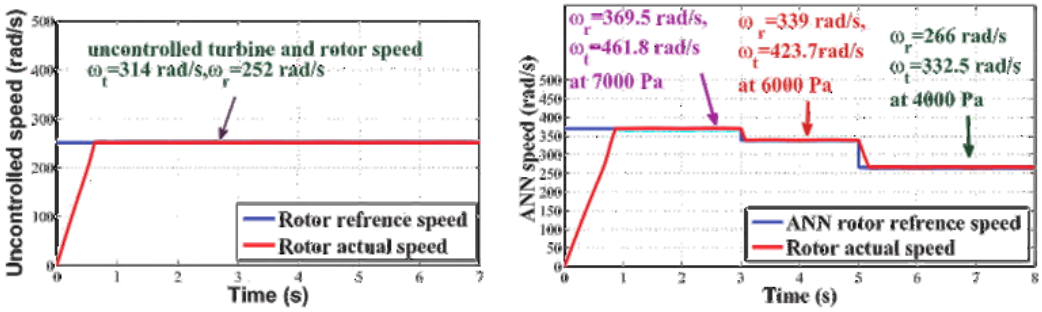

(a) Uncontrolled Turbine Speed (b) Controlled Turbine Speed

Fig. 10: Turbine Speed.

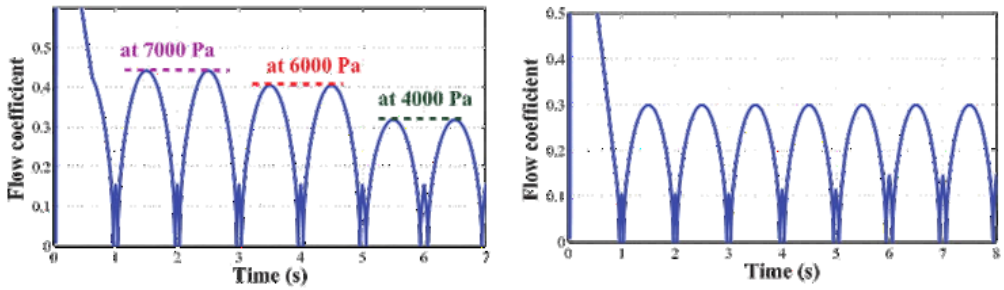

(a) Uncontrolled Flow Coefficient (b) Controlled Flow Coefficient

Fig. 11: Flow Coefficient.

Fig.9(a) shows the applied input differential pressure levels for both the uncontrolled and controlled cases. The turbine speed is constant despite of the input differential pressure level variation as shown

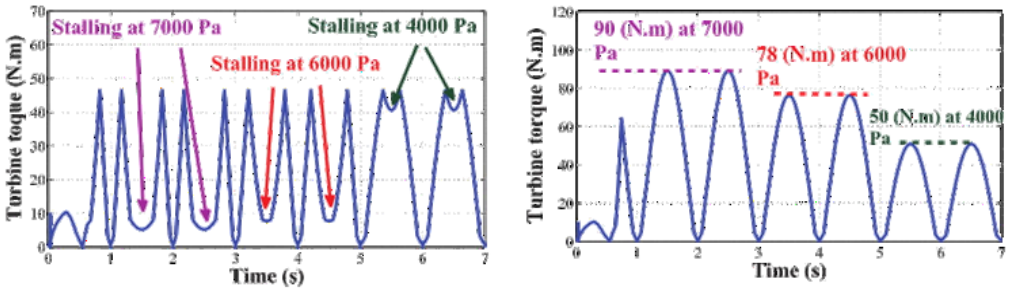

(a) Uncontrolled Turbine Torque (b) Controlled Turbine Torque

Fig. 12: Turbine Torque.

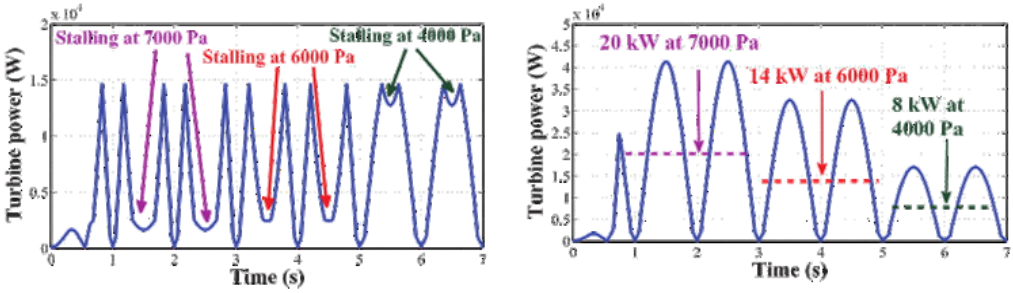

(a) Uncontrolled Turbine Power (b) Controlled Turbine Power

Fig. 13: Turbine Power.

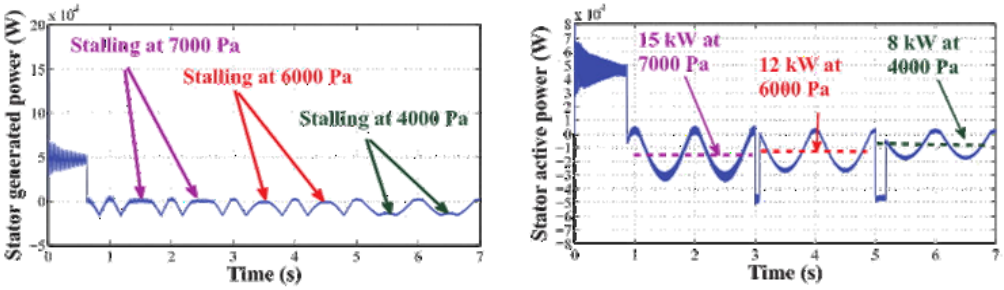

(a) Uncontrolled Stator Active Power (b) Controlled Stator Active Power

Fig. 14: Stator Active Power.

in Fig.10(a), while the proposed ANN based algorithm changes the turbine speed in order to avoid the stalling as clarified in Fig.10(b). The stalling phenomena occurrence under the uncontrolled case is shown in Fig.11(a) as the flow coefficient exceeds the 0.3 critical limit while under the proposed control algorithm, the stalling phenomenon prevention is verified by controlling the flow coefficient value below the 0.3 critical limit even under varying the input differential pressure levels as shown in Fig.11(b).
The stalling phenomenon occurrence/avoidance for uncontrolled/controlled case effect on the turbine torque and power is highly noticeable as turbine torque/power drop instant as clarified in Fig.12 and Fig.13 respectively.
Finally, the proposed technique effectiveness in stalling prevention succeeded in preserving adequate stator active power shown in Fig.14(b), compared to the poor performance of the uncontrolled case presented in Fig.14(a).

Conclusion

The presented paper proposed an ANN based algorithm for OWC energy conversion system stalling phenomenon prevention. The investigated system has been attested under various operating conditions

in terms of turbine speed and input pressure difference. It has been clarified that the proposed algorithm succeeded in attaining flow coefficient below the stalling critical value (0.3) at different input pressure difference and turbine speed. Consequently, the DFIG stator active power injected to grid is maximized for wide range of operation under the proposed algorithm.

References

[1] W. Qiao and R. G. Harley, "Grid connection requirements and solutions for dfig wind turbines," in *Energy 2030 Conference, 2008. ENERGY 2008. IEEE*. IEEE, 2008, pp. 1–8.

[2] J. H. Enslin, "The role of power electronics and storage to increase penetration levels of renewable power," in *Power and Energy Society General Meeting-Conversion and Delivery of Electrical Energy in the 21st Century, 2008 IEEE*. IEEE, 2008, pp. 1–2.

[3] P. Breeze, *Power generation technologies*. Newnes, 2014.

[4] S. K. Mishra, S. Purwar, and N. Kishor, "Air flow control of owc wave power plants using fopid controller," in *2015 IEEE Conference on Control Applications (CCA)*, Sept 2015, pp. 1516–1521.

[5] P. F. do Vale Mateus, "Conception of a didactic module for teaching renewable energies–wave energy."

[6] global status report 2014 - renewable energyl. [Online]. Available: http://www.ren21.net/Portals/0/documents/Resources/GSR/2014/GSR2014_full%20report_low%20res.pdf

[7] B. Czech and P. Bauer, "Wave energy converter concepts : Design challenges and classification," *IEEE Industrial Electronics Magazine*, vol. 6, no. 2, pp. 4–16, June 2012.

[8] M. Alberdi, M. Amundarain, A. J. Garrido, I. Garrido, and F. J. Maseda, "Fault-ride-through capability of oscillating-water-column-based wave-power-generation plants equipped with doubly fed induction generator and airflow control," *IEEE Transactions on Industrial Electronics*, vol. 58, no. 5, pp. 1501–1517, May 2011.

[9] I. Garrido, A. J. Garrido, J. Lekube, E. Otaola, and E. Carrascal, "Oscillating water column control and monitoring," in *OCEANS 2016 MTS/IEEE Monterey*. IEEE, 2016, pp. 1–6.

[10] V. Jayashankar, K. Udayakumar, B. Karthikeyan, K. Manivannan, N. Venkatraman, and S. Rangaprasad, "Maximizing power output from a wave energy plant," in *Power Engineering Society Winter Meeting, 2000. IEEE*, vol. 3. IEEE, 2000, pp. 1796–1801.

[11] W. Tease, J. Lees, and A. Hall, "Advances in oscillating water column air turbine development," in *Proc. of the Seventh European Wave and Tidal Energy Conference, Porto, Portugal*, 2007.

[12] M. Amundarain, M. Alberdi, A. J. Garrido, and I. Garrido, "Modeling and simulation of wave energy generation plants: Output power control," *IEEE Transactions on Industrial Electronics*, vol. 58, no. 1, pp. 105–117, Jan 2011.

[13] M. Alberdi, M. Amundarain, F. Maseda, and O. Barambones, "Stalling behaviour improvement by appropriately choosing the rotor resistance value in wave power generation plants," in *Clean Electrical Power, 2009 International Conference on*. IEEE, 2009, pp. 64–67.

[14] N. Telu and R. Telu, "Design, simulation and control of doubly fed induction generator," *International Journal of engineering research and Applications (IJERA)*, vol. 2, no. 3, pp. 634–639, 2012.

[15] A. K. Abdelsalam, M. I. Masoud, M. S. Hamad, and B. W. Williams, "Modified indirect vector control technique for current-source induction motor drive," *IEEE Transactions on Industry Applications*, vol. 48, no. 6, pp. 2433–2442, 2012.

[16] M. A. Ormaza, M. A. Goitia, A. G. Hernández, and I. G. Hernández, "Neural control of the wells turbine-generator module," in *Decision and Control, 2009 held jointly with the 2009 28th Chinese Control Conference. CDC/CCC 2009. Proceedings of the 48th IEEE Conference on*. IEEE, 2009, pp. 7315–7320.

[17] J. Duquette, D. OSullivan, S. Ceballos, and R. Alcorn, "Design and construction of an experimental wave energy device emulator test rig," in *Proceedings of European wave and tidal energy conference*, 2009.

[18] M. Alberdi, M. Amundarain, A. Garrido, and I. Garrido, "Ride through of owc-based wave power generation plant with air flow control under symmetrical voltage dips," in *Control Automation (MED), 2010 18th Mediterranean Conference on*, June 2010, pp. 1271–1277.

[19] S. L. Dixon and C. Hall, *Fluid mechanics and thermodynamics of turbomachinery*. Butterworth-Heinemann, 2013.

[20] S. Muthukumar, R. Desai, V. Jayashankar, S. Santhakumar, and T. Setoguchi, *ISOPE-I-05-077*. International Society of Offshore and Polar Engineers, ch. Design of a Stand-alone Wave Energy Plant.

[21] I. Garrido, A. J. Garrido, M. Alberdi, M. Amundarain, and M. de la Sen, "Sensor control for an oscillating water column plant," in *2013 World Congress on Sustainable Technologies (WCST)*, Dec 2013, pp. 29–34.

[22] A. J. Garrido, M. Alberdi, I. Garrido, and M. Amundarain, "Control of oscillating water column (owc) wave energy plants."

[23] H. Bouhrim and A. E. Marjani, "On numerical modeling in owc systems for wave energy conversion," in *2014 International Renewable and Sustainable Energy Conference (IRSEC)*, Oct 2014, pp. 431–435.

[24] J. Lekube, A. J. Garrido, and I. Garrido, "Rotational speed optimization in oscillating water column wave power plants based on maximum power point tracking," *IEEE Transactions on Automation Science and Engineering*, vol. 14, no. 2, pp. 681–691, 2017.

[25] I. Garrido, A. J. Garrido, M. Alberdi, M. Amundarain, and O. Barambones, "Performance of an ocean energy conversion system with dfig sensorless control," *Mathematical Problems in Engineering*, vol. 2013, 2013.

[26] A. J. Netto, P. R. Barros, C. B. Jacobina, A. M. N. Lima, and E. R. C. da Silva, "Indirect field-oriented control of an induction motor by using closed-loop identification," in *Fourtieth IAS Annual Meeting. Conference Record of the 2005 Industry Applications Conference, 2005.*, vol. 2, Oct 2005, pp. 1357–1362 Vol. 2.

[27] W. Qiao, "Dynamic modeling and control of doubly fed induction generators driven by wind turbines," in *2009 IEEE/PES Power Systems Conference and Exposition*, March 2009, pp. 1–8.

[28] B. Bose, *Modern power electronics and AC drives*. Upper Saddle River, NJ: Prentice Hall, 2002.

[29] M. I. Abdelkader, A. K. Abdelsalam, and A. A. Hossam, "Asynchronous grid interconnection using brushless doubly fed induction machines: Assessment on various configurations," in *Power Electronics and Motion Control Conference and Exposition (PEMC), 2014 16th International*, Sept 2014, pp. 406–412.

[30] M. I. Abdelkader, A. K. Abdelsalam, and A. A. H. Eldin, "Vector controlled brushless doubly fed twin stator cascaded induction generator for variable speed wind generation connected to weak grids," in *Power Electronics and Applications (EPE'15 ECCE-Europe), 2015 17th European Conference on*. IEEE, 2015, pp. 1–12.

Decoupled Control Strategy for Oscillating Water Column Wave Energy System based on Doubly-Fed Induction Generator

Salwa M. Yousry[1,2], Ahmed K. Abdelsalam[1], Yasser G. Dessouky[1], Hadi M. El Helw[1], Sarath Tennakoon[2]
[1]Electrical and Control Engineering Department, Arab Academy for Science and Technology, Egypt
[2] Electrical and Electronic Department of Engineering, Staffordshire University, UK
Salwa.yousry@aast.edu, ahmed.kadry@aast.edu, ygd@aast.edu, h_elhelw@hotmail.com, S.B.Tennakoon@staffs.ac.uk

***Abstract*—A decoupled active-reactive power control technique is proposed for an oscillating water column (*OWC*) based wave energy conversion system adopting grid connected doubly fed induction generator (*DFIG*). The effectiveness of the technique is investigated under various rotor speed and reactive power reference commands. The results show enhanced performance, better tracking, and improved transient response.**

I. Introduction

In the recent decades, researches have been motivated and focused on renewable energy resources [1]. One of the most promising renewable energy resources is the the ocean waves energy [1]. The Wave Energy Conversion technology *(WEC)* is the most common technology among the ocean based energy sources[2]. Moreover, WEC technology converts wave energy into mechanical energy, then uses a pickup power system to generate electricity. The power pick-up system is usually a turbine that is driven by pressurized oil, air, or water [3]. The research in this paper is focused on a widely used type of WEC technology which is the OWC as it is the most common shoreline WEC sources used to transform the wave movement into a pneumatic energy [2]. This energy in-turn is converted into a mechanical energy by the use of Wells Turbine driving an induction generator [4]. Furthermore, this digest focuses on the usage of DFIG in order to allow variable rotor speed operation, as DFIG is a cost effective, efficient and reliable technology. Modified vector control is adapted for DFIG to achieve decoupled active - reactive power control [5, 6]. A simplified diagram of the investigated system is presented in Fig. 1.

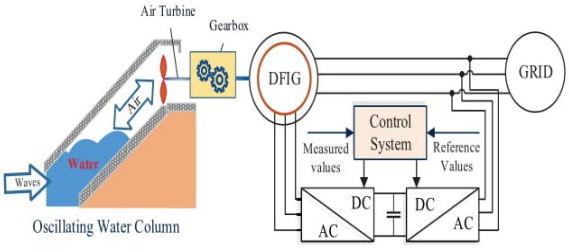

Fig. 1. Grid connected Oscillating Water Column (*OWC*) wave energy system

Following the introduction, OWC mathematical modelling is explained in section II, while section III illustrates the DFIG *d-q* modelling in the stationary reference frame. The proposed DFIG decoupled control is clarified in section IV, with the simulation result for two different cases are discussed in section V. Finally, a conclusion is given in section VI.

II. OWC Mathematical Modelling

A. OWC Operational Explanation

As shown in Fig. 1, the principal component of an OWC is the capture chamber, which is composed of a fixed structure with its bottom open to the sea. The wave motion inside the chamber alternately compresses and decompresses the air above the water level inside the chamber. A conical duct is erected on the top of the chamber with the power take off system, consisting of the turbine and the generator, located within this duct [7, 8].

$$p_{in} = \left(p + \frac{\rho.V_x^2}{2}\right).V_x.a \tag{1}$$

Where P_{in} is the power available to turbine in OWC duct, p is the pressure at the turbine duct, ρ is the air density, $V_x$is the airflow speed at the turbine and a is the area of turbine duct [8, 9].

B. Wells Turbine Modelling

The Wells Turbine is an axial-flow turbine that converts an oscillating flow into a unidirectional rotary motion for driving an electrical generator. Hence, it always rotates in the same direction; both for inbound and outbound air flow [10, 11].The input of the Wells Turbine is the oscillating pressure drop across the turbine rotor which is induced from the air flow off the OWC chamber. The main outputs of the turbine are the torque and the mechanical power. The equations used to model the turbine are described as follows [10, 11]:

$$dP = C_a.k.\left(\frac{1}{a}\right).\left[V_x^2 + (r.\omega_r)^2\right] \tag{2}$$

$$T_t = C_t.k.r\left[V_x^2 + (r.\omega_r)^2\right] \tag{3}$$

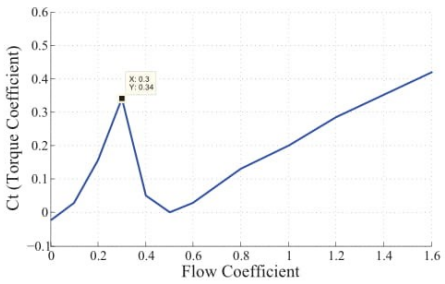

(a) Torque coefficient (C_t) variation

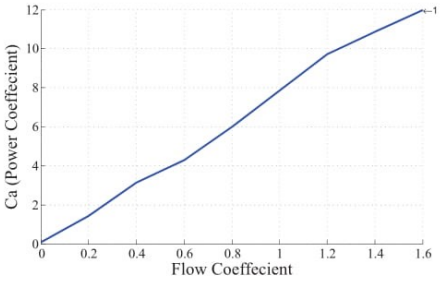

(b) Power coefficient (C_a) variation

Fig. 2. Torque and power coefficients versus flow coefficient.

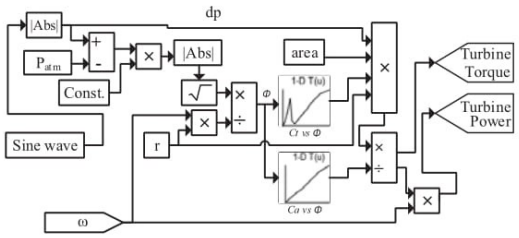

Fig. 3. Wells Turbine Matlab/SIMULINK model

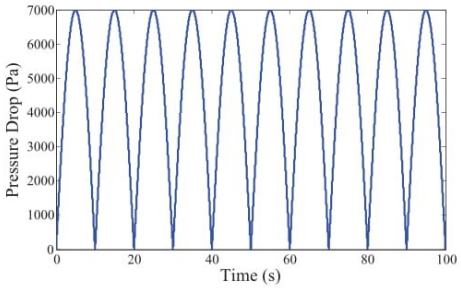

Fig. 4. OWC diffrential pressure

where C_t and C_a are the torque and power coefficients as shown in Fig. 2, where r is the mean radius of the turbine and ω_r is the rotor angular velocity. The subscripts r and s in the following equations indicate rotor and stator sides respectively. The constant k is the turbine constant ; defined as [12]:

$$k = \rho.b.l.n/2 \tag{4}$$

with n is the number of blades , b is the blade height and l is the blade chord length. Hence, the turbine torque and efficiency can be deduced as

$$T_t = \frac{C_t.dP.a.r}{C_a} \tag{5}$$

$$\eta_t = \frac{T_t.\omega_r}{dP.Q} \tag{6}$$

The flow coefficient,ϕ, is usually defined as a non-dimensional quantity corresponding to the tangent of the angle of attack at the blade tip. The flow coefficient and flow rate equations are:

$$\phi = V_x.\left(r.\omega_r\right)^{-1} \tag{7}$$

$$Q = V_x.a \tag{8}$$

The performance of the Wells Turbine is limited by the stalling phenomenon on the turbine blades. The undesired stalling behaviour can be avoided or delayed if the turbine accelerates fast enough in response to the incoming airflow. Turbo-generator equation can be expressed as follows: [13]

$$J\left(\frac{\partial\omega_e}{\partial t}\right) = g_b.T_t - T_e \tag{9}$$

where J is the moment of inertia of the system (in $kg.m^2$) ,ω_e is the electrical rotor speed , $T_t$is the torque produced by the turbine (N.m), T_e is the induction generator electromagnetic torque (N.m) and g_b is the gear box ratio. The Wells Turbine Matlab/SIMULINK modelling can be graphically expressed as shown in Fig. 3 The numerical simulation of the Wells Turbine model was carried on using the parameters listed in Table I [20]. To drive the turbine model, a pressure drop is applied as input to the Wells Turbine taking into account the spectrum of the wave climate. It can be experimentally modeled as $dP = |7000sin(0.1\pi t)|$ Pa as shown in Fig. 4 [2].

III. DFIG Modelling

The DFIG offers adequate performance and is sufficient for a wide speed range required to exploit typical wave energy resources. An AC-DC-AC converter is included in the DFIG rotor circuit. The two power electronic converters need only be to rated to handle a fraction of the total power, typically about 30% of the nominal generator power. Therefore, the losses in the power electronic converter can be reduced, compared to a system where the converter has to handle the entire power, as in the case of full converter driving permanent magnet synchronous generator. The system overall cost is lower due to the partially rated power electronics [14].Fig. 5(a) and Fig. 5(b) show the *d-q* dynamic model equivalent circuits respectively. The main advantage of the *d-q* dynamic model of the machine is that all the sinusoidal variables in the stationary frame appear as dc quantities when referred to the synchronous rotating reference frame [15, 16]. Hence, the equations for the DFIG are given by

The stator voltage *d-q* equations are:

$$v_{qs} = R_s.i_{qs} + \frac{\partial}{\partial t}.\psi_{qs} + \omega_s.\psi_{ds} \tag{10}$$

$$v_{ds} = R_s.i_{ds} + \frac{\partial}{\partial t}.\psi_{ds} - \omega_s.\psi_{qs} \tag{11}$$

While the rotor voltage *d-q* equation can be expressed as:

$$v_{qr} = R_r.i_{qr} + \frac{\partial}{\partial t}.\psi_{qr} + \left(\omega_s - \omega_e\right).\psi_{dr} \tag{12}$$

$$v_{dr} = R_r.i_{dr} + \frac{\partial}{\partial t}.\psi_{dr} - \left(\omega_s - \omega_e\right).\psi_{qr} \tag{13}$$

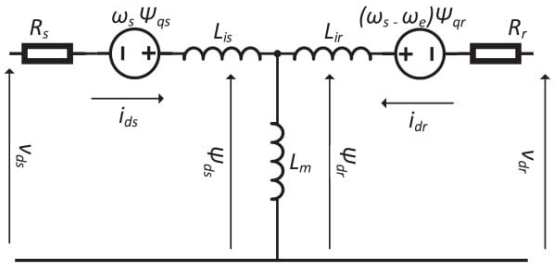

(a) d-axis circuit.

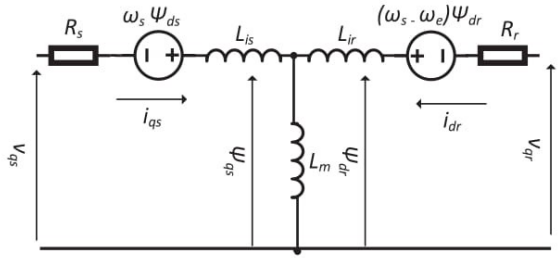

(b) q-axis circuit

Fig. 5. Dynamic $d-q$ equivalent circuits for DFIG.

Hence, the DFIG electromagnetic torque is calculated:

$$T_e = \frac{3}{2}.\left(\frac{p}{2}\right).(\psi_{ds}.i_{qs} - \psi_{qs}.i_{ds}) \quad (14)$$

and the flux linkage expressions in terms of the currents can be written as follows:
for the quadrature flux axis components

$$\psi_{qs} = L_s.i_{qs} + L_m.i_{qr} \quad (15)$$

$$\psi_{qr} = L_r.i_{qr} + L_m.i_{qs} \quad (16)$$

for the direct flux axis components

$$\psi_{ds} = L_s.i_{ds} + L_m.i_{dr} \quad (17)$$

$$\psi_{dr} = L_r.i_{dr} + L_m.i_{ds} \quad (18)$$

Where the stator and rotor self inductances are:

$$L_s = L_{ls} + L_m \quad (19)$$

$$L_r = L_{lr} + L_m \quad (20)$$

ω_s is the stator supply frequency , ω_e is the rotor electrical speed $= \omega_r.(P/2)$ and T_e is the electromagnetic torque [17] Under stator- flux orientation *(SFO)*, in *d-q* axis component form, the stator flux equations are[18–20]:

$$\psi_{qr} = L_r.i_{qr} + L_m.i_{qs} \quad (21)$$

$$\psi_{qs} = 0 \quad (22)$$

Defining leakage factor $\sigma = 1 - \frac{L_m^2}{L_s.L_r}$ and the equivalent inductance as $L_0 = \frac{L_m^2}{L_r}$. The rotor voltage and flux equations are (scaled to be numerically equal to the ac per-phase values):

$$v_{dr} = R_r.i_{dr} + \sigma.L_r.\frac{\partial i_{dr}}{\partial t} - \omega_{slip}.\sigma.L_r.i_{qr} \quad (23)$$

$$v_{qr} = R_r.i_{qr} + \sigma.L_r.\frac{\partial i_{qr}}{\partial t} - \omega_{slip}.(L_0.i_{ms} + \sigma.L_r.i_{dr}) \quad (24)$$

$$\psi_{dr} = \frac{L_m^2}{L_s}.i_{ms} + \sigma.L_r.i_{dr} \quad (25)$$

$$\psi_{qr} = \sigma.L_r.i_{qr} \quad (26)$$

Where the slip angular speed is $\omega_{slip} = \omega_s - \omega_e$. The flux angle is calculated from:

$$\psi_{\alpha s} = \int (v_{\alpha s} - R_s i_{\alpha s})\, dt \quad (27)$$

$$\psi_{\beta s} = \int (v_{\beta s} - R_s i_{\beta s})\, dt \quad (28)$$

$$\theta_s = tan^{-1}.\left(\frac{\psi_{\beta s}}{\psi_{\alpha s}}\right) \quad (29)$$

Where θ_s is the stator-flux vector position. From the rotor voltage equations (23,24) define:

$$v_{dr}^{'} = R_r.i_{dr} + \sigma.L_r.\left(\frac{\partial i_{dr}}{\partial t}\right) \quad (30)$$

$$v_{qr}^{'} = R_r.i_{qr} + \sigma.L_r.\left(\frac{\partial i_{qr}}{\partial t}\right) \quad (31)$$

To ensure better tracking of the *dq-axis* rotor currents, compensation terms are added to $v_{dr}^{'}$ and $v_{qr}^{'}$ to obtain the reference voltages v_{dr}^{*} and v_{qr}^{*} according to:

$$v_{dr}^{*} = v_{dr}^{'} - \omega_{slip}.\sigma.L_r.i_{qr} \quad (32)$$

$$v_{qr}^{*} = v_{qr}^{'} + \omega_{slip}.(L_m.i_{ms} + \sigma.L_r.i_{dr}) \quad (33)$$

The electromagnetic torque is :

$$T_e = -\frac{3}{2}.p.L_0.i_{ms}.i_{qr} \quad (34)$$

As seen the torque can be controlled by the q-axis component of the rotor current i_{qr}. Therefore, the q-axis reference current i_{qrref}

$$i_{qrref} = -\frac{2.T_e^{ref}}{3.p.L_0.i_{ms}} = -\frac{2.T_e^{ref}}{3.p.\psi_s} \quad (35)$$

IV. DFIG Decoupled Control Strategy

The control scheme is shown in Fig. 6,where Fig. 6(a) illustrates the decoupled vector control of the rotor side converter *RSC* in order to achieve independent control of the stator active power P_s (by means of speed control) and the reactive power control by means of rotor current regulation.while Fig. 6(b)illustrates the dc-link voltage and the grid reactive power control using the grid side converter *GSC*.

A. RSC Control

In order to obtain the actual values of the *d-q* rotor current components; i_{dract} and i_{qract} ,the instantaneous three phase rotor currents I_{rabc} are transformed to *d-q* components by using the slip angle θ_{slip} (i.e difference angle between grid and rotor frames in the SFO). Moreover, the reference values of *d-axis* rotor current i_{drref}, and *q-axis* rotor current i_{qrref} can be

determined directly from the stator reactive power Q_{sref} and controlled speed ω_{ref} commands. The actual rotor currents i_{dract} and i_{qract} are compared to the reference rotor currents i_{drref}, and i_{qrref} in order to feedback them to the associated PI controllers to generate the inverter Pulse Width Modulation (*PWM*)signal.

B. GSC Control

Similarly, the rectifier decoupled control technique adjusts the dc-link voltage to 800 V and maintain the rectifier reactive power to zero, hence the reference values of *d-axis* grid current i_{dgref}, and *q-axis* grid current i_{qgref} can be determined directly from the reference dc-link voltage v_{dcref} and grid reactive power Q_{gref} commands.The actual rectifier currents i_{dgact} and i_{qgact} are compared to the reference currents i_{dgref}, and i_{qgref} in order to feedback them to the PI controllers to generate the required PWM signals to control the rectifier.

V. SIMULATION RESULTS

A. System Under Investigation

The investigated system parameters depends on illustrated Wells Turbine, DFIG and grid parameters are listed in Table I.

In order to clarify the proposed technique effectiveness,two case studies have been carried out in this paper: case I and case II respectively.The two investigated cases are used to illustrate the offered decoupled control performance regarding the generator speed and grid reactive power.

TABLE I
DFIG, GRID & WELLS TURBINE PARAMETERS

DFIG	Grid	Wells Turbine
P_{rated}=37kW	Line voltage= 400V	n= 8
Line voltage= 400V	f= 50Hz	b= 0.4m
f=50 Hz		k= 0.7079Kg/m
p=number of poles=2		a= 1.1763m^2
R_r=0.08233Ω		r= 0.7285m
L_{lr} = 0.000724H		
R_s=0.0503Ω		
L_{ls}=0.000724H		
L_m=0.02711H		

B. Case I:Constant rotor speed and variable stator reactive power

In this system, the proposed technique is examined at constant rotor speed of 380 rad/s while the DFIG stator reactive power varies during the simulation interval.

It can be shown in Fig. 7(a)that the speed attains its reference value in a time of 1 s with a good tracking performance. This can be reflected from the *q-axis* rotor current reference and actual mapping for decoupling control illustration shown in Fig. 7(b). The reactive power have been changed from 0 to -10 KVAr(lag) to 10 KVAr(lead) at times 4 s and 7 s respectively. As seen in Fig. 8(a),it can be illustrated that the system achieves the required reference reactive power for RSC as the *d-axis* current tracks its reference as seen in Fig. 8(b). Regarding the GSC, the dc-link voltage converges to the 800

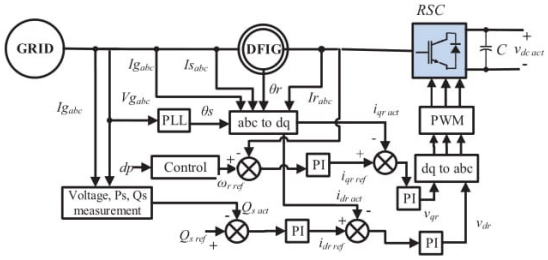

(a) (RSC) control.

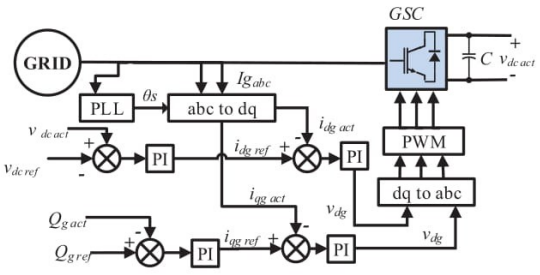

(b) (GSC) control.

Fig. 6. Decoupled DFIG control

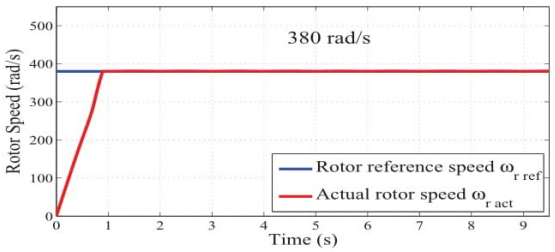

(a) Rotor speed

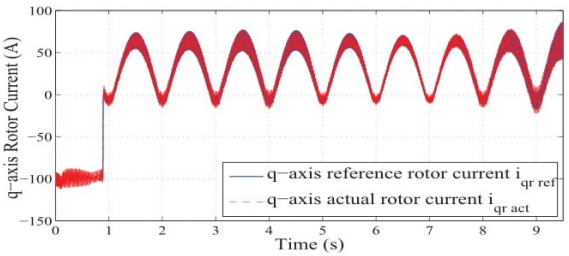

(b) *q-axis* rotor current

Fig. 7. Rotor speed and *q-axis* rotor current

V reference in a time less than 1 s and stick to the reference even under the changes of the reactive power as shown in Fig. 9(a). Moreover the voltage source rectifier is adjusted to a reference of zero reactive power drawn from the grid as shown in Fig. 9(b). The air pressure is represented by a pulsating wave, illustrated in Fig. 4,hence the turbine torque and active power are illustrated in Fig. 10 as a pulsating signals. Under the proposed decoupled control for constant rotor speed, the power injected to the grid(stator active power)is shown in Fig. 11with an average of 15 KW.

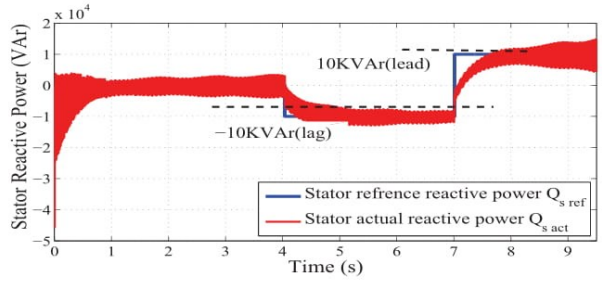

(a) Stator reactive power

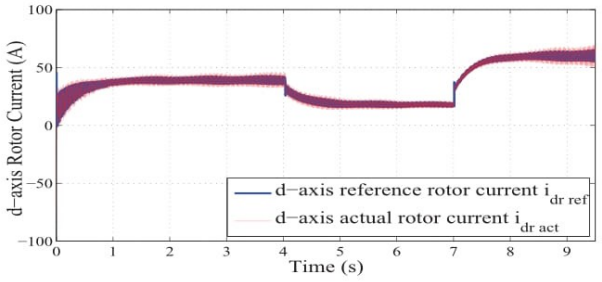

(b) *d*-axis rotor current

Fig. 8. Stator reactive power and *d-axis* rotor current

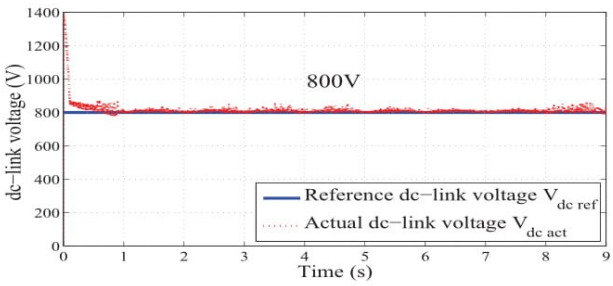

(a) dc-link voltage

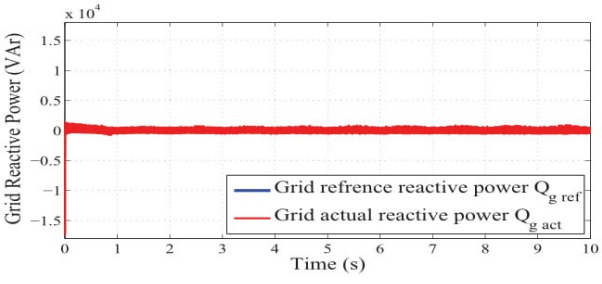

(b) Grid reactive power

Fig. 9. dc-link voltage and grid reactive power.

C. Case II:Variable rotor speed and constant stator reactive power

In this case, the proposed decoupled control is investigated with a reference of zero reactive power injected to the grid from the stator side of the DFIG while the rotor speed have been increased from 380 rad/s to 420 rad/s.

It can be shown in Fig. 12(a)that the speed attains its reference values 380 rad/s and 420 rad/s at 0.9 s and 3.2 s respectively with a good tracking performance. This can be reflected from the *q-axis* rotor current reference and actual mapping for perfect decoupling control as illustrated in Fig. 12(b).In addition, the reactive power has been coherent to zero

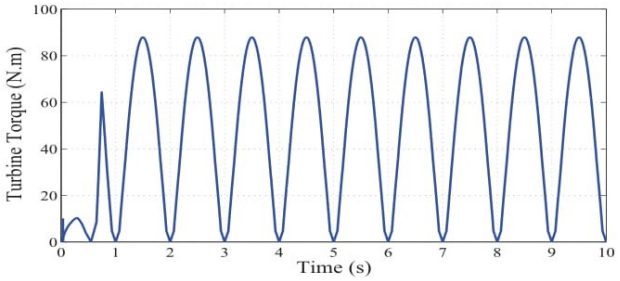

(a) Turbine torque

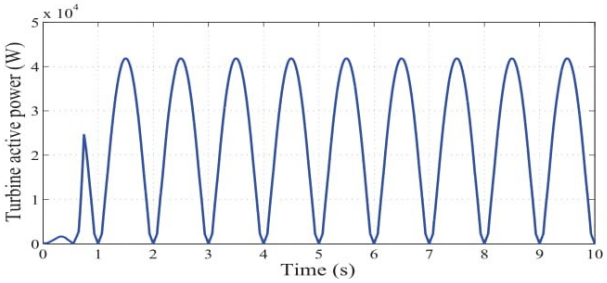

(b) Turbine active power

Fig. 10. Turbine generated torque and active power.

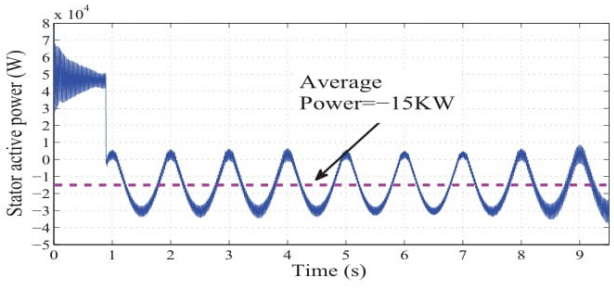

Fig. 11. DFIG stator active power

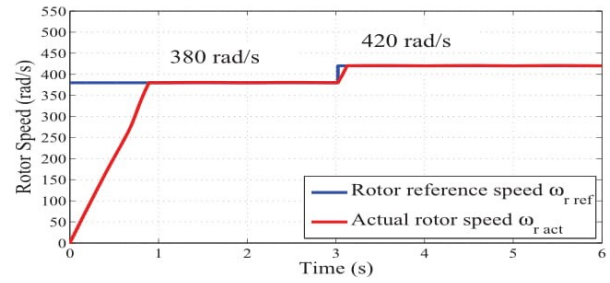

(a) Rotor Speed

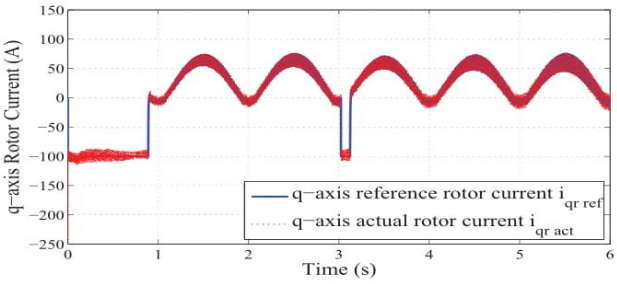

(b) *q*-axis rotor current

Fig. 12. Controlled rotor speed and *q*-axis rotor current

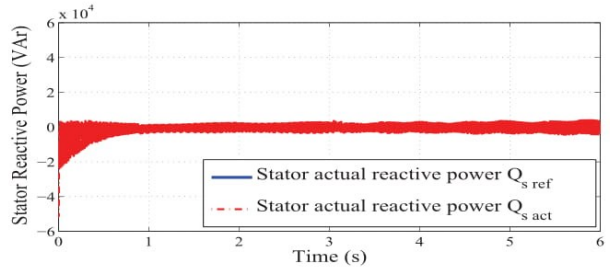

(a) Stator reactive power

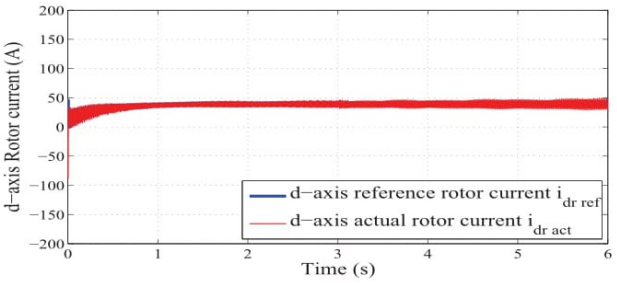

(b) *d*-axis rotor current

Fig. 13. Stator reactive power and *d*-axis rotor current

despite of the change of the rotor speed value as shown in Fig. 13(a) with good tracking of its *d-axis* rotor current represented in Fig. 13(b).Moreover the turbine torque and active power are represented in Fig. 14. The turbine active power and the torque changed their values depending on the changes of the proposed decoupled control. It can be shown in Fig. 16, due to the speed variation from 380 rad/s to 420 rad/s, the peak of the flow coefficient changed from 0.2995 to 0.266 under the investigated system in order to keep the flow coefficient under 0.3 and avoid the stalling phenomena.

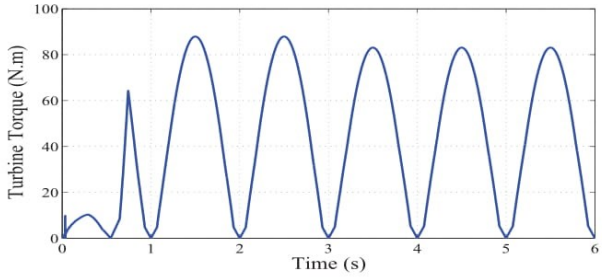

(a) Turbine torque

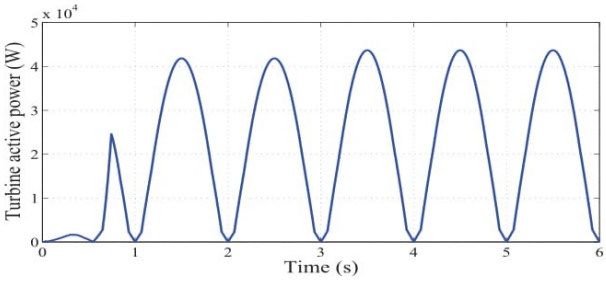

(b) Turbine active power

Fig. 14. Turbine generated torque and active power.

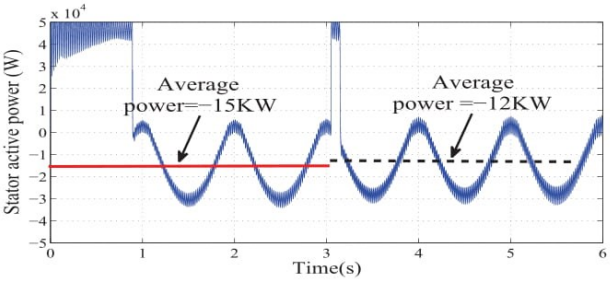

Fig. 15. DFIG stator active power

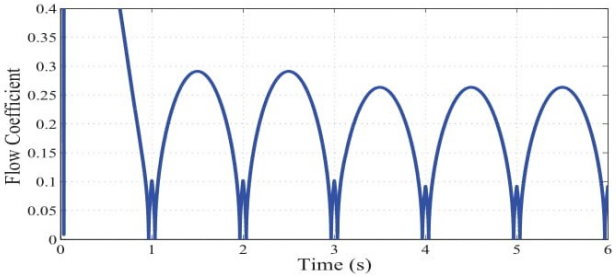

Fig. 16. Flow coefficient

VI. Conclusions

The presented paper proposes an enhanced performance control technique for OWC based wave energy conversion system featuring grid coupled DFIG. The proposed control technique offers decoupled control for the DFIG rotor speed corresponds to the stator active injected power and the stator reactive power. The proposed techniques effectiveness has been assessed by various simulation cases under varying generator speed and reactive power references. The investigated system under the proposed decoupled control techniques exhibits minimal steady-state oscillations and fast transient tracking.

References

[1] S. K. Mishra, S. Purwar, and N. Kishor, "Air flow control of owc wave power plants using fopid controller," in *2015 IEEE Conference on Control Applications (CCA)*, Sept 2015, pp. 1516–1521.

[2] M. Alberdi, M. Amundarain, A. J. Garrido, I. Garrido, and F. J. Maseda, "Fault-ride-through capability of oscillating-water-column-based wave-power-generation plants equipped with doubly fed induction generator and airflow control," *IEEE Transactions on Industrial Electronics*, vol. 58, no. 5, pp. 1501–1517, May 2011.

[3] D. Dunnett and J. S. Wallace, "Electricity generation from wave power in canada," *Renewable Energy*, vol. 34, no. 1, pp. 179 – 195, 2009. [Online]. Available: http://www.sciencedirect.com/science/article/pii/S0960148108001377

[4] W. Tease, J. Lees, and A. Hall, "Advances in oscillating water column air turbine development," in *Proc. of the Seventh European Wave and Tidal Energy Conference, Porto, Portugal*, 2007.

[5] A. J. Netto, P. R. Barros, C. B. Jacobina, A. M. N. Lima, and E. R. C. da Silva, "Indirect field-oriented control of an induction motor by using closed-loop identification," in *Fourtieth IAS Annual Meeting. Conference Record of the 2005 Industry Applications Conference, 2005.*, vol. 2, Oct 2005, pp. 1357–1362 Vol. 2.

[6] F. S. Trindade, A. J. S. Filho, R. V. Jacomini, and E. Ruppert, "Experimental results of sliding-mode power control for doubly-fed induction generator," in *2013 Brazilian Power Electronics Conference*, Oct 2013, pp. 686–691.

[7] T. J. T. Whittaker, "Learning form the islay wave power plant," in *EU's Initiatives in Satellite Communications - fixed and Broadcast (Digest No.: 1997/156), IEE Colloquium on*, May 1997, pp. 3/1–3/5.

[8] H. Bouhrim and A. E. Marjani, "On numerical modeling in owc systems for wave energy conversion," in *2014 International Renewable and Sustainable Energy Conference (IRSEC)*, Oct 2014, pp. 431–435.

[9] M. Alberdi, M. Amundarain, A. Garrido, and I. Garrido, "Ride through of owc-based wave power generation plant with air flow control under symmetrical voltage dips," in *Control Automation (MED), 2010 18th Mediterranean Conference on*, June 2010, pp. 1271–1277.

[10] M. Alberdi, M. Amundarain, A. J. Garrido, I. Garrido, O. Casquero, and M. D. la Sen, "Complementary control of oscillating water column-based wave energy conversion plants to improve the instantaneous power output," *IEEE Transactions on Energy Conversion*, vol. 26, no. 4, pp. 1021–1032, Dec 2011.

[11] S. Muthukumar, R. Desai, V. Jayashankar, S. Santhakumar, and T. Setoguchi, *ISOPE-I-05-077*. International Society of Offshore and Polar Engineers, ch. Design of a Stand-alone Wave Energy Plant.

[12] I. Garrido, A. J. Garrido, M. Alberdi, M. Amundarain, and M. de la Sen, "Sensor control for an oscillating water column plant," in *Sustainable Technologies (WCST), 2013 World Congress on*, Dec 2013, pp. 29–34.

[13] S. Anand, V. Jayashankar, S. Nagata, K. Toyota, M. Takao, and T. Setoguchi, "Turbines for wave energy plants," in *Proceedings of the 8th International Symposium on Experimental and Computational Aerothermodynamics of Internal Flows*, 2007, pp. 1–7.

[14] G. Abad, J. Lpez, M. Rodrguez, L. Marroyo, and G. Iwanski, *Testing the DFIM*. Wiley-IEEE Press, 2011, pp. 241–263. [Online]. Available: http://ieeexplore.ieee.org/xpl/articleDetails.jsp?arnumber=6047764

[15] B. Bose, *Modern power electronics and AC drives*. Upper Saddle River, NJ: Prentice Hall, 2002.

[16] M. I. Abdelkader, A. K. Abdelsalam, and A. A. H. Eldin, "Vector controlled brushless doubly fed twin stator cascaded induction generator for variable speed wind generation connected to weak grids," in *Power Electronics and Applications (EPE'15 ECCE-Europe), 2015 17th European Conference on*. IEEE, 2015, pp. 1–12.

[17] M. Amundarain, M. Alberdi, A. J. Garrido, and I. Garrido, "Modeling and simulation of wave energy generation plants: Output power control," *IEEE Transactions on Industrial Electronics*, vol. 58, no. 1, pp. 105–117, Jan 2011.

[18] J. Fletcher and J. Yang, *Introduction to the doubly-fed induction generator for wind power applications*. INTECH Open Access Publisher, 2010.

[19] A. Abdelsalam, M. Masoud, S. Finney, and B. Williams, "Vector control pwm-vsi induction motor drive with a long motor feeder: performance analysis of line filter networks," *IET electric power applications*, vol. 5, no. 5, pp. 443–456, 2011.

[20] A. K. Abdelsalam, M. I. Masoud, M. S. Hamad, and B. W. Williams, "Modified indirect vector control technique for current-source induction motor drive," *IEEE Transactions on Industry Applications*, vol. 48, no. 6, pp. 2433–2442, 2012.